BRNO UNIVERSITY OF TECHNOLOGY
VYSOKÉ UČENÍ TECHNICKÉ V BRNĚ

FACULTY OF MECHANICAL ENGINEERING
FAKULTA STROJNÍHO INŽENÝRSTVÍ

INSTITUTE OF MATERIALS SCIENCE AND ENGINEERING
ÚSTAV MATERIÁLOVÝCH VĚD A INŽENÝRSTVÍ

BEHAVIOUR OF THE INTERFACE OF LOW TOUGHNESS MATERIALS
CHOVÁNÍ ROZHRANÍ MATERIÁLŮ S NÍZKOU HOUŽEVNATOSTÍ

DOCTORAL THESIS
DIZERTAČNÍ PRÁCE

AUTHOR — **Ing. Martina Halasová**
AUTOR PRÁCE

SUPERVISOR — **Ing. Zdeněk Chlup, Ph.D.**
ŠKOLITEL

BRNO 2017

CONTENT

BIBLIOGRAPHIC CITATION

HALASOVÁ, M. *Behaviour of the Interface of Low Toughness Materials*. Brno: Brno University of Technology, Faculty of Mechanical Engineering, 2017. 161 p. Supervisor of the doctoral thesis Ing. Zdeněk Chlup, Ph.D..

BIBLIOGRAFICKÁ CITACE

HALASOVÁ, M. *Chování rozhraní materiálů s nízkou houževnatostí*. Brno: Vysoké učení technické v Brně, Fakulta strojního inženýrství, 2017. 161 s. Vedoucí dizertační práce Ing. Zdeněk Chlup, Ph.D..

STATEMENT

I hereby declare that I have written the PhD thesis on my own according to advice of my supervisor Ing. Zdeněk Chlup, PhD, and all the literary sources are quoted correctly and completely. This dissertation thesis is the property of the Faculty of Mechanical Engineering in Brno and it can be used for commercial purposes only with consent of the doctoral thesis supervisor and the dean of FME.

V Brně 29.5.2017 Ing. Martina Halasová

ACKNOWLEDGEMENT

I would like to thank to my supervisor Ing. Zdeněk Chlup, Ph.D., for giving me the opportunity to work in material research. I also thank him for his valuable advice, helping hand, and his endless patience and understanding.

I would like to thank to Ing. Martin Černý, Ph.D., from Institute of Rock Structure and Mechanics ASCR, v.v.i., and Ing. Adam Strachota, Ph.D., from Institute of Molecular Chemistry ASCR, v.v.i., for providing me the materials for my work and for the cooperation in the research work.

I would like to thank to Ing. Ivo Kuběna, Ph.D., for SEM and TEM sessions and EDS analysis.

I thank to all my colleagues in the Group of Brittle Fracture, for being a great collective, and to the Institute of Physics of Materials, for providing me the hinterland and instrumental equipment for my work.

The very special thank goes to my family and to my boyfriend for their love, care and support during the whole studies.

ABSTRACT

The work is focused on evaluation of factors influencing behaviour of interface in low toughness ceramic materials reinforced with fibres. The main aim was to characterise processing effects influencing the quality of fibre-matrix interface, with respect to final behaviour of composites at various loading type. The partial goal was to map the possibility of influencing the composite material by choice of matrix material, eventually by change of its processing, leading to change of interfacial properties without need of modification of reinforcement surface. The materials used in studied composites as a matrix were based on thermal transformation of polymer precursors, thus, the resulting materials were characterised in partially as well as in fully pyrolyzed state. Behaviour of interface in cpomposite materials was first evaluated from the global behaviour (i.e., change of mechanical properties) and in chosen representative composites also from the point of local changes in close surrounding of the interface (i.e., microstructure, chemical processes, fracture-mechanic processes, etc.) due to thermal exposition. In experiment were used particularly composite materials prepared by pyrolysis of polysiloxane resins reinforced by basalt fibres or Nextel™720 fibres. With respect to thermal resistance of the reinforcement, the basalt reinforced composites contained only partially pyrolyzed matrix (i.e., to temperature of 800°C), and in composites with Nextel™720 reinforcement was the matrix in form of fully pyrolyzed polymer into ceramic (SiOC). At partial pyrolysis of polysiloxane resin occurs rapid change of behaviour at temperature of 600°C. It was demonstrated, that around this temperature the formed interface with basalt fibre exhibits optimum adhesion/strength, allowing to reach sufficient level of composite strength at acceptable fracture toughness. Above temperature of 750°C occur significant difusion processes in the area of the interface and formation of new crystalline phases in the fibre, what deteriorates the fibre strength, and on the contrary, strengthen the interface cohesion, what leads to degradation of properties of the whole composite. At composite materials determined for high temperatures, reinforced by Nextel™720 fibres, was detected significant resistivity against oxidation caused especially by fully pyrolyzed matrix. As similarly important factor was observed the formation of mullite interphase in surface area of the fibre. Volume changes caused by formation of the interphase, difusional transport of the matter and thermal exposition led to formation of thermally and stress-induced micro-cracks, weakening interfacial surrounding in matrix as well as in fibre. This mechanism in contrast to amplifying chemical bond between fibre and matrix led to preserving of the composite properties also at high temperatures up to 1500°C. The work also dealed with effects of loading rate, where in contrast to static loading were observed different failure mechanisms. Realized research led to description and explanation of the influence of the fibre-matrix interface by change of matrix material processing parameters, which allow processing of economically advantageous and thermally stable composite.

KEYWORDS

Pyrolysis, Ceramic, Composites, Interface, Mechanical properties

ABSTRAKT

Práce je zaměřená na hodnocení faktorů ovlivňujících chování rozhraní v křehkých keramických materiálech vyztužených vlákny. Hlavním cílem bylo charakterizovat procesní vlivy působící na kvalitu rozhraní vlákno-matrice s ohledem na výsledné chování kompozitů při různém typu namáhání. Dílčím cílem bylo zmapovat možnost ovlivnění chování kompozitního materiálu volbou materiálu matrice, případně změnou postupu její přípravy, vedoucí ke změně vlastností rozhraní bez nutnosti modifikace povrchu výztuže. Jelikož materiál použitý ve studovaných kompozitech jako matrice byl založen na termické přeměně (pyrolýze) polymerních prekurzorů, byly výsledné materiály charakterizovány jak v částečně, tak i v plně pyrolyzovaném stavu. Chování rozhraní v kompozitních materiálech bylo hodnoceno nejprve z hlediska globálních projevů (tj. změn mechanických vlastností) a u vybraných reprezentativních kompozitů i z hlediska lokálních změn v blízkém okolí rozhraní (tj. mikrostruktury, chemických procesů, lomově mechanických procesů, atd.) vlivem různé teplotní expozice. V experimentu byly použity zejména kompozitní materiály připravené pyrolýzou polysiloxanových pryskyřic vyztužených čedičovými vlákny nebo vlákny typu Nextel™720. S ohledem na tepelnou odolnost výztuže obsahovaly čedičové kompozity matrici pyrolyzovanou pouze částečně (tj. do teploty 800°C), u kompozitů s výztuží z vláken Nextel™720 byla matrice již ve stavu po úplné přeměně polymeru na keramiku (SiOC). Při částečné pyrolýze polysiloxanové pryskyřice nastává rapidní změna chování kompozitu kolem teploty 600 °C. Bylo prokázáno, že v okolí této teploty má vytvořené rozhraní s čedičovým vláknem optimální adhezi/pevnost dovolující dosáhnout dostatečné úrovně pevnosti kompozitu při jeho přijatelné houževnatosti. Nad teplotou 750 °C již dochází k výrazným difúzním procesům v oblasti rozhraní a k tvorbě nových krystalických fází ve vlákně, čímž se zhoršuje pevnost vláken a naopak zesiluje soudržnost rozhraní, což vede k degradaci vlastností celého kompozitu. U kompozitních materiálů určených pro vysoké teploty, vyztužených vlákny Nextel™720, byla zjištěna výrazná odolnost proti oxidaci způsobená zejména plně pyrolyzovanou matricí. Neméně důležitým jevem byla pozorovaná tvorba mullitové mezifáze v povrchové oblasti vlákna. Objemové změny způsobené tvorbou mezifáze, difúzní přesun hmoty a teplotní expozice vedly k vytvoření tepelně a napěťově indukovaných mikro-trhlinek oslabujících okolí rozhraní v matrici i vlákně. Tento mechanismus v kontrastu se zesilující chemickou vazbou vlákna a matrice vedl k zachování vlastností kompozitu i při vysokých teplotách do 1500°C. Práce se také zabývala účinky rychlosti zatěžování, kde na rozdíl od statického zatěžování byly při dynamickém namáhání pozorovány jiné mechanismy porušení. Provedený výzkum vedl k popisu a vysvětlení ovlivnění vlastností rozhraní vlákno-matrice pomocí změny parametrů přípravy materiálu matrice, umožňující výrobu ekonomicky výhodného teplotně odolného kompozitu.

KLÍČOVÁ SLOVA

pyrolýza, keramika, kompozity, rozhraní, mechanické vlastnosti

1 STATE OF THE ART

Composite materials combine advantages of used components and gain the advantage of toughening mechanisms, the ability specific for composites, such as crack bridging, fibre pull-out, etc. [1-4]. The term composites covers a wide range of material combinations that can be classified for example according to the material used for: a) a matrix or b) a reinforcement.

Composites can be classified according to the type of matrix, simply named as X – Matrix Composites, where X stands for Polymer, Metal, Ceramic (abbreviated as PMCs, MMCs, CMCs). Classification according to the reinforcement can be further divided by: a) type (i.e., fibre-reinforced, particle-reinforced, structural, nanocomposites, etc.), b) shape (fibres, particles, discs and platelets, etc.), c) length (long, short), d) orientation (i.e., alignement: uni-, bi-, or multidirectional; misaligned = randomly oriented), and e) material (glass, ceramics, polymer, metal, concrete, etc.). A scheme of typical classification according to the reinforcement (a, b) and the matrix type (c) is represented in **Figure 1.1**.

A special type of composite which does not clearly belong to any cathegory is denoted as a hybrid composite. The hybrid composite can be for example reinforced by a combination of reinforcement types (e.g. fibres and particles) or by materials used (for example polymer + metal). Specific classification reflecting the application field may also appear, e.g. the classification of dental composites based on filler particle size [5].

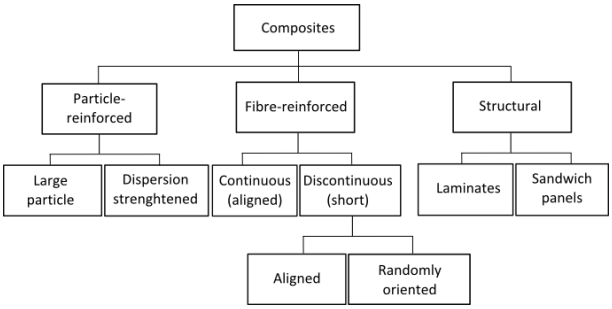

a)

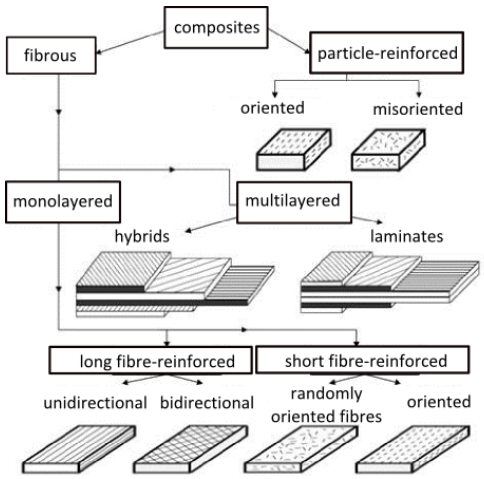

b)

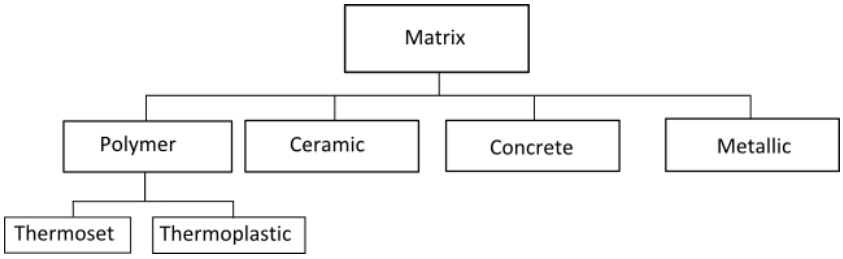

c)

Figure 1.1 *Classification of composites according to used reinforcement (a, b) and matrix (c).*

1.1 REINFORCEMENT

The principle of a reinforcement as a secondary phase in a composite is to improve properties of a primary phase – a matrix. There are several requirements on the reinforcement properties, dependently on the needs of final application. The main function of the reinforcement is to transfer the load from the matrix, i.e., to provide strength, stiffness, fracture toughness, or to affect thermal or electrical properties of the composite [4]. In a particular applications the reinforcing role of secondary phase is neglected and it serves only as a filler [6, 7], to decrease weight or cost of the final product, or, to act as a fire retardant (usually in polymer materials) [8].

According to the requirements on the composite function, there are various materials for reinforcement, similarly as in the case of matrix. The reinforcement can be natural or synthetic, organic or inorganic, ceramic/glass, polymer, metallic, etc. [9]. Reinforcements for CMCs are ceramic fibres, which can be divided into oxide and non-oxide group [10]. Oxide fibres are predominantly formed by silica (SiO_2) and alumina (Al_2O_3), e.g. Nextel fibres, Saphikon, etc. [10]. The non-oxide fibres are practically based on silicon (SiC, Si_3N_4) or carbon (e.g. Nicalon, Tyranno, Kevlar or Twaron [1]).

Besides the variability in materials, the reinforcement may have various shapes. There are two basic types: fibres and particles. The fibres are in one dimension extremely larger than in the other two directions. According to their length, or more precisely, aspect ratio (length to diameter *l/d*) they can be distinguished as short (discontinuous) or long (continuous) fibres [2, 11]. On the one hand, short fibres can be prepared from the continuous fibres by chopping, on the other hand, they can be prepared by a crystal growth, having only a low number of structural defects. These are called whiskers (length/diameter ratio is > 5000 [12]). The particles have approximately similar dimensions in all three directions. They can be spherical, polyhedral, or in form of flakes (or platelets) [13-15], etc.

The reinforcement shape, distribution, alignment and volume fraction influences the properties of the whole composite. The best reinforcement shape for transfer of load from the matrix is considered long fibres, as schematically captured in **Figure 1.2**.

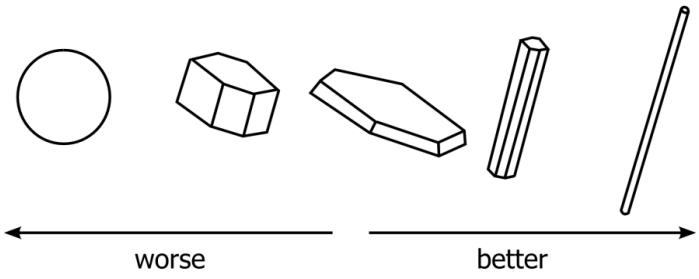

Figure 1.2 *Schematic representation of the effect of reinforcement shape on fracture toughness of a composite – from left to right: spherical, particular, platelet, whisker or short fibre, long fibre.*

Material in the fibrous form is much stronger than it would be in a bulk form. It is due to so called size-effect – the smaller the size (diameter), the lower is the probability of the presence of any imperfection. The defects still may be present in the fibre, but they are smaller, and rather

oriented in the direction of the fibre length. When the fibre is loaded to its limit, the failure occurs at the largest defect. Broken fibre is still able to carry some load and the broken parts become stronger than the previous unbroken part, because any further defect must be smaller than the previous one. At certain point, the fibre becomes too small to enable loading it to fracture, i.e., the fibre reaches its critical length l_c [1]. The critical length of the fibre can be obtained by a fragmentation test, used for quantitative measure of the fibre-matrix interfacial strength [1]. The critical length depends on the fibre strength σ_f, diameter d_f, and critical shear stress τ_c (see equation (1.1)). As written earlier, the length of the fibre is important for the load transfer from the matrix to the fibre. The fibre is used the most efficiently when the fibre length is such that the matrix and the fibre fail at the same strain.

$$l_c = \frac{\sigma_f d_f}{2\tau_c} \tag{1.1}$$

The distribution of the reinforcement in the composite should be ideally homogeneous. Homogeneously distributed fibres are fully surrounded by matrix, what allows transfer of load from the matrix to the fibre. Inhomogeneous distribution leads to formation of unsaturated fibre bundles, and the strength of the composite is of about 70 – 80 % of the homogeneous one, due to the inter-fibre friction [1]. On the contrary, in literature [16] was the inhomogeneous distribution of fibres considered as an advantage, in case that the composite (CMC) formed strong fibre-matrix interface and then the unsaturated fibre bundles allowed pull-out (toughening mechanism, explained further) to occur on the bundle level.

The alignment (or orientation) of the reinforcement becomes important especially in fibre reinforced composites. Each composite system is characterized by elastic constans (elastic modulus E, shear modulus G and Poisson ratio μ). In homogeneous isotropic materials, or composites with homogeneously dispersed particles, the elastic constants are independent on the loading directions. In fibre reinforced composites, the constants become orthotropic, i.e., the properties of a composite depend on the loading direction. The highest strengthening occurs when the fibres are aligned in the direction of loading (0°), as schematically depicted in **Figure 1.3**. The strengthening ability rapidly decreases, as the angle between the fibre direction and the loading direction increases (up to 90°).

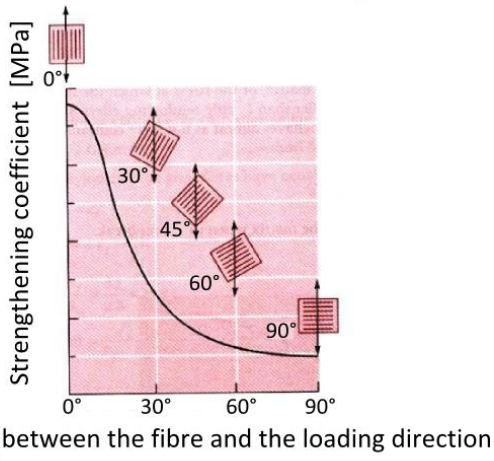

Figure 1.3 *An effect of the fibre orientation on the toughening of an epoxide composite [17].*

An important parameter is the volume fraction of the reinforcement, because it affects the composite properties linearly with increasing content of the reinforcement. Composite properties can be estimated by a rule of mixture, a weighted mean, used to estimate overall composite property, taking into account the volume ratio of individual components. For fibre reinforced composites were proposed two models, Voight (equation 1.2) for axial loading and Reuss (equation 1.3) for transversal loading, providing theoretical upper and lower bound, respectively, of elastic modulus, ultimate tensile strength, mass, density, or thermal and electrical conductivity.

$$E_c = \nu_f E_f + \left(1 - \nu_f\right) E_m \tag{1.2}$$

$$\frac{1}{E_c} = \frac{\nu_f}{E_f} + \frac{1 - \nu_f}{E_m} \tag{1.3}$$

E_c represents elastic modulus of the composite, v_f represents fibre volume, E_f represents elastic modulus of the fibres and E_m represents elastic modulus of the matrix. Both relationships are graphically expressed in **Figure 1.4** [18], which shows the influence of the reinforcement volume (x-axis) on the elastic modulus (y-axis) of the composite. The elastic modulus in longitudinal direction of the fibre reinforcement (the upper bound) is represented by line (7) in the image. The situation in the transversal direction (the lower bound) is represented by line (2) in the image. The graph shows theoretical elastic modulus from 0 % (pure matrix) to 100 % (pure reinforcement) of the fibre volume fraction. The effective volume ratio of the reinforcement is considered maximum up to 60-70 % [19] because higher content leads to the insufficient saturation by a matrix and the fibres are not supported effectively.

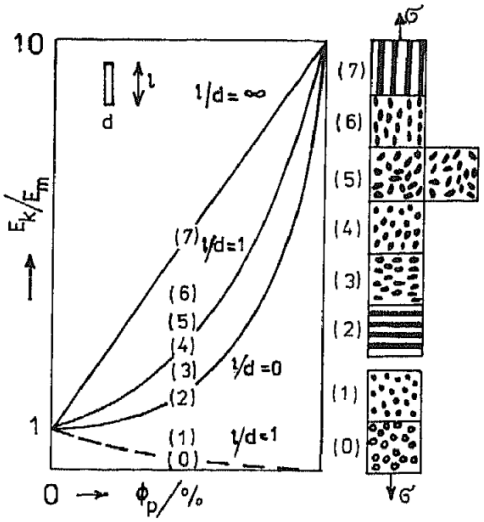

Figure 1.4 *The effect of the reinforcement shape on a relative change of elastic moduli. E_k, E_m, E_p and E_d are the elastic moduli of a composite, matrix, reinforcement/filler, and a voids (E_d = 0,) respectively. l, d are longitudinal and transversal dimensions of particles. Numbers in brackets represent following composite types: 0 – matrix with voids (solid foam), 1 – matrix with elastomer particles ($E_m > E_p$), 2, 7 – matrices with long fibres ($E_m < E_p$), 3, 6 – matrices with aligned short fibres ($E_m < E_p$), 4 – matrix with spherical particles ($E_m < E_p$), 5 – matrix with random fibres ($E_m < E_p$) [18].*

The reinforcement type, volume fraction and orientation determines the final properties of the composite. The reinforcement is oriented according to the loading conditions of the final application. Fibre reinforced composites (FRCs) are suitable for uniaxial loading, i.e., tensile loading in the direction of fibres, or flexural loading perpendicularly to the fibre alignment. Under the biaxial or multiaxial loading the composite would fail, therefore, the alignment must be arranged accordingly to the application.

The reinforcement structure in the composite is highly variable and also the composite processing has to be adapted to the composite final shape. In processing of FRCs are used also rovings and prepregs. Roving is a bundle of fibres, used for weaved composite structures such as cylindrical rods, pipes and tanks. Prepreg is a thin layer of fibres infiltrated and cured with a resin. The reinforcement can be simply layed-up of the rovings or prepregs, placed in desired orientations, or weaved from fibres into knitted or braided fabrics. Some examples are given in **Figure 1.5**.

a) Nextel fibre (3M) roving

b) prepreg of carbon fibre (Zoltek)

c) hand lay-up of woven fabric

d) braided reinforcement

Figure 1.5 *Possible forms of the reinforcement. a) roving [20], b) prepreg [21], c) hand lay-up of woven fabric [22], d) braided reinforcement [23].*

Mechanical properties of the composite change accordingly to the orientation of the reinforcement, as explained earlier. In comparison with the composite with certain volume fraction of unidirectionaly aligned fibres, the composite with the same volume fraction of e.g. plain woven fabric will have lower strength in the longitudinal direction, which will oppositedly increase in the transversal direction, dependently on the amount of fibres in the respective direction. Composites designed for multiaxial loading with variable arrangement of individual layers (laminae or plies)

are known as laminated fibre-reinforced composites. Such laminates combine e.g. longitudinal (0°), transversal (90°), and/or oblique (45°/-45°) lamina direction in the so-called stacking sequence. The stacking sequence is a code describing orientation of individual layers in laminate from bottom to top, or with respect to the midplane.

1.2 MATERIALS FOR COMPOSITE MATRICES

Matrix is a continuous phase of certain properties, which are enhanced by adequately chosen reinforcement. The choice of the reinforcement is influenced by composite properties requirements and also by the properties of the material for composite matrix. Advanced ceramics for CMCs can be prepared from polymer solutions and transformed into ceramics by a thermal process known as pyrolysis (described in detail in respective chapter). According to the processing method, such materials are denoted as Polymer-derived Ceramics. However, the level of transformation into ceramics depends on final temperature of the pyrolysis process, which governs whether the composite behave rather as PMC or CMC.

Polymers in general have low strength and elastic modulus (in comparison with metals and ceramics) and the main aim of the reinforcement is to strengthen the matrix and to enhance the overall elastic modulus of the composite. In return, the polymer matrix ensures toughness of the composite and protects the fibre from outter environmental conditions [24]. The ceramics have much higher strength than polymer or metal, but the ceramics suffer with brittleness. Moreover, ceramics sustain high temperature applications in comparison with metals and polymers. Thus, the main role of the reinforcement in the CMCs is to toughen the ceramic matrix, to prevent the composite from brittle failure, and concurrently to sustain high temperature environments, to be able to contribute to the composite toughness even at high temperature (>1000°C).

1.2.1 Polymers

Polymers are divided into thermoplastics and thermosets, according to their molecular structure. Thermoplastics are polymers with linear molecules what allows them to be melted at appropriate temperature to viscous liquid and cooled back to solid state. This ability to melt is highly advantageous for recycling of thermoplastics (e.g. polyester (PE), polyethyleneterephtalate (PET), polycarbonate (PC), polystyrene (PS), etc.). Thermosets are polymers with 3D cross-linked structure, formed by heating of viscous resins, due to that the thermosets sustain higher temperatures than thermoplastics. The most known thermosets are epoxides, polyurethanes, aminoplastics, phenols, and polyesters. Some thermoplastics with long chains and small substituents on the chains have the ability to crystallize, i.e., to arrange the polymer chain into lamellae with spherulitic structure, for example polyetheretherketone (PEEK), polyethylene (PE), polyethyleneterephthalate (PET), etc. [25, 26].

Typical stress-strain curve of amorphous polymer is displayed in **Figure 1.6**. At the beginning of the loading, linear elastic response can be observed from which the elastic modulus can be estimated. The elastic response is given by elongation of polymer chains, which is reversible process. Increment of the loading stress leads to untangeling of the chains, which is ireversible change. The material cross-section reduces, which leads to adequate decrease of the

stress. When the polymer chains are straightened enough, the stress increases again and at the critical point the fracture occurs.

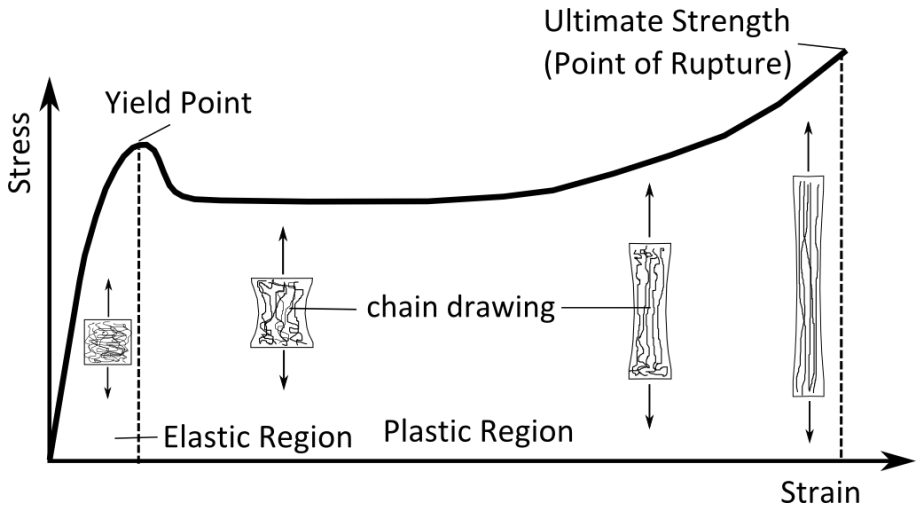

Figure 1.6 *Typical stress-strain curve of polymer.*

Shape of the loading curve of of the polymer material depends on the polymer type (i.e., the structure), loading temperature and loading rate. The influence of polymer type and loading temperature on the stress-strain behaviour can be seen in **Figure 1.7 a)** and **b)**. In the image is shown the effect of testing temperature on the stress-strain behaviour of **a)** PMMA (from [27]), and **b)** thermosetting epoxy resin [27]. The mechanical response of polymer to increasing loading rate is similar to decreasing temperature, i.e., slope of the stress-strain curve increases because the polymer becomes stiffer.

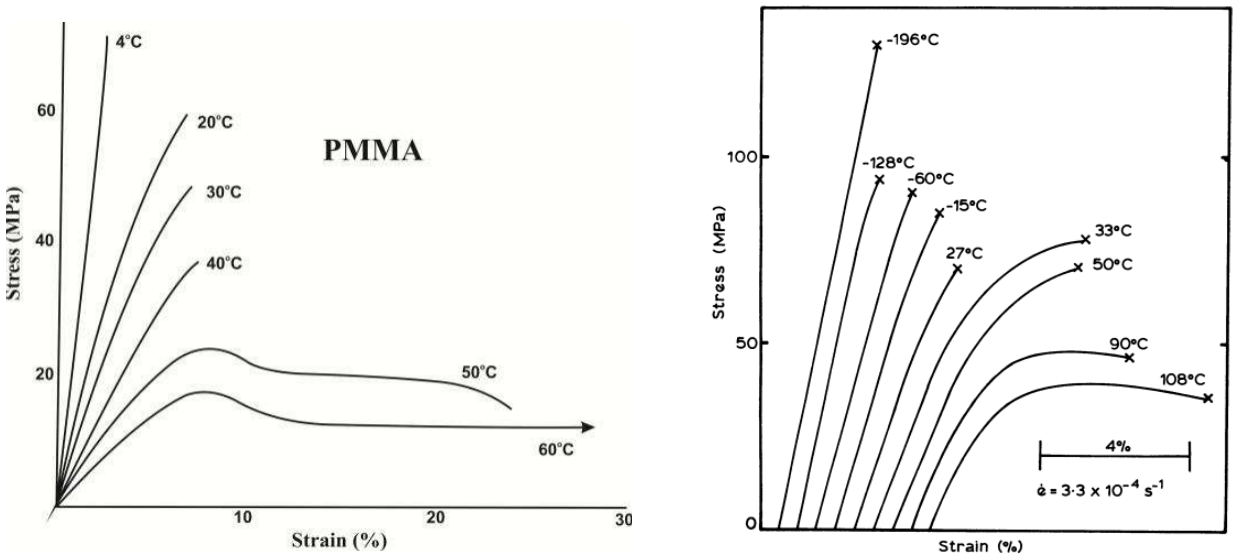

a) b)

Figure 1.7 *Tensile stress-strain curves: a) various polymers, b) effect of temperature on thermoplast [27].*

By comparison of images in **Figure 1.7 a)** and **b)** it is visible, that 3D cross-linked thermosets do not yield even at reasonably high temperatures. According to the polymer structure

and loading conditions, two types of plastic deformation during tensile loading can be observed: crazes and shear bands (shear yielding).

Linear amorphous polymers (e.g., PS, PMMA, PC, ABS,…) fail with brittle fracture at a room temperature. Under the loading, when a crack is present, crazes are formed at the crack tip. They are formed by microvoids between fibrils of polymer chains (see **Figure 1.8**). Crazes can be initiated also by surface defects or impurities in polymer structure. They are always oriented perpendicularly to the loading direction. They can only appear after tensile loading, never compressive. Craze growth can be terminated by formation of shear band at the end of the craze. Craze formation is closely related to fracture behaviour of polymer [28].

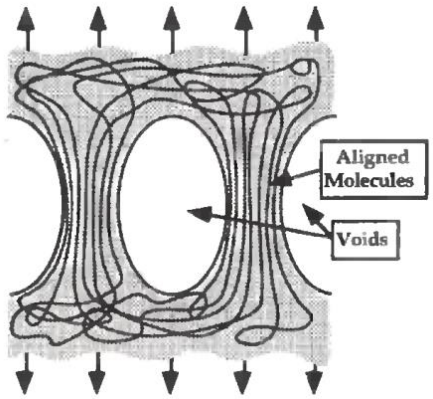

Figure 1.8 *Scheme of crazes in polymer material [28].*

Failure of the fibrils may lead to the open fracture. The fibrils mostly fail in the most opened (middle) part of the craze. Coalescence of microvoids forms cavities, which simplifies the crack growth. Primary crazes which initiated the fracture can be usually seen on the fracture surface. On the other hand, crazes can inhibit the crack growth by their formation in the crack front, partially consuming the elastic energy accumulated in material [28].

Shear bands in polymers are similar to those in crystalline metals, made by shear stress. They are oriented in 50 to 60° to the maximum tensile stress and 35–45° to the compressive stress axis. Their orientation is close to maximum shear stress plane (45°). The shear bands are preferably formed in shear or compressive loading at temperatures much lower than glass transition temperature (*Tg*) at which the polymer melts into visouc liquid. Morphology of the shear bands depends on the type of polymer and loading conditions, and they have significant role in the initiation of quasi-brittle fracture in semicrystalline polymers (PP, HPPE) [28]. The mechanism of the shear band formation is displayed in right bottom of **Figure 1.9**. Two mutually perpendicular slip lines appear in material. As a first is formed shorter, transversal type, followed by the second type, which is longer and longitudinal. They exist independently on each other and they can interact to form a cavity, which can initiate the crack formation [18].

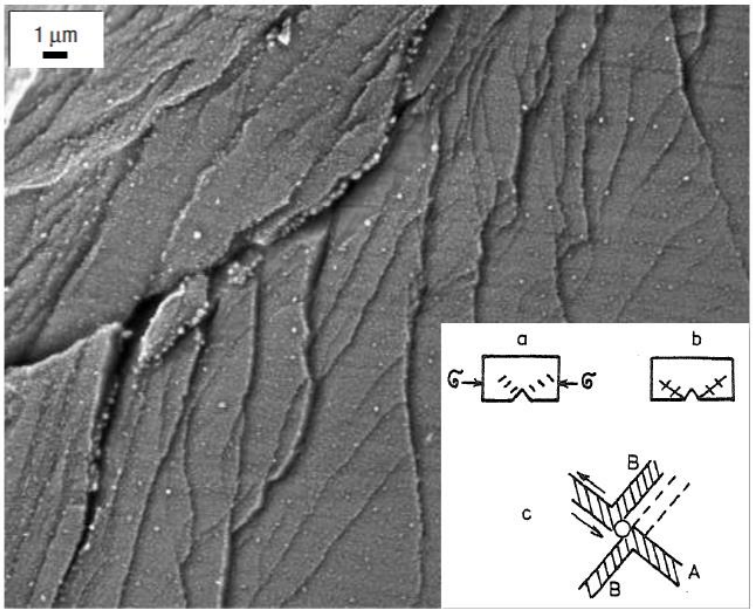

Figure 1.9 *The shear bands in metallic glass – (adapted from [29]). Inserted scheme: a) formation transversal slip lines, b) formation of longitudinal slip lines, c) interaction of primary and secondary formed slip. Reprinted from [18].*

In metals, basic fracture surfaces are brittle and ductile. This designation does not work well for polymers, due to the presence of plastically deformed regions in brittle fracture surfaces. Due to that the term quasi-brittle was introduced. The brittle fracture in polymers occurs when the surface does not show visible plastic deformation and the cross-section of the body in the area of the fracture surface remains practically the same as before loading. The fracture surface is oriented perpendicularly to loading direction. Ductile fracture from macroscopic point of view occurs after extensive plastic deformation. Plastic deformation can be initiated by various processes, depending on local strain velocity, temperature in the necking area and following strengthening process [18].

Most of the amorphous polymers exhibit characteristic brittle failure at temperature lower than is the glass transition temperature *Tg*. A crack front can propagate in several close planes (not in just one) which gradually join together. The situation is schematically shown in **Figure 1.10 a)**. In transition zone B the main crack front interacts with secondary cracks to form parabolas, which initiate secondary cracks. Sometimes they can divide into separated fields, typically in thermosets (e.g. epoxides) [18]. This type of fracture is called cleavage and it can be observed also in metals with restricted plastic flow. River pattern is typical fracture appearance, given by multifaceted surface, where each facet corresponds to a single grain in polycrystalline material. Propagating cleavage crack meets a grain boundary and accommodates to different angle of its crystal lattice. Crack propagates in several planes which join together in one plane by tearing, which consumes fracture energy [28].

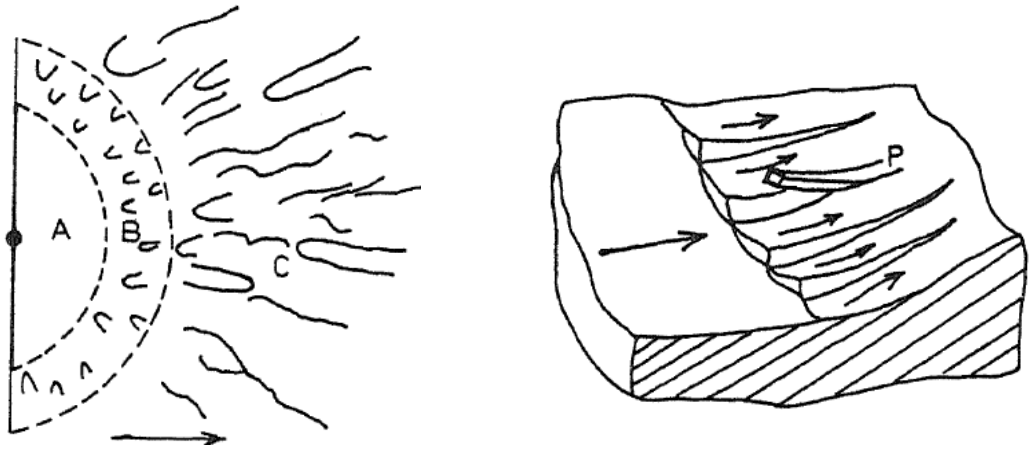

a) b)

Figure 1.10 *Scheme of brittle fracture in polymer: a) A – slow thermally activated fracture with smooth surface, B – transition zone with parabolic units (higher speed of propagating crack), and C – fast atermic residual fracture. b) division of crack front into several independent fields and formation of filaments [18].*

1.2.2 Ceramics

Ceramics prepared by sintering of powders usually have polycrystalline structure. Polymer-derived glasses, which belong to the group of advanced ceramics, have amorphous or nanocrystalline structure [30]. Common ceramic structure is formed by atoms or ions, having covalent or ionic bonds in regular arrangement. The arrangement depends on the relative size of chemical particle, type of bonding, and the need to balance electrostatic charges [31]. According to elemental composition, oxide (Al_2O_3, SiO_2, ZrO_2, etc.) and non-oxide (carbides, sulphides, nitrides, etc.) ceramic is recognized.

Ceramics can be processed from powder or slurry by sintering to the solid ceramic body at high temperatures. Polymer-derived ceramics are prepared by sol-gel process which later transforms through pyrolysis into a ceramic body [32]. This process has many advantages – the structure is more homogenized and pyrolysis requires lower temperature than sintering.

Typical properties of ceramics are high strength, hardness and abrasion resistivity at a comparatively low density. It withstands high temperature, which makes it attractive for burners, nozzles, heat exchangers, abrasives, grinding wheels, cutting tools, etc. [33-35]. On the other hand, ceramic contains flaws and defects introduced in the structure and especially on the surface during processing and machining. Due to these defects and absence of plasticity, the ceramics are inherently brittle. The brittleness is the limiting factor, because ceramics are stronger in compression than in tensile loading (about one order of magnitude). It is due to response of the present flaws to the direction of applied loading. The situation is schematically presented in **Figure 1.11** (reprinted from [36]). Under the tensile load, stress concentrates on the largest defect (particularly if located on the surface) and the crack propagates in the opening mode (i.e., tensile stress normal to the crack plane), until fracture. Under the compression load the crack twists from its original direction and propagates parallelly with the direction of acting force, which results in

the crushing. Increased stability in tensile load may be ensured by pre-stressing [37] or by introducing reinforcement.

Examples of typical ceramic and glass fracture surfaces are given in **Figure 1.12** (in image a) is a soda lime glass rod with the scheme of fracture marks [38], in image b) is a SiCN fibre [39]). The fracture surface shows characteristic marks. The failure begins usually at a flaw, called origin or nucleation point [38] (see scheme for image a), in image (b) is the origin marked with an arrow). Around the origin is smooth initial region called mirror, visible at the fracture surface, dependently on the applied stress [40]. After the crack reaches its critical velocity, it branches forming mist and hackle. The hackle marks indicate the crack propagation direction.

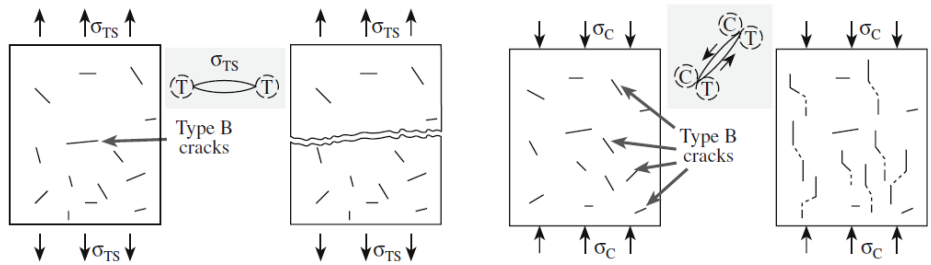

a) b)

Figure 1.11 Crack propagation under a) tensile (T) and b) compressive stress (C) [36].

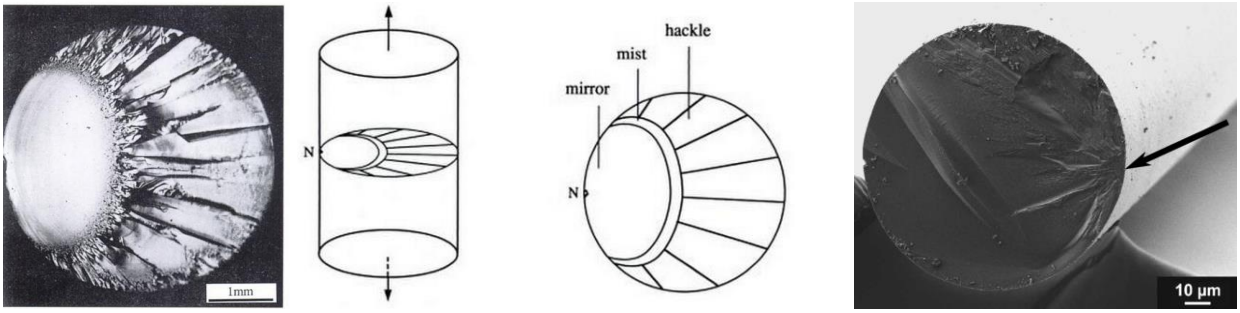

a) b)

Figure 1.12 *An example of fracture surface with characteristic marks: a) soda lime glass rod with the scheme of crack propagation in the rod [38], b) ML33S-derived SiCN fibre [39].*

1.3 COMPOSITE PROCESSING

In this chapter will be discussed processing techniques of CMCs and PMCs. The CMCs can be processed conventionally by powder techniques or by liquid routes. Gas phase infiltration process is also applicable [41, 42].

1.3.1 Sol-gel

Sol-gel is a liquid phase method used in many processes as a first step, in which the matrix material is synthesized. Initially, monomer molecules in the liquid solution have to react with each other to form colloidal sol. The reaction has two steps: hydrolysis and condensation, which occur in the solution practically at the same time [43].

Hydrolysis means cleavage of bonds in aqueous solution. It is equibalanced reaction and its speed and yield depends on the amount of water, pH of reaction solution and catalyst. Base-catalysed hydrolysis is slow and incomplete. Acidic catalysed hydrolysis is fast and almost all molecules of water (in stoichiometric amount) enter the reaction. Alkoxide and water are immiscible and as a solvent methanol or ethanol is used. In the reaction, alkoxysilane group is replaced by hydroxyl group and hydrolysed molecules condense while molecule of water is formed [44].

$$\equiv SiOR + H_2O \leftrightarrow \equiv SiOH + ROH \quad (1.4)$$

$$\equiv SiOH + \equiv SiOR \leftrightarrow \equiv SiOSi\equiv + ROH \quad (1.5)$$

Condensation means reaction of two molecules to form a large molecule and small molecule (usually water). Products of condensation are affected by pH of the polymer solution. Below the value of 1.5 [44] (<3 [42]), condensed molecules are rather short, forming dimers, short linear or cyclic oligomers. Higher value (pH=3 [44]; 5-7 [42]) leads to formation of more condensed oligomers.

$$\equiv SiOH + \equiv SiOH \leftrightarrow \equiv SiOSi\equiv + H_2O \quad (1.6)$$

During the condensation increases the gel viscosity as the molecules aggregate together by their surface SiOH groups and form runny 3D network of stable gel, filled with mobile residuum of sol. Gelation process (condensation) is irreversible [42]. As the gel dries into a xerogel, valence angle of the siloxane network decreases, which causes internal stress in the network [44]. Gel is then dried from solvents and cured (cross-linked). Cross-linking of the gel leads to formation of 3D-polymer network, accompanied with volume shrinkage and material densification. It occurs at low temperature, around 200°C, and the structure preserves the organic nature [43].

Sol-gel method is widely used for synthesis of powders, coatings, fibres or bulk materials with amorphous or crystalline structure. The mixing of the matrix component occurs at molecular level and the final product is chemically homogeneous. Because the final product – gel – is amorphous, sintering occurs at lower temperature, in comparison with conventional powder mixing methods [36]. The price of initial compounds is low and the purity of the final products is high; also the ceramic yield is low, due to shrinkage. Liquid state of the solution allows casting of variable shapes and forms.

1.3.2 Pyrolysis

Pyrolysis is usually subsequent step in processing of advanced ceramics, after the polymer compound synthesis, for example by the sol-gel method. Pyrolysis is heat induced decomposition of organic compounds under inert atmosphere of argon or nitrogen, in absence of oxygen. Decomposition of organic structure starts around 400–600°C, with loss of low-molecular volatile compounds (CH_4, H_2). The heat rate to the maximum temperature should be slow (units °C per minute); otherwise the gas expansion may cause serious damage of the structure. Full transformation occurs usually around 1000°C [42], depending on the composition of pyrolyzed

material. The duration of the pyrolysis depends on the dimensions of pyrolyzed specimen or required structure.

Pyrolysis is usually performed in conventional heating furnaces, and the whole specimen piece is first preheated and subsequently pyrolyzed at the same time. Some applications require selective heating, which is non-conventional method using laser, microwaves or ion radiation [42]. This approach allows preparation of complex shapes and solves the problem of joining, due to gradual processing of the ceramic body.

During the pyrolysis of the sol-gel synthesized materials, polymer-to-ceramics transformation takes place. During the transformation, specimen body either shrinks, changing its final shape, or many cracks are formed in its structure, as represented in **Figure 1.13**. This can be avoided by addition of fillers [6], which can suppress the matrix shrinkage and preserve intended shape of the processed ceramic part.

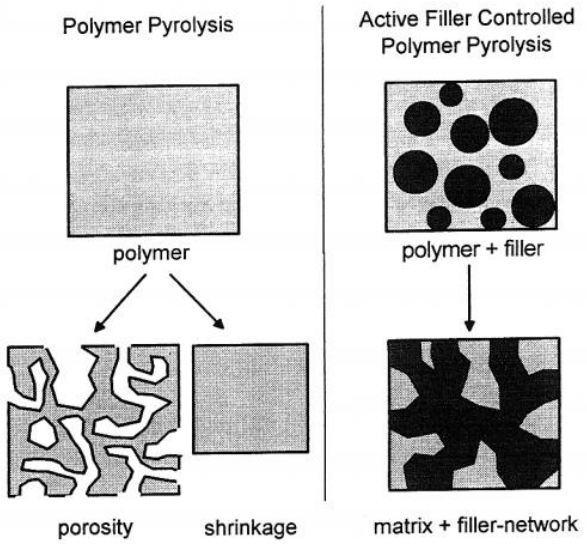

Figure 1.13 *The effect of filler addition into polymer mixture before the polymer-to-ceramic transformation: a) transformation without fillers – volume change or large porosity. b) transformation with active fillers [6].*

1.3.3 Polymer infiltration and pyrolysis – PIP

PIP is a liquid-state processing technique, initially used in fabrication of Polymer Matrix Composites and later in a modified way also for CMCs [45]. It is versatile method which can be used for large or complex-shaped structures [41]. The PIP process is schematically shown in **Figure 1.14**. Ceramic matrix is formed from liquid precursor or slurry and then infiltrated into reinforcement. Prior to the infiltration, the reinforcement can be coated to prevent formation of strong interfacial bond. The shaping of impregnated reinforcement includes filament winding, hand lay-up, etc. [41]. Shaped preform is cured (i.e., the polymer solution forms 3D crosslinked network) and pyrolyzed. The infiltration may be repeated, which minimizes the occurrence of the pores and cracks and increases the final product density.

The advantage of this process is low consolidation temperature between 800–1000°C, when the polymer is transformed into ceramics. Low processing temperature also prevents the reinforcement from damage [1]. Designing of the precursors composition makes the PIP method flexible for the manufacture of various ceramic matrices. The disadvantage of PIP can be seen in matrix shrinkage and cracking, which can be prevented for example by the repeated infiltration, hot pressing or addition of fillers into the polymer solution prior to material pyrolysis.

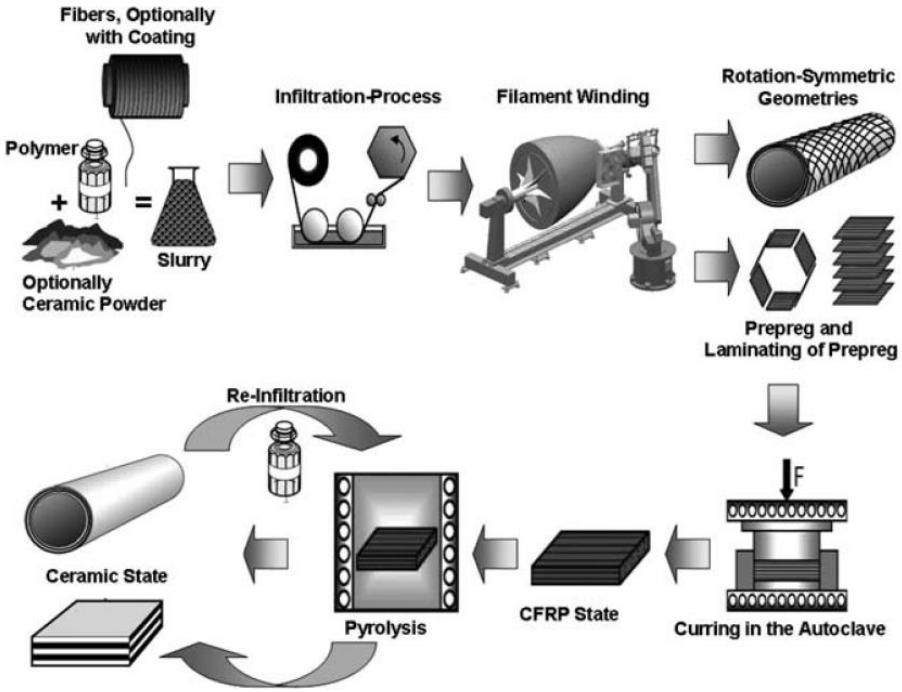

Figure 1.14 *Schematic representation of PIP process [41].*

1.3.4 Reactive melt infiltration – RMI

RMI is a pressureless infiltration process driven by capillary forces and surface tension. The processing temperature is quite high, above 1450°C [1], depending on melting temperature of infiltrated solution. The material can reach up to theoretical density [1, 45]. The method is suitable for components with complex geometries. The infiltration process is faster in comparison to CVI or PIP [45]. Nevertheless, this technique is not very popular for processing of CMCs because it is time consuming and expensive [36, 46]. By RMI method may be prepared SiC (for details see further in chapter 1.3.5) or Al_2O_3 by melting of Al in oxidative atmosphere (denoted as direct metal oxidation – DIMOX [47]).

1.3.5 Liquid Silicon Infiltration – LSI

LSI is a type of RMI; it is a method for production of CMC by infiltration of molten silicon into porous carbon preforms. The process occurs at temperature above 1600°C and in vacuum conditions [48]. The method is divided into a) manufacturing of preforms (by Resin Transfer Molding – RTM, or in autoclave) on which the carbon preform will be formed, b) forming of porous carbon preform and its infiltration by silicon-containing polymer solution and c) ceramization of the infiltrated preform by pyrolysis of polymer substrate (PIP, described in 1.3.3).

1.3.6 Chemical Vapor Impregnation/Infiltration – CVI

CVI is derived from Chemical Vapor Deposition (CVD), using comparatively larger amount of material. The method can be used for deposition of protective coating (or an interphase [49]) onto composite reinforcement. The gaseous phase is deposited on heated (<1200°C [10]) fibrous or 3D shaped preforms [1, 50]. The method is used in large scale where many preforms can be treated all at once, under low temperatures, in large infiltration furnaces. The method is not limited by product shape. The major advantage over another methods is low temperature between 150–1200°C [51], similarly to PIP. Precise control of processing temperature, gas flow and chamber pressure is critical in CVI [45]. The method is slow due to the requirement of several cycles, which makes it expensive. The porosity of the final product is between 10–15% and depends on the number of CVI cycles.

The mechanical properties of CMCs produced by Chemical Vapor Infiltration (CVI), Reactive Melt Infiltration (RMI) and Polymer Infiltration Pyrolysis (PIP) have similar tensile strengths and strain to failure if the same fibre coating have been applied [45]. CVI is advantageous due to the need of lower processing temperatures and CMCs processed by RMI have higher interlaminar shear strength because of the higher reached density. This also causes higher thermal conductivity, which makes them suitable for application in combustion liners [45].

1.3.7 Electrophoretic deposition – EPD

Electrophoretic deposition is a liquid phase method for processing of coatings, composites, or functionally graded materials, with thickness from nanometres to centimetres [42]. It can be also used for deposition of carbon nanotubes [52]. It is versatile, fast method, requiring simple and cheap equipment. EPD is a two-step process. In the first step (electrophoresis) the particles suspended or dispersed in a liquid acquire an electric charge and are forced through the electric field towards one of the two electrodes. In the second step (deposition) the particles form a coherent deposit on one of the electrodes. The deposited material is then dried and removed from the electrode. A shaped ‘green body’ of the composite is obtained and can be fired to CMC [53, 54].

1.3.8 Vacuum infiltration

Vacuum infiltration can be used for example to enhance mechanical properties of foam structures. These structures can be prepared by replica method, in which polymer foam is coated with ceramic slurry and then burned out in a furnace. The burnout of the polymer leads to formation of holes inside the ceramic foam struts, which decreases their mechanical properties. Thus, such sintered foam is placed into a vacuum tight cylinder, filled with slurry, and evacuated with a vacuum pump. After the foam is infiltrated, it has to be dried and sintered. Described method significantly increases strength of infiltrated material, while the weight increases by approximately 10 % [55].

1.3.9 Hot pressing – HP

Hot pressing is a solid phase technique, used for enhancing the density of sintered materials by application of a high temperature (~1300–2000°C) [56, 57] under a pressure. The application of pressure may be limited by the material of pressing dies [56]. The pressure is applied via hydraulic

press of pistons and the heat is induced via a furnace in which the die assembly is placed, as shown in **Figure 1.15**. The technique may involve consolidation of a powder or dried gel by pre-pressing it prior to hot press process itself. The material body (powder pressed into a pellet or dried gel) is put into the space between two pistons in a cylindrical mold and a pressure is applied, consequently, temperature in the furnace is increased to required level. The method is applicable for example for densification of laminate composites [58].

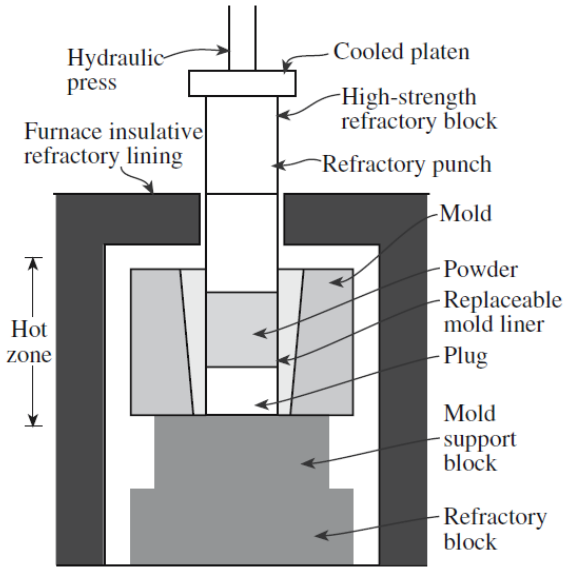

Figure 1.15 *Scheme of equipment for Hot Pressing [36].*

Application of pressure decreases required melting temperature, allowing using moderate temperatures, far below the melting temperature, which is usually needed for sintering (i.e., solidification) of the powder into a bulk material. Therefore, the grain growth or secondary recrystallization does not occur and also the densification of final bulk material is achieved without additives (binders) [36].

1.3.10 Spark plasma sintering – SPS

Spark plasma sintering, also known as Field-Activated Sintering Technique (FAST) or Pulsed Electric Current Sintering (PECS), is relatively new method that allows fabrication from powder to bulk materials with nearly theoretical density. The heat is generated internally, inside the sintered material. That allows very high heating or cooling rates (1000°C/min), short holding times (minutes) and low sintering temperatures (~250°C), compared to conventional powder sintering techniques, e.g. hot pressing, powder sintering or chemical vapor deposition (isothermal or isostatic). The method allows to sinter materials and their combinations. SPS was found to be successfull in direct joining of ceramics, with high quality of the joint, as reported in [59].

1.4 MECHANICAL PROPERTIES OF FIBRE-REINFORCED COMPOSITES AND THE INTERFACE EFFECTS

Mechanical properties of composites depend on the choice of both components – matrix and reinforcement – and their interface, which is of the same importance. Each component has their unique properties, depending on their nature. For example, the elastic modulus for ceramics is high, usually higher than for metals, whereas polymers have low modulus.

Ceramics are the only materials which can withstand extremely high temperatures. Unfortunately, ceramics have basically no plasticity and fail in brittle manner. Such insufficiency can be overcame with the use of the reinforcement. In **Figure 1.16** is shown the failure behaviour of a brittle monolith versus a fibre reinforced composite. The elastic modulus and maximum strength of the reinforced material significantly increased in comparison to unreinforced material and the difference in failure mechanism is obvious. After the maximum strength is reached, the monolith fails immediately, whereas in the composite occurs gradual decrease of strength as a consequence of toughening mechanisms, acting thanks to the presence of the fibre reinforcement. Crack propagating through the matrix approaches the reinforcement and the crack is forced to change its path, which leads to increase in energy absorption. The fracture toughness is in close relationship with the material strength. The highest strength is observed in ceramics, which exhibit no plasticity. On the contrary, more ductile materials (such as metals or plastics) do not reach the strength of ceramics but posses high ductility. The toughness of material reflects a compromise between the requirements on material strength and/or ductility [60].

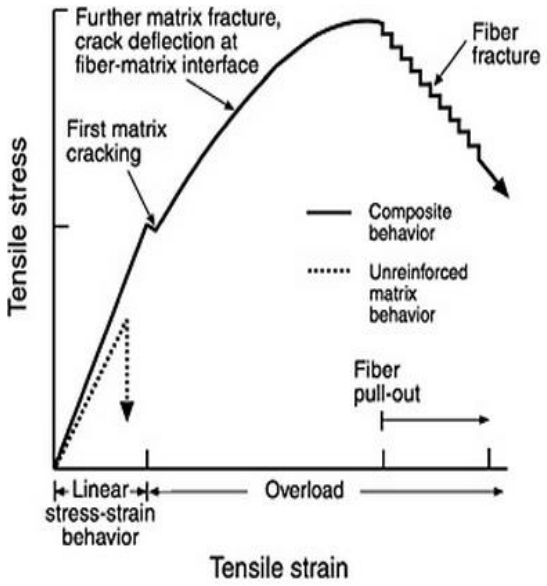

Figure 1.16 *Failure mechanism for monolithic ceramics and high-strength fibre-reinforced composite with lower-strength unreinforced matrix material [61, 62].*

The properties of composites are a function of the content of their components. Some properties are driven by the rule of mixture, such as density and mass. Strength and toughness of the composite are a result of composite synergism effect, i.e., combination of the materials possesses new material (composite) with properties that cannot be reached by use of individual components. Elastic modulus of composite depends on the loading direction (see chapter 2.1). In

the longitudinal direction the modulus obeys both rule of mixture and the Voight model, which assumes that the strain is limited by matrix [36, 63] and in the transversal direction implies Reuss model, which assumes that the stress is limited by strength of the fibres in transversal direction. Similar expression based on the rule of mixture can be obtained for strength of the composite σ_c, calculated in the direction of the reinforcement (2.5):

$$\sigma_c = v_f\sigma_f + (1-v_f)\sigma_m \tag{2.5}$$

where the v_f is the volume fraction of fibres and σ_f, σ_m is the stress of the fibres and matrix, respectively.

1.4.1 Toughening

The main reason of using the reinforcement is to enhance the property of material, usually strength or toughness, which brings us to two fundamentally different approaches – flaw control and toughening [64]. Flaw control accepts the brittleness and attempts to control the composite microstructure by processing. Toughening attempts to create microstructures imparting sufficient fracture resistance in such a way, that the strength becomes insensitive to the size of flaws [64].

Composite behaviour is influenced by the behaviour of matrix, reinforcement and the interface. Therefore, toughening mechanisms depend on individual type of composite (fibre-, particle-reinforced, laminate, etc.) and often appear as a combination of more types of toughening mechanisms (e.g. pull-out, crack bridging, crack deflection, etc.) at one time. Initially, the basic approach was to transfer the loading from the matrix to the reinforcement, usually fibrous, which had higher elastic modulus than matrix [65]. The principle of ceramic composite toughening is to slow down the crack propagating through the material and prevent it from the catastrophic failure. This is performed by absorption of energy on the crack front through the deflection or bifurcation (branching) of the crack path. The toughening mechanisms such as debonding, pull-out, bridging or microcracking can take place.

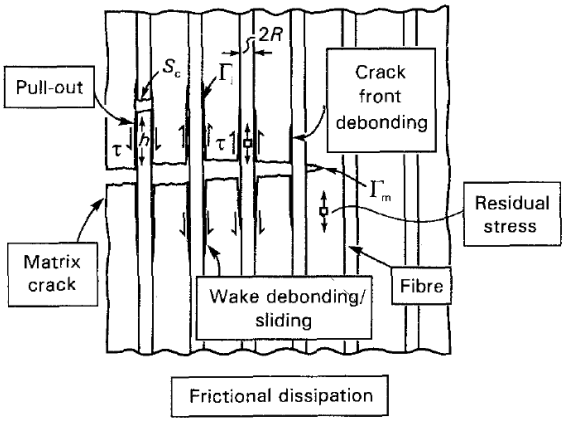

Figure 1.17 *Combination of various toughening mechanisms in fibrous composite [66].*

The toughening acts via combination of various mechanisms, as shown in **Figure 1.17** for fibrous composite. In fibre-reinforced PMCs, the main toughening mechanisms are fiber/matrix debonding, fibre pull-out, fibre fracture and polymer crazing (matrix fracture). The debonding and the pull out depend on the strength of the fibre/matrix interfacial bonding [1]. Failure in PMCs is

more dependent on the temperature than in CMCs. At lower temperatures the PMC matrix fails in brittle manner, accompanied by the fibre pull out. At room temperature, the same matrix locally deforms in a plastic manner, showing crazes [1]. When the failure of typical PMCs (i.e., low strength matrix with high strength fibres) occurs, the brittle fibre break at the first place, embedded in ductile matrix.

For toughening of CMC, presence of weak fibre/matrix interface is required. That may be complicated by high processing temperatures and thus possible chemical reaction between fibre and matrix, CMCs have a tendency to form a strong interfacial bond. The strength of the interface can be influenced by coating (sizing) of the reinforcement. The role of the coating is to prevent fibre-matrix bonding by formation of debonding interface layer (an interphase) between fibre and matrix, defending possible chemical reactions between fibre and matrix and thus, ensuring the crack deflection occurrence. For example monazite $LaPO_4$, which reduces fibre sliding misfit by its plastic flow [67], or boron nitride layer [68] which can be used for reinforcement coating. The role of coating will be discussed further.

Toughening mechanisms typically acting in fibre-reinforced CMCs are: fibre-matrix debonding, fibre pull-out, crack bridging by long fibres and matrix microcracking, as depicted in **Figure 1.17**. The failure of the CMC is usually a combination of them. Debonding between the fibre and the matrix occurs, when both components are weakly bonded and the crack propagates through their weak interface. The weak interface helps also pull-out mechanism to occur. After the fibre debonds and breaks, it pulls out of the matrix, dissipating the fracture energy. In the case that the reinforcement remains unbroken, crack bridging (impeding) mechanism takes place. The fibre holds both sides of the crack tip, blocking it from opening.

Special mechanism observed in ceramic matrix composites is microcracking [28]. The damage usually starts in the ceramic matrix and can initiate the fibre fracture, interface debonding or delamination [9]. Microcracks occur in regions of local residual tension, caused by thermal expansion mismatch and/or by structural transformation of the matrix [64]. It can be located in the interphase between the fibre and the matrix, or in the fibre coating, due to sliding movements of the fibres in the matrix.

1.4.2 Interface

Interface is a region between primary and secondary phase, matrix and reinforcement, respectively, where the properties change. It is comparably large area with crucial role for composite properties, because it ensures the stress transfer between the matrix and the reinforcement or toughening mechanisms take place there. Individual toughening mechanisms depend on composite systems and on the type of loading [28, 66, 69]. We recognize for example debonding, bridging, pull-out, mircroocracking, etc.

To understand the concept of the interface, a closer look on material bonding is required. The most important factors for bonding of two surfaces are the surface roughness and wettability, affecting the adhesion [1]. The most important types of interfacial bonding are chemical, physical and mechanical bonding. Schematic examples are given in **Figure 1.18**.

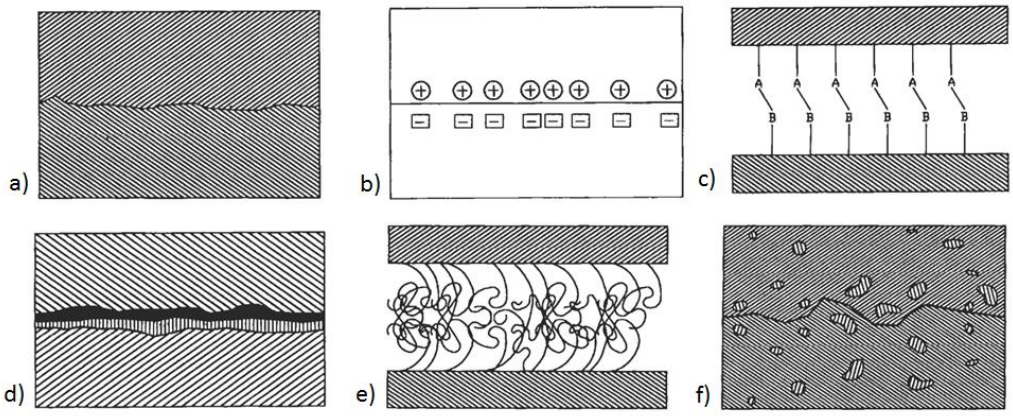

Figure 1.18 *Schematic representation of interfacial bonds: a) mechanical bonding: interlocking, b) physical bonding: electrostatic interactions, c) chemical reaction between two chemical groups from both surfaces, d) forming of a new compound – an interphase – by chemical reaction (particularly in MMCs), or by coating of reinforcement (e.g. in CMCs) e) chemical bonding: entanglement of molecules, f) chemical bonding: inter-diffusion of elements [70].*

Mechanical bonding, also called mechanical keeying or interlocking, is a situation when two surfaces are locked toghether. A particle of the reinforcement may be locked by a shrinking matrix, during processing, when the reinforced matrix is cooled down from a high temperature. It may happen when a large shrinkage occurs, it separates both phases and the only bond between them may be the mechanical one. A good mechanical bonding depends on wettability of a dispersed secondary phase by the continuous (primary) phase. The low wettability may negatively affect the mechanical bonding. A schematic illustration of mechanical bonding is shown in **Figure 1.19**, where scheme a) shows good adhesion of fibre to the matrix and b) shows voids present at the interface, caused by poor wetting of the fibre by the matrix [1].

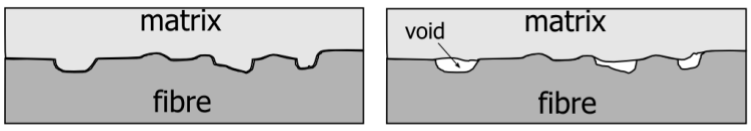

a) b)

Figure 1.19 *Scheme represents a) an interface with good adhesion of phases, b) an interface of fibre which is poorly wetted by matrix.*

Chemical bonding involves atomic or molecular transport between both surfaces, which leads to formation of a new compound at the interface [70]. Unlike physical bonding, chemical bonding is a matter of primary bonds - covalent, ionic or metallic (**Figure 1.18 c)**), which act in a short-range distances. The bond energy is approximately 40–400 kJ.mol^{-1} [1]. Depending on the character of acting particles, chemical reaction may occur by dissolution mechanism (electrons) or by reaction bonding (atoms, molecules or ions). The interface will have some certain thickness and we can rather call it an interphase (**Figure 1.18 d)**). The size of reaction area depends on the reactivity, particle motion and their concentration on interacting surfaces. The interphase can be introduced during composite processing, applied as a fibre coating [47, 67, 71-73]. A special case is an inter-diffusion. In PMCs, the interphase is formed between polymer and coupling agent applied on the surface of reinforcement, by entanglement of their molecular chains

(**Figure 1.18 e)**). The interphase has different properties than bulk matrix, e.g. can be significantly softer. A special case of inter-diffusion called exchange reaction was also observed in MMCs, where undesired products may be formed (**Figure 1.18 f)**) [70].

Physical bonding between two materials is a consequence of surface attractive forces. These forces are driven by a presence of charge fluctuations in atoms, which induces a dipole moment in them. This dipole moment causes two macroscopic surfaces to attract each other (**Figure 1.18 b)**). Physical bonding is conducted by weak or secondary forces (or secondary bonds) with very low energy, e.g. van der Waals forces and hydrogen bond, generally on the order of 10 $kJ \cdot mol^{-1}$ [74, 75]. The effect of van der Waals forces is used in interfacial coatings when carbon or boron nitride is used [10].

1.4.2.1 Strength of the interface

The strength of the interfacial bonding is affected by chemical or mechanical interactions between the matrix and the reinforcement surfaces. Strong interface is formed by chemical reaction or by mechanical clamping of reinforcement by the matrix. Weak interface can be achieved when the materials of the matrix and the reinforcement do not interact chemically or the matrix shrinkage does not occur, or only minimally. These requirements together with smooth fibre surface ensures the fibre sliding inside the matrix during the composite loading.

The requirement on the interfacial strength depends on the type of composite. In PMCs the fibre has much higher elastic modulus and strength than the matrix. The load is transferred from the matrix to the reinforcement which is able to carry more load than the matrix. The polymer matrix usually has a low strength and elastic modulus, and primarily serves as a protection of the reinforcement. Strong interface between the fibre and the matrix is required to increase the strength in PMCs, but block toughening mechanisms like debonding and pull out, which results in fracture of fibres embedded in the matrix. The fibres are able to effectively transfer the load until they reach their critical length by their several rupture. Weak interface will cause lower increase in strength, but when the composite fails, the toughening mechanisms will take place and the fracture surface will show fibres pulled out of the matrix [9]. The strength of the interface has to be balanced proportionally, according to requirements of mentioned application.

In polymer composites with soft matrix the strong interface is required. It can be reached by treatment of the reinforcement, to increase surface roughness, or addition of coupling agent, to allow reinforcement bonding with matrix [76]. Absorption of energy is performed through the cracking of the reinforcement and the strong interface preserves its shape, even with broken reinforcement. It can be compared with safety glass, which is only inversely designed. Broken glass fragments keep their position thanks to strong adhesion with polymer foil [77].

In CMCs is the situation completely different. The main application of ceramics is in high temperature environments, which only ceramics can sustain. Due to high temperatures the chemical reactions between fibres and matrix lead to formation of a strong bond. However, if there is a strong interface, the reinforcement loses the sense. Thus, weak interface is required, and several approaches can be used. The most common one is to form an interphase with appropriate properties.

1.4.2.2 Interphase

In CMCs, strong bond between the matrix and fibres may form during for example the infiltration process as a result of chemical interaction or their diffusion into each other, induced by elevated temperature. To prevent this situation, an interphase can be introduced. Interphase is an individual phase layer (or multilayer) in a narrow area between matrix and reinforcement in the composite. It can be formed either as a product of chemical reaction between the matrix and the reinforcement, or, it can be introduced on the fibres in form of coating prior to infiltration by matrix. The thickness of the coating is usually of 0.1–1 μm.

The function of the interphase is to ensure debonding and to protect the reinforcement from oxidation or to prevent it from aggressive action of the matrix, either during the preparation by infiltration process and either when compacted at elevated temperatures [47]. The interphase zone should act as a reaction barrier between the fibre and the matrix, inhibit diffusion of atmospheric species to the fibres and remain intrinsically stable at high temperatures in differing atmospheres, e.g. to avoid channelled oxidation from exposed fibre ends or via matrix microcracks [71]. Some types of interphase failure are given in **Figure 1.20**.

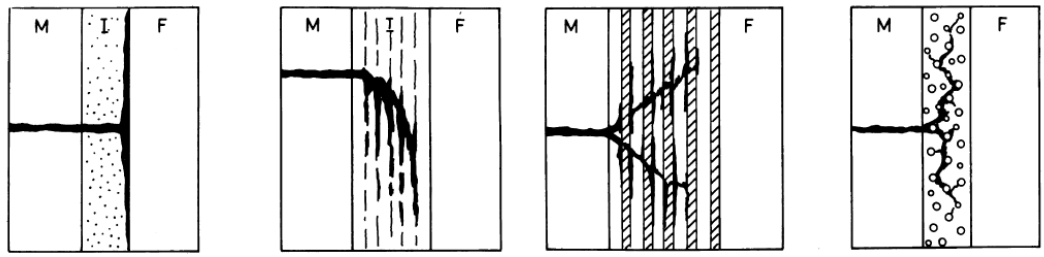

Figure 1.20 *Interphase (I) concepts between fibre (F) and matrix (M) in CMCs: a) weak interface, b) interphase with layered structure, c) multilayered interphase, d) porous interphase [49].*

To ensure good debonding between the composite components at the moment of composite failure, the interphase must have low shear strength, to allow slippage between the components. This of course, leads to decrease of the composite strength [78]. The most suitable materials for the formation of interphase are pyrolytic carbon and boron nitride, which form an interphase with layered structure of strongly bonded atoms in the plane of the layer and individual layers are bonded to each other with weak van der Waals forces [47, 63].

Some types of coatings can also increase the interfacial shear strength, by roughening of the fibre surface (etching, bleaching, etc.), or bonding to both fibre and matrix (coupling agents). This is good for PMCs, where the stronger bonding ensures better transfer of load from matrix to fibre.

During the processing of the composite (e.g. curing, pyrolysis, annealing), the coating may change its properties, or it can be removed (decomposed) from the reinforcement, during the composite processing. Removed coating leaves a gap between the fibre and the matrix. Such type of coating is called fugitive coating and it is applied to ensure no chemical bonding between matrix and reinforcement. As the fugitive coating is often used carbon. Carbon interphase is good

in non-oxidizing atmospheres up to 500°C and it can be removed by oxidation at ~500°C. Similar function fulfils for example boron nitride, withstanding oxidating atmospheres even up to 1200°C [47]. Composites with a gap between the matrix and the reinforcement cannot be loaded in direction transversal to the reinforcement direction [63, 79].

1.5 FAILURE OF COMPOSITES

1.5.1 Failure in PMCs

Plasticity of polymers plays significant role in composites mechanical properties. Ductile fracture starts from cavities at interface. Increasing stress causes fibril formations which strenghten, and with good adhesion onto reinforcement they significantly increase toughness of ductile materals. Brittle thermosets exhibit high toughness in PMCs, on the contrary, the effect is reversed for high toughness matrices. Experimental observations shown that the reason is the fibre constraint [80]. The fibre restrains the crack-tip yielding, which leads to smaller damage zone, thus, lower fracture energy.

In some situations, conventional fracture mechanics is appropriate for composites, but it has to be kept in mind, that the theories are intended for homogeneous materials. Conventional fracture mechanics assumes dominant crack which grows during propagation through the material. Fracture in Fibre-reinforced Polymer Composites (FRPC) is often controled by numerous microcracks distributed throughout the material, rather than a single macroscopic crack [28].

In tensile loading several mechanisms such as matrix cracking, fibre bridging, rupture, fibre-matrix debonding and pull-out take place in the composite failure. Due to orthotropic mechanical properties of continuous Fibre-reinforced Polymer Composites, out of plane loading leads to delamination, because the fibres do not contribute to the strength in this direction. Compressive loading can lead to microbuckling of fibres, in case of soft matrix which does not support the fibres. Moreover, the fibres have tendency to wave during the composite processing, which causes their less stability in the loading. Additionally, preexisting delaminated region (caused by loading, bad wettability of reinforcement by the polymer mixture prior to matrix synthesis, or caused by the composite manufacturing) can cause macroscopic delamination buckling. The failure mechanisms are represented in **Figure 1.21** [28].

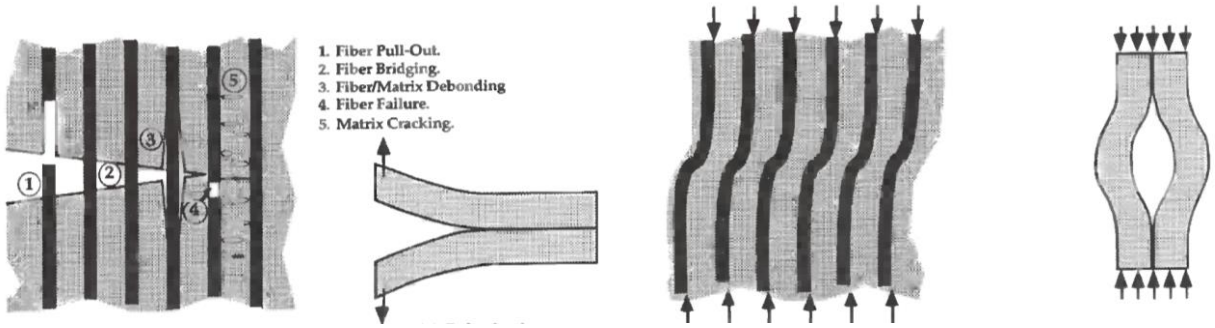

Figure 1.21 *Failure mechanisms in fibre-reinforced polymer composites: a) in-pane damage, b) delamination, c) microbuckling, d) buckling delamination [28].*

1.5.2 Failure in CMCs

CMCs were originaly developed for military and aerospace applications. They exhibit high mechanical properties (strength and stiffness) at high or very high temperatures (400–3000°C) [10]. With respect to other composites (PMCs, MMCs), CMCs are called inverse composites, due to the fact, that the matrix strain at the moment of failure is much lower than that of the fibres [49], i.e., the failure of CMC composite starts by failure of the matrix. As a result, microcracking in CMC composite takes place, which cannot be observed in PMCs or MMCs. The microcracking leads to residual stress release and reduction of the elastic modulus in the microcracked area, and the toughening takes places by the absorption of strain release energy [65, 81]. Besides the microcracking, other common types of toughening mechanisms (e.g. fibre-matrix debonding, fibre bridging and fibre pull-out) in CMCs can take place [1, 28].

In CMCs, the fibre-matrix debonding mechanism can be described as mode II fracture phenomenon, a shear. In the fibre reinforced composite under load, the crack propagates through the matrix and when it approaches the fibre-matrix interface, two situations dependently on the interfacial strength can occur. In weakly bonded interface the crack can deflect at the fibre and continue in the direction along the fibre. In case of strong interface, the crack will not deflect along the interface and rather continue through the fibre, resulting in its failure, which in CMC composite can lead to brittle failure of the whole composite, with no or minimum toughening effect [66].

The mechanism of crack propagation depends on the debond energy Γ_i, as schematically represented in **Figure 1.22**. For debonding and sliding, the value of the debond energy cannot exceed an upper bound, relative to energy of fibre failure Γ_f. Most ceramics fibres have $\Gamma_f \approx 20$ Jm^{-2} which according to the equation (1.7) indicates the upper bound to be $\Gamma_i \approx 5$ Jm^{-2} [66].

$$\Gamma_f \leq \left(\frac{1}{4}\right)\Gamma_i \tag{1.7}$$

For debonded fibre-matrix interface becomes important friction stress. That is affected by the fibre surface roughness (because matrix is applied onto them and adopts their shape), wettability and pre-stressing, which causes the presence of residual stress in the composite.

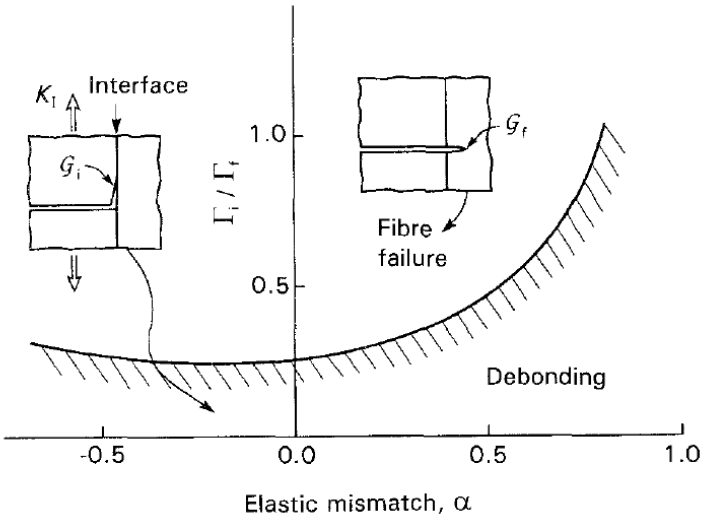

Figure 1.22 *Crack at the interface and its deflection along the fibre (in case of weak interface) and its propagation through the fibre [82].*

1.6 SIOC-BASED MATERIALS

Silicon-oxycarbide (SiOC) is a black-coloured material obtained by pyrolysis of organometallic resins (polysiloxanes), prepared via sol-gel process [43]. During the pyrolysis the organometallic resin – polysiloxane – transforms from liquid solution through cross-linked polymer into black, glassy material. According to the processing method, it is classified as the polymer-derived ceramics [83, 84], although the structure of SiOC remains amorphous when pyrolyzed at and above 1000°C [85]. Nevertheless, the crystalline structure may be achieved by controlled thermal processing [86].

Si-O-C contains SiO_2 and SiC rich phases (**Figure 1.23**). Although it cannot be arranged into regular crystalline structure (due to different length of Si–O and Si–C bonds [87]), it is stable ternary phase, Si–O–C, represented by the diagram in **Figure 1.24**. Besides Si–O and Si–C, C–C bonds are present, too, in form of turbostratic (free) carbon (in sp^2 hybridization) [88], which causes the typical black colour of the SiOC glass [89]. C=O bond can exist in SiOC glass [90] but not necesarily [89].

Si-based glasses can be prepared from various organic compounds with Si as central atom, for example polycarbosilanes, polysilsesquioxanes, polysiloxanes (see **Figure 1.25**). Into the group of polysiloxanes belong methyltriethoxysilane (MTEOS, T) and dimethyldiethoxysilane (DMDEOS, D), the basic siloxane monomers for the synthesis of SiOC [91-93]. T is trifunctional (branching) and D is bifunctional (linear) unit. The ratio T/D = 2 possesses composition of SiOC glass, which lies on the stoichiometric tie line between SiO_2 and SiC in ternary diagram of Si, O and C (see **Figure 1.24**). The stoichiometric composition of the SiOC is presented as $SiC_xO_{2(1-x)}$ [94]. Compositions with T/D $\leq$ 2 leads to the formation of excess (free, turbostratic) carbon [86] in SiOC structure, T/D $\geq$ 2 exhibits the excess of Si [95].

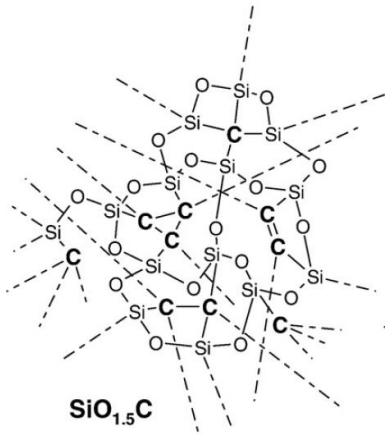

Figure 1.23 *Scheme of the structure of a pyrolyzed SiOC glass [96].*

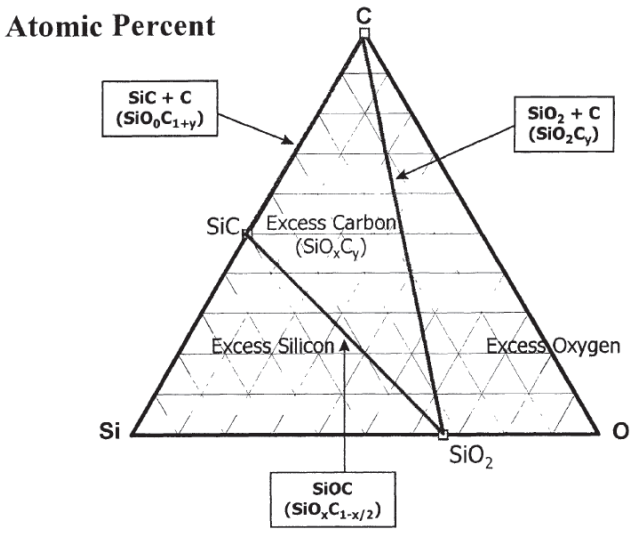

Figure 1.24 *Ternary phase diagram of Si–O–C [97].*

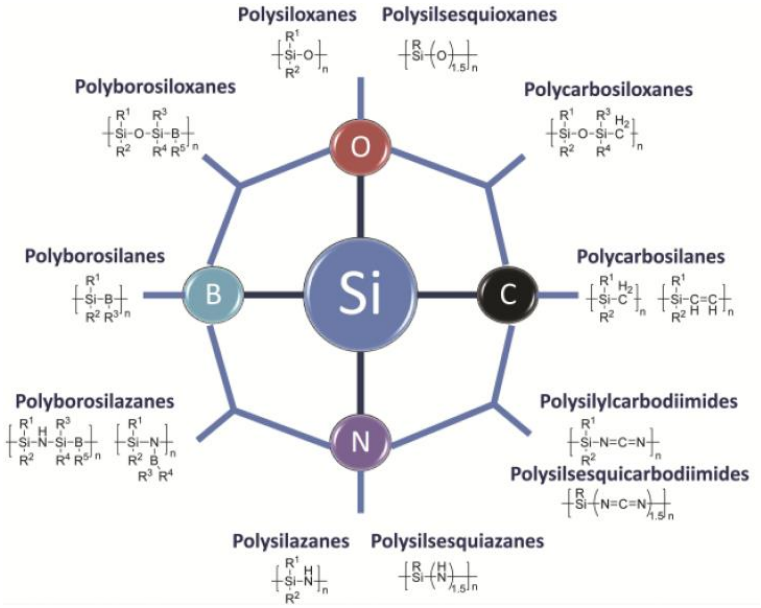

Figure 1.25 *Silicon containing polymers [84].*

The structure and mechanical properties of SiOC glass can be affected by the processing [98]. Also, incorporation of various elements, mostly metals (Al, Zr, Hf, Ti, Sn, Fe, etc.) [99, 100] moderates the SiOC properties. For example, boron increases the porosity of SiOC glass with formation of large pores [101], probably due to formation of B_4C (carburization) [102]. Iron helps to decrease the adhesion of SiOC glass to glass fibres (according to the correspondence with dr. A. Strachota). Strontium enhances flexural strength, probably due to induced crystallization of *β*–cristoballite and *β*–SiC modification. Addition of α–alumina microsized powder to SiOC leads to formation of mullite above 1500°C. When nanosized *γ*–alumina is used, it reacts with SiOC at 1250°C to form single phase mullite [84]. Formation of mullite is accompanied with volume expansion, which competes with the shrinkage of SiOC [103].

1.6.1 Processing of SiOC glass

SiOC material is prepared by powder and/or liquid route. Liquid route involves sol-gel solutions and liquid polymers. Sol-gel is probably the most widely used method for producing of solid bulk SiOC from liquid polymers. It consists of two steps: first is formation of a sol and second is transformation of sol into a gel. In case of SiOC, sol is a solution, formed by alkylsiloxanes hydrolyzed in alcohol, with low pH [44]. Hydrolysis is followed by condensation of monomers into polymeric structure, which aggregates and gelates. The gel is a weak porous structure which usualy contains residual water and alcohol, and those have to be removed. The gel undergo large shrinkage (see scheme in **Figure 1.26**) which can lead tothea crack formation. During polymer-to-ceramic conversion (curing and pyrolysis) cracks and pores are formed, too, which negatively affects the mechanical properties. The cracking may be more significant around carbon-rich regions which shrinks more than the other regions [104].

Due to the cracking and pores present in the structure, repeated infiltration was introduced in the composite processing, enhancing the density [105-107]. Nevertheless, crack-free SiOC without fillers can be prepared for example by Field-assisted Sintering Technique (FAST) from powders, obtained by milling of bulk SiOC glass [108].

Drying can be done at room temperature, followed by curing at elevated temperatures. The curing (cross-linking) takes place at 100–400°C and during that the polymer chains rearange via radical polymerization into 3D network. This process is crucial for later ceramic yield [109, 110]. Cured material preserves its organic nature, which is ceramized in pyrolysis process. At temperatures between 400–1000°C the material undergoes the polymer to ceramics transformation, i.e., it is pyrolyzed only partially, and contains both organic and inorganic phases [111]. Their ratio depends on the condition of the synthesis of the gel [44], as well as on the pyrolysis process (duration, temperature). The transformation of the polymer to glass/ceramics during pyrolysis is schematically captured in **Figure 1.27**, represented through the reorganisation of the polymer polycarbosilane structure to initially amorphous, and later crystalline SiC structure [6]. During the transformation from gel to glass the number of Si–O bonds remains constant [112].

Usually, study of mechanical properties of individual SiOC glasses (not composites) is hindered due to the limitation in fabrication of suitable bulk specimens. Methods for preparation of small bulks specimens involve warm pressing of gels, casting of sol-gel solution or liquid polymer [84].

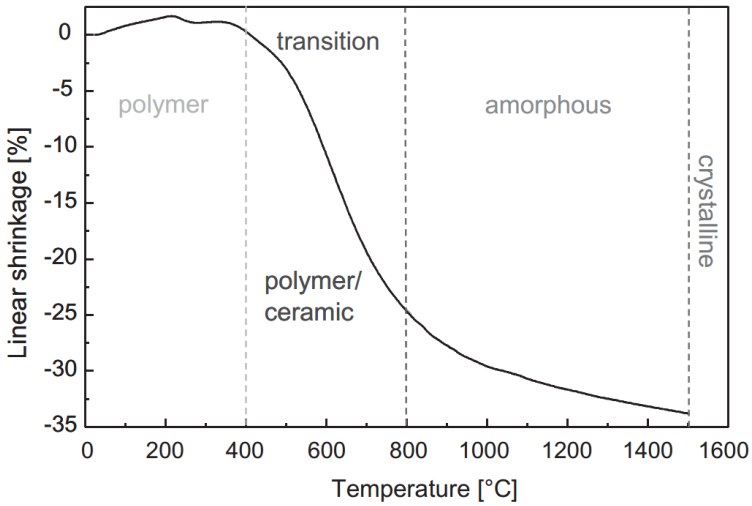

Figure 1.26 *Scheme of temperature dependence of shrinkage for SiCN with indication of transformation stages [41].*

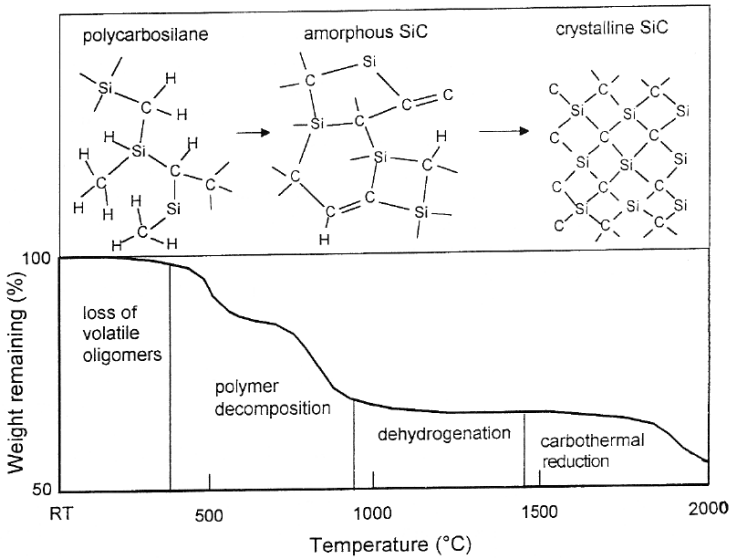

Figure 1.27 *Polymer to glass (ceramic) transformation of polycarbosilane [6].*

1.6.2 Structural changes at elevated temperatures

The SiOC structure and the processes at elevated temperatures depend on many factors – chemical composition of starting monomers, or the mixing ratio of the monomers [92, 93, 113], pH of the solution, temperature of sol-gel and of cross-linking and transformation processes (pyrolysis) [44, 114]. For example, in [93] was reported that pyrolysis of polysiloxane resins at the temperature of 1100°C gives slightly better values in hardness and indentation elastic modulus, compared to pyrolysis at 1000°C. In [94] was reported dependence of the SiOC powder grain size on the temperature of the SiOC structure degradation. During processing, SiOC glass undergoes loss of volatile compounds accompanied with weight loss and extensive volume shrinkage [115].

Pyrolyzed SiOC glass is stable up to 1400°C in inert atmosphere [94, 116]. At 1200°C, starts the formation of SiO_2 and crystalization of β–SiC [92, 101, 117]. β–SiC is still present in SiOC structure at 1400°C [101]. Above 1500°C gaseous SiO and CO are evolved [118].

Production of gaseous SiO increases the porosity of SiOC glass and is associated with high content of linear monomer (MTEOS) [92].

In the oxidation atmosphere, the oxidation of SiC is accompanied with weight gain (SiC oxidizes to SiO [113]) and oxidation of free carbon leads to weight loss, which initiates the structural degradation of SiOC [94]. The SiOC glass has enhanced resistivity agains oxidative atmosphere at elevated temperatures thanks to oxygen atoms incorporated in the structure [89]. Annealing at 1000°C does not induce any changes associated with oxidation of SiOC structure. At higher temperatures, crystalline cristoballite forms at the surface [89, 119] and at 1550°C was found in the inner structure, which led to deterioration of mechanical properties [119].

1.6.3 Properties of SiOC glass

Density of SiOC glass ranges between 2.1 to 2.4 $g \cdot cm^{-3}$ (stoichiometric SiOC (i.e., T/D = 2, the structural formula is often represented as $SiC_xO_{2(1-x)}$) ~2.2 [104], 2.23 [120], 2.35 [88], ~2 [119], and 2.16 $g \cdot cm^{-3}$ [99]). SiOC is insensitive to moisture [105], which is an advantage for measurement of the SiOC density, evaluated by weighting of SiOC materials via Archimedean displacement method (for details see chapter 3.2.3). In composites, density can be increased by repeated infiltration of the polymeric resin [79] (i.e., the matrix before it is cured and pyrolyzed) into the reinforcement, which reduces the number of pores in the composite structure.

Elastic modulus of stoichiometric SiOC measured by four point bending on round rods (hot-pressed at 1400–1600°C) was 90–130 GPa [92]. Indentation elastic modulus (E_{IT}) (loading 300g = HV0.3) of SiOC glass prepared by crosslinking of powdered polymethylsilsesquioxane pyrolyzed at 1100°C at the level of 100 GPa was reported in [120]. E_{IT} of stoichiometric SiOC glass annealed between 1100–1500°C was 60–80 GPa, with deterioration of the modulus from 1300°C and above. In T/D = 1 (with excess of carbon) the highest value of E_{IT} was 70 GPa at 1300–1400°C, at 1500°C deteriorated to 50 GPa.

Hardness is an important characteristic of SiOC glasses. In fully pyrolyzed glass, high internal stress leads to formation of small fragments of SiOC. Therefore, the major mechanical characterisation of individual SiOC material (not composites) is instrumented hardness measurement, analysing Vickers and Martens hardness. The hardness value of SiOC glass lies in the range from 7 to 12 GPa [88, 91, 108, 119, 120]. The stoichiometric SiOC reached its maximum hardness on the level of 13 GPa (1350 HV0.2) when pyrolyzed at 1300°C. Martens hardness was 4800 MPa already at the pyrolysis state of 1200°C and then deteriorated with large scatter in the data [93], reflecting the structural changes of SiOC glass. Excess of Si slightly increases the hardness, according to the literature [93]. In [91], Vickers hardness of ~9 GPa on the T/D = 1 pyrolyzed at 1000–1200°C was reported. Hardness of SiOC material pyrolyzed only partially at 600–800°C under loading of 10 N reached 1–4 GPa in [92].

The hardness of SiOC glass may be influenced by the processing conditions, e.g., pyrolysis temperature [91] or annealing. Also, the SiOC glass composition plays significant role. For example, an increase of hardness after the pyrolysis is ascribed to crystallization of SiC [108]. Annealing may deteriorate the hardness of fully pyrolyzed material dependently on the content of free carbon [92].

Flexural strength of the SiOC glass with excess free carbon (SiOC glass prepared from the mixture of polysiloxanes in the ratio T/D = 1) pyrolyzed at 1000–1200°C in three-point flexure geometry on cylindrical specimens reached values of 550 and 450 MPa, respectively [91]. Young's modulus evaluated by sonic resonance on a bar cut from a hot pressed billet of SiOC pyrolyzed at 1250°C reached value of 98 GPa in [88].

Reasonable excess of silicon in SiOC structure may increase the flexural strength [92], as well as the excess of free carbon phase [91]. The SiOC glass prepared by mixing of monomers in the ratio of T/D = 2 and pyrolyzed at 1000°C reached the flexural strength at the level of 600 MPa in standard four point bend test. In the interval of pyrolysis temperature 1200–1500°C the strength dropped to ~200 MPa, regardless the T/D ratio and pyrolysis temperature [92]. T/D = 1 is impossible to be prepared in reasonable dimensions at temperatures higher than 1000°C, due to presence of cracks in the structure [92]. Flexural strength of SiOC (derived from polymethylsilsesquioxane) prepared by Field-Assisted Sintering and pyrolyzed at 1400–1600°C evaluated by ball on three balls test lies between 170–220 MPa [108]. In [121], flexural strength of SiOC pyrolyzed at 1000°C (prepared from commercial resin Y3370; chemical composition after pyrolysis at 1200°C was $SiO_{1.5}C_{0.68}$ [122]) tested on hot-pressed bar-shaped specimens in four point bending was 150 MPa.

Propagation of radial and Hertzian crack in SiOC glass dependently on the content of C or Si was studied in [92, 104]. Higher content of C causes ‚normal' behaviour of SiOC glass, i.e., propagation of radial cracks. Lower content of C, i.e., higher content of Si causes formation of Hertzian cracks. Fracture toughness of SiOC glass was evaluated only in a few works. Most of measurements were performed on densified materials [84]. Stoichiometric SiOC glass (T/D = 2) has the fracture toughness of 0.7 $MPa \cdot m^{1/2}$, T/D = 1 (with slight excess of free carbon) reached 0.57 $MPa \cdot m^{1/2}$. Typically glassy fracture of T/D = 1 was reported in [91], the fracture surface of the stoichiometric SiOC glass (T/D = 2) was published in [92]. For comparison, both fracture surfaces can be viewed in **Figure 1.28** a) and b), respectively.

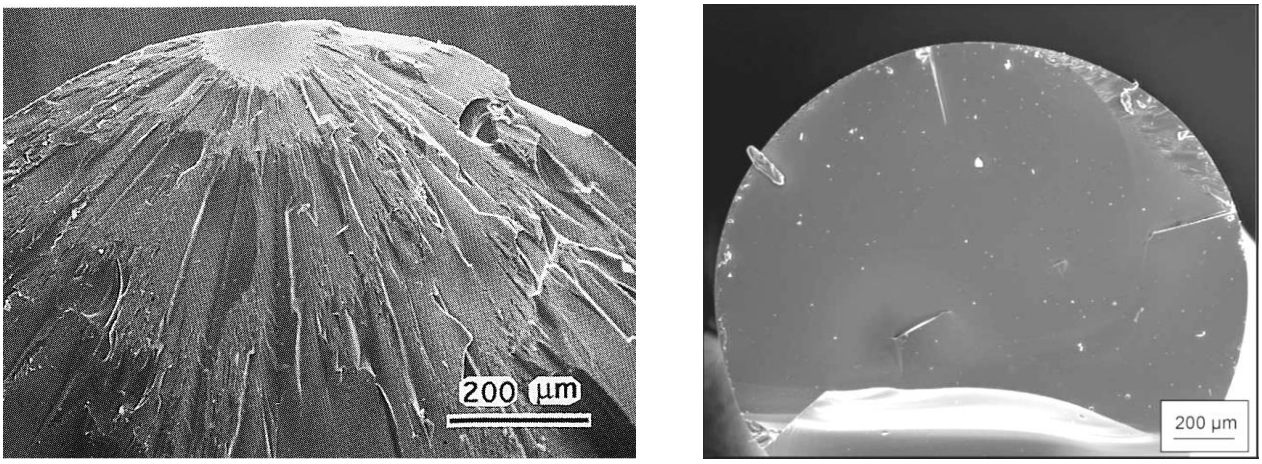

a) b)

Figure 1.28 *Fracture surfaces of stoichiometric SiOC glasses: a) T/D = 2 as pyrolyzed at 1000°C [91], b) T/D = 2, pyrolyzed at 1400°C [92]. In both cases the cross-head speed was 1 $mm \cdot min^{-1}$.*

Fracture surfaces of SiOC glass pyrolyzed at 400–800°C exhibits river patterns [123], which are formed when the crack front propagates in more than one plane, which gradually connects together. This type of fracture is typical for brittle or semi-brittle materials [38], for most of the amorphous polymers below glass transition temperature *Tg*, especially thermosets [18]. The patterns may be accompanied with formation of filaments, as reported in [123]. According to the literature, the polysiloxanes can form both thermoplastic [124-126] and thermosetting [127, 128] systems. In this work, the materials are supposed to be 3D cross-linked, thus, their nature is rather thermoset.

The cleavage fracture of materials transforming into SiOC glass were presented in literature [123]. The SiOC glass was derived from polymethylsilsesquioxanes, which were investigated in pyrolysis states from 400 to 1000°C. Significant river patterns were observed after tensile loading in the microstructure of material pyrolyzed at 400 and 600°C (**Figure 1.29**). In work [129] were presented fracture surfaces of composites with SiOC-forming polysiloxane matrix, pyrolyzed at 750°C, tested in static (flexural) and dynamic loading. Under the static loading, the fracture surface was a combination of brittle fracture and cleavage. Under the dynamic loading, the same material exhibited cleavage and river patterns on the fracture surface. There was also observed unique fracture pattern, which may be broken crazes visible at the fracture surface (**Figure 1.30**).

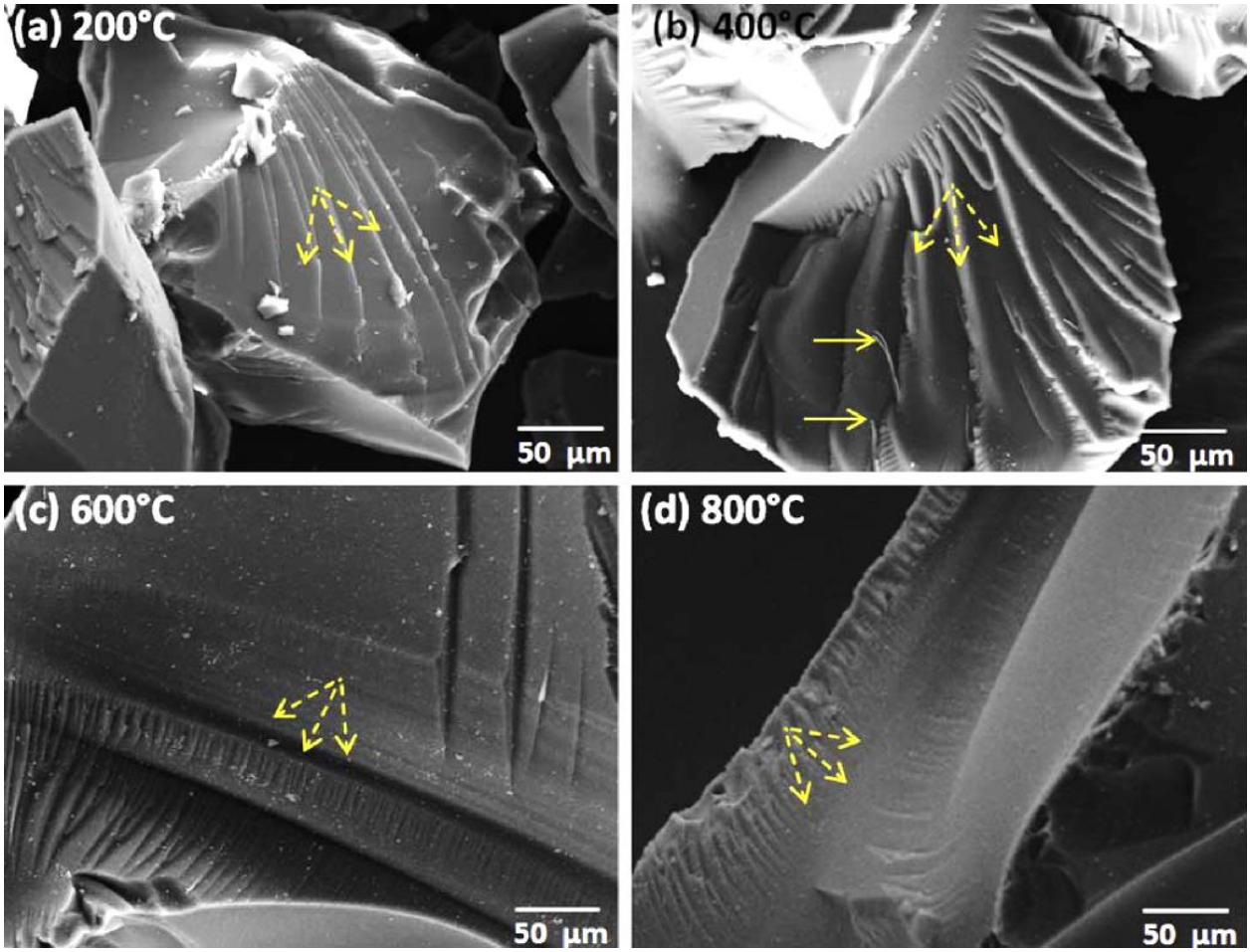

Figure 1.29 *Fracture surfaces of partially pyrolyzed (400–800°C) polysilsesquioxanes after tensile loading (River pattern marked by arrows. Reprinted from [123]).*

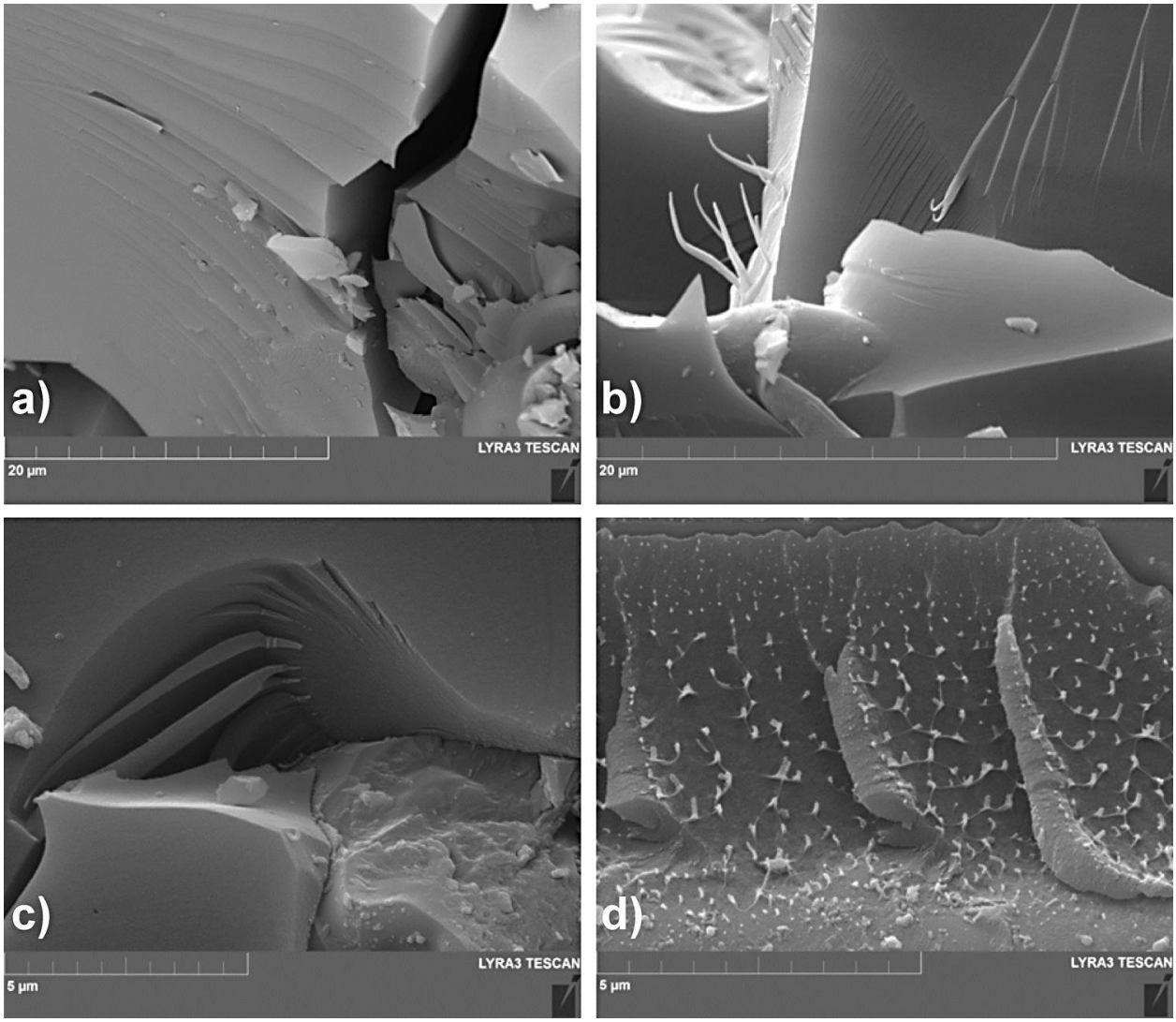

Figure 1.30 *Fracture surfaces of polysiloxane material partially pyrolyzed at 750°C under a) static and b)–d) dynamic loading (reprinted from [129]).*

1.6.4 Applications and research of SiOC glass and derived materials

Although the SiOC is broadly studied, there is not many of commercial products. The most known product with SiOC structure is Nicalon fibre [130]. It was developed by Yajima in 1976 and it is produced by Nippon Carbon Co. (Yokohama, Japan) by the sol-gel method from polycarbosilane. The fibre can be used in CMCs at temperatures up to 1500°C. The fibre itself can be considered as a microcomposite, composed of β–SiC microcrystals and SiOC phase acting as grain boundaries [131]. Another type of SiOC-based fibre is Tyranno, produced by UBE Industries, Japan. The elemental composition is similar to Nicalon plus it contains 4 wt. % of Ti [1], Zr and Al [132], depending on the type of Tyrano fibre [133]. The fibre is produced by sol-gel, with addition of titanium tetrabutoxide. It contains SiC_2O_2, $SiCO_3$ and SiO_4 groups [134] and has granular structure [135]. The lack of fibres based on SiOC materials may be caused due to the fact that the processing of SiOC fibres from polysiloxane resins is complicated due to the rheology, as it is complicated to regulate fibre diameter during melt-spinning [97].

Another product based on SiOC is Blackglas™ (denoted as Blackglas™ type-493 or Blackglas 493 A grade), made by pyrolysis of polysilsesquioxane, produced by AlliedSignal [136] (since 1999 up to now Honeywell [137]). Reinforcing the Blackglas™ with Nextel™ 312 created a composite which was broadly studied in [105] and also practically tested as a tailcone of a jet engine and prototypes of brake discs in various types of vehicles. These prototypes were known under Temrok tradename (Northrop Grumman), but since 1999 it is no longer used and the tradename is currently for sale [138]. Composite with Blackglas matrix and Nextel™312 was also produced under the name CeraComp® 1201 (originally by Greene Tweed, since 2013 Lancer Systems (PA, USA)) [139].

Under the research program HiPOC (High Performance Oxide Composites) were developed UMOX™ and OXIPOL, SiOC based materials [140, 141] plus UMOX™, which contains also mullite. UMOX™ with Nextel™ 610 as a reinforcement was studied for example in [79]. The composites exhibited overall deterioration of mechanical properties with increasing annealing temperature, caused by formation of strong interfacial bonding through ‚silica bridges'.

Besides these commercial products, the literature provides wide range of various applications in which SiOC glass can be used, for example coating [94] or impregnation of carbon fibres by siloxanes, carbosilanes, etc. [102], due to their propensity to oxidation [94]. In the composite Nicaloceram (SiC/Nicalon NL 607) the fibres were carbon coated and remarkable compatibility was reported [142]. In reverse, in [143] was described an increase of oxidation resistance of carbon fibres by coating them with SiOC.

Many composite types with SiOC material in various roles have been studied. Fibre-reinforced composites, carbon-nanotubes (CNT) reinforced [144], composites reinforced with $MoSi_2$ particles, and SiOC material filled with SiC and Si fillers [145]. Laminate composites with Blackglas 493 reinforced with Nextel 312 plies (with orientation 0/90) [10], or with carbon fibres [146]. Laminates with carbon fibres were also produced by Starfire, which focuses on production of commercial polysiloxane resins known as Polyram®. These composites were tested in brake discs (product named Starblade) [147, 148].

Due to deterioration of mechanical properties of fibre-reinforced composites with processing temperatures above 1000°C, partially pyrolyzed SiOC glasses were studied, too. In the partially pyrolyzed SiOC composites were used E-glass and basalt fibres as a reinforcement. Special type of composite where the porous structure of SiOC was filled with nanofibres of SiC was studied in [149]. The SiOC is also able to foam [150]. Tailoring of the foam structure to obtain good mechanical properties [151] is just one step from 3D print technology, which has been rising [116, 152-155].

Polysiloxane materials have been studied by Černý et al., majorly as a matrix in composites for a decade. The main interest was initially focused on material response of composite for high temperature applications, based on cheap commercial resin. The resin was investigated in a combination with various sufficient reinforcements. Later, in aim to optimize the interaction between fibres and matrix, a variety of polysiloxane resins were synthesized [156, 157]. The effect of various pyrolysis and annealing temperatures was studied for example in [93, 119]. It was examined via instrumented hardness measurement, that the material response depends on the

structure of SiOC glass, i.e., their chemical composition influenced by the mixing ratio of used monomers. The effect of the heating processes was studied for example in [149]. Amongst many other combinations was developed a composite of MS precursor reinforced with basalt fibres and pyrolyzed at particular temperature of 650°C and optimised heating process [149, 158]. The composite showed outstanding fracture toughness, which set up the research of partially pyrolyzed states of polysiloxane based composites. In current research, the mechanical properties of composites are tailored by the processing temperature.

1.6.5 Interface in SiOC composites

In this chapter, selected types of the fibre-reinforced composites with SiOC glass used as a matrix will be discussed with respect to their mechanical behaviour or the interface. Also, fibre coatings are discussed. The aim is to reflect factors influencing the formation of weak/strong interfaces in the SiOC composites.

Composites based on SiOC glass (with excess of Si – precursors T3D1 and T4D1, i.e., T/D = 3, T/D = 4, respectively) reinforced with Nextel™ 720 were studied in work of Černý [159]. The fibres were produced with polyvinylalkohol sizing grade 299. Although the SiOC materials themselves exhibited improving hardness and indentation elastic modulus when annealed at 1200°C in comparison to their pyrolyzed states at 1000°C and 1100°C (two pyrolysis temperatures were tested), flexural strength and modulus of composites tested in three point bending deteriorated. Besides the grain coarsening of the fibres, the composites suffered with formation of strong interface. The main reason seemed to be formation of bond between silicon from matrix with the fibre surface.

Another composite based on SiOC glass, UMOX™ (SiOC + mullite) matrix with Nextel™ 610 fibre, was studied in [160]. The presence of mullite grains in SiOC glass may enhance high temperature properties, e.g. creep. In the composite, carbon coating on the fibre was used to protect the fibres, nevertheless, pyrolysis at the temperature of 1200°C led to formation of strong interface, due to oxidation of the carbon layer from oxygen present in SiOC matrix. Grain coarsening of the fibre and formation of strong fibre-matrix interface still limits the composite application to maximum temperature of 1200°C in oxidizing environment, similarly as reported in [79].

An interface of SiOC glass with SiC was reported in work of Colombo [161]. Reaction bonded SiC bulk material was joined together by application of polysiloxane resin, with subsequent curing and pyrolysis of the joined SiC specimen at 1200°C. The thickness of the SiOC joint was initially approximately 20 μm and further decreased with processing temperature to ~3 μm. Besides the reasonable flexural strength of the joined materials, strong bonding with no compositional gradients or reaction layers around the interface was reported.

The aim to ensure weak interfacial bonding in composite with SiOC glass led to application of boron. In work of Suttor [102] was studied SiOC-matrix composite reinforced with carbon fibres. In the processing, boron powder was dispersed in the matrix (in ratio of 40 vol. % of boron to 60 vol. % of SiOC), in aim to prevent matrix shrinkage during its thermal treatment. The composite exhibited maximum flexural strength of 250 MPa at the pyrolysis state of 1300°C, containing stable SiC and B_4C phases. At the pyrolysis state of 1400°C the composite properties

significantly deteriorated, which was associated with formation of SiC layer on carbon fibres, forming strong bond with SiOC at the fibre-matrix interface.

Boron nitride was used in work [105], as a coating on the Nextel™ 312 fibres in the SiOC matrix (based on Blackglass 493) which led to enhanced strength and toughness of the composite through the presence of an interphase (see chapter 1.4.2.2). In work of Cazzato [67] was compared BN coating with monazite ($LaPO_4$). SiOC blackglas reinforced with Nextel™ 312 and 610 showed that the composite with BN coating had much higher tensile strength; nevertheless, it was probably caused by non-ideal dispersion of the monazite layer.

In works of Černý [111, 162] were studied partially pyrolyzed composites with SiOC matrix reinforced by E-glass and basalt fibres. They formed strong and weak interfacial bond, respectively. The weak bond led to fracture toughness of 20 $MPa \cdot m^{1/2}$ which was presumed to be in a relation with the presence of iron oxide Fe_2O_3 in basalt fibres [111, 149].

2 AIMS OF THE WORK

The main objective of this doctoral thesis can be summarised as the detailed description of the effect of processing parameters on the resulting behaviour of fibre-matrix interface and their influence on the global mechanical properties of fibre reinforced composites.

The objectives of the work can be specified in following tasks:

- Characterization of the microstructure and mechanical properties of commercially available, as well as modified matrix materials made of polysiloxane resins subjected to a various degree of polymer-to-ceramic transformation by the pyrolysis.

- Characterisation of selected fibre reinforced composites with respect to the processing temperature of the polymer-to-ceramic transformation subjected to the static or dynamic loading.

- Description of the fracture behaviour through the detailed fractographic analysis of fracture surfaces of tested composite specimens after various loading conditions (i.e static or dynamic loading, and high-temperature exposition).

- Comprehensive evaluation of the interface at the microscopic level using advanced characterization methods. Description of the interface development and microstructural changes after annealing of the composite.

3 EXPERIMENT

3.1 MATERIALS

Experimental materials investigated in this work are composites, consisting of matrices based on polysiloxane precursors, reinforced by various long ceramic fibres or fabrics made of them. The materials predetermined for matrix are investigated in various states of polymer to ceramic transformation, achieved by thermal processing called pyrolysis.

Interfaces between fibres and matrix, formed within the composite, predetermine the composite overall behaviour and can be successfully adjusted only when properties of each composite constituent are well known. To follow the main goal of production of economically reliable composite materials, the fibres were taken in as-received state and only the adjustment of matrix composition or treatment was used to tune the fibre-matrix interface. Composites for moderate and high temperatures application were investigated at respective temperatures predetermined by used fibres. At moderate temperatures basalt fibres and at high temperatures alumina-mullite fibres were used. All matrix and composite materials including their fibre-matrix interfaces were characterised mainly at room temperature from various points of view. Additionally, in some particular cases of composites with fully pyrolyzed matrix and high temperature resistant fibres a high temperature treatment (up to 1550°C) was applied to be able to describe microstructural changes affecting the interface properties and composite thermal stability.

Due to large number of specimens at different processing conditions, the material preparation is schematically shown in **Figure 3.1**. Individual processing steps deal with different states of transformation of a precursor to the SiOC material and are depicted in the scheme in **Figure 3.2**.

General overview of all materials investigated in this work including their origin, processing route used and post-processing heat treatment, if applied, is provided in **Table 3.1**. Further, a main reason of characterisation and corresponding property for given material is also indicated.

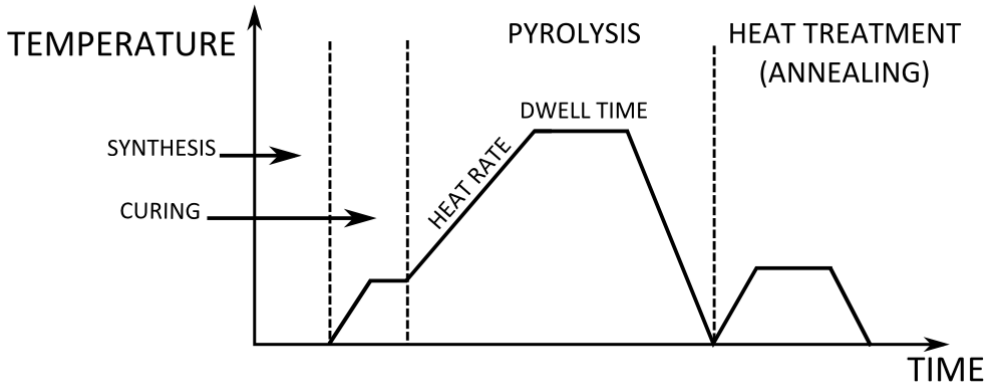

Figure 3.1 *Scheme of material processing.*

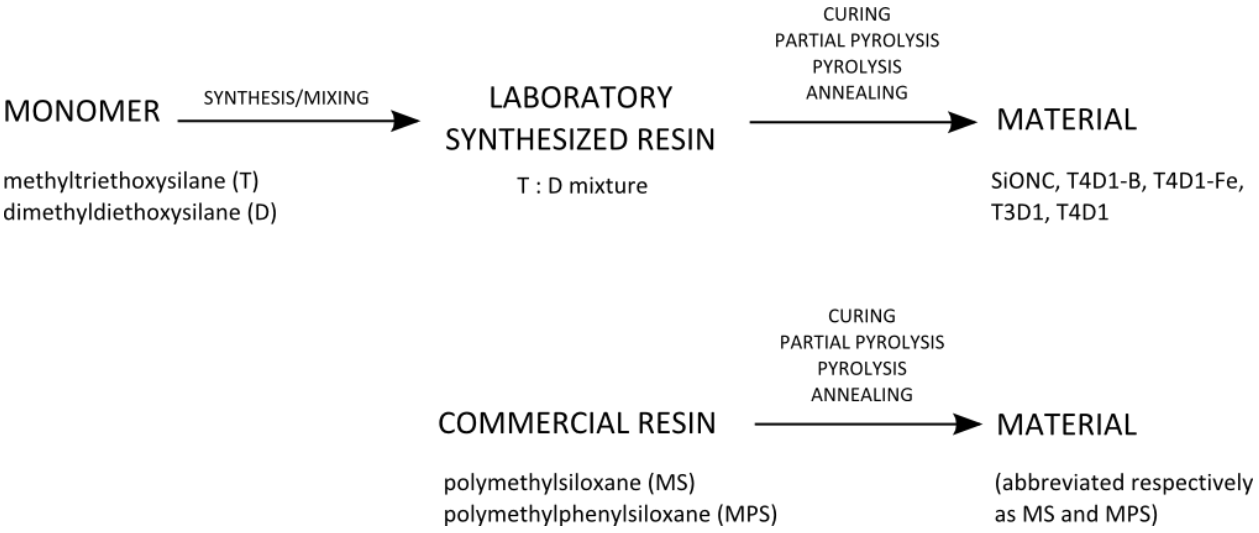

Figure 3.2 *Scheme of preparation and nomenclature of the used materials.*

Table 3.1 An overview of analysed specimens, their treatments and measured properties.

MATERIALS	PROCESSING	HEAT TREATMENT	CHARACTERISATION	ANALYSED PROPERTIES
Material from commercial resins				
MS, MPS	Curing at 250°C/Dwell time 6 hours Pyrolysis at 400, 500, 600, 700, 800, 900, 1000°C/ Dwell time 1 hour	-------	Effect of pyrolysis temperature	Microstructure Density Vickers and Martens hardness Indentation elastic modulus
	Pyrolysis at 520°C (MPS only) and 650°C Dwell time for 0, 1, 2, 5 hours	-------	Effect of pyrolysis dwell time	Microstructure Density Martens hardness Indentation elastic modulus
	Pyrolysis at 1000°C Dwell time 0 hours	Heat rate 0.5, 1, 2 , 4, 6.4 and 10°C/min	Effect of pyrolysis heat rate	Microstructure Density Vickers and Martens hardness Indentation elastic modulus
Material from laboratory synthesized resins				
SiONC, T4D1-B, T4D1-Fe, T19D1	Pyrolysis at 1000°C Dwell time 0 hours	Annealing at 1300°C and 1500°C/3 hours	Effect of precursor modification	Microstructure Density Vickers and Martens hardness Indentation elastic modulus
Composites				
MS+basalt fibres	Pyrolysis at 650°C Dwell time 0 hours	-------	Effect of reinforcement	Microstructure observation Impact strength Fracture toughness Fractography
MS+basalt fabrics MPS+basalt fabrics	Pyrolysis at 600, 650, 700, 750, 800°C Dwell time 0 hours	-------	Effect of reinforcement Effect of processing temperature	Flexural strength Fracture toughness Impact strength Impact energy Fractography
MS+basalt fibres	Pyrolysis at 650°C/Dwell time 0 hours Pyrolysis at 750°C/Dwell time 0 hours	Annealing at 550°C/Dwell time 3x10 minutes	Effect of fibre matric interface	TEM analysis EDS analysis
T3D1+Nextel™720 fibres	Pyrolysis at 1100°C/Dwell time 0 hours	Annealing at 1500°C/Dwell time 3 hours		

3.1.1 Materials for matrices

Precursors for processing of materials for matrices were obtained from two sources: i) **commercial resins** (MS and MPS) originated from Lučební závody Kolín (Czech Republic) and ii) resins synthesized from monomers obtained from Sigma Aldrich (Germany) used for **laboratory tailored materials** (SiONC, T4D1-B, T4D1-Fe, T19D1) prepared by Dr. Adam Strachota at Institute of Macromolecular Chemistry, Academy of Sciences of the Czech Republic (IMC AS CR). Curing, pyrolysis and further thermal treatment of precursors were conducted by Dr. Martin Černý at the Institute of Rock Structure and Mechanics, Academy of Sciences of the Czech Republic (IRSM AS CR).

In this work also appears laboratory synthesized materials T3D1 and T4D1. These were prepared in another work, prior to this thesis. In this thesis was investigated the fibre-matrix interface of the composite based on T3D1 matrix reinforced with Nextel™720 fibres. Material based on T4D1 is described here for comparison with materials T4D1-B and T4D1-Fe.

3.1.1.1 Matrices based on commercial resins

Commercial resins M130 and L901 are chemically poly[methyl(siloxane)] and poly[methyl(phenylsiloxane)] further abbreviated as MS and MPS, respectively, with respect to their initial structure. Molecular structural formulas are presented in **Figure 3.3**. The main difference between both resins is in the substituents joined to the central Si atom: methyl substituent ($–CH_3$) is smaller compared to phenyl ($–C_6H_5$) in MPS. It influences resin's properties such as density and viscosity, which has a substantial impact on the composite processing, the resulting structure and properties of the matrix material, which consequently strongly predetermines the fibre-matrix interaction (from chemical and physical point of view), resulting in the strength of the fibre-matrix interface bonding. Basic properties of liquid resins (in as-received state) were provided by their producer and are listed in **Table 3.2**. Both MS and MPS resins were previously investigated in study [96] **[163]** focused on the effect of composite reinforcements by basalt and E-glass fibres. There the resin precursors were pyrolyzed at 1000°C and their properties are reprinted for convenience in **Table 3.3**. This thesis work is focused mainly on the evolution of mechanical and chemical behaviour of the matrix precursors at different thermal states (various pyrolysis temperatures) and their role when used in composites with basalt fibres.

a) b)

Figure 3.3 *Structural units of alkylsiloxane polymers in commercial resins: a) methylsiloxane (MS) [164] and b) methylphenylsiloxane (MPS) [165].*

Both MS and MPS precursors were processed in several thermal stages. All specimens were first cured at 250°C (heating rate of $3°C \cdot min^{-1}$) and held at the temperature for 6 hours. Then the pyrolysis at required temperature under inert (nitrogen) atmosphere took place. The pyrolysis was conducted at following temperatures: 400, 500, 600, 700, 800 and 900°C and 1000°C with heating rate of $4°C \cdot min^{-1}$ [166]. The pyrolysis temperature of 1000°C and higher the material was found to be fully transformed into inorganic, hard, black-coloured SiOC glass.

Table 3.2 Basic properties of commercial resins in liquid form (producer's data).

	MS	MPS
Density [g·cm^{-3}]	1.00–1.02	1.11–1.15
Viscosity at 20°C [mPa·s]	30–40	50–100

Table 3.3 Basic properties of materials from commercial resins pyrolyzed at 1000°C [163].

	MS	MPS
Density [g·cm^{-3}]	2.02	1.95
Young's modulus [GPa]	80	80
Mass residue [%]	87	82
Volume shrinkage [%]	47	50

3.1.1.2 Matrices based on the resins synthesized from monomers

Laboratory tailored precursors studied in this work are labelled as T19D1, SiONC, T4D1-B and T4D1-Fe. These materials were investigated with the aim to obtain various compositions of SiOC-based glass having potentially tunable properties suitable for composites production such as low weight losses during pyrolysis, low elastic modulus, etc.

The resins T19D1, T4D1-B and T4D1-Fe are based on so-called T/D system. It is a mixture of two monomers: methyltriethoxysilane (T, or T-unit) and dimethyldiethoxysilane (D, or D-unit) in particular ratio, reflected in the name of the polymer precursors. The monomer units affect the linearity and the level of cross-linking, respectively, of the final polymer structure [101]. T19D1 was prepared by mixing of T and D units in respective ratio 19:1.

The T4D1-B was developed from T4D1 resin, modified with addition of liquid H_3BO_3, calculated to be 2.5 wt. % in dried resin. The modification of T4D1 by H_3BO_3 was performed to influence the SiOC structure. Theoretically, addition of H_3BO_3 into the polymer precursor mixture could positively affect the polymer reorganisation during the pyrolysis and thus, reduce the coefficient of thermal expansion of the final matrix material. In literature [96] was reported positive effect of boron in the structure of SiOC (i.e., SiBOC) by inhibition of the formation of silica clusters (SiO_2) at 1200°C, i.e., inhibition of the phase separation.

The T4D1-Fe was also T4D1-based resin modified by tris(acetylacetonato)iron(III). The amount was calculated to be 4.4 wt. % of Fe_2O_3 in dried resin. The iron ion Fe^{3+} was incorporated into the structure of SiOC glass with the aim to decrease adhesion of final SiOC matrix material with silica-based fibrous reinforcement, similarly as in composites based on SiOC matrix with basalt fibres, where the positive effect on the composite toughness was ascribed to the presence of Fe in the basalt fibres [149].

In the group of materials tailored by their T/D ratio also belong precursors T3D1 and T4D1. These materials were already studied in the past [167], therefore they are not included in the material overview provided in **Table 3.1**. Nevertheless, in this work will be analysed interface of the composite with T3D1 matrix reinforced with Nextel™ 720 fibres. The precursor T4D1 was used for modification into T4D1-B and T4D1-Fe, therefore, basic properties of T3D1 and T4D1 materials are listed in **Table 3.4** for convenience.

The SiONC matrix material is based on Tv/D system, containing vinyl functional monomers, silazane, silane and siloxane. These compounds lead to reduced weight loss of the final matrix material. Detailed information about the material production is provided in literature [93].

Table 3.4 Mechanical properties of SiOC materials based on T3D1 and T4D1 materials [159].

	T [°C]	Density ρ [g·cm^{-3}]		Indentation modulus E [GPa]		Vickers hardness (HV0.2)	
		T3D1	T4D1	T3D1	T4D1	T3D1	T4D1
Pyrolyzed at	1000	2.44±0.05	2.38±0.06	69.9±1.9	69.9±1.9	1118±41	1102±22
	1100	2.37±0.06	2.32±0.17	70.0±3.0	78.1±2.1	1132±41	1372±33
Pyrolyzed at 1000°C and annealed at	1200	2.35±0.04	2.35±0.17	73.4±10.8	85.5±2.5	1287±59	1444±87
	1300	2.48±0.05	2.45±0.20	72.4±4.6	77.1±1.6	1375±76	1353±90
	1400	2.31±0.08	2.36±0.20	76.6±2.1	75.0±3.6	1370±56	1356±29
	1500	2.40±0.06	2.32±0.20	70.9±3.1	76.1±2.3	1250±78	1197±50

Polymer matrix precursors were prepared via sol-gel method. During this process the monomers undergo through their functional groups hydrolysis with subsequent condensation of polysiloxanes. The quality of the product depends on the amount of water, pH of the solution and catalyser of polycondensation reaction. Finding of the most suitable precursor at constant polymerization conditions was studied in detail by Strachota et al. [44, 96].

Liquid precursors were heated by 90°C·h^{-1} rate to 250°C to be cured for 4 hours, then heated to 420°C by 50°C·h^{-1} and then to 1000°C by 10°C·h^{-1}, to be fully pyrolyzed under argon protective atmosphere [96]. Curing and pyrolysis processes are illustrated in **Figure 3.4**.

After the pyrolysis, selected specimens were annealed at 1300 and 1500°C in air with dwell time of 2–4 hours. The aim was to study the response of pyrolyzed precursors to the severe thermal and oxidative conditions.

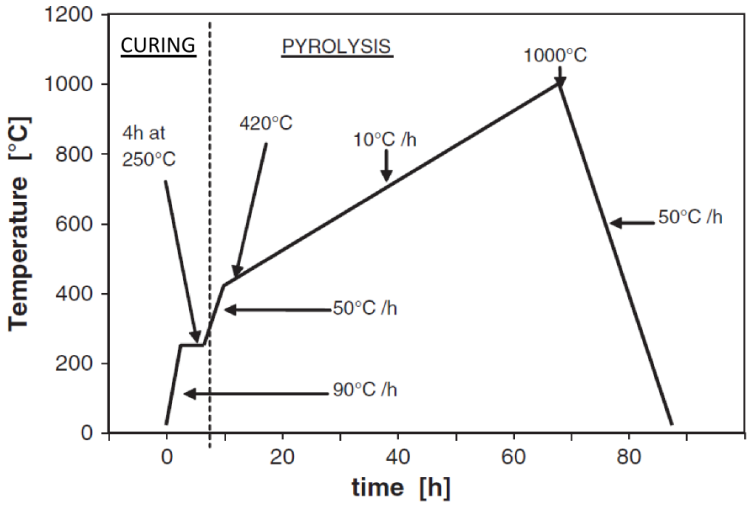

Figure 3.4 *Curing and pyrolysis process of experimental materials. Reprinted from [96].*

3.1.2 Reinforcements

In the present work the fibre-matrix interface was optimised using modification of matrix properties and the reinforcing fibres (in any form) were used in the as-received state without any surface treatment.

3.1.2.1 *Basalt fibre*

Basalt fibres from two producers were used in this work – Kamenny Vek (Russia) (through their Czech importer Basaltex) and Basaltex (Belgium). The chemical composition of the used fibres is listed in **Table 3.5** [149]. The chemical composition of the basalt fibres was measured by Černý [162] using EDS (Electron Dispersive Spectroscopy) and it is provided in **Table 3.6**.

The basalt fibres were used in composites as unidirectional reinforcement or in the form of fabrics. The fibres were plain-weaved into fabric by VÚLV (Výzkumný ústav lněných vláken), nowadays Basaltex a.s. Selected properties of used basalt fibres are listed in **Table 3.7**.

Table 3.5 Chemical composition of used fibres measured by Černý [149].

Compound	Basaltex [wt.%]	Kamenny Vek [wt.%]
SiO_2	50.5	53.6
TiO_2	2.8	1.1
Al_2O_3	13.4	17.4
Fe_2O_3	5.4	4.7
FeO	8.4	4.4
MnO	0.2	0.1
MgO	4	4.1
CaO	8.9	8.5
Na_2O	2.9	2.6
K_2O	1.6	1.6
P_2O_5	0.3	0.2

Table 3.6 EDS elemental analysis of Basaltex fibre [168].

Element	Si	O	Fe	Al	Ca	Mg	Ti	Na	K
[wt.%]	30.7	29.4	11.7	8.5	7.2	3.8	1.9	1.7	0.7

Table 3.7 Properties of basalt fibres produced by Kamenny Vek.

Property	Value
Diameter [μm]	14.2 [111]
Density [$g \cdot cm^{-3}$]	2.6–2.8 [168, 169]
Tensile strength [MPa]	2700–3200 [111]
Tensile modulus [GPa]	85–95 [111, 170]
Thermal expansion coefficient [$W \cdot m^{-1} \cdot K^{-1}$]	0.031–0.038 [170]

3.1.2.2 *Ceramic fibre Nextel™ 720*

The fibre Nextel™ 720 is a commercial product of the company 3M (USA). It was obtained in the form of a tow, used for hand-made processing of unidirectionally reinforced composites with laboratory synthesized matrices based on T3D1 and T4D1 materials. The fibre is

polycrystalline, composed of polycrystals of alumina Al_2O_3 and mullite $3Al_2O_3{\cdot}2SiO_2$ (grain size is less than 500 nm [171]). Basic properties of Nextel™ 720 fibres are listed in **Table 3.8**.

Table 3.8 Properties of Nextel™ 720 [172].

Property	Value
Chemical composition	85 wt. % Al_2O_3, 15 wt. % SiO_2
Crystal phases	α-Al_2O_3, mullite
Fibre diameter	9–12 μm
Tensile strength (25.4 mm gauge)	2.1 GPa
Tensile modulus	260 GPa
Density	3.4 $g{\cdot}cm^{-3}$
Thermal expansion (100–1100°C)	6.0 ppm/°C
Maximum use temperature (1% strain/69 MPa/1000 h)	1150°C

3.1.3 Composites

Based on the obtained mechanical properties, only T3D1, MS and MPS materials were used for composite preparation. Other studied materials did not reach sufficient hardness, elastic modulus, and level of porosity to ensure adequately good mechanical properties of composites.

3.1.3.1 Composites with basalt reinforcement, pyrolyzed partially at temperatures below 1000°C

Composite materials investigated in this thesis were prepared at IRSM AS CR. Composites were composed of two types of matrix – silicon-based organic compounds i) methylsiloxane (**MS**) and/or ii) methylphenylsiloxane (**MPS**) and the reinforcements in the form of a) **long fibres** filaments and b) **fabric** with plain-woven structure.

'MS-based unidirectional' composites were prepared in the form of plates, by laying the roving saturated in respective resin, into in a mould. Composites were dried, cured (the process is depicted in [173, 174]) and partially pyrolyzed at 650°C and 750°C under protective atmosphere. The plates were cut into prismatic blocks with the nominal dimensions of 45 mm×4.3 mm×3.1 mm. Fibre volume fraction was 65 ± 3 %. In this thesis, the unidirectionally reinforced composite with MS matrix pyrolyzed at 650°C was subjected to the dynamic testing, for evaluating of the influence of the dynamic loading on the fracture response in comparison with mechanical response obtained at static loading, described in [111]. Both composites, partially pyrolyzed at 650 and 750°C, were subjected to the thermal treatment and to observation of their fibre-matrix interface. Detailed explanation is provided in chapter 3.1.4.

Composites with woven fabric reinforcement, were made by the polymer infiltration process of 16 layers (prepregs) of plain-woven fabric. The fabric had areal weight of 186 $g{\cdot}m^{-2}$ and thread count (warp/weft) was 100/75. It was oriented by warp in longitudinal direction of the composite. Volume fraction of the reinforcement after curing was approximately 43% of the composite volume and present porosity was predominantly located between the fabric layers [111, 175].

The fabric was saturated in diluted polysiloxane by hand, layered one by one upon each other into a mould. The whole piece was dried in air at ambient temperature and then cured at 250°C in nitrogen atmosphere for 22 hours (see **Figure 3.5 a)**). Curing was conducted in a heated mould under controlled environmental conditions. Dwells at particular temperature for certain period of time were applied to protect material from micro-cracking, which might occur due to internal stresses and gas phase evolution. Maximum pressure of 0.86 MPa was applied in the temperature range of 220–250°C [168]. After the curing, the composites were pyrolyzed at different regimes (see the scheme in **Figure 3.5 b)**), having the target temperature varying from 600°C to 800°C with the step of 50°C. The final composite plates were approximately 250 mm long, 50 mm wide and 2.5 mm thick. The plates were cut into bar-shaped specimens, suitable for further mechanical testing.

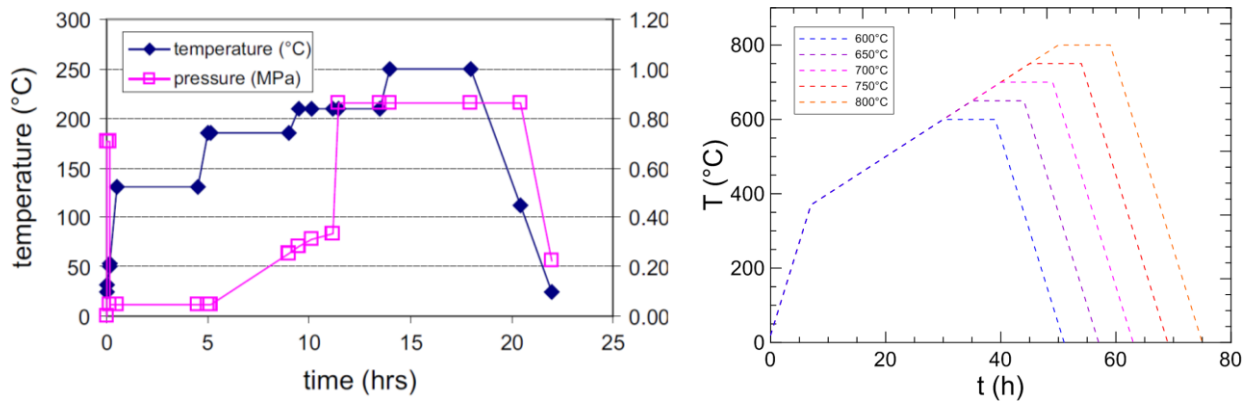

a) b)

Figure 3.5 *Course of a) curing process [168] a) and b) various temperature regimes of partial pyrolysis processes of basalt fabrics reinforced composites.*

3.1.3.2 Composites with Nextel™720 fibres, pyrolyzed at 1100°C and annealed at 1500°C

Composites were composed of SiOC glassy matrix prepared using T3D1 laboratory synthesized precursors by Strachota et al. [96] reinforced by ~58 vol. % of the Nextel™720 fibres. Specimens were gradually cured at 280°C and at a pressure of 0.8 MPa and the whole process took 18 hours (see **Figure 3.4 a)**). Full pyrolysis was conducted at 1100°C, under nitrogen atmosphere and subsequently annealed for 3 hours at 1200–1500°C in air. Pyrolysis process is illustrated in **Figure 3.6 b)**. The dwell time at maximum temperature was ~10 hours and then the specimens were cooled down to room temperature. Detailed information about processing is provided in literature [159].

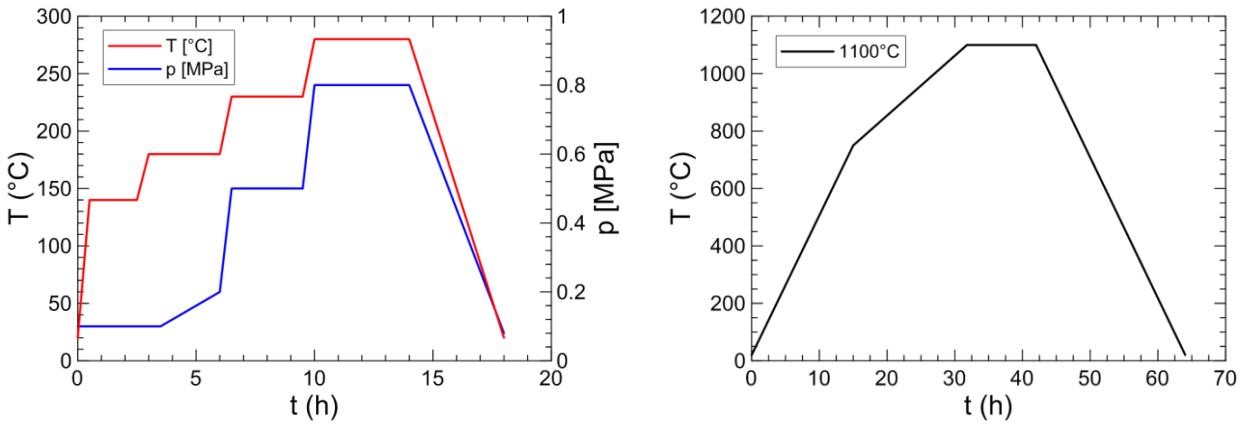

a) b)

Figure 3.6 *Time-temperature/pressure regimes for a) curing and b) pyrolysis for composites with Nextel™ 720 reinforcement.*

3.1.4 Composite interface

Materials described in section 3.1.3 were subjected to investigation of their fibre-matrix interface using transmission electron microscopy (TEM). The observation was aimed to find any changes in the interface area and in individual composite components, induced by the thermal processes and caused by high temperature exposition. Composite materials where the interface was detailed studied using TEM were:

a) composites made of laboratory synthesized T3D1 material based matrix reinforced with Nextel™720 fibres, pyrolyzed at 1100°C, where the 'as received' state was compared with the same composite additionally treated at 1500°C for 3 hours what was above recommended temperature limit of application of fibres. Nevertheless, the matrix was found resistant up to 1550°C; therefore, the effect of harsh environment on the fibre-matrix interface was investigated.

b) composites made of unidirectional basalt fibre reinforced MS-based matrix, pyrolyzed at 650°C and 750°C compared with the same two pyrolysis states additionally annealed three times at 550°C for 10 minutes, according to thermal process schematically depicted in **Figure 3.7.**

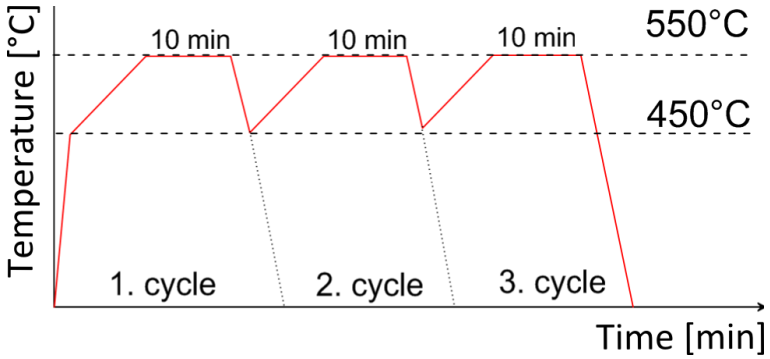

Figure 3.7 *Scheme of heat treatment of composites with methylsiloxane (MS) matrix reinforced with basalt fibres, pyrolyzed at 650 and 750°C.*

3.2 CHARACTERISATION TECHNIQUES

3.2.1 Specimen preparation

Specimen preparation divides into two procedures, based on the material type:

i) materials prepared from resins produced in the form of small pieces (few millimetres only).

ii) composites (both fibre- or fabric- reinforced) were prepared as compact blocks with nominal dimensions 250 mm×50 mm×2.5–3.5 mm.

Due to the small dimensions of materials predetermined for matrix only density and/or hardness were determined. Hardness measurement requires flat polished surface. Therefore, the specimens were mounted into two-component cold mounting SpeciFix epoxy resin (Struers, Denmark) activated by curing agent. After sufficient curing between 12–24 hours, grinding and polishing of specimens was conducted using a Kompakt 1031 polishing machine (MTH, Czech Republic), with various diamond based grinding wheels and MD DUR satin-cloth wheels (Struers, Denmark). As a polishing agent was used diamond suspension DP–Suspension P and lubricant Lubricant Blue (Struers, Denmark). The abrasive size of diamond grains in suspensions was 9, 6, 3, 1 and ¼ μm.

Cutting of the composite specimens into required dimensions or preparation of chevron notches were performed with a precise saw ISOMET 5000 (Bühler, USA) using a diamond cutting wheel M1D08 (Struers, Germany) and a 15 LC (Bühler, USA) with diameter of 102 mm, arbor 12.7 mm and thickness 0.3 mm. The cutting wheel was intensively water cooled to eliminate any sample heating. Typical blade speed was 4000 rpm, and the feed rate was 4.5 $mm \cdot min^{-1}$. Chevron notches were introduced into the bar shape specimens by two thin cuts with top angle of 90°. Specimen types, their dimensions and used testing method are represented in **Table 3.9**.

Table 3.9 Composite specimens, dimensions and testing methods.

Reinforcement type	Reinforcement alignment	Specimen dimensions			Test procedure
		Length [mm]	Width [mm]	Thickness [mm]	
Continuous fibre	Longitudinal	45	3.1	4.3	Impact strength
Fabrics	0°	55	2.5	3.5	Impact strength
Fabrics	0°	45	2.8	3.7	Flexural strength Fracture toughness
Continuous fibre	Longitudinal	84	46	4	Elastic modulus (non-destructive)
Continuous fibre	Transversal horizontal	40	3.3	4.2	Fracture toughness
Continuous fibre	Transversal vertical	40	4.3	5.6	Fracture toughness

3.2.2 Microstructural and fractographic observations

Microstructure observation plays a significant role in material characterization. The observation was conducted for all materials, both matrices and composites, before the mechanical

testing as well as after that. Except of fracture surfaces, observed areas were polished to ¼ μm (see chapter 3.2.1).

An optical stereomicroscope Olympus Z61 (Japan) was used for general overview observation providing useful information about the surface or internal structure of the experimental material. Additionally, it was used finding the specimens with suitable shape and/or surface for indentation test; and for the measurement of the notch depth on fracture surfaces of composites after fracture toughness test.

A laser confocal microscope LEXT OLS3100 (Olympus, Japan) with zoom up to 2400× (digital zoom up to 14400×) was used for microstructure analysis on polished surfaces of both matrices and composites. Additionally, 3D reconstructions of the indents after the instrumented indentation test were prepared. Typically the zoom for 3D reconstructions was 480× with the view field of 640×480 μm or 1200× with the view field of 256×192 μm.

For detailed microstructural and fractographic observations were used both types of electron microscopes, i.e., scanning (SEM) as well as transmission (TEM). Due to the low electrical conductivity of observed materials it was necessary to sputter all the specimens with thin layer of gold before their observation in SEM.

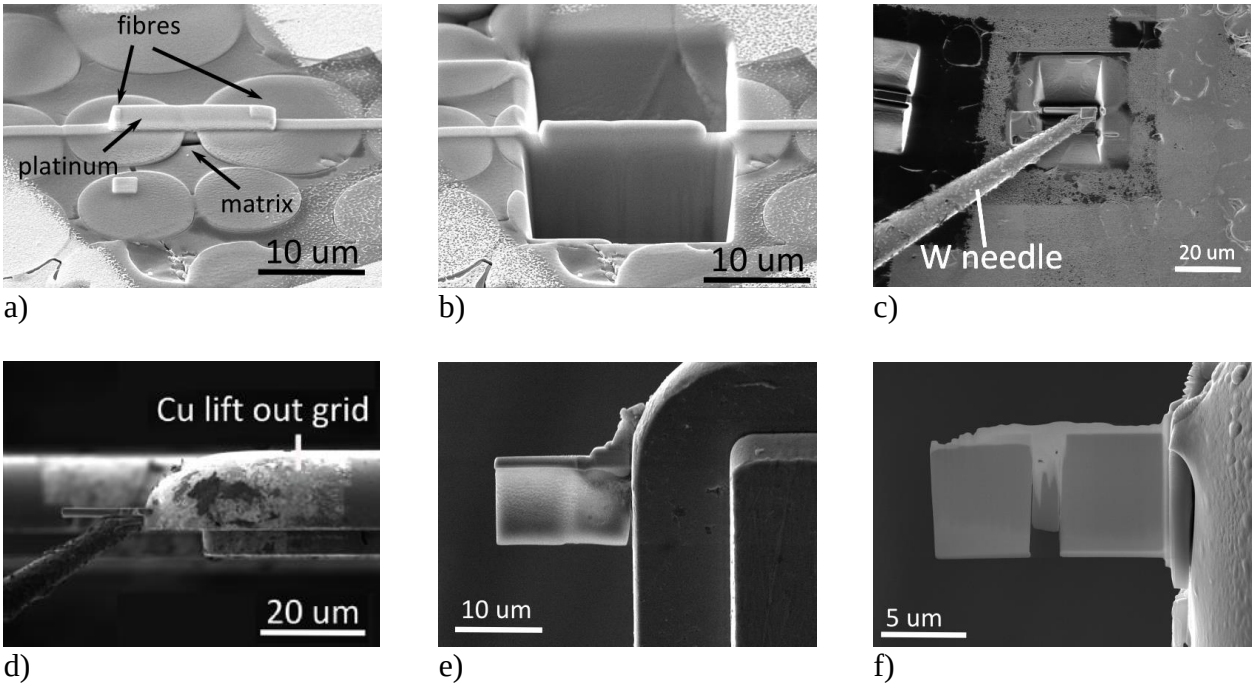

Figure 3.8 *Preparation of thin lamella for TEM observation: a) SEM view – deposition of the protective platinum layer onto chosen area, b) SEM view – trenches around the lamella, c) FIB view – lifting of the lamella welded on the micromanipulator, d) FIB view – welding of the lamella to the TEM grid and cutting-off the micromanipulator needle, e) SEM view – final thinning of the lamella and thinned lamella in f).*

A scanning electron microscope LYRA 3 XMU (FEG SEM/FIB/GIS) (Tescan, Czech Republic) was used for observation of composite microstructure, for fractographic analysis of fracture surfaces and especially for preparation of TEM foils from the fibre-matrix interface.

First step in the preparation of the TEM foil was selection of suitable area, i.e., usually two neighbouring fibres separated by matrix, then its protection against damage by milling ions.

Therefore, the area of intended lamella had to be coated with 1 μm thick platinum layer **(Figure 3.8 a)**), deposited by gallium ions (FIB) using Gas Injection System (GIS). The foil was created by milling two trenches into specimen using FIB (see **Figure 3.8 b)**). The initial lamella thickness (the distance between the trenches) was set to 1 μm, and it was 25 μm wide and 25 μm deep into the material volume. Working distance of the specimen from the pole piece was 9 mm and tilt was 55°. The milling itself was conducted with acceleration voltage of 30 kV, emission current of 2 nA, probe current depending on the process, e.g. rough milling 5 nA, platinum deposition 40 pA, etc. After trenching, the specimen was tilted back to 0° and partially cut. Then, again tilted to 55°, the lamella was welded by platinum deposited by GIS to the micromanipulator's tungsten needle, cut off from the material by FIB and removed from the specimen **Figure 3.8 c)**). The lamella was then moved and welded by platinum to the standard 3 mm TEM holder (copper lift out grid, see **Figure 3.8 d), e)**). The micromanipulator needle was cut-off and the lamella was polished by FIB to the final thickness, less than 100 nm, suitable for the TEM observation (**Figure 3.8 f)**).

Prepared TEM lamellas contained both components, i.e., two fibres and matrix in between. The observation of their interface was conducted using a transmission electron microscope JEOL JEM–2100F (Jeol, USA).

3.2.3 Density

For both types of materials – matrices and composites – the density measurement was conducted. Due to their irregular dimension, matrices were measured using the Archimedes' principle. In this method a density kit adapted on an analytical balance Denver Si-234 (Denver Instruments, USA) was used. The density kit is a beaker filled with a liquid, and a cantilever with a dish (for dry weighting) and a basket (for weighting in the liquid), on which the weighted object is placed. The kit is shown in **Figure 3.9**. As a liquid medium isopropanol was used. The density was calculated using the formula:

$$\rho = \frac{m_{air}}{(m_{air} - m_{med}) \cdot \rho_{solid}} \tag{2.1}$$

where m_{air} is weight of the specimen on the immersion basket (in air), m_{med} is weight of the specimen in the liquid medium, ρ_{solid} is the density of weighted material. Each measurement was repeated three times and the result is provided as an average value with calculated standard deviation.

The density of composites was calculated from specimen dimensions and weight when Archimedes method would be used what eliminates errors coming from possible soaking of medium into the composite pores.

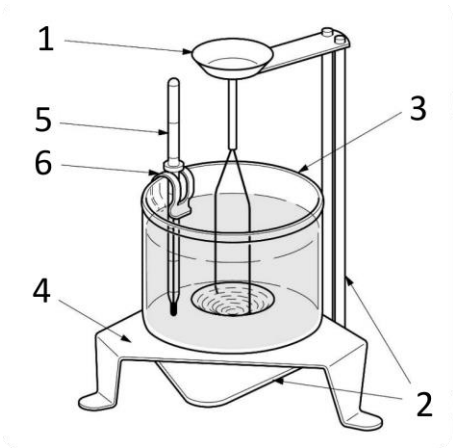

Figure 3.9 *Scheme [176] of the density kit for Archimedean displacement method: 1 – immersion basked for descending solid matter (density > 1g·cm^{-3}), 2 – weighting tray holder, 3 – glass container, 4 – platform for glass container, 5 – thermometer, 6 – holder for thermometer.*

3.2.4 Instrumented indentation hardness

The hardness was measured using an instrumented hardness machine Zwick Z2.5 (Zwick/Roell, Germany) with ZHU0.2 microhardness head equipped with a pyramidal diamond (Vickers) indenter [177]. An indentation process with both loading and unloading parts is schematically drawn in **Figure 3.10**. The indenter is forced into the surface of a test piece until maximum force (and maximum indentation depth) is reached, held for 12 seconds and then is removed. From the slope of the unloading curve is evaluated the indentation elastic modulus (which is described in chapter 3.2.6.1). After removal of the test force *F*, the diagonal length of the indentation left in the surface was measured. For measuring the indent diagonals length directly after the test were used objectives mounted on Zwick Z2.5 device, with zoom of 20× and 60×, depending on the hardness of the material and adequate indent size. (The harder was the material, the smaller was the indent).

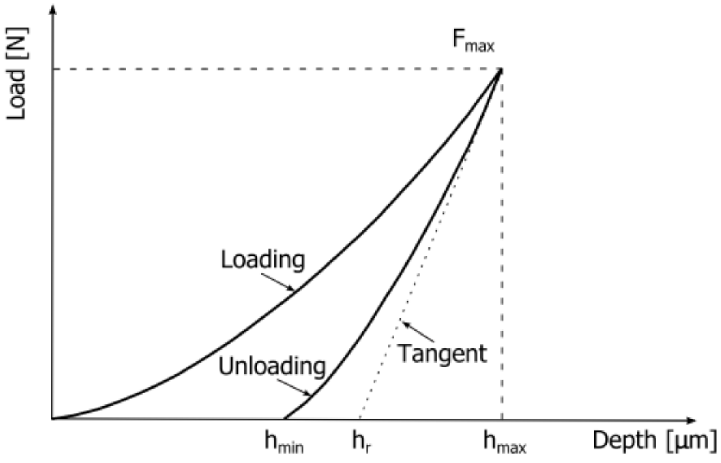

Figure 3.10 *Scheme of load - indentation depth record with loading and unloading curve. From the slope (tangent) of the unloading curve is evaluated indentation elastic modulus of the material.*

For more precise results the 3D reconstruction of the indents using a laser confocal microscop LEXT OLS3100 (Olympus, Japan) with subsequent diagonals measurement was conducted. Nevertheless, it is known from previous work [93] that such evaluated hardness would be around 15 % lower comparing to the hardness evaluated through the objective on the ZHU0.2 hardness head.

An instrumented hardness measurement was conducted for all matrix materials under investigation. The specimens were fixed into mounting resin and polished (the procedure is described in chapter 3.2.1). Usually the specimen planes must be plan-parallel to obtain symmetrical indent performed by the indenter, otherwise the imprint has irregular shape (see **Figure 3.11 a)**). In this case, specimen holder was used; therefore the accurate plane for mechanical testing was always ensured (see **Figure 3.11 b)**).

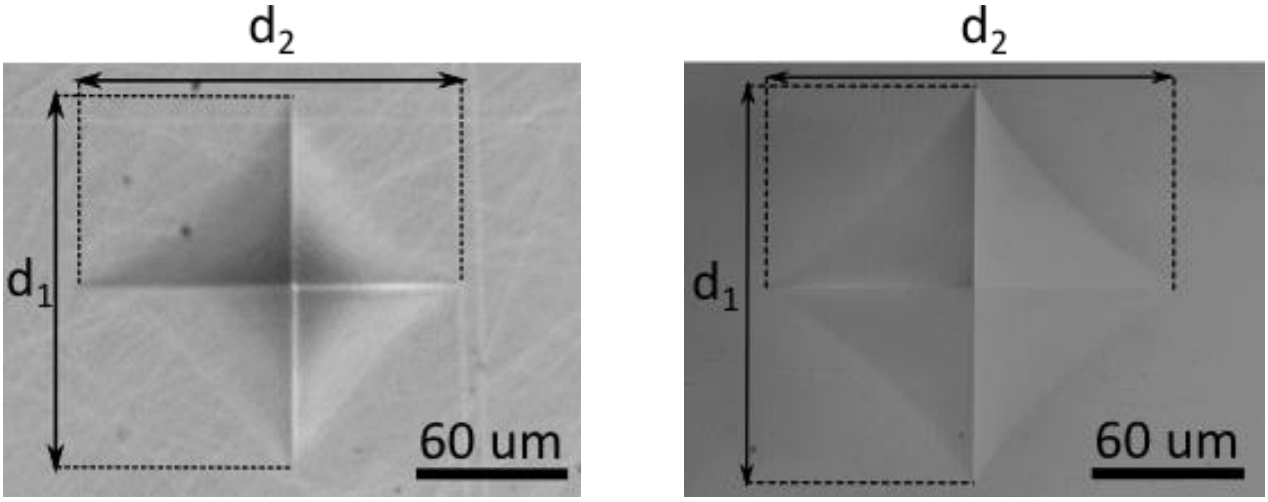

a) $d_1 < d_2$ b) $d_1 \approx d_2$

Figure 3.11 *a) An example of the irregular indent which appears when the specimen plane is not perpendicular to applied load, b) symmetrical indent with schematic representation of diagonals length.*

The maximum load was set to 1.961 N, corresponding to HV0.2, with the force control regime and loading rate of 0.1125 $N \cdot s^{-1}$. Dwell time at the point of maximum load was set to 12 seconds, according to the standard [178]. In some cases, the standard procedure could not be fully followed – the test speed and the material nature led to several aborts of the test and even if not, the machine was unable to measure the indentation elastic modulus correctly. Thus, load application and load removal speed of 0.01 $mm \cdot min^{-1}$ was set in the position control mode. Two types of hardness characteristics were evaluated directly by the incorporated software: Vickers microhardness HV0.2 and Martens universal hardness (HM). The Vickers hardness was evaluated from the maximum applied force *F* in N acting to area *A* in mm [177] (3.2):

$$HV = \frac{F}{A} \tag{2.2}$$

where the area *A* (2.3) is given by the length of indent's diagonals and the indenter's geometry.

$$A = \frac{d^2}{2sin\frac{136°}{2}} \tag{2.3}$$

The equation for HV is then often written in a simplified form (3.4) using maximum applied load and an average of indent diagonals [178]

$$HV\ F = 1.8544\ \frac{F}{d^2} \tag{2.4}$$

where *HV F* is the Vickers hardness number at applied force (expressed as the weight in kg).

Martens hardness (formerly universal) was evaluated from maximum indent depth, due to the elastic response of the material to the loading according to the equation (2.5)

$$HM = \frac{F_{max}}{f_{IT} \cdot h_{max}^2} \tag{2.5}$$

where F_{max} is the maximum force in N after waiting time, f_{IT} is factor for indenter (26.43 for Vickers) and h_{max} is the maximum indentation depth after dwell time in μm.

Figure 3.12 represents the indent's cross-section during the measurement. The indentation depth denoted as h_r shows that the depth changes as the indenter removes from the material from the maximum h_{max} to minimum depth h_{min}. After the elastic deformation of the material is finished, dimension and the indent's dimensions remain still. The darkest area in the image (**Figure 3.12**) represents the appearance of an indent after relaxation of the material.

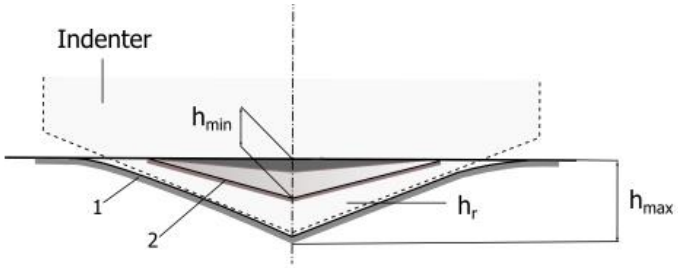

Figure 3.12 *Cross-section of the indent and its parameters.*

3.2.5 Indentation relaxation behaviour

Relaxation behaviour of the material was measured as a rate of viscoelastic recover of the material surface after the indentation test, obtained from the difference between the maximum indentation depth h_{max} measured by the indentation machine and the depth h_{conf} measured after 3D reconstruction of the indent's surface.

The relaxation behaviour was examined on matrix materials based on commercial resins (MS and MPS) subjected to partial pyrolysis in the temperature range 400–1000°C including curing stage at 250°C. The examination was conducted via instrumented indentation test (see chapter 3.2.4) and consequent 3D reconstructions (by a laser confocal microscope) in given time after the test.

Maximum and minimum depth of the imprint (h_{max} and h_{min}, respectively) was collected from the loading curves using hardness machine software. The relaxation was calculated using equation (2.6).

$$Relaxation = \frac{h_{min} - h_{conf}}{h_{min}} \cdot 100\ [\%] \tag{2.6}$$

For observation of relaxation kinetics was used MS precursor in the cured state (250°C) and the pyrolysis states of 400 and 600°C. Individual indentation test at standard conditions was performed to obtain an imprint into specimen surface. The specimen was then immediately placed under objective of confocal microscope and the imprint was 3D reconstructed. The 3D reconstruction was repeated ~5 times. The data were collected within approximately 2 hours since the indentation was performed, in aim to capture relaxation kinetics for chosen states of matrix precursors. The last value h_{24} was obtained 24 hours after the indentation. Depth of the imprint was measured on reconstructed imprint, using the microscope software.

3.2.6 Elastic modulus

Elastic modulus was evaluated by three different approaches. Elastic modulus of matrices was evaluated via indentation method. In composites was the value obtained from flexural bending test and by non-destructive measurement of resonant frequency through the impulse excitation technique (IET). All the techniques are described in details in respective subchapters 3.2.6.1–3.

3.2.6.1 Indentation method

The indentation elastic modulus of matrices was evaluated via indentation test using Zwick Z2.5 instrumented hardness machine with ZHU0.2 hardness head (both Zwick/Roell, Germany), from the slope of the unloading curve (see **Figure 3.10**) by the machine software TestXpert V12.3, according to the equation (2.7) [178]:

$$E_{IT} = \frac{(1 - v_s^2)}{\frac{1}{E_r} - \frac{(1 - v_i^2)}{E_i}} \tag{2.7}$$

where v_s and E_{IT} in MPa are, respectively, the Poisson´s ratio and the indentation elastic modulus of the specimen, v_i and E_i are, respectively, the Poisson´s ratio and the elastic modulus of the indenter. E_r is reduced modulus of the indentation contact in N·mm^{-2}, calculated from the equation (2.8)

$$E_r = \frac{\sqrt{\pi}}{2C \cdot \sqrt{A_p}} \tag{2.8}$$

where C is expressed as (2.9):

$$C = \frac{1}{m_{hr}} \tag{2.9}$$

where m_{hr} is gradient of the straight line h_r in N·mm^{-1} (see **Figure 3.10**) and the square root of A_p is calculated according to the equation (2.10):

$$\sqrt{A_p} = 4.950 h_{max} - \varepsilon(h_{max} - h_r) \tag{2.10}$$

where h_{max} is the maximum indentation depth in mm, ε = 0.75 (for Vickers indenter) and h_r is the intersection of the gradients straight line h_r with the indentation depth axis in mm.

3.2.6.2 Static bending method

Static bending method was used for investigation of static elastic modulus of composites. A screw-driven testing machine Zwick Roell Z50 equipped with 50 kN dynamometer (or additional dynamometers 1 kN or 200 N, depending on expected forces) was used. Cross-head speed (CHS) was 0.5 mm·min^{-1}. Elastic modulus was evaluated from the slope of linear part in the stress – strain (load – deflection) curve obtained from three-point bend test. For its calculation the equation (2.11) from the standard [179] was used:

$$E = \frac{(P_2 - P_1) l^3}{4 b h^3 (d_c - d_s)} \tag{2.11}$$

where the elastic modulus E is expressed in MPa, P_1 and P_2 is lower and upper load expressed in N, l is span in mm, b and h are specimen width and thickness in mm, respectively, and d_c and d_s are displacements (in mm) corresponding to P_1 and P_2, respectively.

3.2.6.3 Impulse excitation technique

Non-destructive measurement of elastic modulus by impulse excitation technique was measured by GrindoSonic MK5i (J. W. Lemmens, Inc., Belgium) with GeneMod software.

According to the free-free beam technique [179] the specimen of uniform section was placed on the nodal points at distances of 0.224 of the length from its free ends. The specimen was excited by means of mechanical impulse (a tap) by suitable hammer and the vibrational motion was detected by hand-held (or fixed) piezoelectric probe (or a microphone) and the resonant frequency was measured. The flexural elastic modulus was calculated from the frequency, dimensions and weight using formula (2.12):

$$\mathrm{E} = 0.946 \left(\frac{\mathrm{m f_n^2 l^3}}{\mathrm{b h^3}} \right) \left(1 + 6.585 \left(\frac{\mathrm{h}}{\mathrm{l}} \right)^2 \right) \tag{2.12}$$

where E is the dynamic Young's modulus, expressed in N·m^{-2}, m is mass of test piece, expressed in g, b is width of test piece perpendicular to flexural mode vibration, expressed in m, h is thickness of test piece in direction of flexural vibration, expressed in m, l is length of test piece, expressed in m, f_n is fundamental frequency of flexural vibration, expressed in Hz.

3.2.7 Fracture toughness

The fracture toughness was measured on composites with commercial-based matrices (MS, MPS) reinforced with continuous basalt fibres and basalt fabric using chevron notch beam technique according to the standard ASTM 1304-97 [180]. It was conducted in three-point bend

test on standard-sized beams, using an universal testing machine Zwick/Roell Z50 (Zwick Roell, Germany). Cross-head speed was 10 μm·min^{-1} and the span was 16 mm. Unidirectionally reinforced composites were prepared in three geometries, according to the fibre alignment. In the first type, the crack propagated perpendicularly to fibres (see **Figure 3.13 a)**). In the second type the specimens were cut in 90° to the fibre direction, which allowed measurement of the fracture toughness of the fibre-matrix interface in horizontal and transversal direction to the fibre alignment (see **Figure 3.13 b**) and **c)**, respectively).

The specimens can be denoted according to the crack propagation direction and the alignment of fibres as in-plane parallel (**Figure 3.13 b)**) and in-plane normal [181] (**Figure 3.13 c)**). Specimens of composites reinforced with plane-weaved fabrics were equipped with a chevron notch according to the standard specimen geometry, but the fabric reinforcement was oriented edgewise to the chevron notch (**Figure 3.13 d)**).

Fracture toughness was evaluated according to standard [180] and calculated using formula (2.13)

$$K_I c = \frac{F_{max}}{B\sqrt{W}} Y^* \tag{2.13}$$

where F_{max} is the maximum force in a load – displacement curve in N, B is thickness in mm, W is width in mm, Y^* is geometrical factor, represented by the minimum of compliance function. The minimum of the geometrical factor was evaluated using Bluhm's slice model [182].

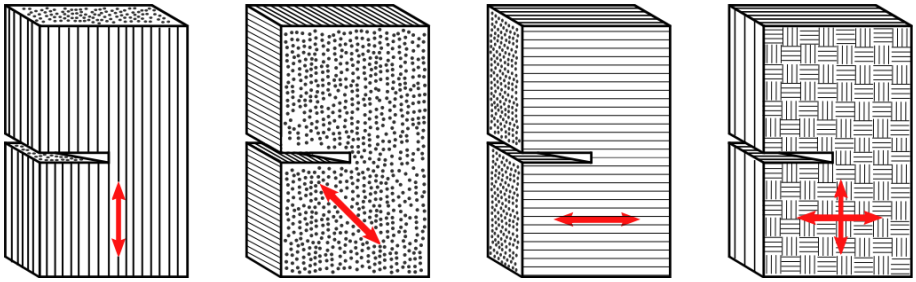

Figure 3.13 *Scheme of chevron notch orientation in specimens with various design of reinforcement. Crack propagates through: a) normal, b) in-plane parallel, c) in-plane normal alignment of fibres, d) edgewise direction to the fabrics. Red arrows show the orientation of fibres.*

3.2.8 Flexural strength

Flexural strength was measured at composites with basalt woven fabric. Specimens were cut from hand-made composite plate. Final specimens of nominal dimensions were tested in the same orientation as in case of fracture toughness. For the measurement of flexural strength was employed an electromechanical testing system Zwick Roell Z50 (Zwick/Roell, Germany), equipped with 50 kN dynamometer (or additional dynamometers 1 kN or 200 N, depending on expected forces). Cross-head speed was 1 mm·min^{-1} and the span was 40 mm.

The flexural strength was calculated according to the standard EN 843-1, using formula (2.14)

$$\sigma_f = \frac{3F_{max} \cdot l}{2bh^2} \tag{2.14}$$

where σ_f is the flexural strength in MPa, F_{max} is the maximum force before specimen failed, expressed in N, l is span in mm, b is width in mm, and h is thickness (i.e., the dimension in the loading direction) in mm.

3.2.9 Impact strength

Measurement of the impact strength was conducted on composites with MS matrix, unidirectionally reinforced with continuous basalt fibres and two more types of composites: with MS and MPS matrix, reinforced with plain-weaved fabrics. Composites with unidirectionaly aligned fibres had rectangular shape (i.e., $b \neq h$) and to recognize the testing orientation, the denomination 'flatwise' was used when the thickness (dimension parallel with the loading direction) was smaller than the width ($b > h$) and 'edgewise' when the thickness was larger than the width ($b < h$). Composites with fabrics were tested in two basic orientations: i) out-of-plane, where the layers were perpendicular to the direction of applied load, and ii) in-plane, where the layers were parallel to the loading direction, as shown in **Figure 3.14**. Three point bend configuration with span of 22 mm was used. The specimens with fabric also had the rectangular cross-section, where for the out-of plane orientation the dimension b is larger than h and for the in-plane orientation the dimension b is smaller than h, according to the formula (2.14).

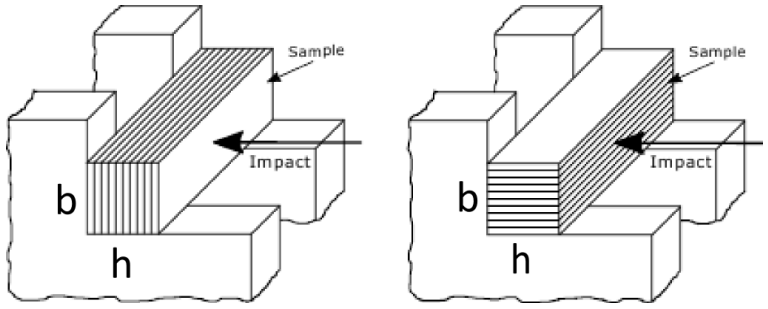

a) $b > h$ b) $b < h$

Figure 3.14 *Scheme of specimen configuration: a) out-of-plane, b) in-plane.*

For the test was employed an instrumented Charpy impact tester Zwick/Roell 5113.303, (Germany) with nominal pendulum energy of 15 J. Selected nominal impact speed was 1 $m \cdot s^{-1}$ which corresponds to respective release angle 30°. The impact speed was used to obtain mechanical response of the composite on impact loading, whereas for the evaluation was used equation for quasi-static loading. Above 1 $m \cdot s^{-1}$ the inertia caused higher dynamic effects, leading to difficult evaluation of the test curves, for example finding the maximum force or the area under the curve, as can be seen in **Figure 3.15**.

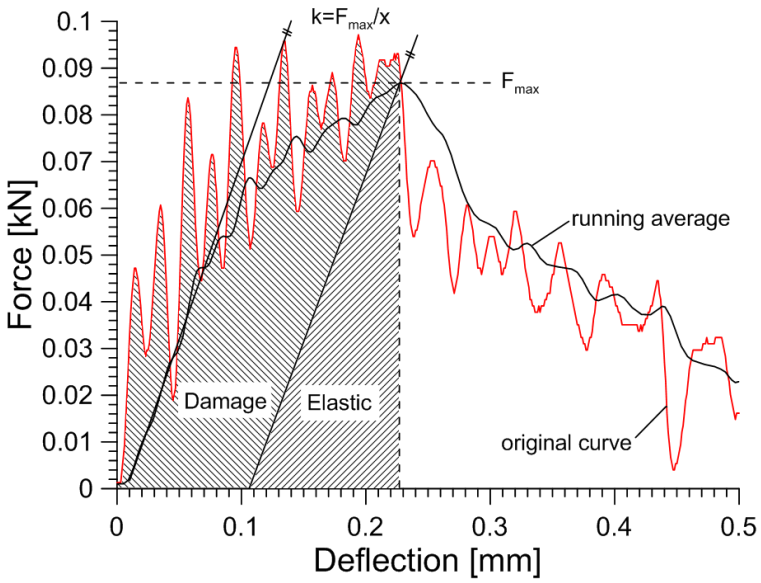

Figure 3.15 *Scheme of the evaluation of the loading curve after the impact test. The original curve (red) is fitted with running average (black) and the area under the curve belongs to individual constituents of the energy absorbed by the specimen up to maximum force.*

A high-speed camera i-Speed 3 (Olympus, Japan) was used for recording of the specimen deformations occurring during the impact test. Frame rate was 50 000 frames·s^{-1}, which helped to understand the fracture processes acting in the composite structure.

The impact strength was calculated from the determined maximal force before failure of the specimen and parameters of the loading configuration according to the CEN EN 843-1 standard [183] used for static flexural strength determination. Calculation of stress is independent on the loading speed and using this formula was governed by the aim to compare quasi-static and impact data.

The important part of the evaluation of the loading curves was the determination of energy consumed during specimen fracture. This process is schematically depicted in **Figure 3.15**. The total fracture energy was calculated as the area below the loading curves which was limited by the maximum load. Each loading curve was fitted with running average (black curve) with window size of 51. The slope of the linear part of the average-loading curve and a limit of a maximum force value were used to calculate the elastic part of energy. The damage energy was calculated by subtracting the area of the elastic energy from the total energy area under the original curve. Both energies were normalized by the sample cross-section to obtain comparable data between samples independently on their dimensions.

4 RESULTS

All the results obtained during the research conducted on the fibre-matrix interfaces of SiOC matrix composites reinforced by selected ceramic fibres are presented in the following chapter respecting the logic presented in the scheme shown in **Figure 4.1**. The preparation of own materials is not the result of this work, however, findings resulting from this investigation were used in the processing of new variants of composite materials during an optimisation process. Primarily, the investigation of the microstructure and corresponding mechanical behaviour of the matrix material itself is presented and it is just a logical continuation of previously done research conducted by the research team. Results presented here are describing matrix materials mainly prepared by the partial pyrolysis. Second part summarises results obtained on the composite materials with optimised fibre-matrix interfaces using modification of the matrix and/or by selection of fibres. Such composites were characterised under various loading conditions which reveal an effect of the fibre-matrix interfaces and additionally their potential in the structural applications. The third part of this chapter is dedicated to the results of chemical, microstructural and micro-fractographic analyses of the fibre-matrix interfaces of fully and partially pyrolyzed composites. The discussion of the main findings will be summarised in the separate chapter.

4.1 TAILORING AND CHARACTERISATION OF MATRIX MATERIALS

4.1.1 Materials from commercial precursors

The behaviour of MS and MPS materials was studied on set of materials prepared at pyrolysis temperatures from 400 to 1000°C, including the only cured state at temperature of 250°C. The materials were also prepared at constant temperature of 650°C with variable dwell time of 5 minutes, 1, 2 and 5 hours. Note in the following, the 5 minutes dwell may be denoted as an 0 hour dwell.

4.1.1.1 Microstructure

MS and MPS materials were supplied in a form of thin fragments with smooth surfaces. Their size was varying from 1 to 10 mm. The overview of materials cured at 250°C and pyrolyzed from 400 to 1000°C was collected in macrophotographs obtained by stereomicroscope, and is given in **Figure 4.1**. MS materials were clear and transparent up to 700°C, where it completely turned dark-brown and from 800°C it was black. MPS material was light brown initially from the cured state and at 600°C turned to dark-brown and from 700°C was completely black.

The observed fragments had different thickness and therefore it was not recognized if there was linear change of colour with the temperature, especially at MPS – specimens 250, 400 and 500 were much thinner than the rest. According to the information found in the literature the colour is probably dependent on the amount of free carbon micro-domains present in the developed microstructure [117]. Darkening of the material is therefore expected to be in correspondence with an increasing pyrolysis temperature.

MS and MPS specimens pyrolyzed at 650°C with various dwells from 0 to 5 hours are captured in **Figure 4.2**. MS material undergoes a change of colour, from completely transparent colourless to dark-brown, still transparent fragment. The MPS specimen was coloured even after

curing, even when the material was pyrolyzed at the temperature of 650°C with practically no dwell. That indicates that the polymer-ceramic transformation (or at least production of free carbon micro-domains) in the MPS material starts at lower temperatures comparing to the MS material.

MPS material was subjected to the same dwell intervals (plus one more specimen with 10 hours dwell) at the temperature of 520°C. The macrophotographs from the stereomicroscope are provided in **Figure 4.3**. Even at this temperature the specimen with the lowest dwell is already brownish. (One reason might be that initially the liquid resin is yellowish, whereas the MS resin is colourless.) A colour change with an increasing dwell time does not seem to be linear, which can be a result of varying thickness of the specimens.

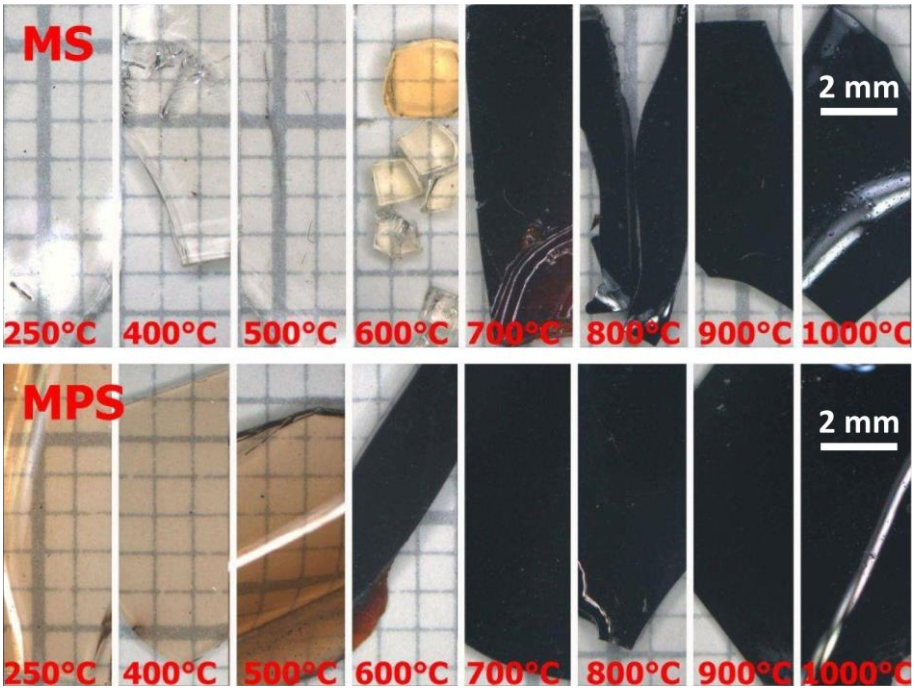

Figure 4.1 *MS and MPS materials in cured state at 250°C (left upper and lower image) then pyrolyzed at temperatures from 400 to 1000°C.*

Figure 4.2 *MS and MPS pyrolyzed at 650°C at various dwells – from 5 min (0 hours), 1 hour, 2 hours and 5 hours.*

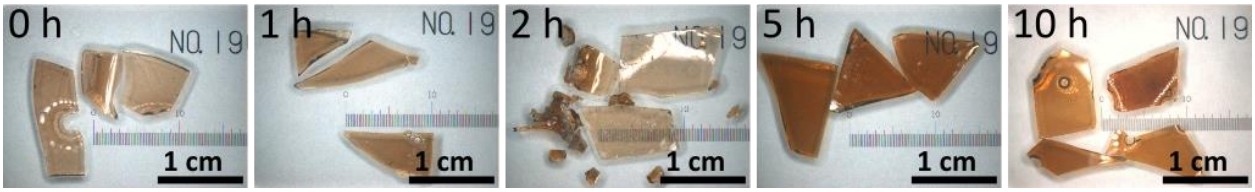

Figure 4.3 *MPS material pyrolyzed at 520°C with dwell from 0 to 10 hours.*

Transparent materials had similar optical properties (colour and refractivity) with used mounting resin, which made them unrecognizable under the standard light, therefore, for microstructural observation the laser imaging was used, as can be seen in **Figure 4.4**.

Except of crushed portions of MS material at 500 and 600°C, both materials were very similar on the top of their surfaces. As the materials darkened (from 700°C), they reflected the light with silverish surface. The higher the pyrolyzing temperature was the more opaque materials were. The curing and pyrolysis up to 500°C did not cause any cracking which can be caused by/accompanied with relatively high level of viscoelastic behaviour of such materials as will be discussed further. The higher temperature led to the formation of cracks. The macro-porosity was found to be on very low level and was predominantly formed before curing process, originating from embedded air bubbles.

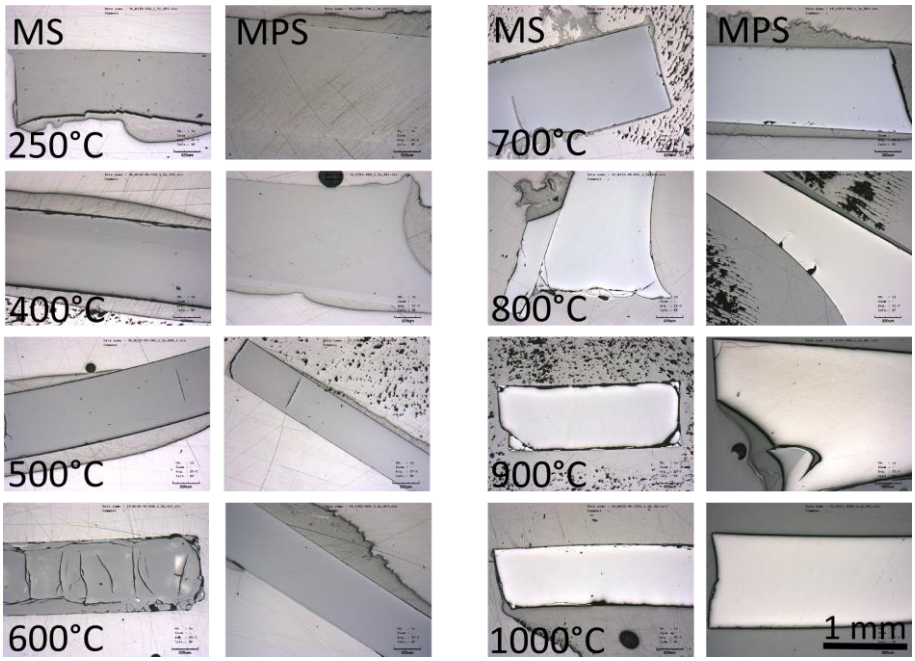

Figure 4.4 *Microstructure of MS and MPS during curing and pyrolysis from 400 to 1000°C.*

During the polishing was observed that the specimens pyrolyzed at 500 and 600°C were more sensitive to shear damage than other specimens. Many cracks were formed in plane parallel to the polishing direction and crumbled, causing extensive scratching of surrounding material surface. Therefore, these specimens had to be polished carefully, to prevent formation of cracks, which may damage the whole specimen, as can be seen in **Figure 4.5**. During the polishing, materials prepared at higher temperatures behaved similarly to the ceramics. Thus, careful

approach led to the high quality surface, without formation of additional cracks except cases of edges where chipping and cracking occurred.

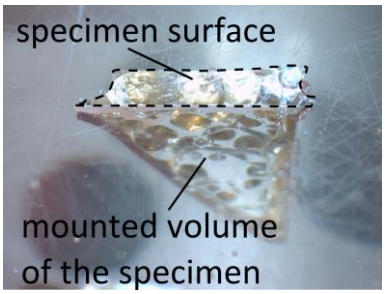

Figure 4.5 *Fragmentation of the whole volume of polished material.*

Microstructure observation of MS and MPS materials at various dwell at temperature 650°C was conducted on specimens displayed in **Figure 4.6**. Both materials with only 5 minutes dwell were fragmented, which was partly caused by sensitivity of the material to water, applied during grinding. The MPS specimen had very specific structure which was not seen at any other MS or MPS materials. Rest of the specimens had uniform appearance - MS seemed to be more transparent and less refractive than MPS, whereas MPS material seemed to be more sensitive to scratching, considering the fact that both materials were prepared by the same procedure.

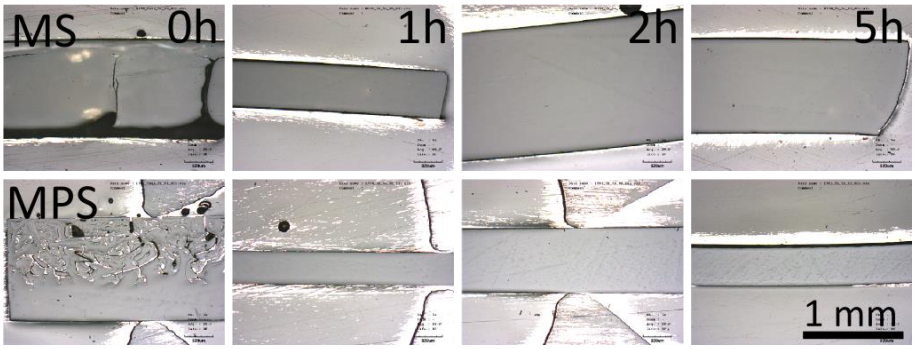

Figure 4.6 *MS and MPS materials pyrolyzed at 650°C at various dwells – from 5 minutes to 5 hours (viewed in a confocal laser microscope).*

4.1.1.2 Density

In **Table A.1** (in Appendix) is provided an average data with standard deviation for density of specimens cured at 250°C and pyrolyzed at 400-1000°C. The density was measured by Archimedes principle. Respective plots are displayed in **Figure 4.7**.

Initially, in a cured state, density of MS was 1.23 $g \cdot cm^{-3}$, and of MPS 1.27 $g \cdot cm^{-3}$. After pyrolysis at 400°C the density of both materials slightly decreased, which could be caused by swelling of the materials, i.e., structural reorganisation of polymer chains and/or formation of the microporosity. This trend changes for materials pyrolyzed at 600°C and the density starts to increase. At pyrolysis states of 600 and 700°C both materials reached almost the same density and even though the density of MPS was initially slightly higher, pyrolysis at 800°C and higher, the trends swap, and the density of MS is higher, increasing linearly up to pyrolysis at 1000°C. At this temperature the material is pronounced to be fully pyrolyzed, thus, the amorphous SiOC glass is obtained [86, 94, 95, 128]. Density of MPS increases linearly, too, but not that significantly as for MS.

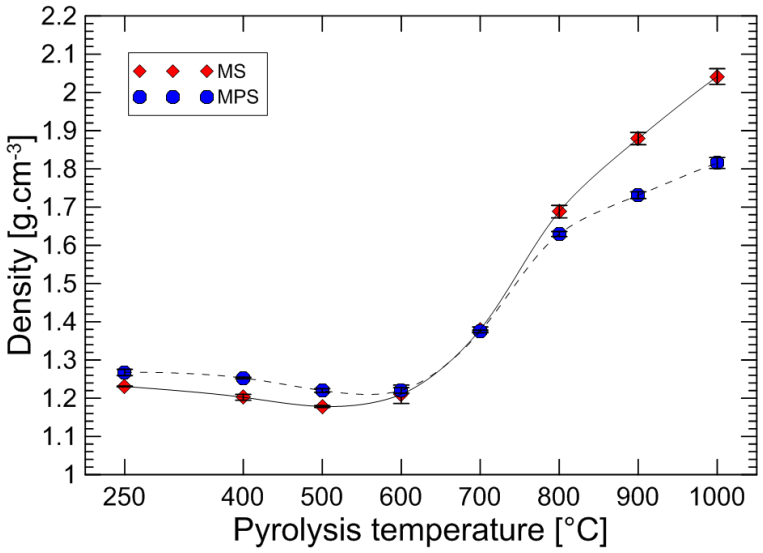

Figure 4.7 *Density development for MS and MPS materials after curing at 250°C and pyrolysis at 400–1000°C. Density was measured by Archimedes' principle in isopropanol.*

Based on the findings previous to this work, investigation was focused on the effect of dwell time at particular pyrolysis temperature. Both MS and MPS materials pyrolyzed at 650°C for 5 minutes, 1, 2 and 5 hours were analysed with the aim to observe the kinetics of ongoing processes. At first, the density was measured by Archimedean method. It was observed that materials pyrolyzed for 5 minutes literally exploded (fragmented) into several pieces of about 1 mm^3, after the contact with water – the standard medium for density measurement. The response usually took only a few seconds, maximum up to one minute. It was probably caused by the hydrophilic nature of the material. The material swelled, which led to an increase of internal stresses followed by its fast failure. Newly formed pieces were approximately 10–20 times smaller than the original one. Since this finding, the density was measured using pure (anhydrous) isopropanol which completely eliminated previously observed behaviour. The evolution of the density is plotted in graph (see **Figure 4.8**) and the data are provided in **Table A.2**.

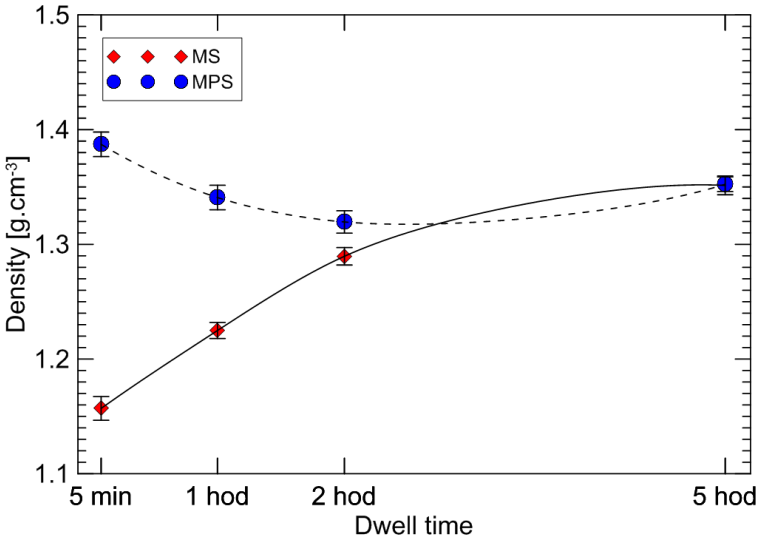

Figure 4.8 *The density of MS and MPS materials pyrolyzed at 650°C with various dwell time.*

The plotted trend in **Figure 4.8** for MS materials shows a linear increase in the density. It can be due to the fact that the polymer structure is simple and easily rearranged in this case, comparing to MPS material. The longer the heat treatment is, the more it densifies. On the other

hand, cured MPS material has higher density than MS, but its density decreases as the dwell time increases. Minimum density value of MPS material was obtained at the dwell time of 2 hours. Pyrolysis at 650°C for 5 hours led to basically identical densities for both the materials.

It was found out that MPS material undergoes polymer – ceramic (glass) transformation at temperatures lower than 650°C. Therefore, additional batch of MPS materials pyrolyzed at 520°C for 5 minutes, 1, 2, 5 and 10 hours was analysed. The dependence of the density was plotted in graph in **Figure 4.9**. The density for the material pyrolyzed at 520°C is lower than for pyrolysis temperature of 650°C. Although, the absolute value of density is affected by the pyrolysis temperature, the trend of transformation kinetic seems to be unchanged. Higher temperature causes better mobility of molecules and the cooling from higher temperature gives to the material more time to organize its inner structure. The density increases after 5 hours of the thermal treatment at 650°C. A decrease of the density value after 1 hour of thermal treatment may be caused by an evolution of gaseous by-products.

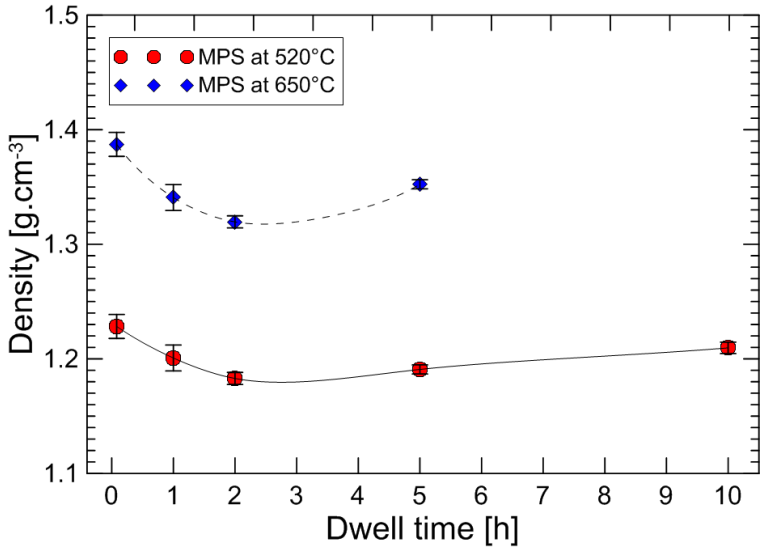

Figure 4.9 *Comparison of the density of MPS material pyrolyzed at 650°C and 520°C with various dwell time.*

The effect of heating rate on the material behaviour was studied using specimens pyrolyzed at 1000°C with heating rates: 0.5, 1, 2, 4 (only MPS), 6.4 and 10°C per minute. The results are plotted in graph in **Figure 4.10** and are listed in **Table A.3**.

The data for MS lies in interval from 2.0 to 2.06 g·cm^{-3} and for MPS from 1.80 to 1.85 g·cm^{-3}. Both materials show basically the same trend at low heating rates from 0.5 to 2°C·min^{-1}. For the data at higher loading rates (4–10°C·min^{-1}) cannot be given any consistent conclusion, because one sample (MS pyrolyzed at 1000°C with heating rate 4°C·min^{-1}) was not supplied and the last state of MS show rather decrease in the density, opposite to MPS. Nevertheless, the missing value can be estimated as approximately 2.04 g·cm^{-3}, as it was measured on MS precursor pyrolyzed at 1000°C with heating rate of 4°C·min^{-1} (see **Table A.1**). For control, respective value for MPS pyrolyzed at 1000°C with heating rate 4°C·min^{-1} was 1.82 ± 0.01 g·cm^{-3}, which is in a good agreement with 1.83g·cm^{-3}, obtained in this experiment.

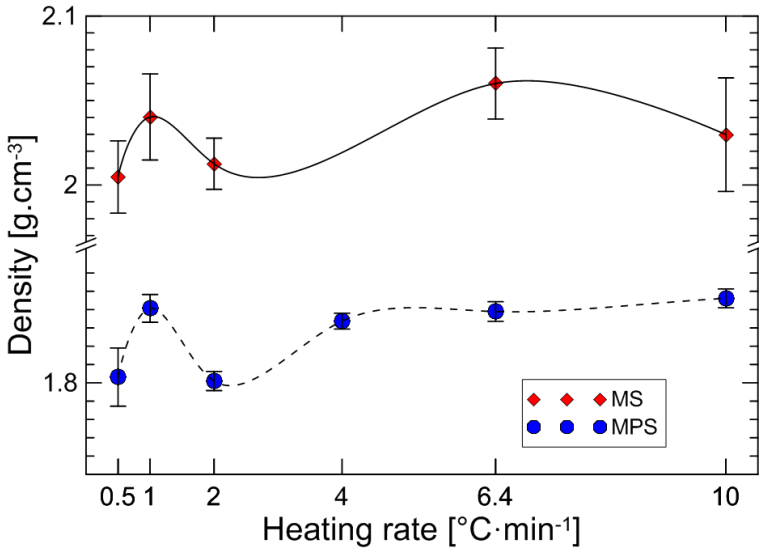

Figure 4.10 *Density at various heating rates of MS and MPS materials pyrolyzed at 1000°C.*

An effect of ageing on the density of both materials was measured on the original batch of MS and MPS specimens cured at 250°C and pyrolyzed at 400–1000°C two years after the initial experiment. The comparison is provided in **Table A.4** and the plots are displayed in **Figure 4.11**. Data with full symbols and solid line trends represent the original measurement; empty symbols with dashed lines represent data collected on the same batch after 2 years (+2Y). Values from both the measurements were almost identical. In average, the new values were slightly lower or remained the same. For most of the specimens, especially of MPS, the standard deviation a bit decreased as the new results were little more consistent than those of the first experiment.

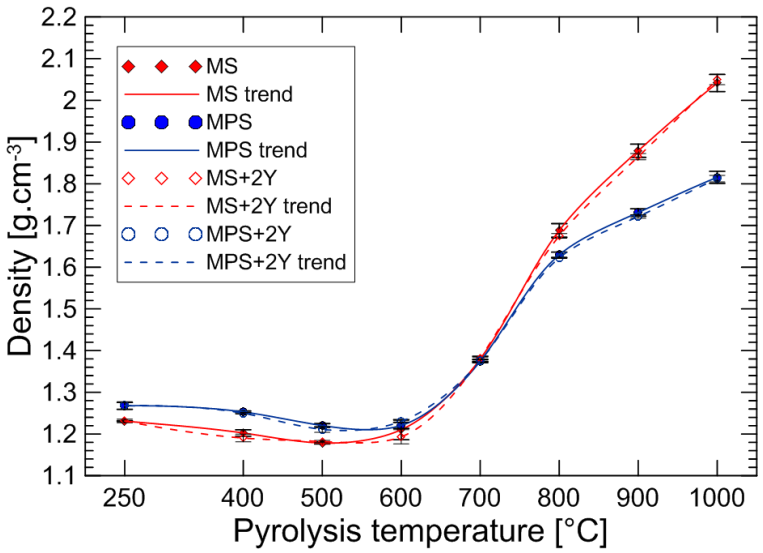

Figure 4.11 *Density of MS and MPS materials cured at 250°C and pyrolyzed at 400–1000°C after two years from the first measurement – a comparison.*

4.1.1.3 Hardness

On the set of MS and MPS materials cured at 250°C and pyrolyzed at 400–1000°C were evaluated to obtain Vickers, Martens hardness and indentation elastic modulus. According to the observed aging stability of materials examined through the density measurement, specimens from

the second batch (+2Y) were added and evaluated together with the first batch (i.e., newly prepared materials). As can be seen from the values in **Table A.5** and/or the plots in **Figure 4.12**, the standard deviation is very low in most of the cases. It increases for materials pyrolyzed at 900 and 1000°C due to their ceramic nature resulting in predominant probabilistic behaviour.

In this experiment was found out that measurement of the Vickers hardness (evaluated from the indents' diagonals) could not be used. In some temperature states of the partial pyrolysis the problem with detection of indent diagonals dimensions occurred. The presence of visco-elastic flow of such materials not allowed an exact and repeatable measurement of the indent size using an optical method, because no permanent and time independent deformation (indent) was detected. The strong visco-elastic behaviour was observed for MS precursor, pyrolyzed at temperatures in the range of 400–600°C and for MPS material pyrolyzed at 400 and 500°C. Representative imprints are provided in **Figure 4.13**. The difference of indent shape between individual pyrolysis states is obvious. The cured only material exhibits soft and rather plastic response and the indents are large comparing to the fully pyrolyzed state. The pyrolysis at 400°C led to the formation of materials with high ability to recover after loading. Oppositely, fully pyrolyzed materials resisted well to the applied force. The indents were much smaller than in partially pyrolyzed states and its dimensions were stable. Nevertheless, the Vickers hardness was evaluated, as well; listed in **Table A.5** and displayed in **Figure 4.12 a)**. Y-axis in graph (a) has a break from 15 to 100. From this graph could be assumed, that MS has identical Vickers hardness with MPS at almost all pyrolysis states, except 900°C, where the MS material showed higher scatter in data. To ensure the reliability of measured data, the Martens hardness, independent on the imprint size, was evaluated from the maximum force and maximum indentation depth of the the loading curve. The results of the Martens hardness are displayed in **Figure 4.12 b)**, for comparison with Vickers hardness. The Martens hardness provides more consistent plots. From the trend it is clearly visible, that although the MS material starts to harden later (at 600°C) than MPS (at 500°C), it reaches higher hardness than MPS, when fully pyrolyzed. The difference between both approaches can be explained that graph in **Figure 4.12 a)** represents material response after the indentation measurements contrary the graph **Figure 4.12 b)** describes the behaviour of material under loading.

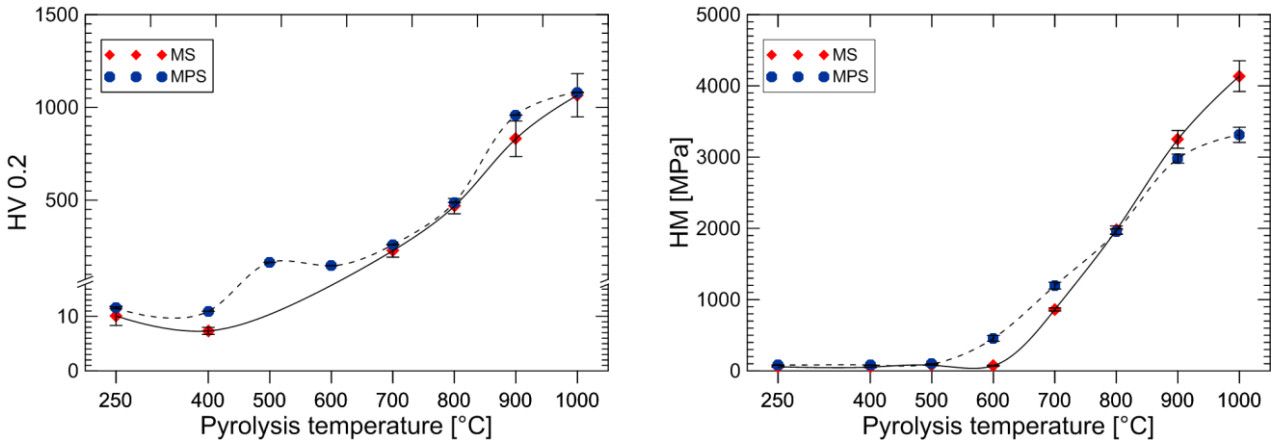

a) b)

Figure 4.12 *Development of a) Vickers and b) Martens hardness of MS and MPS materials in cured (250°C) and pyrolyzed (400–1000°C) states.*

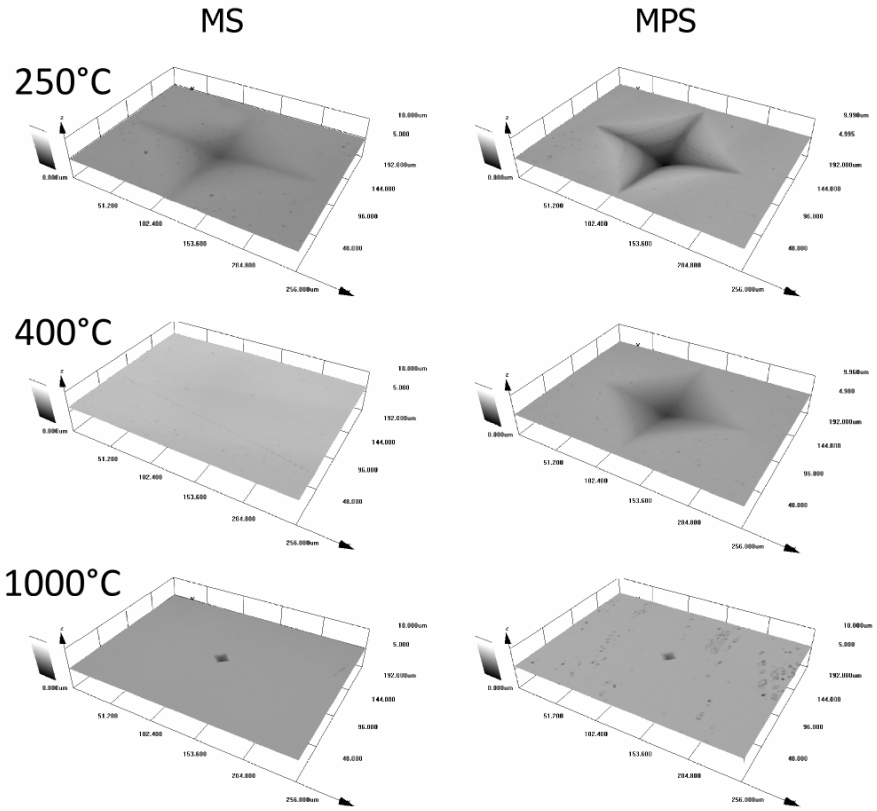

Figure 4.13 *Comparison of 3D reconstructed indents in particular states of MS (left) and MPS (right) materials. From top to bottom: cured state, partial pyrolysis at 400°C, full pyrolysis at 1000°C. The reconstruction was conducted 24 hours after the indentation.*

The nature of individual pyrolyzed states can be compared using the load – indentation depth curves, represented in **Figure 4.14**. Graph a) stands for MP and b) for MPS. The graphs show dependence of the load-indentation depth curves on processing temperature of MS and MPS materials. In both the graphs can be recognized three types of material response. The first group of materials reached the highest maximum indentation depth h_{max} (at the level of 35 μm for MS and 30 μm for MPS). In this group belong both MS and MPS materials cured at 250°C and in case of MPS, also the material pyrolyzed at 400°C. In the first group the materials exhibited delayed visco-elastic response. The second group is formed by specimens pyrolyzed at 400, 500 and 600°C for MS, and specimens pyrolyzed at 500 and 600°C for MPS. Materials in the second group reached lower maximum indentation depth (h_{max}) in comparison with the first group. Additionally, the character of the loading curves in the second group showed reasonably soft, but highly elastic material behaviour, with significant ability to surface recover after the indenter removal (compare the minimum indentation depth h_{min} of the second group with the first group). The third group is comprised of specimens pyrolyzed in the interval 700–1000°C, of both MS and MPS materials. These materials reached the lowest maximum indentation depth h_{max} at maximum load (F = 1.96 N) of all the tested materials. At the same time, the unloading curves revealed the plastic deformation of the materials. In MS material the two states (500 and 600°C) seem to be swapped, which will be investigated further in detail, by comparison of the indentation depth and the relaxation behaviour in particular pyrolysis states. The difference between the mechanical response at 600°C and 700°C in MS reveals the upcoming polymer-ceramic transformation

(700°C). For MPS material the transformation starts at 600°C. Overall, the MS material up to 600°C tends to have rather polymeric character, which can be accompanied with cleavage of Si–methyl bonds and release of cyclic siloxanes [166] in comparison with MPS material. MPS structure contains phenyl units, which are more sensitive to temperature and tend to dissociate earlier than methyl substituents.

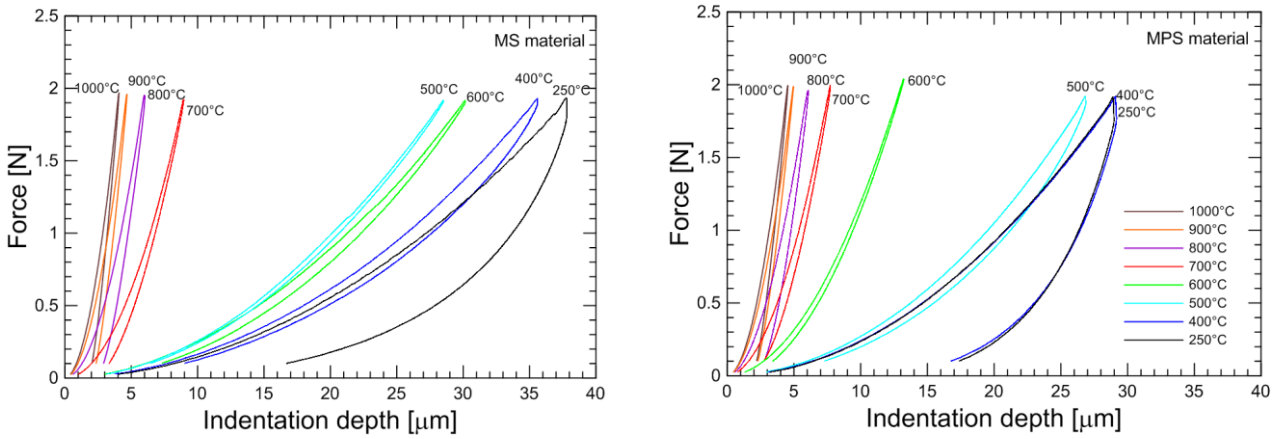

a) b)

Figure 4.14 *The effect of pyrolysis temperature on force-indentation depth curves obtained during hardness measurement for a) MS and b) MPS materials.*

The indentation elastic modulus is represented in **Figure 4.15**. The data are listed in **Table A.6**. For the cured state it reached value of 1.32 GPa for MS and 2.53 GPa for MPS material. The pyrolysis at 400°C caused slight decrease of E_{IT} to 0.95 GPa for MS and negligible increase to 2.58 GPa for MPS. The indentation elastic modulus started to increase at the pyrolysis state of 600°C for MPS and 700°C for MS. At the pyrolysis state of 800°C both the materials reach almost identical value of 32 GPa. At the pyrolysis state of 1000°C the MS precursor reached almost 67 GPa, whereas MPS precursor reached its maximum at the level of 53 GPa. The data was precise up to 900 and 1000°C, where the increase of standard deviation was observed.

Similarly to the density measurement, the Martens hardness and indentation elastic modulus of both MS and MPS materials exposed to the temperature of 650°C for various dwell times were determined (see **Figure 4.16**). Hardness values of MS material increases from 100 to ~1000 with increasing dwell time, i.e., dwell of 5 hours increases the hardness 10 times compared to 5 minutes long exposition. Similar trend can be observed for the indentation elastic modulus, which increased from ~1 to 12 GPa. Specimen pyrolyzed for 5 hours exhibited again slightly higher scatter. By the detailed analysis of indents position in the specimen cross-section it was found that increased standard deviation can be caused by the material variation near the specimen edges. From the data obtained for MPS material can be stated that the hardening process is stronger and vary comparing to the MS material. In between, some processes in the structure could take place – e.g. loss of less volatile compounds, or structural rearrangement, etc. Martens hardness and indentation elastic modulus dependences on the length of pyrolysis process at 520°C for the MPS material is shown in **Figure 4.17**. From the graph can be assumed, that the hardening takes place from 2 hours and longer dwell, but even after 10 hours dwell at 520°C the material is

less hardened than that, which was exposed to 650°C for a very short processing time. The indentation elastic modulus is exactly copying the trend of Martens hardness.

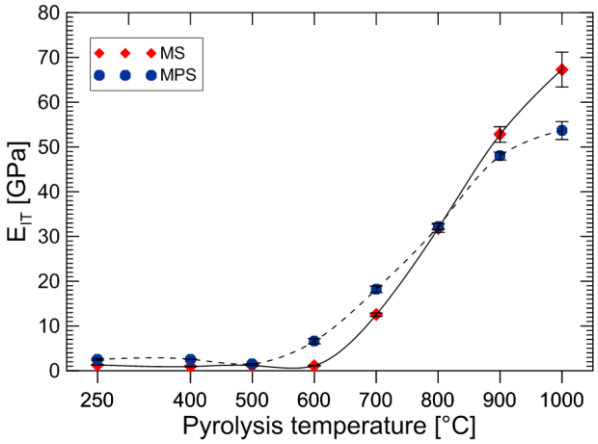

Figure 4.15 *Pyrolysis temperature effect on the indentation elastic modulus of MS and MPS based materials.*

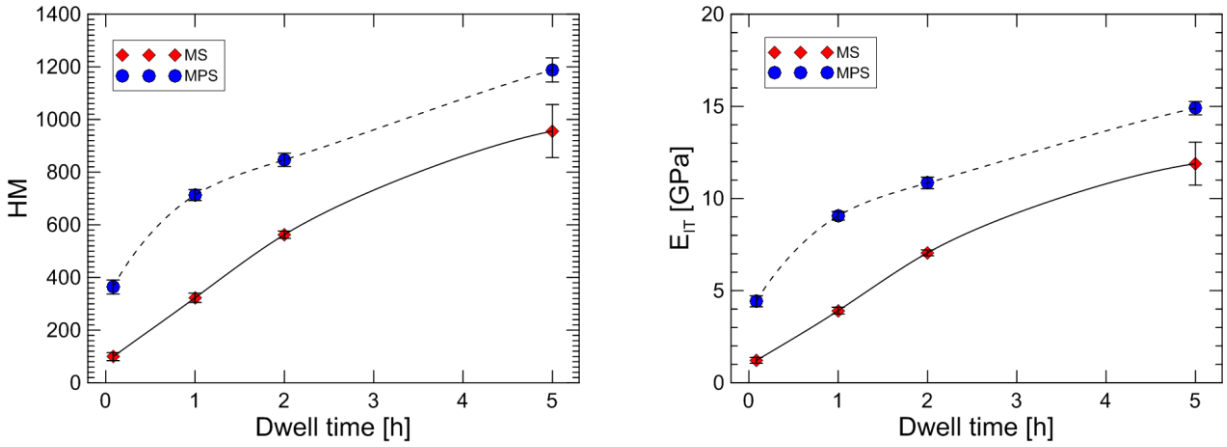

a) b)

Figure 4.16 *Development of a) Martens hardness and b) indentation elastic modulus for MS and MPS materials pyrolyzed at 650 °C for 0–5 hours.*

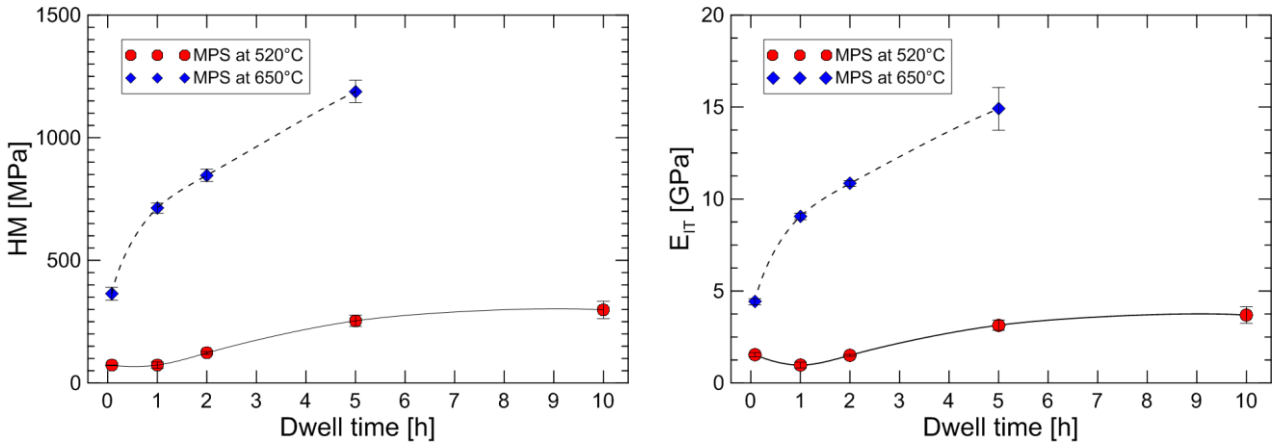

a) b)

Figure 4.17 *Development of a) Martens hardness and b) indentation elastic modulus measured for matrix precursor MPS at 520°C. Material pyrolyzed at 650°C was plotted for comparison.*

4.1.1.4 Relaxation behaviour examined by indentation

The relaxation of deformation caused by indentation was examined on the set of MS and MPS materials, cured at 250°C and pyrolyzed at temperatures from 400 to 1000°C according to the process described in [96]. The data containing an indentation depth h_{max}, reached at the maximum load F_{max} = 1.961 N and a minimum indentation depth h_{min}, obtained at the moment at which the indenter loses its contact with examined material, were determined during the measurement, i.e., at the relaxation time zero. Consequently, the indents were 3D reconstructed by a confocal laser microscope immediately after the test and then in a time sequence (24 h), to obtain information of the material relaxation.

Comparison of both indentation depths h_{max} and h_{min} obtained from the instrumented indentation, as well as h_{conf} from 3D reconstructed surface using laser confocal microscope, is provided in **Table A.9**. Relaxation was calculated from the difference between h_{min} determined from the machine software and h_{conf} measured using laser confocal microscope. Graphic representation of the data is provided in **Figure 4.18**. The most extensive relaxation was observed at pyrolysis state of 500°C for MPS (99.5 %). With increasing pyrolysis temperature the level of relaxation decreases. MPS relaxes of around 50 % better comparing to MS, even at pyrolysis states of 900 and 1000°C which may have positive effect on deformation behaviour of composites.

In **Figure 4.19** is provided graphic comparison of indentation depths in individual pyrolysis states of MS and MPS materials. In graph a) are compared maximum and minimum depths obtained during instrumented hardness measurement. In graph b) are compared minimum depth obtained from the machine and the same dimension measured by confocal microscope immediately after indenter removal and transport onto the microscope table. The most significant change of h_{min} was observed at pyrolysis state of 400°C for MPS. Although the MS at pyrolysis state of 600°C exhibits higher depth, in the 3D reconstructed indent (i.e., relaxed material) this trend was not observed.

Comparison of the indents depth shows that the indent dimensions in materials pyrolyzed under 700°C change significantly using different measuring methods and both measuring approaches are comparable only in fully pyrolyzed materials.

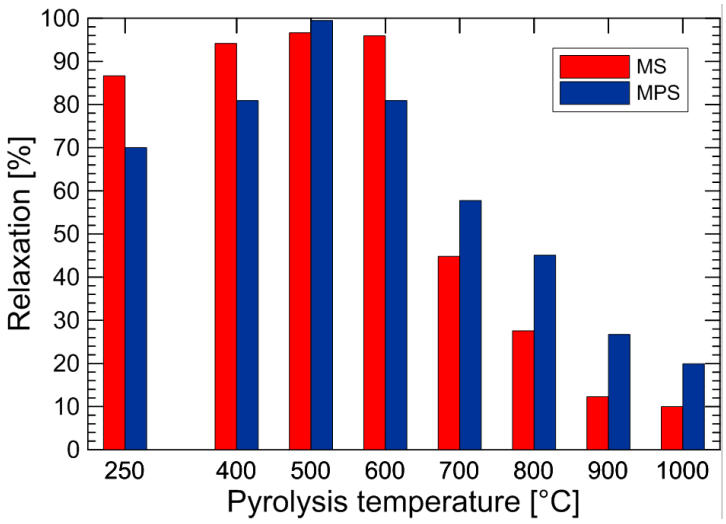

Figure 4.18 *Comparison of the relaxation of the indents in MS (red) and MPS (blue) precursors.*

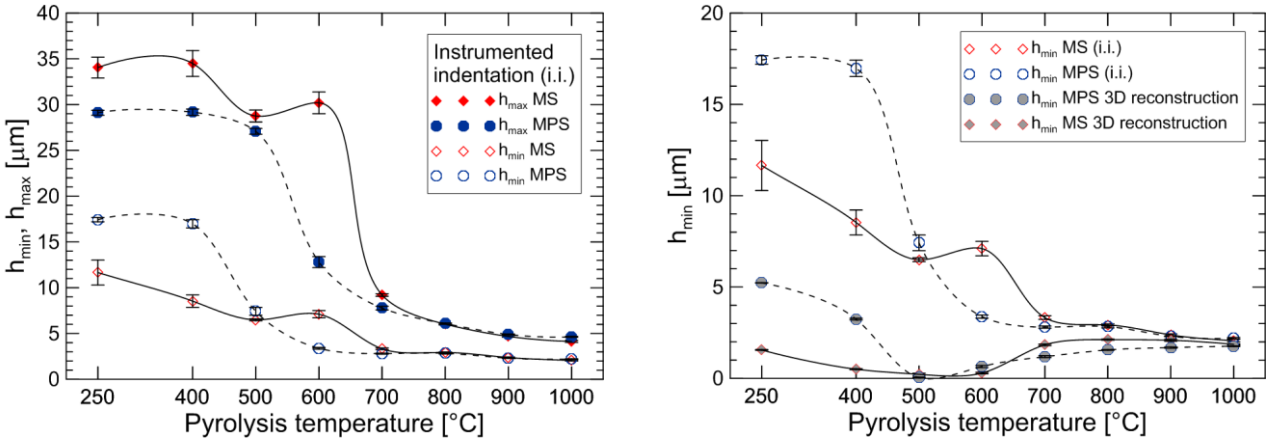

a) b)

Figure 4.19 Comparison of a) maximum and minimum indentation depth and b) minimum depth measured by the indentation machine and by the confocal microscope.

As can be seen from the graphs in **Figure 4.19**, with increasing pyrolysis temperature the material transforms and densifies, thus the indentation depth decreases. Maximum indentation depth of the cured state is comparable to the pyrolysis state of 400°C. MS material pyrolyzed at 600°C exhibits anomalous behaviour. This behaviour was confirmed by repetition of the experiment on newly prepared, where the same trends were observed, as can be seen in **Figure 4.20**. Newly prepared batch exhibited slightly higher indentation depth for the MS material pyrolyzed at 400°C.

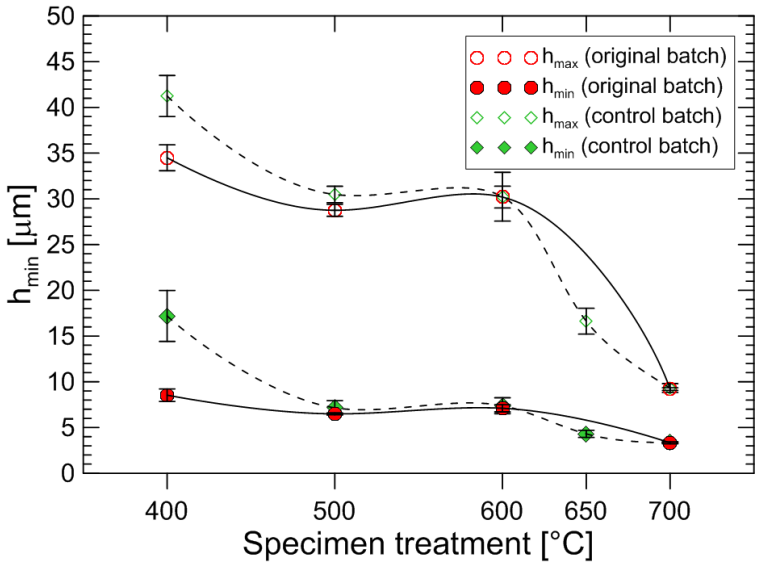

Figure 4.20 *Comparison of original (red) and new (green) batch of MS precursor.*

The time – indentation depth dependence was measured with the aim to capture relaxation kinetics for chosen states of materials. The indentation depth measurement was collected from 3D reconstructions, performed on the cured state and pyrolyzed states (400 and 600°C) of the MS precursor, which exhibited slightly higher relaxation (as could be seen in **Figure 4.18**) than MPS. During the measurement was observed that most of the indent volume recovered within two hours and when the decrement of depth decreased under certain level the uncertainty of the depth

measurement increased. The last value was measured 24 hours after the indentation was performed. The depth was slightly decreased, but the scatter in obtained data was quite high. The results are represented in semi-log plots in **Figure 4.21**. Standard error of the mean was affected by quality of the reconstructed image and accuracy of manual measurement of the depth. An example of the indentation depth measurement is depicted in **Figure 4.22**.

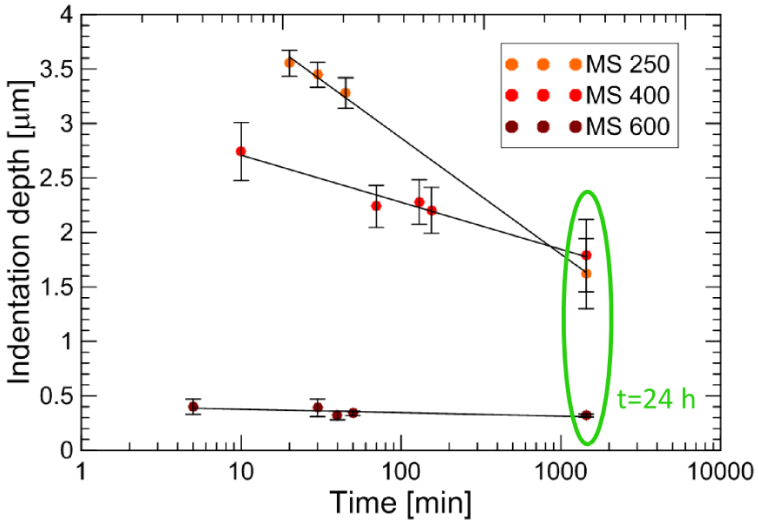

Figure 4.21 *Development of the indentation depth of the MS material in cured state (250°C) and pyrolyzed at 400 and 600°C.*

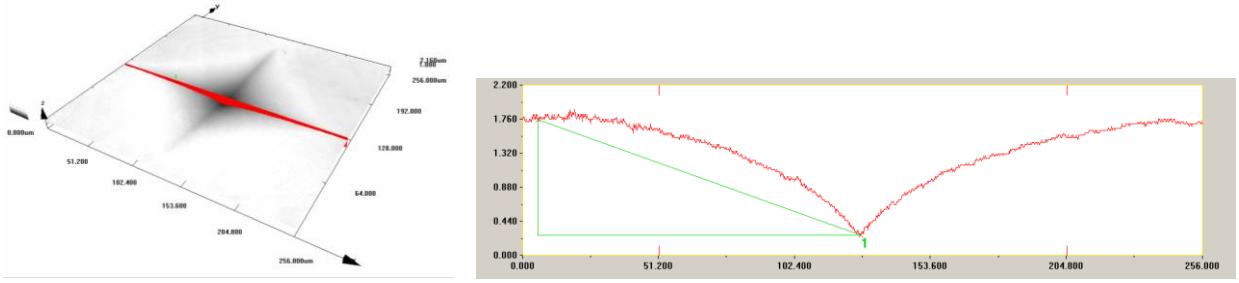

a) b)

Figure 4.22 *a) 3D reconstructed indent of the MS material cured at 250°C and b) the indentation depth measurement from the indent's profile analysis.*

4.1.2 Materials from laboratory synthesized resins

4.1.2.1 Microstructure

Laboratory prepared materials SiONC, T4D1-B, T4D1-Fe and T19D9 were analysed in fully pyrolyzed state (at 1000°C) and after consequent annealing for 3 hours at 1300 and 1500°C, two times in a row. Images of the microstructure are displayed in **Figure 4.23**. The sequence of captured images shows the microstructure evolution of particular laboratory prepared materials with the heat treatment temperature.

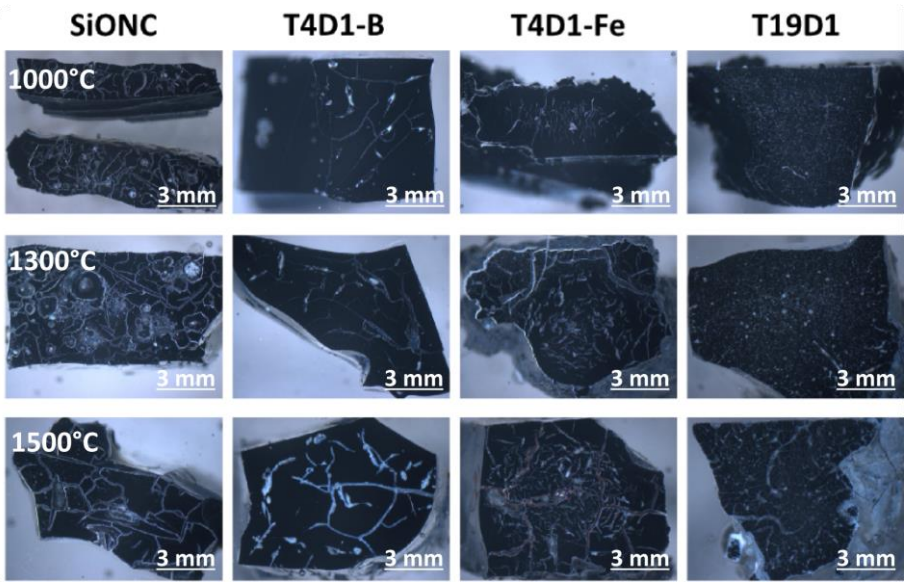

Figure 4.23 *Materials from laboratory synthesized resins in pyrolyzed (1000°C) and annealed (1300 and 1500°C) states.*

All materials revealed very fragmented structure, full of cracks and micro-cracks. SiONC material, in all the cases, contains besides the cracks also a number of large pores (bubbles). Specimen annealed at 1500°C seems to have reduced number of cracks, probably due to occurrence of some healing process.

T4D1-B has basically identical structure in both specimen states – pyrolyzed at 1000°C and annealed at 1300°C. In material annealed at 1500°C the pores seem to be a bit wider, which may be caused by higher sensitivity of material to oxidation, caused by boron atoms. The main reason for incorporation of boron atoms to the material was its possible positive influence on the structural reorganisation of the polymer during pyrolysis and lowering shrinkage (causing decrease of developed internal mechanical stresses) of the final product. This presumption was fulfilled and this material exhibited the lowest amount of cracks developed during pyrolysis.

T4D1-Fe has a very specific structure. In most the cases were observed significantly different structures in outer (shell) and inner regions (core) of the specimen. The outer region of thickness of several millimetres is compact, mostly without cracks, as visible especially for T4D1-Fe in pyrolyzed state (at 1000°C) and for specimen annealed at 1300°C in **Figure 4.23**. Specimen treated at 1500°C has also visibly different structure in the core and the shell of the specimen. The shell also contains a few cracks of larger dimensions, but it is still more compact than the core, which contains a lot of short randomly aligned cracks and pores. In cracks of the specimen (T4D1-Fe annealed at 1500°C) were also visible copper-coloured marks, introduced by a copper wire during machining.

T19D1 has a structure which is completely different from previous specimens. The structure is full of tinny pores and the appearance resembles a frozen ice. Pyrolyzed specimens annealed at 1300°C have basically identical structure with material annealed at 1500°C, which contained also a few large cracks. The development of large cracks is connected with the expansion of gases entrapped in the micropores during annealing at temperature of 1500°C.

4.1.2.2 Hardness

The results depicted in **Figure 4.24** follow the trend known from [93] that the materials hardness decreases by increasing the annealing temperature from 1300 to 1500°C. Unfortunately, the microstructure suffers from damage (crack, pores) and due to that the hardness values are very scattered. Both hardness determination methods used resulted in similar trends. Regardless the material states, the hardness is the highest for SiONC, second is T4D1-B and third follows T4D1-Fe. In the case of T19D1, Vickers hardness is similar to SiONC, but the Martens hardness values are the lowest of the examined materials and have large standard deviations in all the material states. The deviation in hardness is caused by large differences in maximum depth reached by the indenter. Additionally, the porous structure exhibited certain level of elasticity, which led to partial surface recovery and thus smaller indent diagonals, leading to higher determined Vickers hardness. Values are listed in **Table A.10** and **Table A.11**.

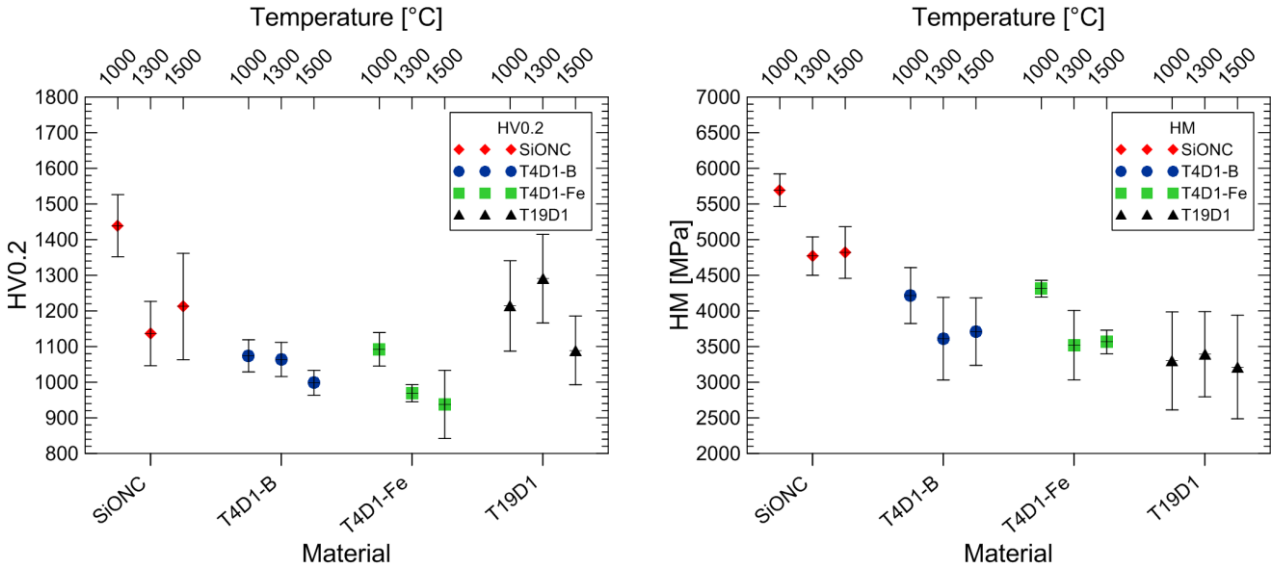

a) b)

Figure 4.24 *Hardness of laboratory synthesized materials: a) Vickers hardness, b) Martens hardness.*

4.1.2.3 Indentation elastic modulus

Indentation elastic modulus is plotted in graph in **Figure 4.25**. The trend is similar to that observed for Martens hardness. The elastic modulus decreases from SiONC over T4D1-B and T4D1-B to T19D1. All the tested specimens exhibited the highest indentation modulus in their pyrolyzed state (1000°C), which decreased with increasing annealing temperature. For comparison of obtained values see the **Table A.12**.

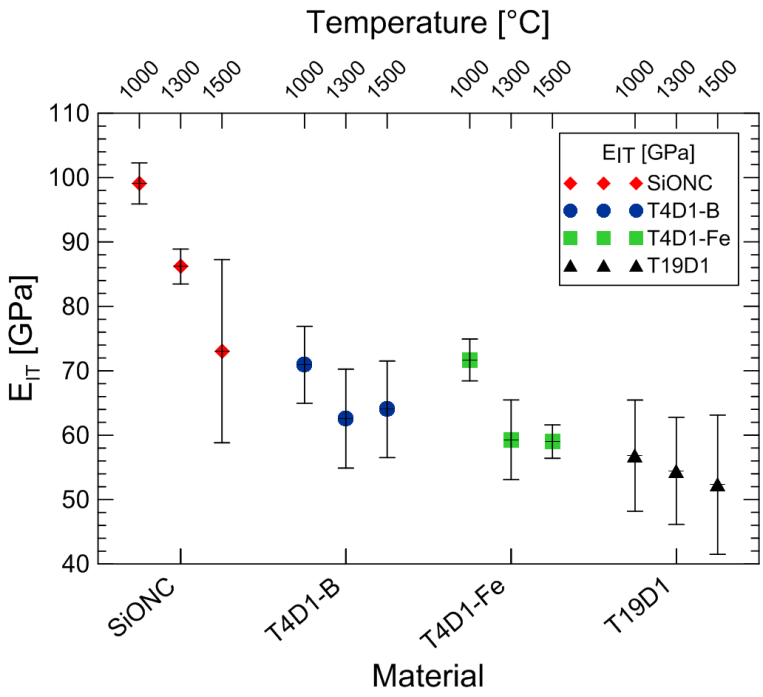

Figure 4.25 *Indentation elastic modulus of laboratory synthesized materials SiONC, T4D1-B, T4D1-Fe and T19D1.*

4.2 CHARACTERISATION OF COMPOSITES

4.2.1 Unidirectionally reinforced MS matrix composites

4.2.1.1 Microstructure

In this section, the microstructure of basalt fibre reinforced composites with MS based matrix, partially pyrolyzed at 650°C and 750°C, and also the specimens annealed for 3 hours at 550°C, are analysed. Polished surface of composites partially pyrolyzed at 650°C showed no obvious fibre degradation. As can be recognized from **Figure 4.26 a)**, the fibres had regular, circular-shaped cross-sections with opaque colour. After treating of the material at 550°C for 3 hours no structural change of fibres was observed, as represented in **Figure 4.26 b)**.

On the contrary, significant degradation was observed on composites pyrolyzed at 750°C; see **Figure 4.27 a)**. Major number of fibres is no longer circular in their cross-section, their shape change to polygons. Only the stay alone fibres which were surrounded by matrix and not touching other fibres remained rather circular. The cross-sections of the fibres remarkably glittered, as their structure became crystalline. Annealed specimen is displayed in **Figure 4.27 b)**. Also there were observed crystals in the cross-section of the fibres. Detailed view of both specimens is provided in **Figure 4.28 a)**, **b)**. In the structure of the specimen pyrolyzed at 750°C and heat treated for three hours at 550°C were found few regions of fibres surrounded by material resembling a solidified melt. The appearance of the fibres, i.e., deformed cross-section, visible crystallisation and marks of solidified melt, refer to upcoming melting of basalt fibres.

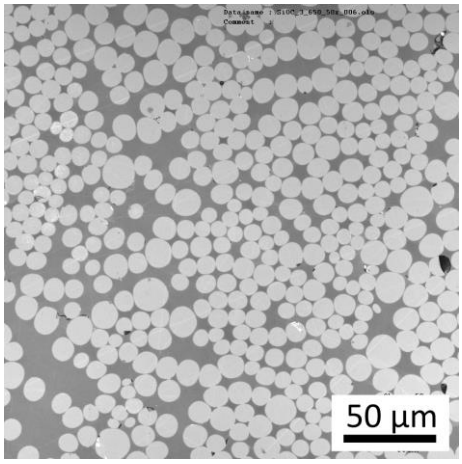

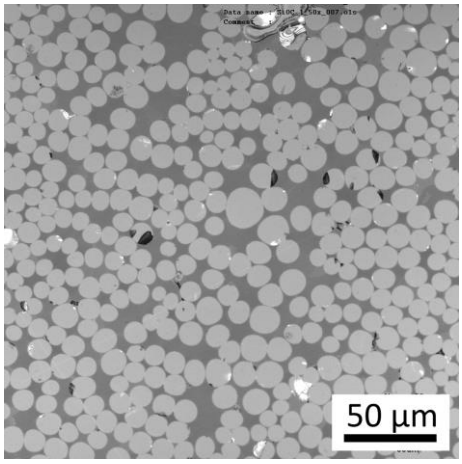

a) b)

Figure 4.26 *Microstructure of MS composite a) after partial pyrolysis at 650°C and b) additional annealing for 3 hours at 550°C.*

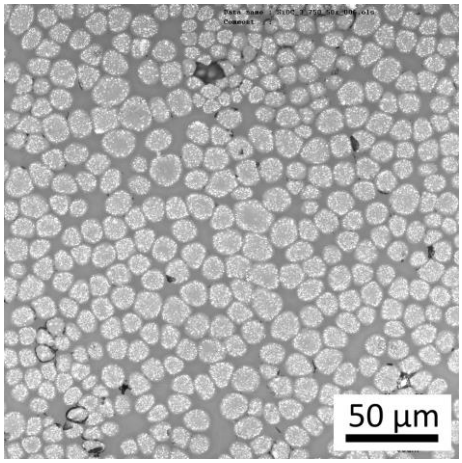

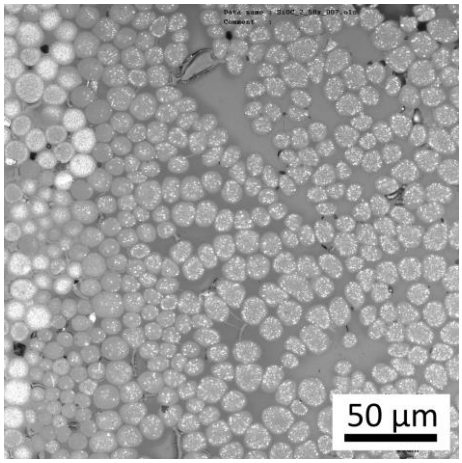

a) b)

Figure 4.27 *Microstructure of MS composite pyrolyzed at a) 750°C and b) annealed at 550°C. Basalt fibres exhibit grain coarsening in both pyrolysis and annealing.*

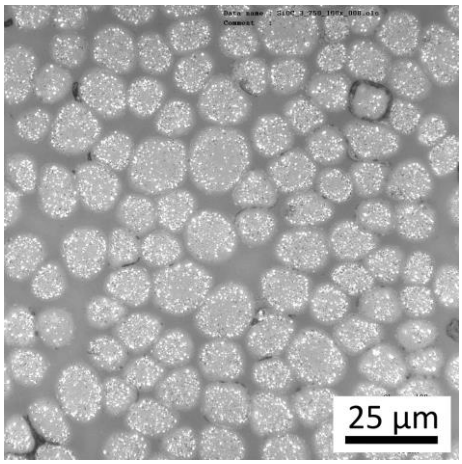

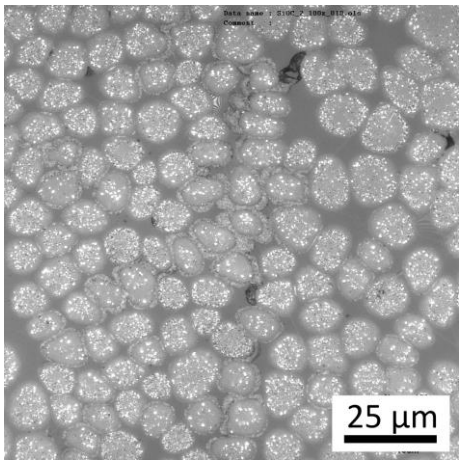

a) b)

Figure 4.28 *Detailed view of the microstructure of MS composite a) partially pyrolyzed at 750°C and b) additionaly annealed at 550°C, with thermally affected basalt fibres*

4.2.1.2 Density

Calculation of the composite density is based on the rule of mixture [1] , using known density and volume fraction of both components – bulk pyrolyzed resin at respective pyrolysis state (1.3 g·cm^{-3}) and the density of the reinforcement declared by producer (2.72 g·cm^{-3}). Density of MS material pyrolyzed at 650°C was interpolated from known measured density values measured on material pyrolyzed at 600°C and 700°C (see **Table A.1**). The processing of the composites faces the problem of slightly variable content of the reinforcement. In this case the fibre content determined as an average from several measurement was 58 wt. % [159] and density of the composite pyrolyzed at 650°C was calculated according to the rule of mixture (3.1):

$$\rho_c = \rho_f v_f + \rho_m v_m \tag{3.1}$$

where ρ_c is density of the composite, ρ_f is density of the fibre, v_f is fibre volume, ρ_m is density of the matrix, v_m is matrix volume:

$$\rho_c = 2.72 \cdot 0.58 + 1.30 \cdot (1 - 0.58) = 2.1215\ g{\cdot}cm^{-3} \tag{3.2}$$

Calculated value of density corresponds well with values obtained by a boiling water method, which is 2.07±0.06 g·cm^{-3} [111]. Apparent density of the composite was also calculated from dimensions and calculated weight of the composite plate. Weight of the plate was 34.62 g and volume 17.96 cm^3 thus the volume density was 1.93 g·cm^{-3}. The slightly lower geometrical density can be ascribed to the fact that dimensions were measured using calliper which is taking the maximum distance, however, the surface was not perfectly smooth.

4.2.1.3 Elastic modulus

The theoretical value of elastic modulus of the composite (MS precursor with unidirectional reinforcement of 58 wt. % of basalt fibres), was calculated using the rule of mixture, from the formula (3.4):

$$E_c = E_f v_f + E_m v_m \tag{3.4}$$

where E_c is elastic modulus of the composite, E_f is elastic modulus of the fibre, v_f is fibre volume, E_m is elastic modulus of the matrix, v_m is matrix volume.

Elastic modulus of the fibres (85 GPa) was taken from the manufacturer's data sheet. The elastic modulus of the MS material pyrolyzed at 600 and 700°C was measured by the indentation method. The value for matrix was interpolated for the temperature 650°C as 6.68 GPa. The value was compared with the data of the MS material pyrolyzed at 650°C for various time periods (0–5 hours, see **Figure 4.17 b)**). There was found that the interpolated value fits the best to the pyrolysis with dwell time of 2 hours at 650°C, i.e., 7.058 GPa. With this value the theoretical elastic modulus of the composite would be 52.26 GPa (3.5):

$$E_c = 85 \cdot 0.58 + 7.058 \cdot 0.42 = 52.26\ \text{GPa} \tag{3.5}$$

Elastic modulus of MS material reinforced with basalt fibres measured by the impulse excitation method was 68.41 GPa, which corresponds with ~65 GPa, reported in [111], measured by three point bend test on MS composites pyrolyzed at 650°C with dwell of ~15 hours. With respect to the dwell time, the theoretical elastic modulus of the composite was calculated again,

with indentation elastic modulus for MS material pyrolyzed at 650°C for the maximum measured dwell time of 5 hours. The respective value was 11.88 GPa and resulting theoretical modulus for the composite was calculated as 54.30 GPa. The disparity in calculated value might be caused by higher content of fibres and/or by composite inhomogeneity.

G-modulus (torsional) was measured, too, and the value was found to be 7.18 GPa. It is relatively low number, which may indicate number of microcracks present in the composite. The shear modulus measured from resonant frequency in [111] was around 18 GPa. From the relationship (3.3) between *E* and *G*, and the knowledge of Poisson ratios of SiOC [120] and basalt fibre [184], the *G* of defect-free composite is ~28 GPa:

$$G = \frac{E}{2(1+\nu)} \tag{3.3}$$

where *G* is shear modulus in MPa, *E* is Young's modulus in MPa and *v* is Poisson ratio (of the composite piece in this case).

Table 4.1 Properties of composite based on MS material reinforced unidirectionaly with ~58 wt. % of basalt fibres pyrolyzed at 650°C.

Composite property	Value	Note
Density [g·cm^{-3}]	2.12	calculated from the rule of mixture
	1.93	calculated apparent (volume) density
Elastic modulus [GPa]	52.26	calculated from the rule of mixture
	68.41	impulse excitation method
Shear modulus [GPa]	~28	calculated for defect-free composite
	18	18 impulse excitation method

4.2.1.4 Fracture toughness

Determined fracture toughness values of MS composite with basalt fibres pyrolyzed at 650°C, were calculated from maximum force in the three point bend test of MS matrix composite specimens with two orientations (to remind, see) and all resulted values are plotted in graph in **Figure 4.29**. In fact, the composite weakest planes were analysed where the crack propagates along the fibres eliminating activation of all typical toughening mechanisms. In both loading orientations most of the fibres remained unbroken and the whole fracture process (crack propagation) took place through the matrix and/or fibre-matrix interface. Fracture toughness of specimens with horizontal fibre alignment reached the value of fracture toughness to be 0.40 ± 0.13 MPam$^{1/2}$ and in vertical alignment 0.25 ± 0.05 MPa·m$^{1/2}$. The data collected on the specimen with horizontal alignment were more scattered than in the case of fibres aligned in the vertical direction to the loading force. Highlighted values belong to particular fracture surfaces displayed in following images. Overall, fracture toughness of basalt reinforced MS-based composite in transversal direction is negligible in comparison with 20 MPa·m$^{1/2}$ obtained in longitudinal direction [111].

In the case of composite with horizontal fibre alignment the crack has large number of options how to propagate over the fibres. The crack path differs from the specimen to the

specimen, dependently on the stress distribution in front of the crack front and given material properties at this point (i.e., in the case of present defects). Composite with the vertical alignment of fibres is the situation slightly different. Once the crack started at the chevron notch tip, the propagation usually continues along given fibres-matrix plane in opening mode right there, where the fibres started to separate from each other.

The scatter in data is also caused by the variable content of matrix among the fibres, thus the strength of fibre-matrix interface, given by inhomogeneous distribution of fibres in matrix.

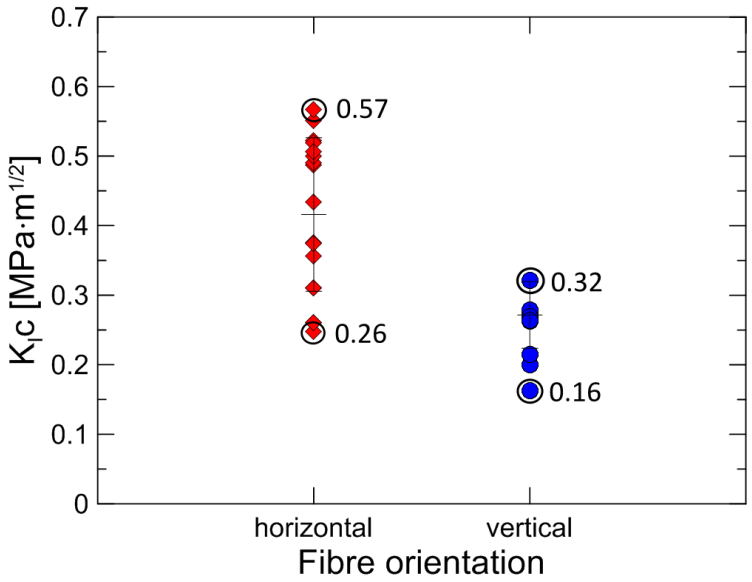

Figure 4.29 *Fracture toughness of MS-based composites with unidirectional basalt fibre reinforcement measured in transversal direction – comparison of vertical and horizontal fibre alignment.*

Images of selected fracture surfaces of tested specimens are given in **Figure 4.30**, **Figure 4.31** and **Figure 4.32**. Each image represents the specimen with a) the lowest and b) the highest fracture toughness value of composite with particular fibre orientation. From these optical images is not possible to clearly determine ongoing fracture processes and consequently describe the differences between materials with the maximum and minimum values of the fracture toughness. Nevertheless, on the surfaces with the lowest fracture toughness values can be clearly recognized presence of defects, such as missing top of the notch (**Figure 4.30 a)**) or voids between fibre bundles (**Figure 4.30 c))**. Detailed analysis will be provided on SEM images further.

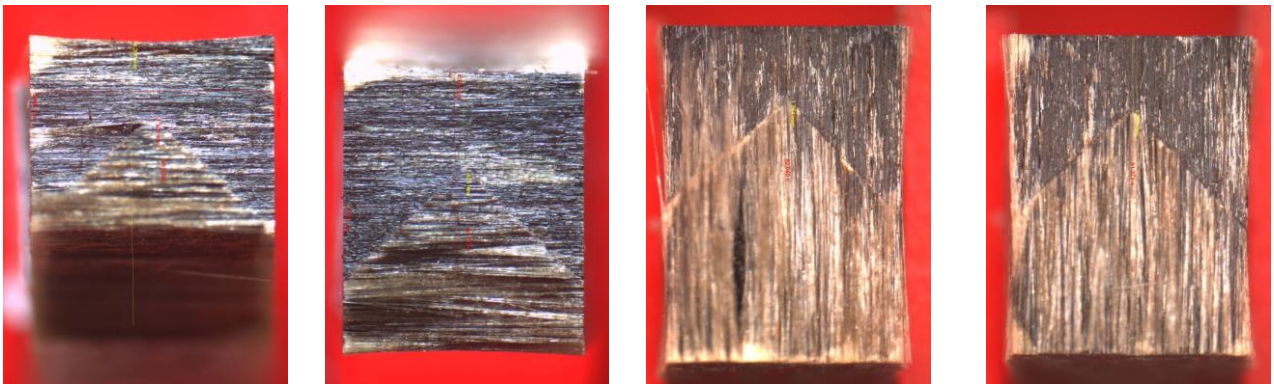

a) b) c) d)

Figure 4.30 *Fracture surface of horizontally (a, b) and vertically (c, d) aligned fibres in the transversal direction; composite with the lowest (a) and c)), and (b) and d)) the highest fracture toughness.*

By the comparison of fracture surfaces in SEM images was found that specimen with higher fracture toughness had more delaminated fibres on its surface whereas specimen with lower value had rather flat, compact fracture surface without crack branching. Detailed images of fracture surfaces are provided in **Figure 4.31** and **Figure 4.32**.

The **Figure 4.31 a**) shows the fracture surface of specimen with the lowest fracture toughness for horizontally aligned fibres. On the right side of the chevron notch tip are two regions of fibres where the matrix is partially missing. The upper region (high-lighted with red ellipse) continues over the chevron notch tip to the left, forming a cavity filled with a contamination. The lower non-perfectly-impregnated region (in blue ellipse) collides with the plane of the chevron notch and contributed to lower resulting fracture toughness (due to no matrix present there). It is visible that fibres in that area stand out of the cutting plane. That is why the value of K_{Ic} reached only 0.26 MPa·m$^{1/2}$ and became the lowest. The highest reached value of K_{Ic} for MS composite with horizontaly aligned fibres was 0.57 MPa·m$^{1/2}$ and the detail on the fracture surface in chevron notch tip is displayed in **Figure 4.31 b)**. The chevron notch is sharp, without fraying; no visible matrix-free zones are present. As the fracture continued through the notch, the profile became rougher, with delaminated fibres (red circle), acting as a toughening mechanism against the crack propagation.

In **Figure 4.32** is displayed detail of fracture surface of the MS composite with vertically aligned fibres with a) the lowest and b) the highest fracture toughness. On both of the specimen surfaces are visible fibres chipped of the fracture plane (green circles). The fracture surface in **Figure 4.32 a)** seems to be more compact, whereas in **Figure 4.32 b)** the surface is more profiled and separated fibres are covered with broken matrix. Both phenomenons increased the fracture toughness due to the applied toughening mechanisms.

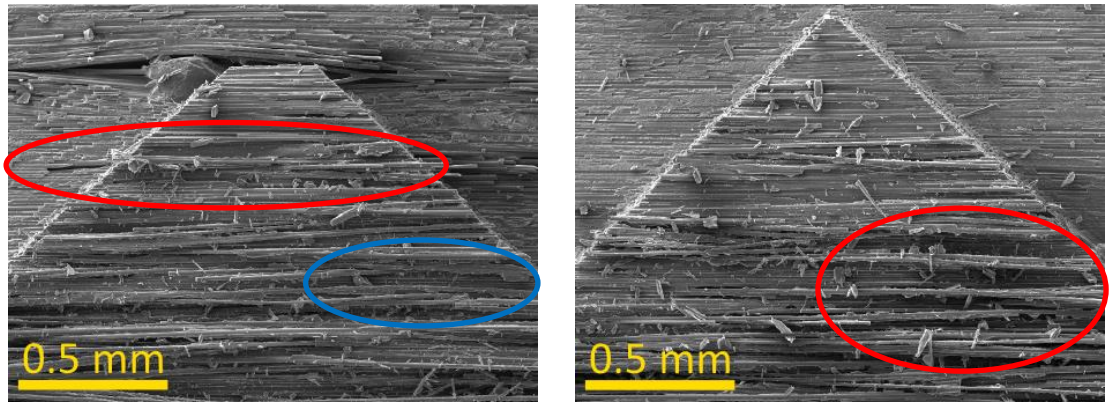

a) b)

Figure 4.31 *Detail of the fracture surfaces of MS composite specimens with horizontally aligned fibres with a) the lowest and b) the highest fracture toughness. Width of both images is 1.78 mm.*

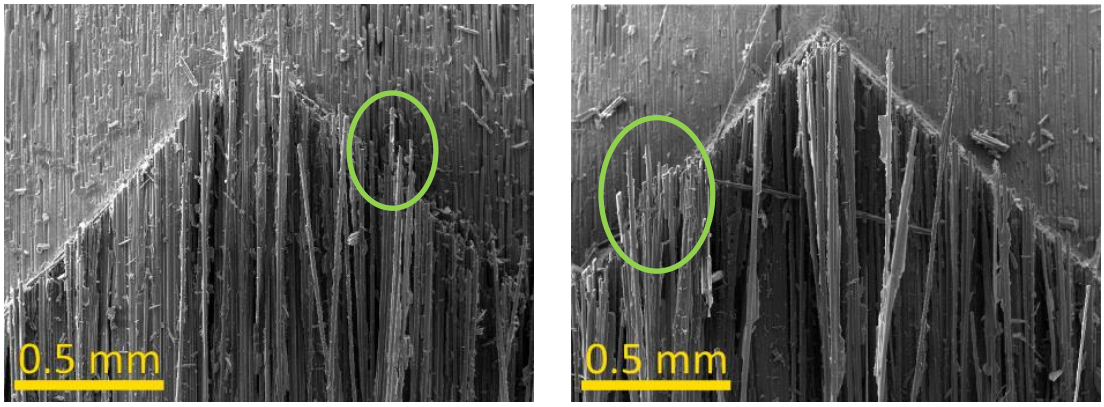

a) b)

Figure 4.32 *Detail of the fracture surfaces of MS composite specimens with vertically aligned fibres with a) the lowest and b) the highest fracture toughness. View field represents the width of the visible specimen area.*

The major outcome of this experiment is the knowledge of low fracture toughness in transversal direction, comparing with the longitudinal direction of fibres, which confirms that the basalt fibres in polysiloxane matrix preserve their integrity and does not form strong bonding at the fibre-matrix interface. Additionally, the low fracture toughness of matrix, and possibly incorporated residual stresses contribute to the overall toughening of the composite by the matrix fragmentation (microcracking), toghether with the pull-out of individual basalt fibres when the fibre-matrix interface is relatively strong. Observed superior properties of the composite based on the MS material unidirectionaly reinforced with basalt fibres and pyrolyzed at 650°C, can be explained by reaching of the optimal combination of the fracture mechanisms. Additionally, thanks to the fact that the crack propagates in both configurations mostly in the matrix or the fibre-matrix interface, can be estimated that the fracture toughness of the MS matrix material itself is close to the observed fracture toughness values of MS matrix composite with basalt fibres.

4.2.1.5 Impact strength

The impact strength of composites with MS matrix, unidirectionally reinforced with basalt fibre was measured on unnotched (compact) specimens in two orientations, flatwise and edgewise. The impact strength and corresponding maximum force for individual specimen and their average values are displayed in **Table 4.2**, together with specimen dimensions. All the specimens after the impact test remained in one piece, so it was not possible to reveal fracture surfaces. Thus, in this part the investigation does not contain the fracture surface observation. However, the fracture process can be evaluated from the record of high speed camera, taken during each test.

Table 4.2 Maximum force and nominal impact strength for individual specimens of the composites with MS matrix unidirectionally reinforced by basalt fibre.

Specimen No.	B [mm]	W [mm]	Orientation	F_{max} [N]	σ_{max} [MPa]
01	4.24	3.11	flatwise	588.1	474.9
03	4.38	3.17	flatwise	658.7	551.4
05	4.42	3.52	flatwise	662.8	399.2
07	4.39	3.09	flatwise	382.4	301.0
Average value				**573.0 ± 131.6**	**431.6 ± 107.0**
02	3.05	4.24	edgewise	558.0	335.7
04	3.18	4.28	edgewise	585.2	331.1
06	3.23	4.24	edgewise	560.7	319.0
08	2.96	4.34	edgewise	488.6	289.8
09	3.27	4.22	edgewise	648.0	368.0
Average value				**568.1 ± 57.3**	**328.7 ± 28.3**

The graphs in **Figure 4.33** display stress – time (deflection) dependence plots for each specimen orientation. Curves for the flatwise orientation showed higher scatter in normalized impact strength (σ_{max}) values than in the case of edgewise orientation. The flatwise orientation exhibits significantly higher fracture resistance than the edgewise orientation what indicates that the initial laying of the reinforcement during the composite processing plays an important role. The fibres were applied into the composite in form of fibre tows, which led to layered, inhomogeneous distribution of the fibres in the composite. The consumed energy during the impact test is 1.3 times higher comparing to the edgewise orientation. These findings are in the controversy with expectations based on the laminated structure where individual layers can slide over each other after their delamination. Therefore, they provide rather lower strength but higher reliability and higher consumption of fracture energy, than in the edgewise orientation. The reasons of such behaviour can be explained on the basis of high speed camera records analysed further (see **Figure 4.34**).

Specimens with the highest and the lowest impact strength in the flatwise orientation were chosen for detailed fractographic analysis. The highest impact strength value measured for the specimen with the flatwise orientation is represented by the curve No.03 (orange) and the lowest by the curve No.07 (dark red) in the graph in **Figure 4.33**. Curves for edgewise oriented specimens were rather consistent, therefore, only one detailed analysis is provided. The analysis of the high

speed video for the edgewise orientation was chosen for the specimen represented by the curve No.02 (light blue).

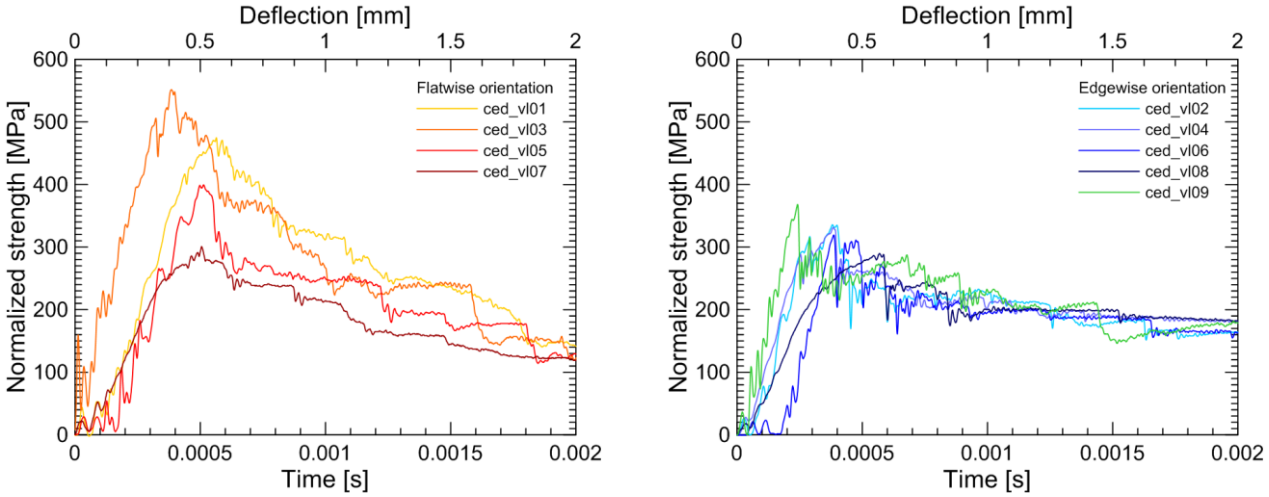

a) b)

Figure 4.33 *Impact strength plots of MS matrix unidirectionally reinforced basalt fibre composites in two orientations: a) flatwise, b) edgewise.*

The video records from the high speed camera synchronized with the loading curves were analysed and representative video frames are displayed in **Figure 4.34**. The images borders are the same as respective colours used in the impact strength graphs. There are three images selected for each specimen at the moment of: a) first contact of the hammer tup with the specimen (at t = 0 s), b) the maximum force or deflection at respective F_{max} (time in milliseconds is displayed in the image), and c) the hammer tup removal and instant specimen damage becomes visible.

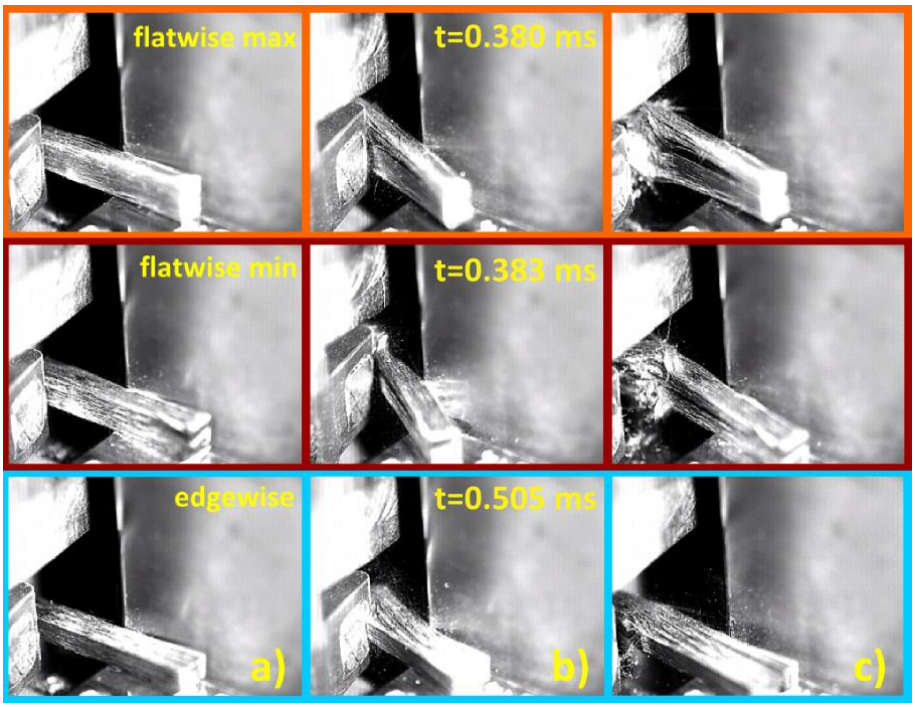

Figure 4.34 *Video frames from the Charpy impact strength measurement.*

It was observed that the specimen No.03 – flatwise orientation (orange curve) with the highest impact strength delaminated along certain planes with lower specimen damage than the specimen No.07 (dark red curve) with the lowest impact strength. The delamination occurred alongside the plies of the rovings which were layered upon each other to build up the composite body. The situation in composite is represented by the scheme in **Figure 4.35**. Fibres in the roving were less saturated with the matrix. The matrix was rather localized between the plies. Thus, the composite reinforcement was not homogeneously distributed within the composite and delamination behaviour was observed.

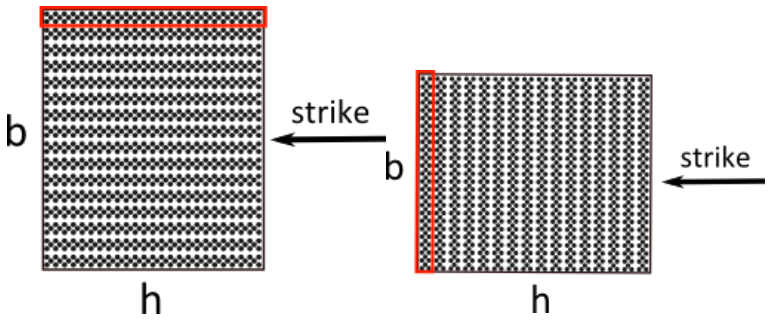

a) b)

Figure 4.35 *Scheme of two loading orientations: a) flatwise, b) edgewise, of the basalt fibre reinforced MS matrix composite. In the cross-section is indicated the inhomogeneous distribution of the fibres, forming layered structure. Individual layers are highlighted in red rectangle in both loading orientations.*

From the area below the curve, the total fracture energy (E_{TOT}) of individual specimens was calculated. The nominal fracture energy was calculated according to the specimen cross-section, and both the impact energy values are listed in **Table 4.3**. The nominal energy of the edgewise orientation is higher by 36 % in comparison with flatwise orientation.

Table 4.3 Total energy of fracture (E_{TOT}) and normalized energy (E_{NORM}) of MS matrix basalt reinforced composite pyrolyzed at 650°C under the dynamic loading.

Specimen No.	Orientation	E_{TOT} [kJ·m^{-2}]	Cross-section [mm^2]	E_{NORM} [kJ·m^{-2}]
01	flatwise	1.15	13.16	1.08
03	flatwise	1.29	13.89	1.28
05	flatwise	1.42	15.56	1.57
07	flatwise	1.03	13.57	0.99
Average value		**1.22 ± 0.17**	**14.04 ± 1.05**	**1.23 ± 0.26**
02	edgewise	1.80	12.93	1.74
04	edgewise	2.13	13.62	2.17
06	edgewise	1.78	13.68	1.82
08	edgewise	1.66	12.84	1.59
09	edgewise	2.27	13.78	2.33
Average value		**1.92 ± 0.26**	**13.37 ± 0.45**	**1.93 ± 0.31**

4.2.2 Fabric reinforced MS and MPS matrix composites

In this section, MS and MPS based composites with basalt fabric reinforcement are investigated. The mechanical response of composites with basalt fabrics treated at the same conditions (as of the unidirectionally reinforced composites) was examined. An attention was paid especially to specimens partially pyrolyzed at 650 and 750°C. The MS and MPS based composites are further abbreviated as MSC and MPSC, respectively.

4.2.2.1 Microstructure

The microstructure of both composites at particular pyrolysis states (pyrolysis temperature in range 600–800°C) is summarised in **Figure 4.36**.

It can be concluded that the composite specimen with MS matrix treated at 600°C was sensitive to the materialographic specimen preparation, which may be caused by the brittleness of the matrix and its low adhesion to the reinforcement. In the cross-section of the fabric are visible individual fibres which are evenly distributed in the bundles. At treatment temperature 650°C the composite seems to be a bit more compact, the polishing caused less damage and the fibres are still unaffected by the processing. The pyrolysis temperature from 700°C to 800°C led to the composite appeared to be compact and stiff. Also the fibre bundles seem to be very compacted due to shrinkage of the matrix and at 800°C, the dark portions, clearly representing the presence of matrix at lower temperatures, are not very visible here.

In contrast to MSCs, in MPSCs pyrolyzed at 600°C the matrix did not crumble. Some fibres in bundles which were not embedded properly (free fibres) got broken as a consequence of polishing. That indicates that sometimes no matrix was present inside the bundles. From the cross-sections displayed in **Figure 4.36**, MPSC seems to be more porous than MS, which is also confirmed by porosity measurement reported in [168]. Its structure contains large pores in low amount, which are located between individual fabric layers (highlighted by yellow arrows). They were probably introduced during the processing of composites, when bubbles of air were captured in between crossing warp and fill of the fabrics. Presence of the bubbles is caused by higher viscosity of the MPS resin, i.e., 50–100 $mPa \cdot s^{-1}$), which is doubled in comparison with the MS one (30–40 $mPa \cdot s^{-1}$).

4.2.2.2 Density

The density was calculated from mass and dimensions of the composites. The density dependence on the thermal treatment is provided in **Figure 4.37**. Density for partially pyrolyzed composites (between temperatures 600–800°C) was ranging from 1.7 to 2.1 $g \cdot cm^{-3}$. At the pyrolysis state of 600°C the MS composite has slightly lower value than the MPS composite, at pyrolysis temperature of 650°C is their density on the same level. At 700°C, the MSC linearly increases to the density of 2.05 $g \cdot cm^{-3}$; but the data is quite scattered. In case of the MPSC was observed non-linear increase, as the density is rather close to the previous pyrolysis state. For both the composites the density increased at pyrolysis temperature of 750°C, where for the MSC the density is slightly higher. The pyrolysis temperature of 800°C had no further effect on the composite densification. In case of the MSC composite was observed even a little decrease of density. Density of MPSC at pyrolysis state of 800°C was comparable with pyrolysis state

of 750°C. As known from the density measurement of individual materials used for matrix at various pyrolysis states (400–1000°C, including curing at 250°C, see chapter 4.1.1.2), the MS and MPS materials themselves densifies up to 1000°C. Thus, the decrease of composite density at 800°C may be caused by the presence of the reinforcement. Values are provided in **Table A.13**.

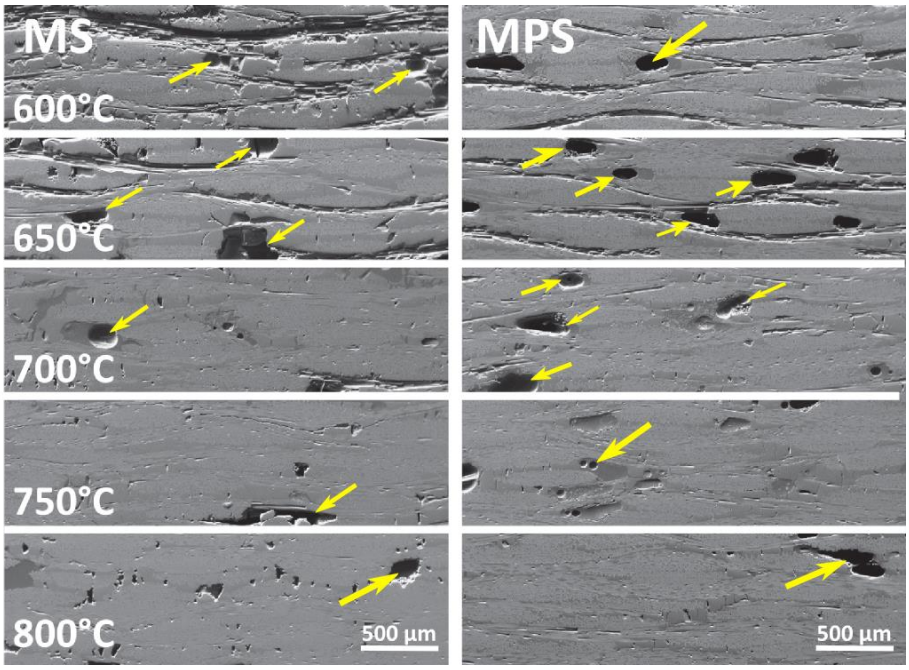

a) b)

Figure 4.36 *Composite microstructure at particular pyrolysis states: a) MS based composite (MSC), b) MPS based composite (MPSC). Yellow arrows indicates the pores.*

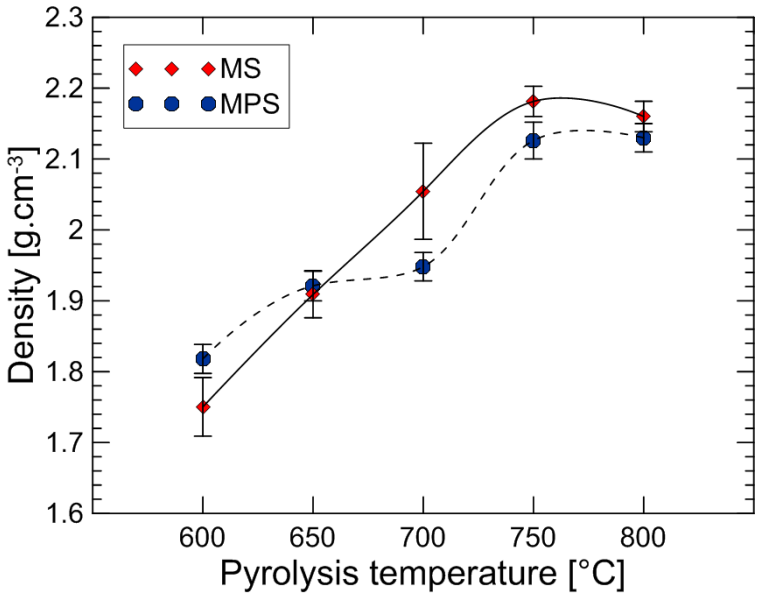

Figure 4.37 *Apparent density of fabric reinforced composites with MS and MPS matrices.*

4.2.2.3 Elastic modulus

Elastic modulus values of basalt fabric reinforced composites were calculated from the loading curves obtained in the three point bend test. The resulting data are presented in **Table A.14** and plotted in graph (see **Figure 4.38**). For both the composites the elastic modulus increases in the whole range of investigated pyrolysis temperatures ranging from 17 to 45 GPa for the MSC, and from 25 to 50 GPa for the MPSC. The biggest difference between the elastic moduli of individual materials is for composite materials pyrolyzed at 600°C, but for composites pyrolyzed at 700°C it is nearly the same, only the data for MSC exhibits higher scatter than for the MPSC. However, compared to MPSC, the MSC exhibited higher scatter in data at all pyrolysis states, and the highest scatter was observed for composite pyrolyzed at 800°C. Both materials exhibited a little drop in the increasing trend of elastic modulus at pyrolysis temperature of 700°C, which is similar to the composite density development (see **Figure 4.37**).

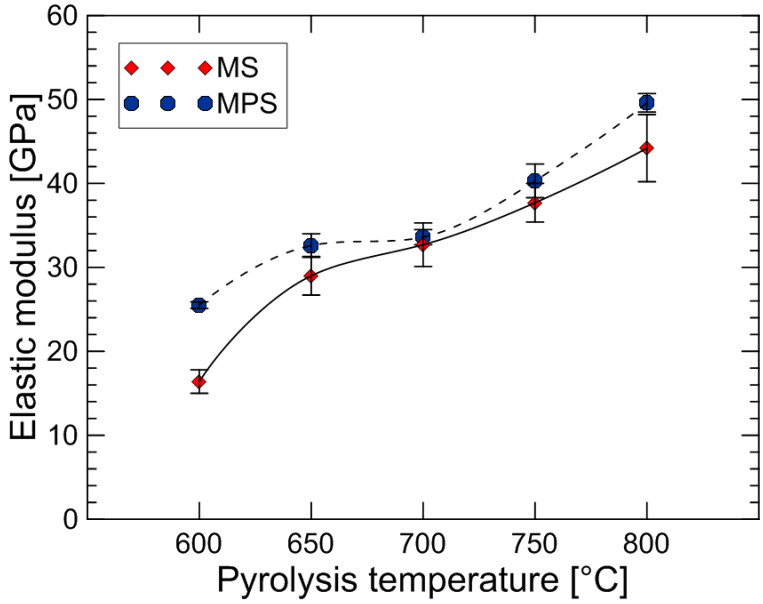

Figure 4.38 *Elastic modulus of basalt fabric reinforced composites with MS and MPS matrices.*

4.2.2.4 Flexural strength

Data obtained from the three point bend test is plotted in graph shown in **Figure 4.39** (respective **Table A.15** can be found in Appendix). The flexural strength of the MSC rapidly increased from 40 MPa for composite partially pyrolyzed at 600°C to 120 MPa for composite partially pyrolyzed at 650°C. The extremely high scatter of flexural strength values was found at pyrolysis temperature of 650°C. Starting from this pyrolysis state the strength values only decreases, until it reaches 80 MPa for composite prepared by the pyrolysis at temperature of 800°C. The MPSC is more reliable, ranging from 115 to 130 MPa for the whole pyrolysis temperature range. For both the composites the flexural strength a bit dropped for pyrolysis state at 700°C. In the case of MS based composite, the flexural strength continually decreases until composite pyrolyzed at 800°C. In MPS based composite the strength fluctuates between the minimum and maximum value obtained at 600°C and 650°C, respectively.

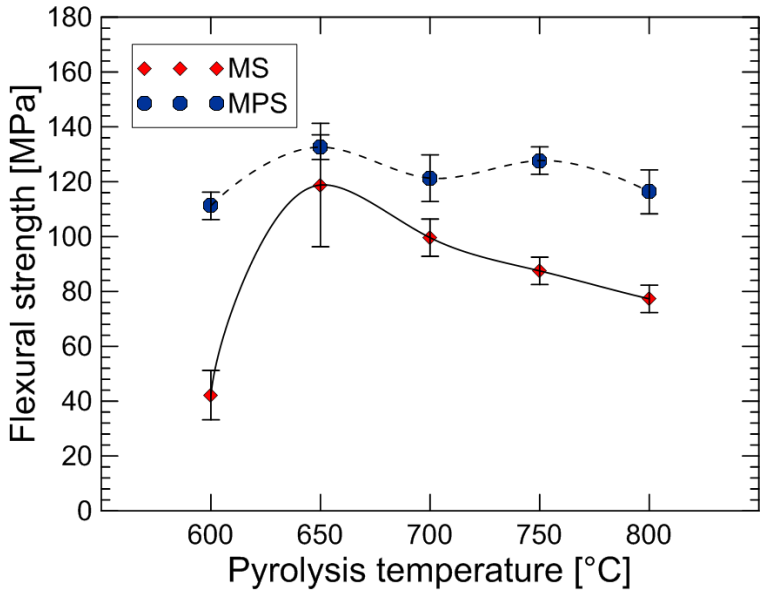

Figure 4.39 *Flexural strength of MSC and MPSC with basalt fabrics.*

4.2.2.5 Fracture toughness

The evolution of fracture toughness values is plotted in **Figure 4.40**. The mechanical response of both composites exhibits similar trends as for the flexural strength. The MPSC evolved to values between 3 and 6 MPa·m$^{1/2}$. The fracture toughness increased to its top of around 5.5 MPa·m$^{1/2}$ for materials pyrolyzed at 650 and 700°C. For composite pyrolyzed from 700°C the fracture toughness slowly decreases to the level of 3 MPa·m$^{1/2}$. The fracture toughness of MSC rapidly increased from initial level of 2.5 MPa·m$^{1/2}$ for composite pyrolyzed at 600°C to the maximum value of 10 MPa·m$^{1/2}$ for composite pyrolyzed at temperature of 650°C. Fracture toughness of composite prepared at pyrolysis temperature of 700°C again rapidly decreased to ~5 MPa·m$^{1/2}$, which is comparable value to the MPSC prepared at the same processing temperature. For MSC pyrolyzed at temperature of 750°C the fracture toughness decreased to 2 MPa·m$^{1/2}$ and remained on the same level also for the composite pyrolyzed at 800°C.

On the one hand, the composite with MS matrix has outstanding peak response when pyrolyzed at 650°C. On the contrary, the composite with MPS matrix has more reliable fracture toughness values across whole temperature range used for composite pyrolysis. The maximum fracture toughness of 10 MPa·m$^{1/2}$ reached for fabric reinforced MSC corresponds with the fracture toughness value of 20 MPa·m$^{1/2}$, obtained for MS composite with unidirectional basalt fibre reinforcement in [168]. It can be stated that approximately 50 % of fibres in the fabric were in the transversal direction, in which only low influence on the toughening mechanisms can be expected during measurement. This fact can easily explain the two times higher fracture toughness values obtained for the unidirectional composites from [111] comparing to the fabric reinforced materials. To remind - the fracture toughness in the transversal direction of the fibre reinforced MSC composite was less than 1 MPa·m$^{1/2}$ (see **Figure 4.29**).

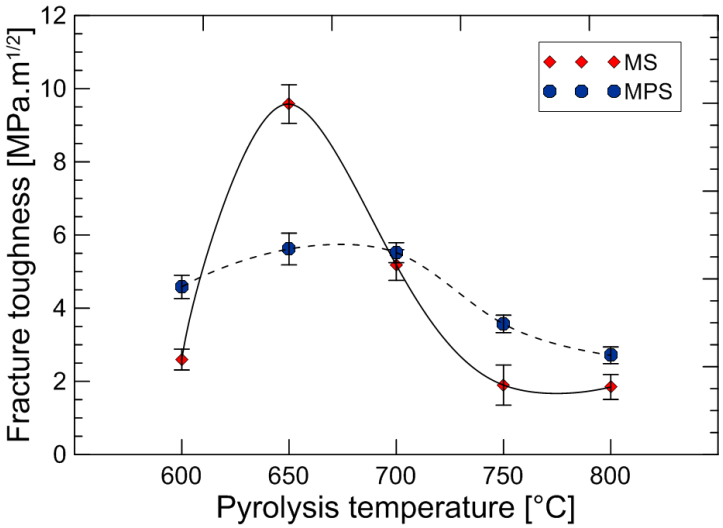

Figure 4.40 *Fracture toughness of basalt fabric reinforced composites with MS and MPS matrix.*

4.2.2.6 Fractography

The typical fracture surfaces of specimen broken during the flexural test of basalt plain-woven fabric reinforced MS and MPS composites are displayed in **Figure 4.41**. Fracture surfaces of the composites revealed that the partial pyrolysis at 600°C is yet insufficient due to the fact that fibre-matrix interface seems to be very weak and resulting material did not form compact composite. The weak interface led to poor load transfer from the matrix to fibres and thus the fracture toughness was at unsatisfactory level. The fibres on the fracture surface are very scattered and it is hard to recognize what was their original orientation. The situation in the case of the MPS material is slightly better. The MPSC pyrolyzed at 600°C exhibits signs of remaining matrix on the pull-outed fibres. The situation there appears that the fabric broke in bundles of particular fibres. The difference is much clearer when both materials pyrolyzed at pyrolysis temperature of 650°C are compared. The fracture surface of MSC is quite unique amongst the others. It seems that each fibre delaminated (was pulled-out) individually, increasing the effectivity of this toughening mechanism. It was proved that the fibres pulled-out at this composite body are longer than in other cases.

With increasing pyrolysis temperature the specimen fracture surface becomes more flat which is more pronounced for composites with the MS matrix than for MPSCs. The change in the fracture surface character for pyrolysis temperature from 600 to 800°C is significant. The weak interface composite behaviour turn to the very strong interface exhibiting brittle behaviour of the composite resembling behaviour of monolithic materials. On the fracture surfaces of both composite materials pyrolyzed at 750°C and higher can be recognized pores between individual fabric layers (see the arrows), oriented perpendicularly to the fabric plane similar to those observed on polished surfaces.

a) MSC pyrolyzed at 600°C

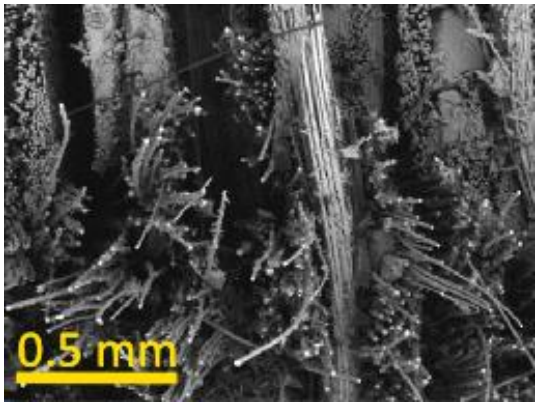

b) MPSC pyrolyzed at 600°C

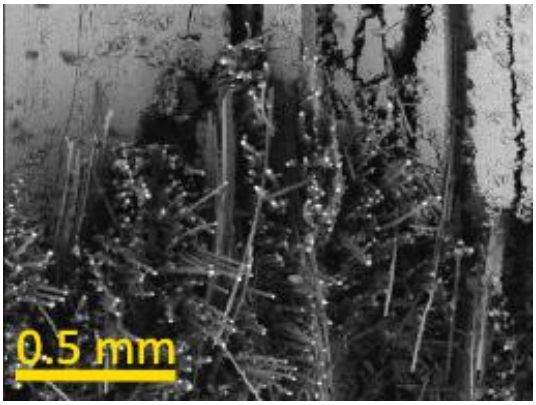

c) MSC pyrolyzed at 650°C

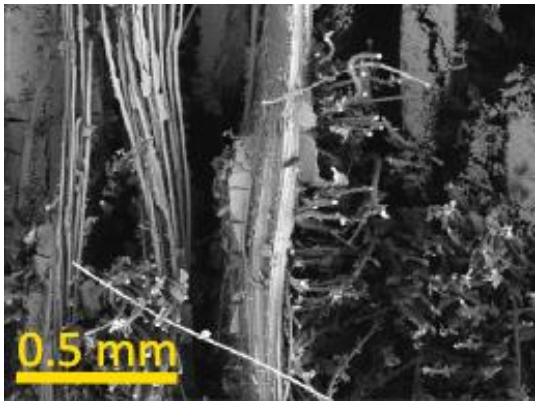

d) MPSC pyrolyzed at 650°C

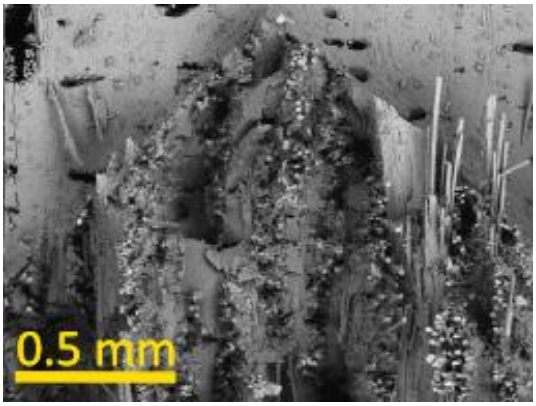

e) MSC pyrolyzed at 700°C

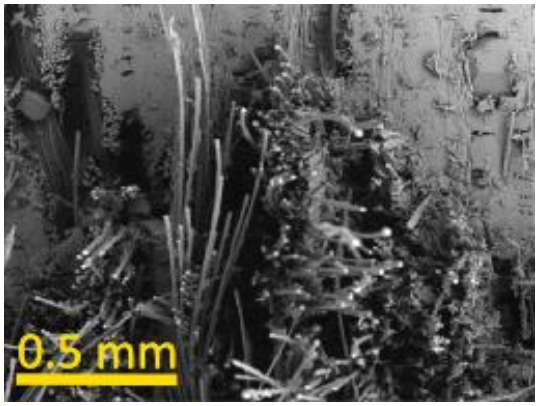

f) MPSC pyrolyzed at 700°C

Figure 4.41 *Fracture surface of composites with plain-woven basalt reinforcement pyrolyzed in temperature range 600–800°C (MSC in the left, in images a), c), e), g), and i), MPSC in the right, in images b), d) f), h and j)).*

Continuation of **Figure 4.41**:

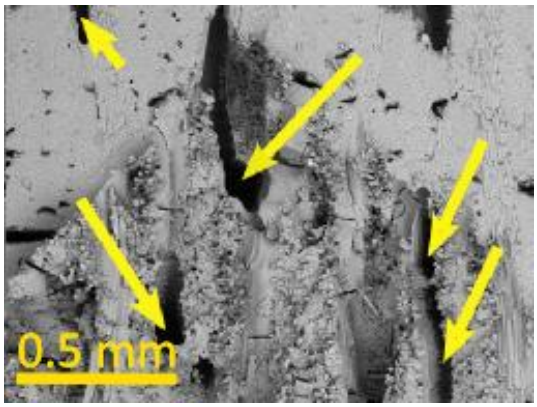

g) MSC pyrolyzed at 750°C

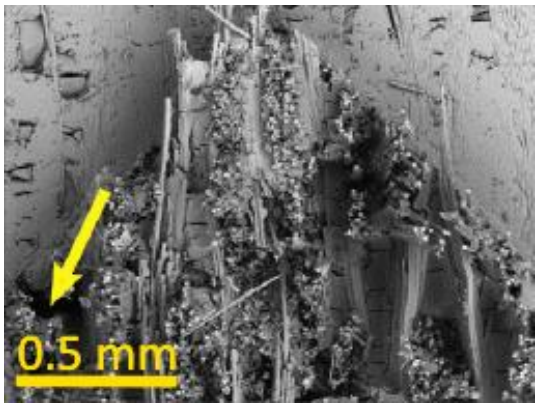

h) MPSC pyrolyzed at 750°C

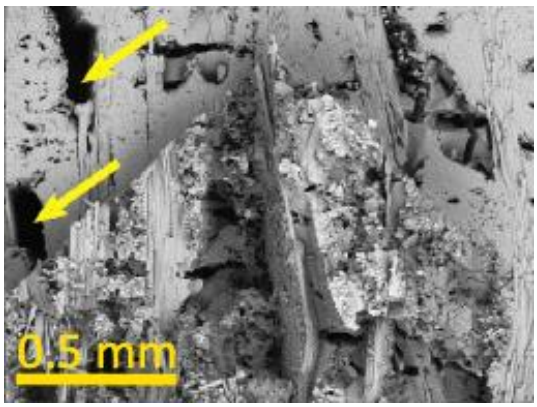

i) MSC pyrolyzed at 800°C

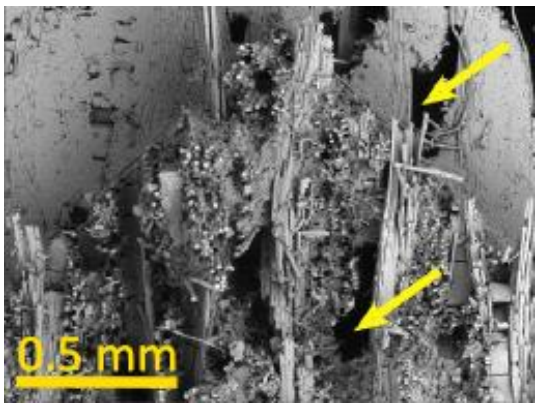

j) MPSC pyrolyzed at 800°C

4.2.2.7 Impact strength

Loading curves recorded during impact tests conducted on fabric reinforced composites were analyzed from the force and energy point of view. **Figure 4.42 a)** compares the loading curves for both tested orientations of the MS composite pyrolyzed at 650°C, and **Figure 4.42 b)** displays the effect of pyrolysis temperature on the MS composite in the out-of-plane orientation. The same loading curve of the MSC pyrolyzed at 650°C was used in both graphs, for better comparison of both the effects. The left graph (**Figure 4.42 a)** clearly shows that the in-plane orientation led to reasonably stable deformation of the specimen. In the in-plane orientation the specimen reached maximum force 2 times higher than for the out-of-plane geometry, but with rapid drop of the force to zero at a smaller deflection. This is connected to the mechanism of failure, which depends on the loading direction to the internal structure (reinforcement orientation) of the composite. As the composite in the out-of-plane orientation bends, two types of stress take place: tensile stresses act on the specimen side of supports and compressive stresses act on the side which is stroked by the hammer tup. Stress waves propagate through the specimen, from the centre to its ends. On the contrary to the out-of-plane orientation, in the specimen with the in-plane orientation, the cracks occur in more than one interface (at the same moment of the first contact with the pendulum hammer tup during the impact). Generally, the fracture starts with approximately the same number of major cracks propagating in the loading direction, as is the

number of interfaces between individual reinforcement layers. The stress developed during this delamination causes (together with the applied force) buckling of the individual layers and the material exhibits higher stiffness and consequently higher strength, as is visible from the slope of the linear part of the loading curves – see the difference in the linear part (time 0–0.0004 s for the out-of-plane, 0.0003 s for the in-plane) of dashed and solid line in **Figure 4.42 a)**.

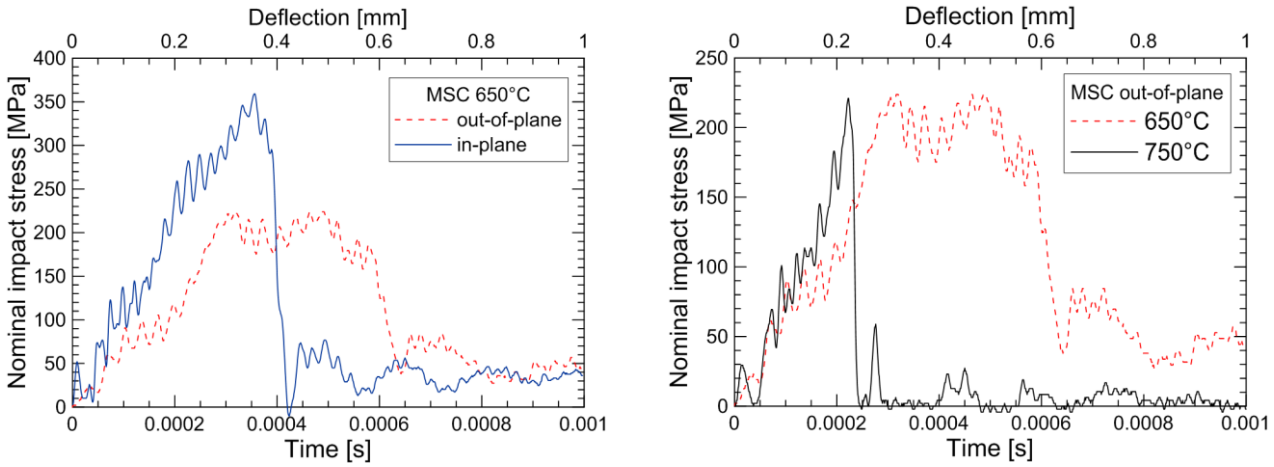

a) b)

Figure 4.42 *Influence of a) the specimen orientation at pyrolysis temperature of 650°C, and b) of temperature of partial pyrolysis on the loading curve of MSC composite.*

In **Figure 4.42 b)** there are compared two pyrolysis states of the MSC having the out-of-plane orientation. Loading curve of the MSC pyrolyzed at 650°C is there represented by a dashed line, and the MS composite pyrolyzed at 750°C by a solid line. An increase of pyrolysis temperature by 100°C changes the failure mechanism from stable to unstable. Although the maximum force was preserved, the energy consumption decreased significantly. The material pyrolyzed at temperature of 650°C exhibited activation of various toughening mechanisms (resulting in larger area lazing under the loading curve). On the contrary, the pyrolysis at 750°C led to brittle failure of the composite. The impact strength was calculated from load – deflection curves with respect to the dynamic oscillations. The graphs in **Figure 4.43** show trend lines (spline) and error bars of average data, anyway, due to the response of particular specimens all values were displayed. Testing of the composite in the in-plane reinforcement orientation was performed only on two specimens for each treatment, thus, no standard deviation could be calculated.

In **Figure 4.43 a)** are displayed plots of the dependence of impact strength on the pyrolysis temperature of the MS composite tested in both the tested orientations. Specimens pyrolyzed at 600°C reached very similar results of impact strength, around 80 MPa, where the in-plane oriented composite reached value only a slightly higher, comparing to the out-of-plane orientation. (It is important to point out that due to the specimen geometry all the results of in-plane orientation are expected to be higher, due to buckling mechanism). Maximum impact strength of MSC specimens in the out-of-plane orientation was measured for composite pyrolyzed at 700°C (~240 MPa) and for the in-plane for composite pyrolyzed at 650°C (~320 MPa). The shift of maximum impact strength in the in-plane composite orientation to lower pyrolysis temperature

(650°C) is probably caused by higher stiffness of the composite pyrolyzed at 700°C, due to stronger bonding between the layers, caused by the higher pyrolysis temperature. Delamination, which is an important fracture mechanism for the in-plane oriented composite, does not occur, whereas the fibre pull-out in the out-of-plane is still possible even for composite prepared at the pyrolysis temperature of 700°C. From the pyrolysis temperatures where the maximum values were reached the strength quickly decreases with the increasing pyrolysis temperature, with comparable trends for composites tested in both the orientations. This can be caused by the deterioration of fibres, observed earlier in this work (see chapter 4.2.1.1).

In **Figure 4.43 b)** are displayed trends of the impact strength for both specimen orientations of the MPSC. For composites prepared at pyrolysis temperature of 600°C was reached higher impact strength than it was determined for the composite with MS matrix. Further, with increasing pyrolysis temperature up to 750°C the impact strength was observed to be slightly higher and consistent for both the MPSC orientations. For composite prepared at the pyrolysis temperature of 800°C the impact strength dropped to ~150 MPa. The data are listed in appendix in **Table A.16**.

Regardless the orientation or matrix used, all the specimens (both MSC and MPSC) pyrolyzed at 800°C failed in brittle manner, as can be observed from loading curves and fracture surfaces of particular specimens after the test. Respective fracture surfaces are provided futher in chapter 4.2.2.9.

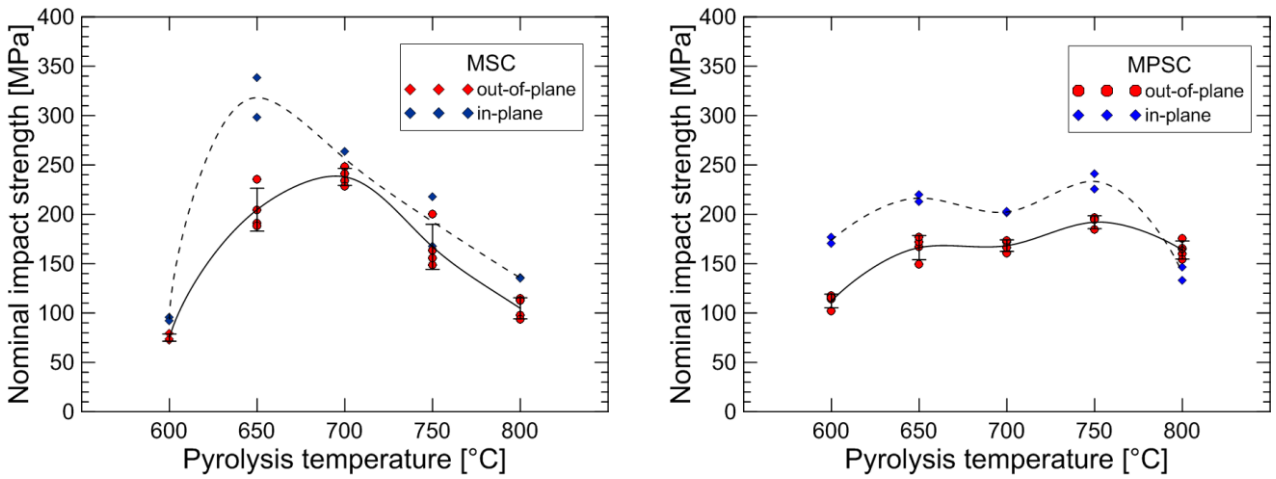

a) b)

Figure 4.43 *The dependence of impact strength on the pyrolysis temperature for a) MSC and b) MPSC.*

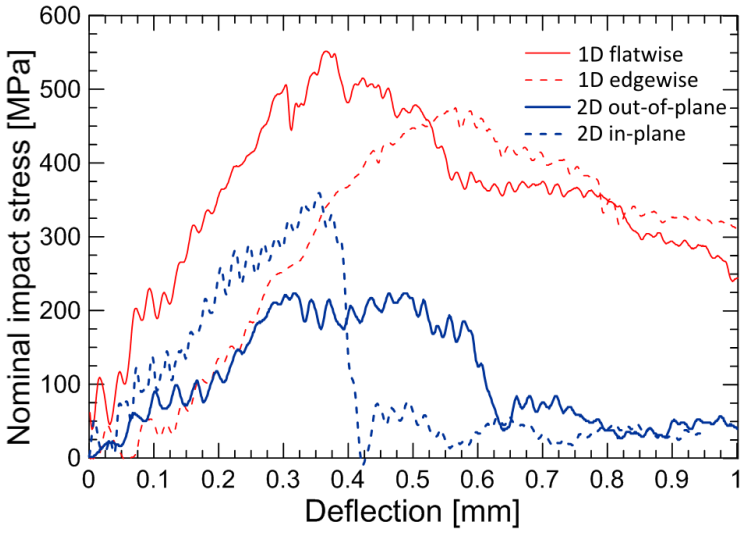

Figure 4.44 *Comparison of load – deflection curves of 1D and 2D MS matrix composites pyrolyzed at 650°C and tested at Charpy's impact tester. 1D – unidirectionally reinforced basalt fibre composite, loaded in two orientations (see* ***Figure 4.35****), 2D – composite with plain-weaved basalt fabric.*

Comparison of impact loading curves for both reinforcement types in two testing orientations is provided in **Figure 4.44**. Both compared composites have the same MS matrix and were partially pyrolyzed at the same temperature of 650°C. The loading curves represent the normalized impact strength, recalculated with respect to the specimen dimensions.

In the impact test, unidirectionally (1D) reinforced composites were more reliable than those with fabrics (2D). The major reason is the orientation of the fibres – the load transfer in 1D is performed by the whole volume of the reinforcement, in contrast to the fabrics, where approximately only a half of the fibres are in the direction suitable for the load transfer. Fibres which are in the transversal direction (to the normal alignment of the reinforcement) do not improve composite mechanical response because of low strength of the fibre-matrix interface (see the chapter 1.4.2.1). Also the contact between the matrix and fibres in the fabrics is different from the unidirectional composites (crossing tows in the fabric are not perfectly infiltrated by the matrix) and present defects may have a negative influence on the resulting composite strength. It was observed that the composites reinforced by fabrics delaminated easily. In the graph in **Figure 4.44** is also clearly visible that the in-plane orientation for 1D composites had higher strength than for 2D.

4.2.2.8 Impact energy

An overview of the fracture energy for all the tested MSC and MPSC specimens is represented by the bar chart in **Figure 4.45**. The total fracture energy values of both MSC and MPSC specimens at all pyrolysis states and both orientations are presented in the graph. Each bar represents the ratio between the elastic (dark portion) and the damage (white portion) contribution. Data of the total energy for both materials and orientations are listed in **Table A.17**.

The more brittle was the specimen, the higher was the ratio between the elastic energy of the total energy, as is visible at all types of matrices and orientations of composites pyrolyzed at

800°C. Materials with the highest damage energy were identified at pyrolysis states at 650°C and 700°C. With an increasing temperature the contribution of damage energy decreases. The trend of energy consumed during fracture process is similar to the results of the impact strength.

Failure mechanisms took place accordingly to the specimen orientation (i.e., the orientation of the reinforcement), pyrolysis temperature and type of matrix. The out-of-plane delamination was a result of shear stresses developed between the layers during their bending; the in-plane failure was a mix of tensile stresses (opening mode) and layer buckling. Failure mechanisms consequently changed with pyrolysis at 700°C. The MSC specimens broke in two pieces in both composite orientations whereas in the case of MPSC, the specimens delaminated and/or broke, regardless the testing orientation. From the pyrolysis at 750°C every specimen was fractured in two pieces, no matter which type of matrix or orientation was tested.

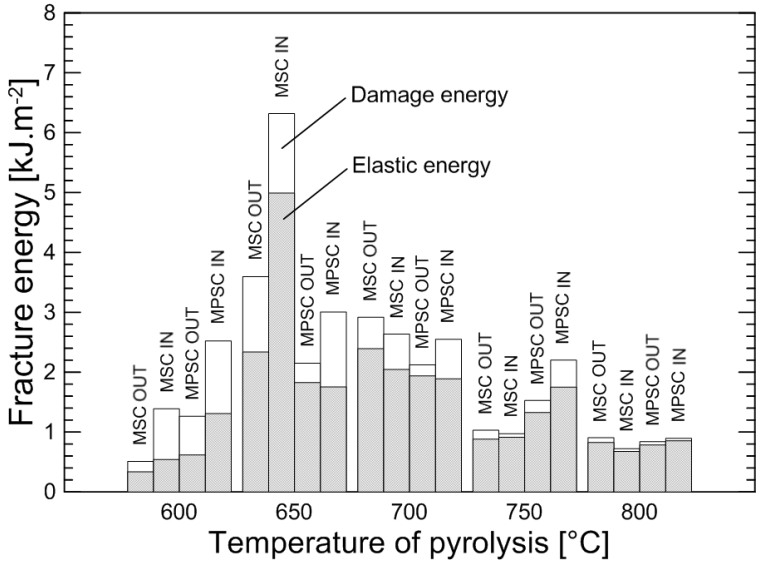

Figure 4.45 *Absorbed energy to failure (fracture energy) of basalt fabrics reinforced composites with partially pyrolyzed MS and MPS matrix (OUT = out-of-plane orientation, IN = in-plane orientation).*

Table 4.4 Total fracture energy of MS and MPS composites.

Pyrolysis temperature [°C]	Fracture energy [kJ·m^{-2}]			
	MSC		MPSC	
	out-of-plane	in-plane	out-of-plane	in-plane
600	0.51 ± 0.15	1.39 ± 0.67	1.26 ± 0.64	2.52 ± 0.24
650	3.60 ± 1.71	6.32 ± 1.12	2.15 ± 0.82	3.00 ± 0.21
700	2.92 ± 0.94	2.64 ± 0.34	2.12 ± 0.22	2.55 ± 0.13
750	1.03 ± 0.16	0.97 ± 0.21	1.53 ± 0.60	2.20 ± 0.26
800	0.90 ± 0.48	0.72 ± 0.04	0.84 ± 0.44	0.89 ± 0.25

4.2.2.9 Fractography

All SEM micrographs presented here show specimen surfaces after the impact test. For comparison were chosen pyrolyzed states at 650°C and 750°C, represented in **Figure 4.46** and **Figure 4.47**, respectively. In most the cases, specimens with high fracture resistance remained damaged but compact, in one piece, thus, the fracture surface was not analysed. In **Figure 4.46 a)** is displayed the MSC exposed to the out-of-plane impact loading. The layers on the tensile side of the specimen ruptured and delaminated off. In **Figure 4.46 b)** is displayed the MSC pyrolyzed at 650°C in the in-plane orientation. This specimen performed the highest fracture resistance of all tested specimens. No fracture through the specimen cross-section was observed and as the acting toughening/fracture mechanisms were identified the delamination and the layer buckling on the macroscopic level accompanied by the fibre pull-out in the microscopic level.

In the MPSC (**Figure 4.46 c)**) the delamination occurred in every single layer. At most of the specimens, the mechanism was typically located on only one side of the specimen, probably because the specimen was not fully symmetrical to the point of applied load. The asymmetry might have caused differences in elastic waves going through the specimen at the moment of impact. In-plane tested MPSC (**Figure 4.46 d)**) was more stiff, with less pronounced delamination than MSC, which increased the impact strength as well as the damage energy.

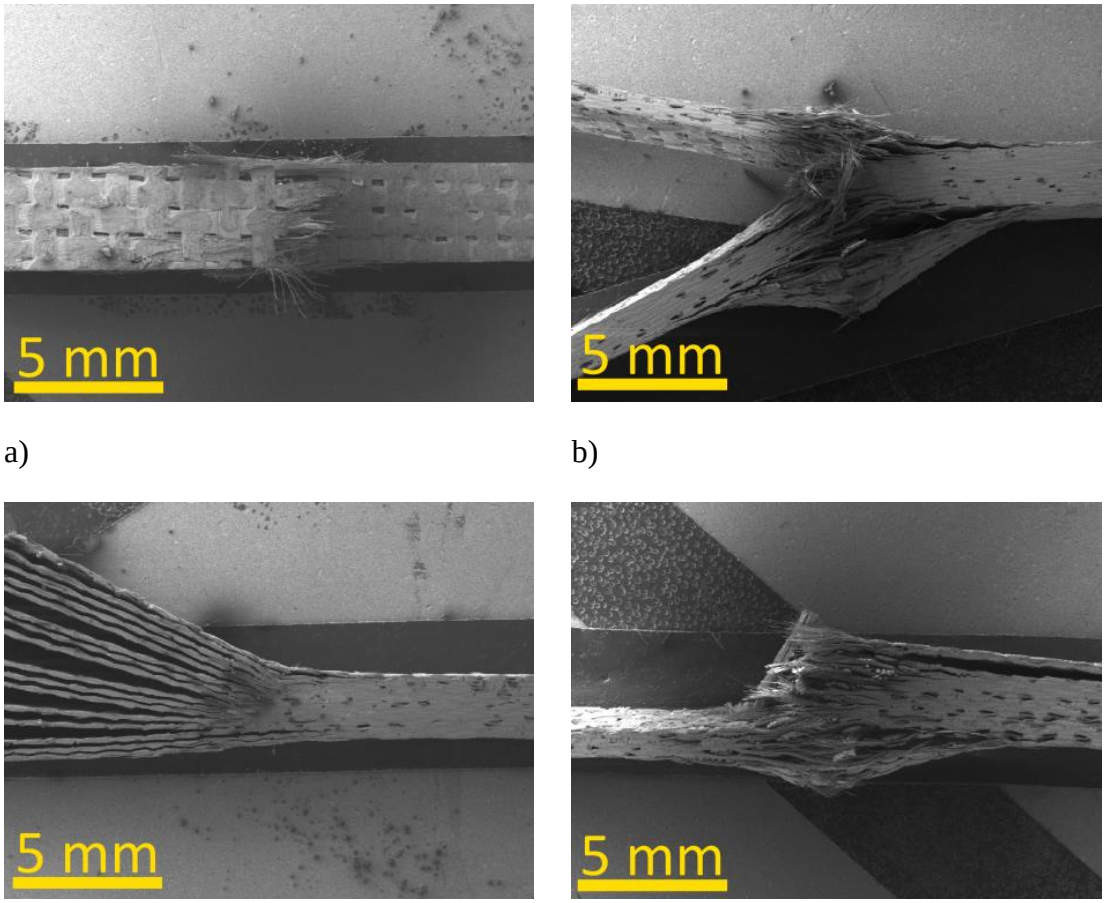

Figure 4.46 *Side views of composite specimens partially pyrolyzed at 650°C after the impact test: a) MSC out-of-plane, b) MSC in-plane, c) MPSC out-of-plane, d) MPSC in-plane orientation.*

In **Figure 4.47** are displayed specimens of the MSC and the MPSC pyrolyzed at 750°C, in the out-of-plane (a, c) and in-plane (b, d) orientations. Specimens of both materials were broken in two pieces, showing higher brittleness than composites pyrolyzed at 650°C. The MS composite displayed in **Figure 4.47 a)**, **b)** seemed to be very compact, with suppressed function of the reinforcement. The specimen in **Figure 4.47 a)** has quite high fracture relief which is connected with increased fracture resistance. On the contrary, the fracture surface shown in **Figure 4.47 b)** is also with relief but compared to the out-of-plane tested specimen, it is more flat.

The MPS composite displayed in **Figure 4.47 c)** and **d)**, show toughening through the fibre pull-out mechanism. The length of the fibre pull-out is low, which is in agreement with determined level of the impact strength and energy data (see **Figure 4.43** and **Figure 4.45**).

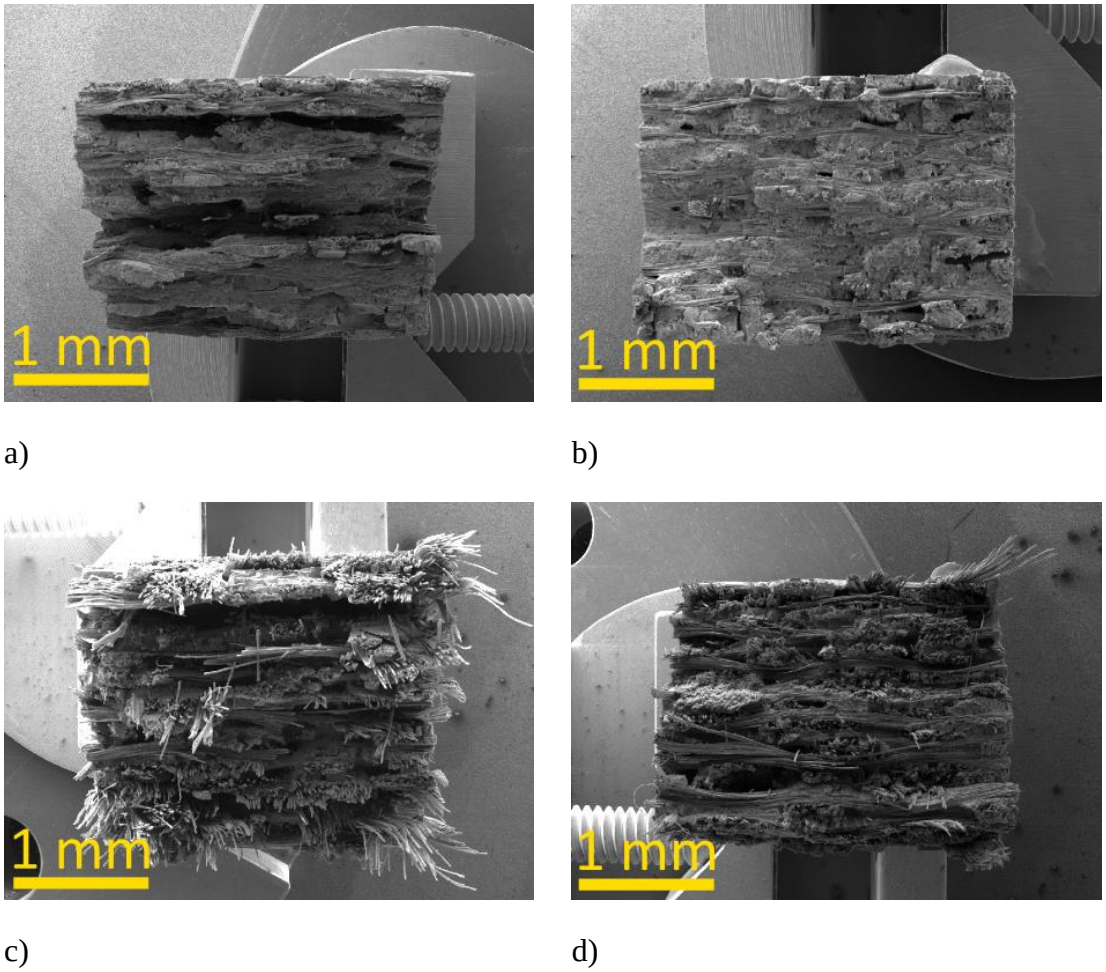

Figure 4.47 *Fracture surfaces of composites partially pyrolyzed at 750°C: a) MSC out-of-plane, b) MSC in-plane, c) MPSC out-of-plane, d) MPSC in-plane orientation.*

4.2.2.10 Video analysis

The impact loading and the fracture process was recorded for additional analysis of specimen failure behaviour using a high speed camera. The mechanical response of the basalt fabric composites formed by stacking of prepreg layers depending on its orientation is shown in following video frames. Consequent images represent the MS composite pyrolyzed at 650°C in both out-of-plane and in-plane orientations, for convenience. Particular events are highlighted

directly in the images. It has to be kept in mind that the frames are captured according to the events, which may occur at a different moment in particular specimens and their orientations.

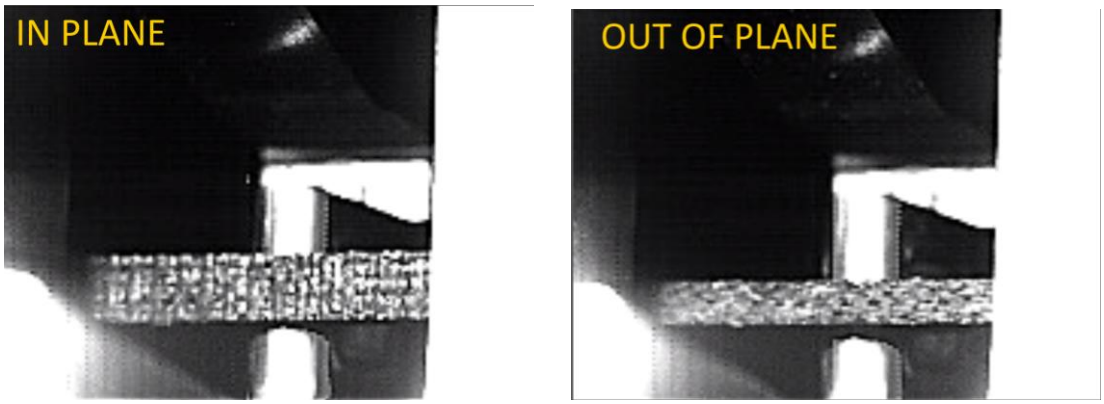

a) b)

Figure 4.48 *MSC specimens recorded right before the impact. The specimen in: a) out-of-plane and b) in-plane orientations. The pendulum approaches the specimens from behind, towards the viewer.*

In the first couple of images (**Figure 4.48**) the specimens are captured in the moment just before the first contact with hammer. The orientation of both specimens is clearly recognized in the image – the image a) shows the out-of-plane orientation, image b) shows the in-plane orientation. The beginning of the fracture process is displayed in **Figure 4.49**. As the hammer strikes the specimen, the energy dissipates, according to the orientation of the layers.

Bending of the specimen in the in-plane orientation leads to an increase of the shear stresses between individual layers. The highest shear is localized on the side, which is in the contact with supports. The delamination of specimen depicted in the video frames was localized on the left side (from observer's position). The layers subsequently delaminated one after another and slipped through the supports. Their deflection behind the supports can be observed in **Figure 4.50 a) - Figure 4.53 a)**. In **Figure 4.54 a)** can be seen how the first layer swings back from its maximum deflection, hitting the layers approaching in the opposite direction.

In the SEM image in **Figure 4.46 a)** was observed different response of the material in the same treatment and orientation. Few layers on the tensile side were broken and off. Such behaviour refers to the strong interface between layers. Delamination was suppressed and high tensile stress led to failure of layers, i.e., consumption of energy. After the energy of the crack was partly absorbed, there was not enough energy for the failure of the following layers. The crack deflected between the layers which led to delamination of the broken layers. Loading the specimen in the in-plane orientation causes symmetrical delamination starting from the outer layers on both sides (**Figure 4.49 b)** - **Figure 4.50 b)**). The material in this direction is stiffer which leads to an increased impact strength and energy absorption, too. At the moment of hit, certain portion of outer layers starts to delaminate, they twist and slide along the hammer tup front, and the remaining inner part of the specimen buckles (**Figure 4.51 b)** – **Figure 4.52 b)**). In further images (**Figure 4.53** - **Figure 4.56**) the extensive damage continues until the specimens leave the focused plane (and the supports).

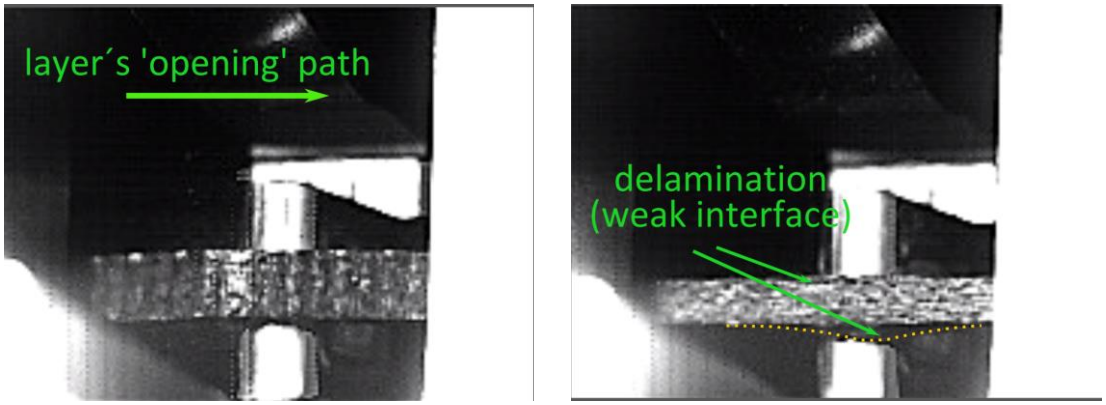

a) b)

Figure 4.49 *Moment of hit: a) elastic waves propagate through the whole cross-section and the first layer delaminates on the left half of the specimen (from viewer's position), b) both outer layers delaminate, leading to higher energy consumption.*

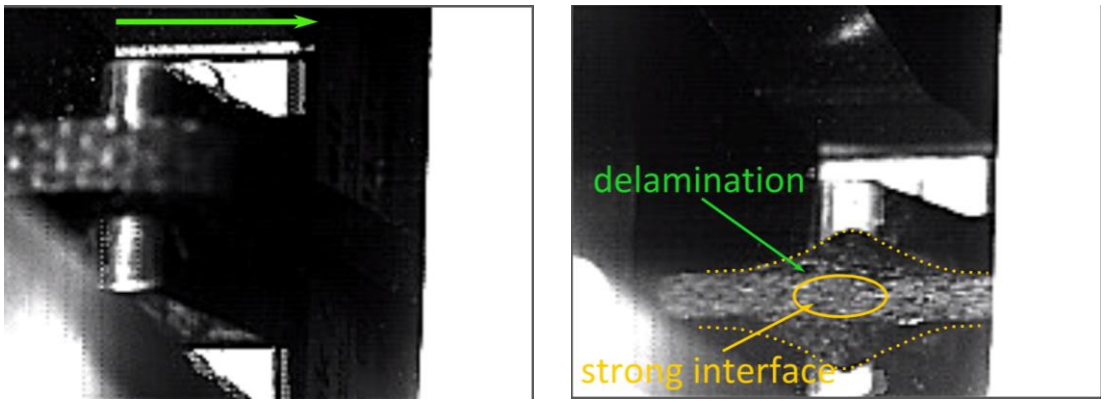

a) b)

Figure 4.50 *a) first layer has delaminated in opening mode,. b)second layer delaminated (in the video observed as a hit).*

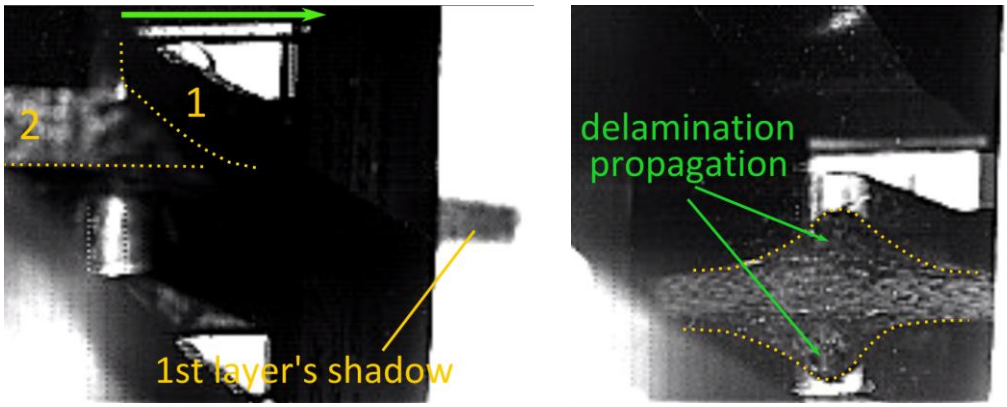

a) b)

Figure 4.51 *a) shadow of the first layer appears on the machine construction. This note is necessary because it can be substituted with the layer which appears later. b) layers 'open' up and slide on the hammer tup. Little twisting of layers occur on the side which is in contact with hammer.*

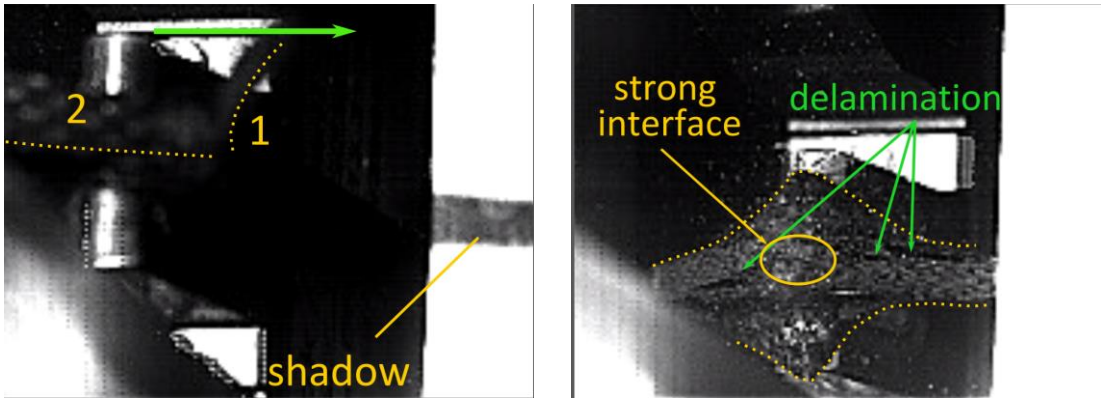

a) b)

Figure 4.52 *a) Shadow of the second layer appeared (see its shadow of the first layer on the right side of machine construction). b) Little fragments of the matrix are thrown out from the space between the layers.*

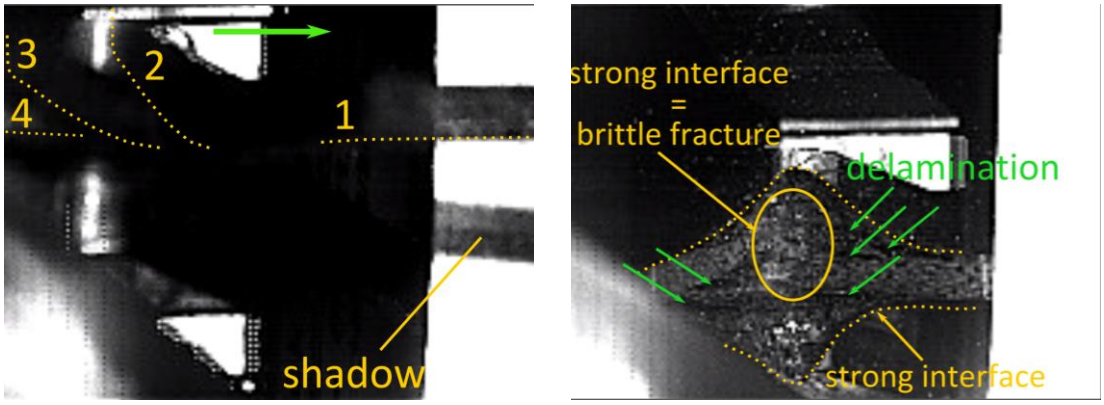

a) b)

Figure 4.53 *a) First layer swings to its maximum deflection. b) The last layer stopped delamination due to the strong adhesion with matrix.*

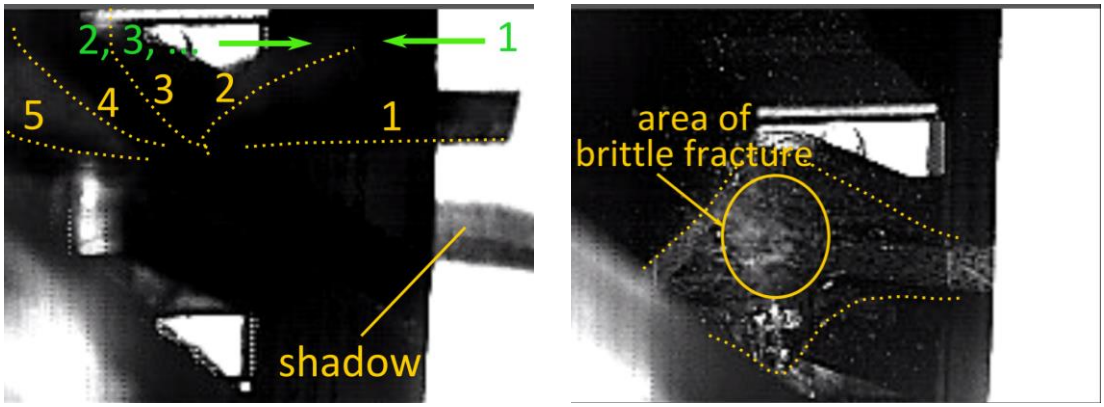

a) b)

Figure 4.54 *a) The first layer swings back towards to the second layer. b) Rupture in the centre of the specimen (white area) is formed by fractured fibres and matrix fragments.*

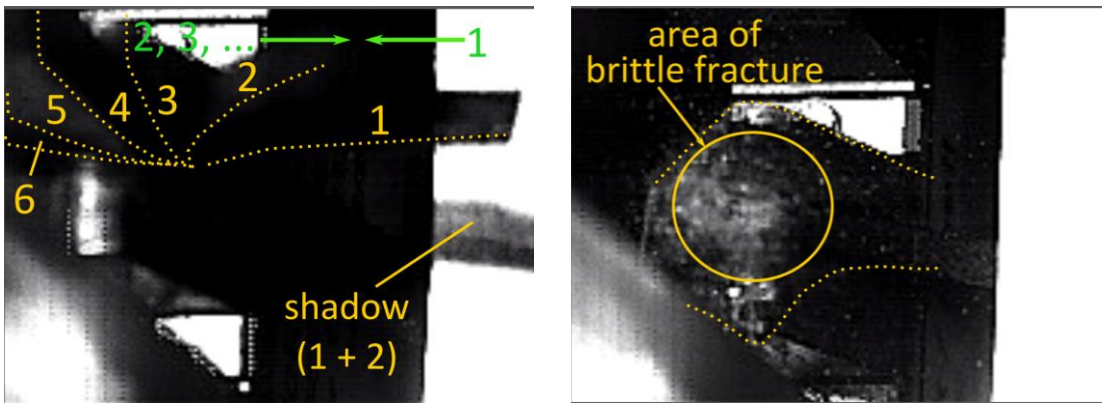

a) b)

Figure 4.55 *a) Shadow of the second layer appears 'behind' the first layer's shadow. b) The area of fracture surface is getting bigger. Broken ends of the fibres swing in both directions (visible in the record).*

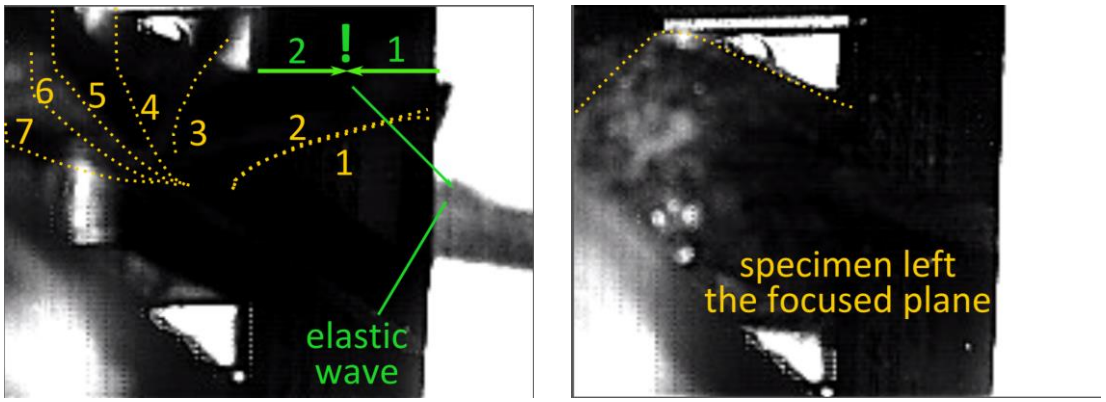

a) b)

Figure 4.56 *a) Elastic wave observed in the shadow of specimen. b) The specimen was pushed out of the focused plane by the hammer tup.*

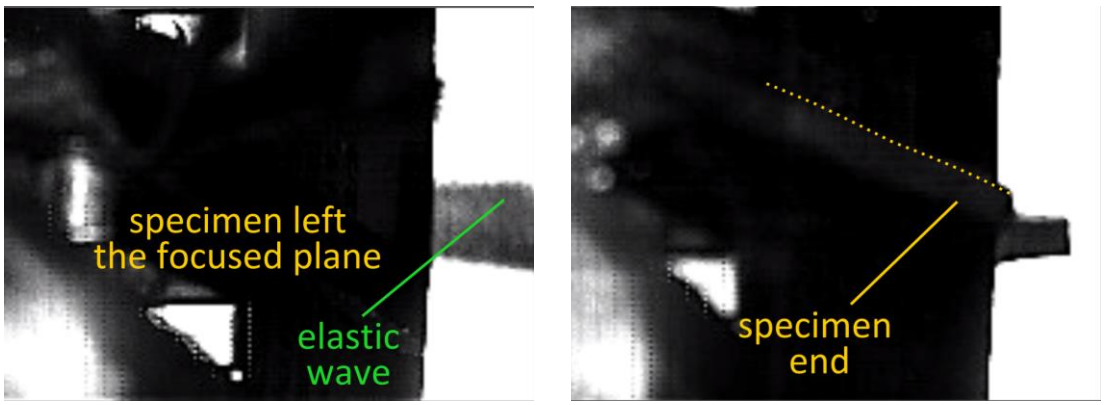

a) b)

Figure 4.57 *a) Layer 1 hits layer 2 and both of them move back to the left where layer 3 hits them and continues with them where it hits layer 4, etc. b) Specimen is leaving the supports of the hammer and its end (and the shadow) is now visible in the frame.*

4.3 CHARACTERISATION OF THE COMPOSITE INTERFACE

4.3.1 Basalt fibre – MS matrix

MS matrix composites with basalt reinforcement exhibited superior mechanical response to static and dynamic loading, especially when pyrolyzed at 650°C. At higher pyrolysis temperatures their properties deteriorated due to changes in the fibre microstructure and fibre-matrix interfaces. The effect of harsh environment on composite properties was simulated by applied annealing under air atmosphere. The fibre-matrix interface of such composites was then observed using a transmission microscope. To simplify, specimens pyrolyzed at 650°C and 750°C were tested at laboratory temperature and will be further denoted as 650RT and 750RT, respectively. Annealed specimens at 550°C will be further denoted as 650/550 and 750/550, respectively.

In **Figure 4.58** are displayed low magnification TEM images of foils prepared from specimens 650RT and 650/550 (a, b) and 750RT and 750/550 (c, d). The images show two neighbouring fibres with approximately 1 μm thick layer of matrix in between, thus, two fibre-matrix interfaces can be observed at the same TEM lamella.

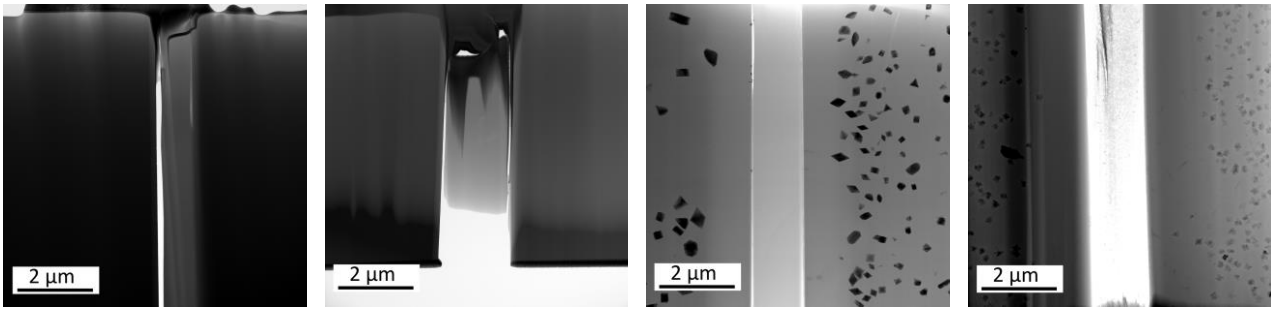

a) b) c) d)

Figure 4.58 *TEM lamellae of as received and annealed composites: a) 650RT, b) 650/550, c) 750RT, d) 750/550. All images were obtained in a bright field mode, SEM.*

Pyrolysis at 650°C (see **Figure 4.58 a)**) neither subsequent annealing at 550°C (see **Figure 4.58 b)**) did not cause any visible change in the composite microstructure, both of the materials were in fully amorphous state. At this point, diffraction analysis showed diffraction rings, typical for fully amorphous materials and it is not displayed here.

Application of pyrolysis at 750°C (see **Figure 4.58 c)**) led to the formation of particles within basalt fibres. Annealed specimen (see **Figure 4.58 d)**) also contains particles in fibres but these objects are smaller and of a different shape (resembling structure of spherulite), comparing to composite without annealing. After annealing, the matrix seemed to be partially crystalline.

In both lamellae – of as pyrolyzed at 750°C and of the annealed state, the particles (crystalline phases and spherulites) were distributed in the whole fibre, except approximately 1 μm thick region in the vicinity of fibre-matrix interface, i.e., surface layer of the fibre. In this region no crystals were observed, except few randomly placed particles in the 750/550 specimen. In all the observed lamellae except the 750/550 (**Figure 4.58 d)**), the fibres appear to be separated from the matrix, nevertheless, the whole thin foil remains compact, thanks to the platinum cover on the top of the foil. The foils were extracted from the polished out fracture surface of already tested

(loaded) specimens, thus, toughening mechanisms such as fibre-matrix debonding or fibre pull-out can cause observed fibre-matrix separation. Another reason can be that the basalt fibres do not bond to the silicon containing matrix, probably due to low adhesion of matrix to the fibres [1]. The lamellae of individual pyrolysis states were subjected to an EDS micro analysis to evaluate change of chemical composition across the fibre-matrix interface. The EDS method is not reliable for quantification of carbon, thus, it was excluded from the analysis and the values of atomic percentage are only relative. Nevertheless, prospective change in the chemical composition of studied materials is proportional and possesses an insight into processes which might take place at the interfaces. Exact chemical composition of the materials used for matrices was already reported in [166, 168].

Point analyses were used to identify chemical composition of particular area or selected particles. Line analyses were applied to reveal possible gradient of chemical composition through fibre-matrix interface. All presented data here are reported in atomic percentage. The data of the point analysis performed on the materials pyrolyzed at 650°C is listed in **Table A.18**. Analysed area of the fibres in both as pyrolyzed (a) and annealed state (b) is displayed in **Figure 4.59**. The fibres were amorphous in both treatment states, as confirmed by the presence of diffraction rings (not showed here). The dark objects visible in the images are holes, burnt by EDS electron beam.

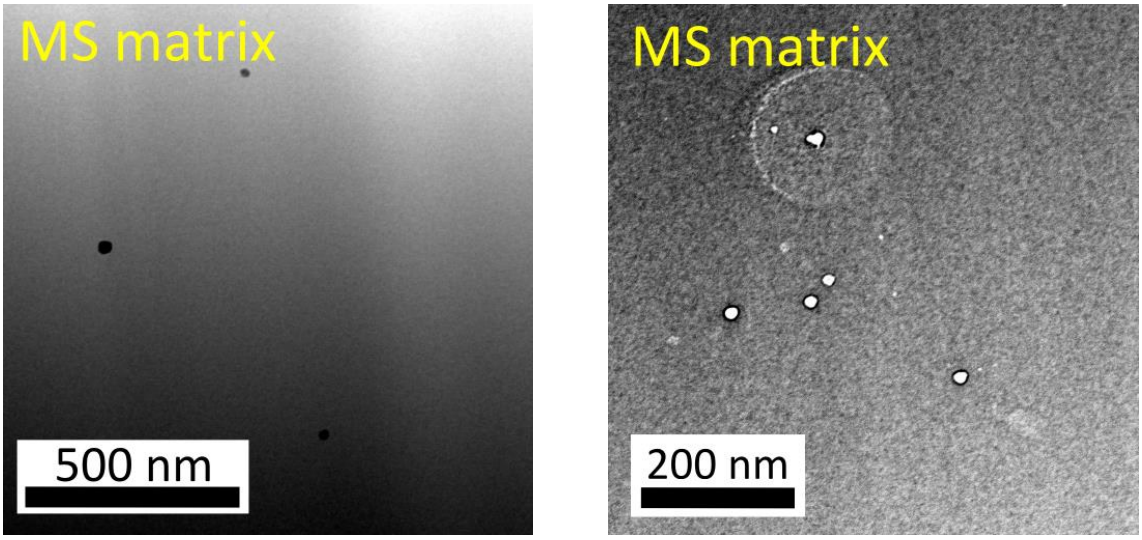

a) b)

Figure 4.59 Point analysis of the MS matrix in the composite pyrolyzed at: a) 650/RT, b) 650/550. The points in the images are holes burnt by the EDS electron beam.

The development of chemical composition through the fibre-matrix interface of the 650RT is provided in **Figure 4.60 a)**. X-axis length represents the yellow analysis line in micrometres. The full lines in the graph indicate trends trough running average of the initial data. The analysis of the matrix revealed the ratio between O and Si. The fibre contain majorly O and Si; plus the fibre contains maximum 10 at. % of Al and less than 5 at. % of Ca and Mg. In contrast to the point analysis (displayed in **Table A.18**), no iron was detected in this case.

In the direction from the left to the right, in narrow area on the fibre surface (the light portion before the shinning zone, which is presumed to be a free space between the fibre and the

matrix) the content of O and Si slightly increased. The increase was ~5 at. % and 10 at. %, respectively, in approximately 0.5 μm distance from the fibre surface. The situation is clearer at the right side of the fibre – matrix interface. There the matrix appears to be bonded to the fibre. There is a short region of approximately 0.2 μm, in which the gradient of element concentration slowly changes, indicating decrease of Si and O towards the fibre. In the matrix was the content of Si higher by ~15 at. %, the content of O by maximum 10 at. % in comparison with the fibre.

In annealed material (650/550) displayed in **Figure 4.60 b)** was observed an increase of the content of O in both the fibres and the matrix in comparison with specimen pyrolyzed at 650°C, which is likely due to the oxidation of the composite during annealing. The content of silicon in both the fibre and the matrix is now more balanced, in comparison with composite pyrolyzed at 650°C (specimen 650RT). In annealed specimen (650/500) the content of the Al decreased, which is probably due to the variable elemental composition of the basalt material.

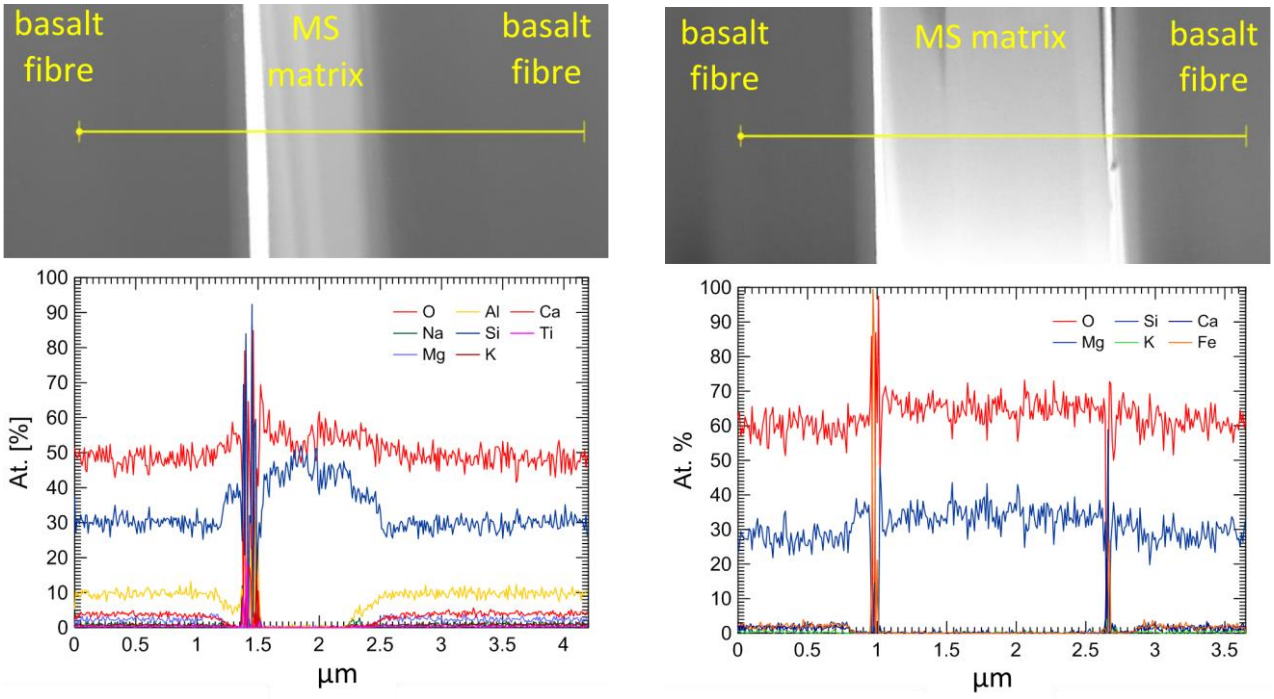

a) b)

Figure 4.60 *EDS line analysis on fibre-matrix interface of a) 650RT and b) 650/550.*

In materials pyrolyzed at 750°C and annealed at 550°C was studied possible upcoming crystallisation. During the standard observation, the matrix of 750RT appeared amorphous and the matrix in the 750/550 specimen appeared refractive, which could indicate crystallinity. The diffusion rings of the matrix and the fibre of the composite pyrolyzed at 750°C are displayed in **Figure 4.61** and of composite pyrolyzed at 750°C and annealed at 550°C are displayed in **Figure 4.62**. Images (a) show the diffusion ring of the matrix, which remains amorphous even after the annealing process, images (b) show the diffraction pattern of fibre, which starts to crystallize already during pyrolysis. In both composite states (750RT and 750/550) was performed point EDS analysis, especially on the particles observed in the fibres. The data of the point

analysis is collected in **Table A.19** and **Figure 4.63** showing where in the fibres and on which particles the analysis was performed.

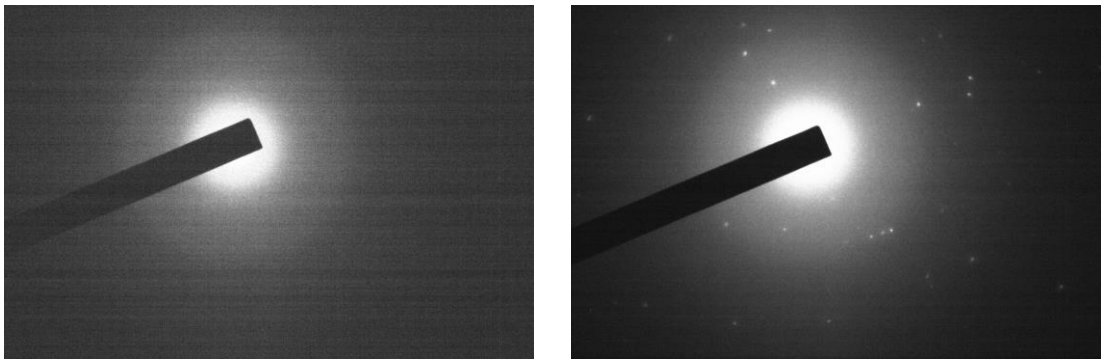

a) b)

Figure 4.61 *Diffraction patterns with diffusion rings for material pyrolyzed at 750°C: a) MS matrix, b) basalt fibre.*

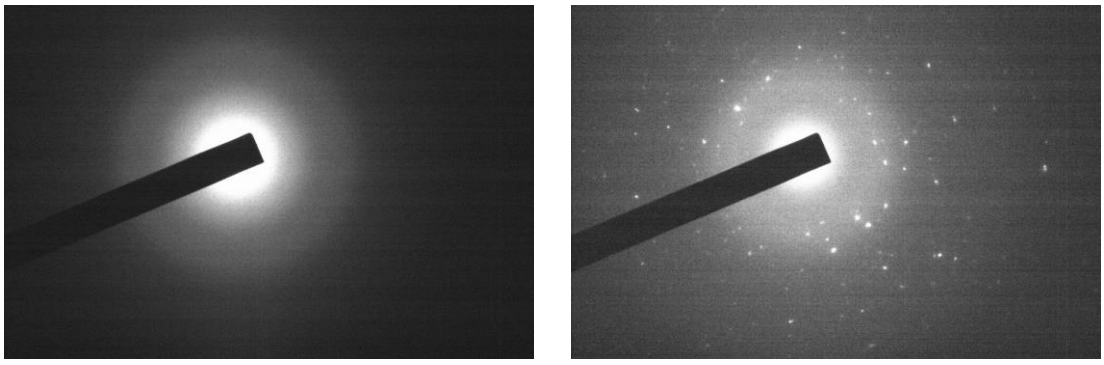

a) b)

Figure 4.62 *Diffraction patterns with diffusion rings for material pyrolyzed at 750°C and annealed at 550°C : a) MS matrix, b) basalt fibre.*

Based on the data of the EDS point analysis was found that the particles observed in the 750RT were majorly based on iron, which was found to be present in an amount between 50 and 90 at. % according to the respective spectra. Oxygen was present in an amount from 10 to 30 at. % and silicon was observed in the portion up to 20 at. %. Remaining elements (Ca and Al) were only in a trace amount. The dependence of chemical composition on the particle distance from the fibre-matrix interface was studied at the 750RT, see. **Figure 4.63**. The spectrum No. 32 (in black ellipse in the graph) represents chemical composition of amorphous basalt fibre (0.7 μm under its surface). As can be seen in the **Figure 4.63 b)**, the distance of the particle from the matrix does not play significant role. The chemical composition of individual spectra might reveal a presence of a mineral. The most probable would be olivine with formula $(Mg,Fe)_2SiO_4$, forsterite (Mg_2SiO_4) or fayalite (Fe_2SiO_4). Presence of olivine or forsterite can be declined, due to the low content of Mg. The presence of fayalite in basalt fibres would be confirmed, if the content of Si would correlate with the content of Fe in the respective ratio (O/Si = 4 at. %, or 2.3 if calculated in wt. %). To find out, the EDS analysis results were plotted as the dependence of the molar rate on the content of iron and the graph is displayed in **Figure 4.64**. The trend of the molar rate of Fe/Si shows that the

content of Fe does not correlate with Si and O. That leads to hypothesis, that the analysed grains are formed of iron and surrounded by amorphous phase of the basalt fibre, containing mostly Si and O. As the grain size increases, it is less surrounded by the amorphous phase, due to defined thickness of the analysed lamella.

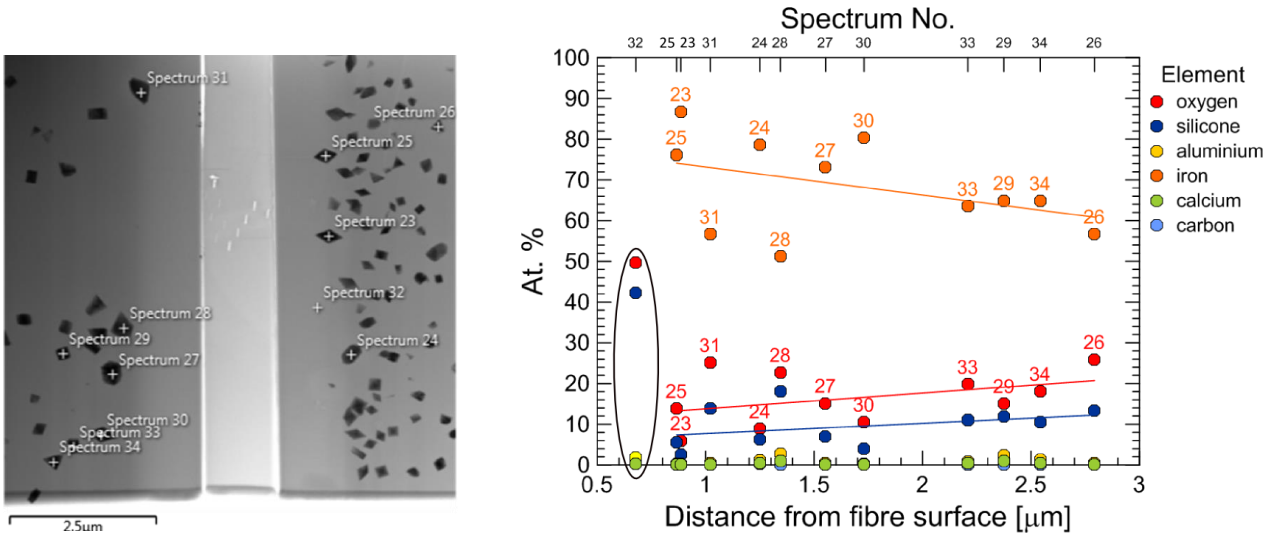

a) b)

Figure 4.63 *The fibre-matrix interface in 750 RT – two basalt fibres with the matrix between them: a) analysed area with individual spectra, b) dependence of elemental composition of the particles on their distance from the fibre-matrix interface.*

Similarly, in the specimen 750/550 was analysed chemical composition of spherulitic particles, represented by spectra 3, 21 and 22 in **Table A.18**. All three measured spectra were mostly composed of oxygen ~56 at. % and approximately 25 at.% of Si. Further elements were Mg, Al and Fe, Ca and Ti. Spectrum 3 was majorly composed of O and Si, other analyzed elements (Mg, Al, Fe, Ca, Ti) were present in maximum up to 2.3 at. % of individual element. Its values were slightly different from the spectra 21 and 22, which were mutually more comparable. Both spectra contained up to 8 at.% of Mg, almost 5 at. % of Al and up to 4.5 at. % of Fe. Others elements were Ca and Ti, their content was maximum up to 3 at. %.

In both the studied composites pyrolyzed at 750°C (especially in the 750RT) were clearly visible regions at the fibre surface. This region contained usually no grains and its thickness was approximately 1 µm for the 750RT and almost 2 µm for the 750/550. The particles-free region in 750RT was mostly formed of oxygen (52.61 at. %) and silicon (45.01 at. %), see spectrum 32 (**Table A.18**). In the 750/550 the border area was analyzed in spectra 17 and 19 (in **Table A.17**). In comparison with 750RT, the content of oxygen remains on the level of 50 at. %, Si dropped to a half (26.5 at. %), Al increased from 2 to 10 at. % and the content of Ca and Fe increased to 4 at. %.

The gradient at the fibre – matrix interface was studied using line analysis. The situation for 750RT is represented in **Figure 4.65**. The content of Si and O is almost constant within the inspected line; it only slightly decreases in direction to the fibre centre. The apparent decrease of Si and O at the fibre-matrix interface is a consequence of the presence of Al in the fibre.

Crossing the particle, Si and O rapidly dropped and an increase of Fe, which was not detected in the matrix nor the fibre, was observed. The elemental composition of the matrix evaluated by line analysis is in agreement with the point analysis (spectrum 11 in **Table A.19**).

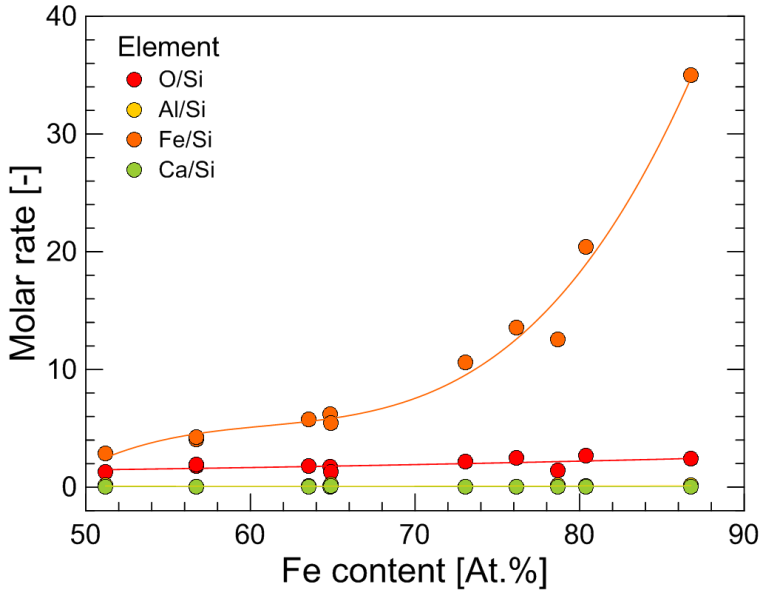

Figure 4.64 *Dependence of the molar ratios of O/Si, Al/Si, Fe/Si and Ca/Si (analysed in crystalline phases of the basalt fibre in composite pyrolyzed at 750°C) on the content of iron.*

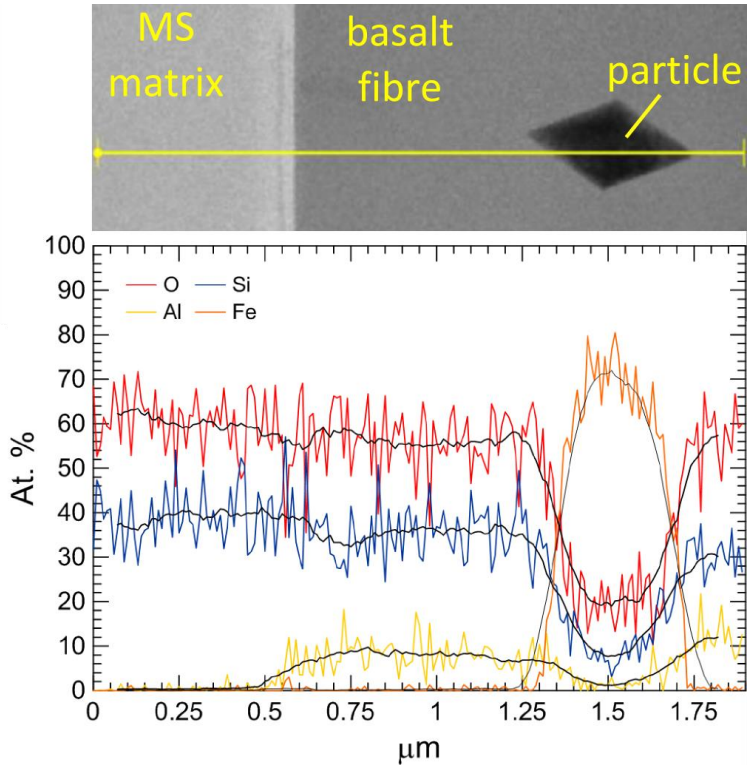

Figure 4.65 *EDS line analysis on the fibre-matrix interface of 750RT with present iron particle.*

For the composite 750/550 is the EDS line analysis represented in **Figure 4.66**. The annealing led to visual change of the matrix and change of the particles in the fibres. The matrix is represented solely by O and Si, approximately 62 at. % and 38 at. %, respectively. The crystallisation in the matrix was not confirmed by the diffusion rings. The oxygen, silicon and aluminium seem to change gradually over the fibre-matrix interface. The content of O and Si decreases by ~10 % in the direction of fibre, on the contrary, the content of Al gradually increases from 0 % in the matrix to ~10 % in the fibre in distance smaller than 0.5 μm. Fe and Ca were detected in the fibre in the amount up to maximum 2 at. %. Notice that the aluminium content (yellow line) starts to increase closer to the fibre-matrix interface by approximately 0.2 μm than Fe (orange line) and Ca (purple line). Analyzed particles contain particularly Fe.

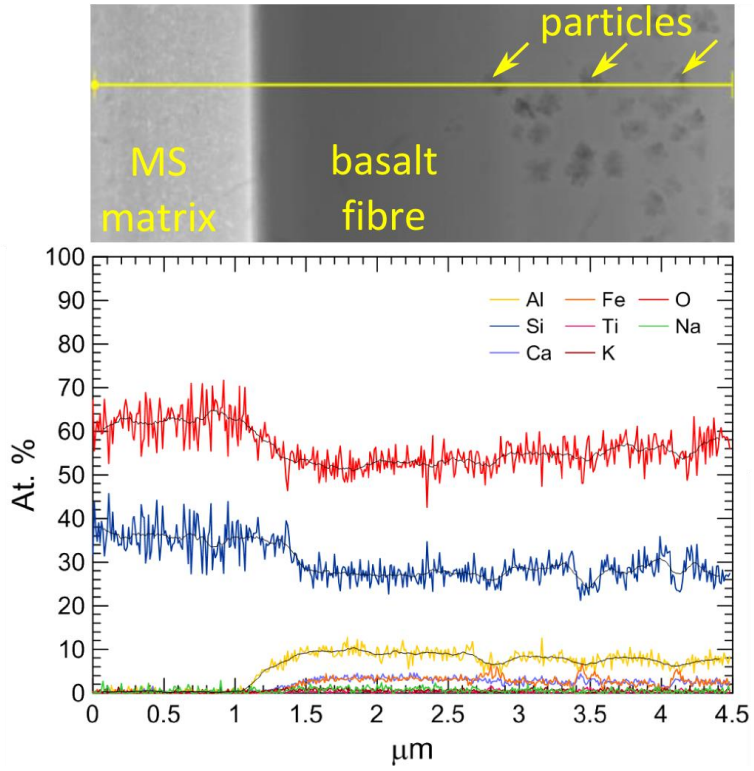

Figure 4.66 *EDS line analysis on the fibre-matrix interface of 750/550 with present iron particles.*

Besides the particles, the amorphous part of the fibres was analysed, too. For 750RT, see spectra 10 and 13 to 16, and for 750/550 spectra 17 to 20 (in **Table A.19**). The amorphous fibre phases in both the composite states had basically identical elemental composition. They were composed of approximately 50 at. % of O, 27 at. % of Si, up to 3 at. % of Mg, and 0.5 at. % of Ti. In annealed specimen the content of Na, Al and Si decreased by 1 at. % and Ca increased by 1 at. % in comparison with only pyrolyzed state. The most significant change was observed for iron content, which increased by 3 at. % for annealed specimen comparing to 750RT.

The elemental composition in higher distance from the interface of the composite 750/550 (amongst the particles, see spectra 20 and 18) was only a slightly different from the spectra 17 and 19. The graphs for both the specimens are provided in **Figure 4.67**.

Chosen particles observed in the 750RT specimen were subjected to a diffraction analysis of the crystal lattice for analysis of the basaltic minerals. Initially, the particles were expected to be

the crystals of minerals fayalite, forsterite or olivine. The low content of Mg excluded olivine $(Mg,Fe)_2SiO_4$ and forsterite (Mg_2SiO_4). Nevertheless, the diffraction pattern was compared with the model for forsterite (represented by red dots) as shown in **Figure 4.68**. The size of the dots of the diffraction model expresses the intensity of the reflection in the diffraction – the higher is the intensity, the larger are the dots. The simulated pattern of the forsterite does not fit to the measured diffraction pattern, due to different intensity of individual reflections. The forsterite and olivine have very similar crystal lattices, which leads to the hypothesis that the olivine is not present in the analysed basalt fibres as well.

According to the high content of iron in the analysed particles, diffraction pattern of pure Fe was simulated. The diffraction pattern of the Fe is displayed in **Figure 4.69**. As can be seen, the calculation of the Fe diffractions (red dots) fits very well to the diffraction pattern of the particles analysed in the basalt fibres of the 750RT specimen, acquired during the TEM observation.

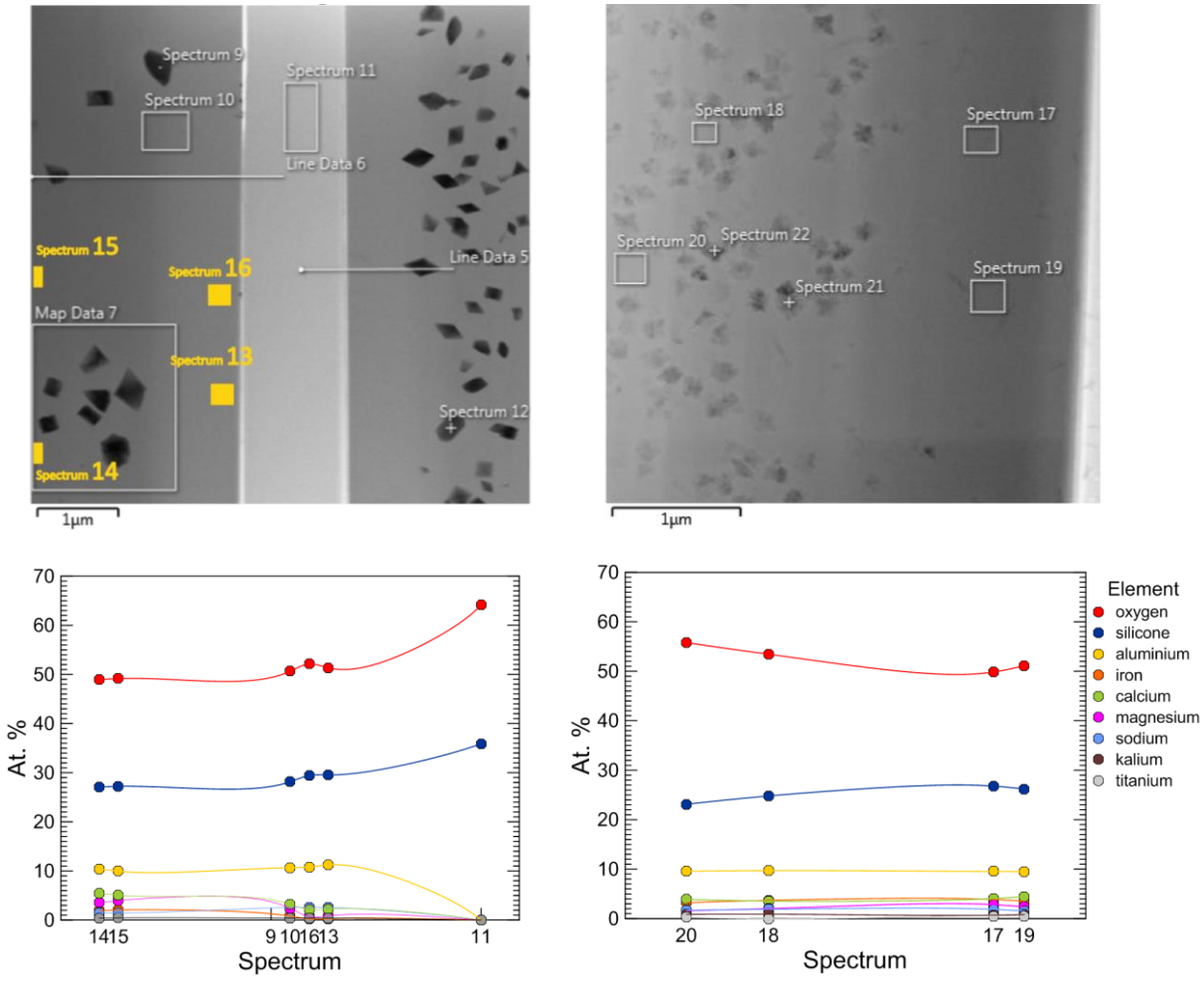

a) b)

Figure 4.67 *Gradient of elemental composition in amorphous part of the fibre: a) 750RT, b) 750/550.*

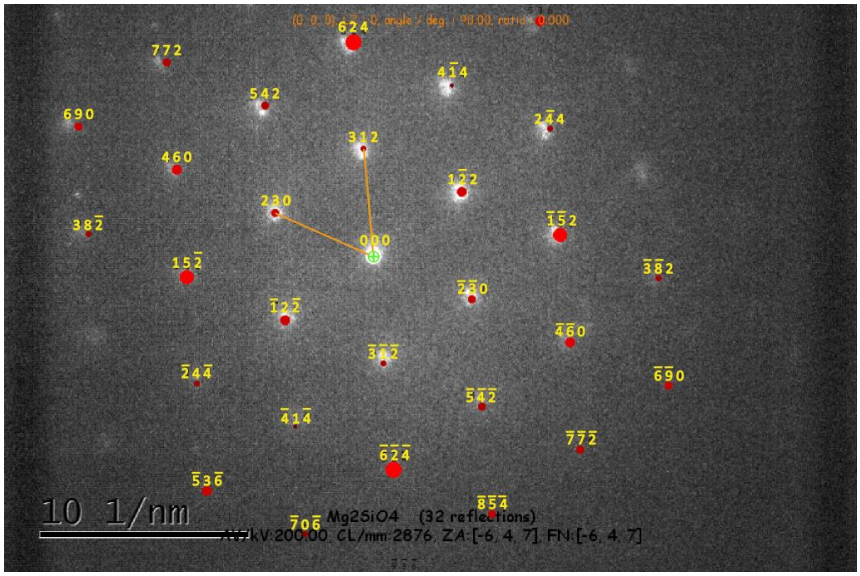

Figure 4.68 *Diffraction pattern of forsterite.*

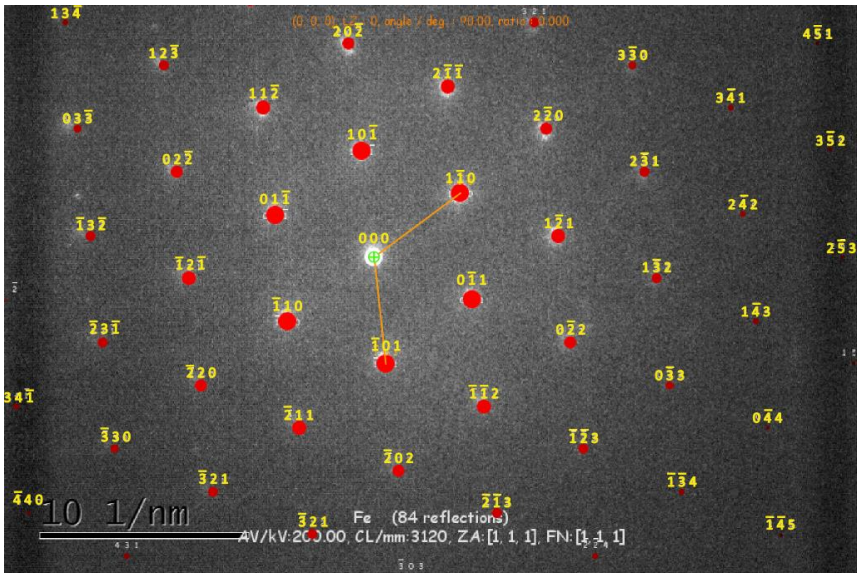

Figure 4.69 *Diffraction pattern of iron.*

4.3.2 Nextel ™720 – SiOC matrix

The interface of chosen composites which are based on fully pyrolyzed SiOC glass with Nextel™720 fibres is investigated in this chapter. The matrix is based on T3D1 material and the fibre is polycrystalline ceramics, composed of alumina (Al_2O_3) and mullite ($Al_2O_3 \cdot SiO_2$).

Two lamellae represent materials pyrolyzed at 1100°C (a) and annealed at 1500°C for three hours (b). The lamellae with the fibre-matrix interface are shown in **Figure 4.70**.

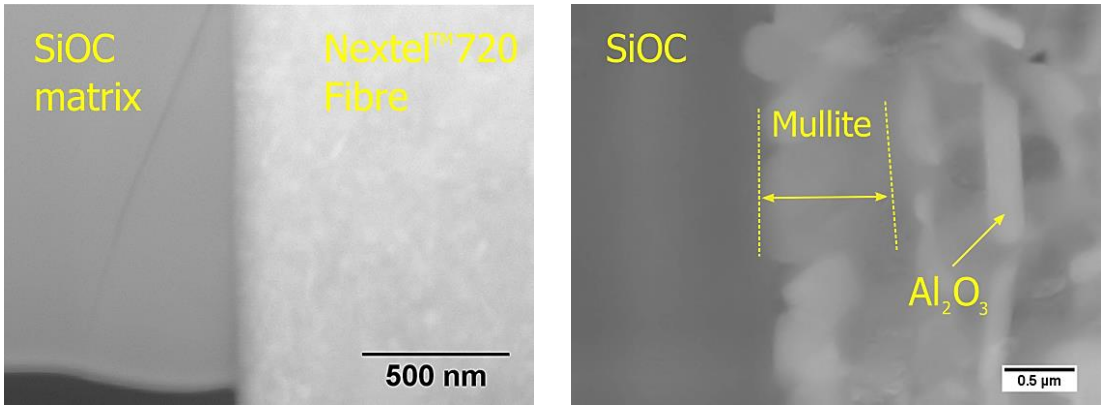

a) b)

Figure 4.70 *Fibre-matrix interface of composite with SiOC matrix and Nextel™720 fibre, a) pyrolyzed at 1100°C and b) annealed for 3 hours at 1500°C [185].*

Significant changes were observed in the fibre microstructure due to the annealing. By comparison of both images (a) and b) in **Figure 4.70**, the size of the grains in the Nextel™720 fibre in the pyrolyzed composite increased after annealing between 5 to 10 times. The size of alumina grain was almost 1 µm in the specimen annealed at 1500°C. At a room temperature, the fibres are polycrystalline with mullite (300 nm) and α-Al_2O_3 grains (70 nm) and the grain growth (recrystallization) was reported to start at temperature of about 1300°C [186]. Toghether with the grain growth, the roughening of the fibre surface (see **Figure 4.70** b)) was observed, too. Detailed microstructure of the Nextel fibre after pyrolysis at 1100°C and subsequent 3h-annealing at 1500°C is displayed in **Figure 4.71**. The long white grains were identified by EDS analysis as α-Al_2O_3, grey granular objects represent mullite.

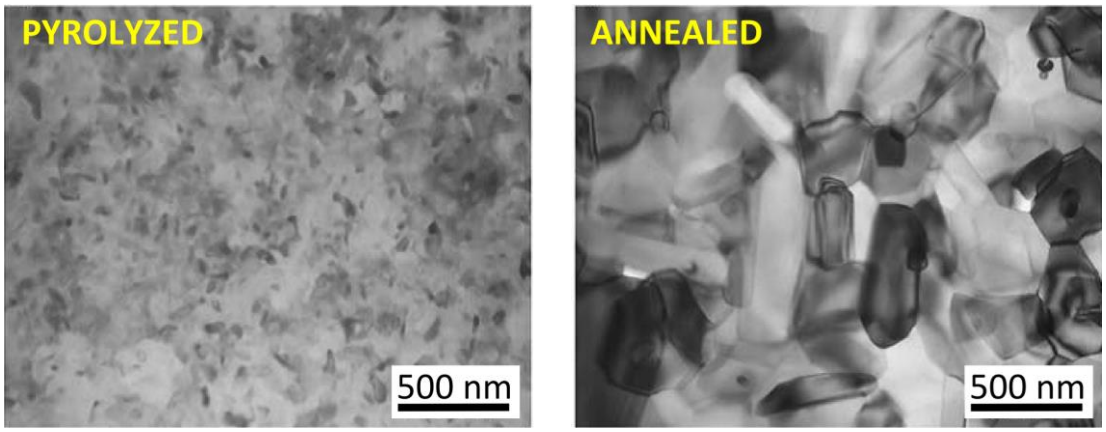

a) b)

Figure 4.71 *Microstructure of Nextel™ 720 fibre after a) pyrolysis and b) annealing for 3 hours at 1500°C (already published in [185]). The scale represents 500 nm in both images.*

The composite pyrolyzed at 1100°C contained large amount of cracks, as represented in **Figure 4.72**. In image (a) is captured the crack propagating in the direction from the matrix to the fibre, induced probably by the matrix shrinkage, induced by elevated temperature. The crack stops its propagation at the interface and does not continue into the fibre, indicating strong bond of the

fibre with the SiOC matrix. Observed phenomena confirm the formation of strong interfacial bonding, which led to deteriorated toughening mechanisms (fibre-matrix debonding and fibre pull-out) and therefore low composite fracture toughness. Image (b) shows the crack inside of the fibre. The crack is branched at both of its ends, which is typical feature of thermally induced cracks. Both types of observed damage were induced by thermal loading.

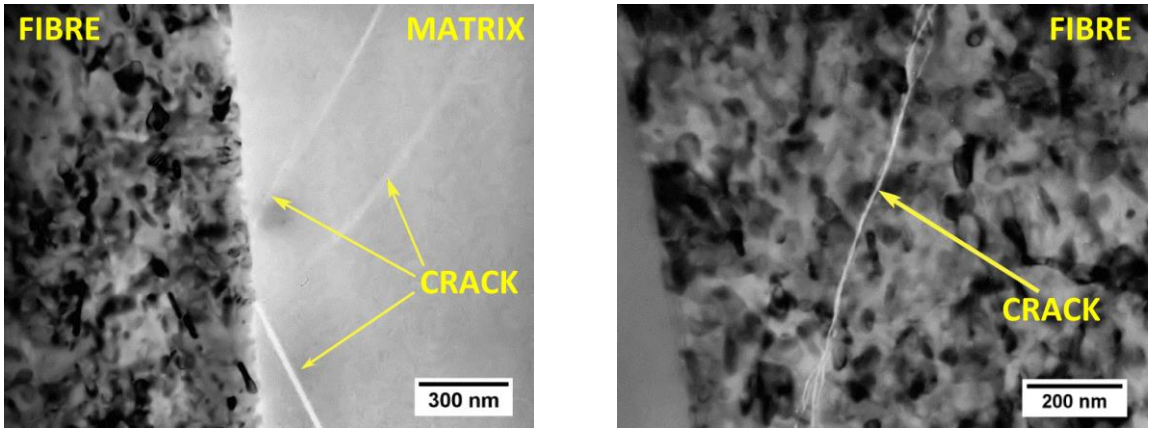

a) b)

Figure 4.72 *Crack propagation a) through the fibre-matrix interface, b) inside of the fibre (published in [185]).*

Although the typical toughening mechanisms (such as fibre-matrix debonding and pull-out) were hindered due to the formation of the strong fibre-matrix interface, the properties of annealed composite were comparable (flexural strength) or even better (fracture toughness) than the properties of only pyrolyzed composite [185]. Observed composite behaviour was caused by activation of the microcrack toughening mechanism, introduced by thermally induced network of microcracks in the annealed composite.

In the composite with SiOC glass fully pyrolyzed at 1100°C with Nextel™ 720 fibres was employed line EDS analysis to find if any gradient in elemental composition over the fibre-matrix interface occurs. The image of the analysis toghether with the graph is provided in **Figure 4.73**. In the image, the fibre is light-coloured, located in the left side and the matrix is a bit darker and located in the right side of the analysis line. The interface between both the components is clearly recognized from the change of the aluminium and silicon content. The fibre contains 85 wt. % Al_2O_3 and 15 wt. % SiO_2, [10] (which is 77.2 at. % and 22.8 at. % for Al_2O_3 and SiO_2, respectively). In elements, it is ~50 wt. % of O, 23.5 wt. % for Si and 26.5 wt. % of Al (recalculated in atomic percent: 19.9 at. % of Al, 16.9 at. % of Si and 63.2 at. % of O) and the elemental composition of T3D1 material is 53.7 wt. % of Si, 42.2 wt. % of O and 4.1 wt. % of C (39.1 at. % of Si, 53.9 at. % of O and 7 at. % of C) [96]. The graph shows the element distribution in individual composite components in agreement with the calculated atomic percent of the aluminium, silicon and oxygen, listed above. The content of oxygen is rather ballanced in both phases, thus, no gradient was recognized. Content of aluminium rapidly changes accros the narrow area and in narrow area (< 0.5 μm) of the matrix can be observed gradual decrease of the aluminium content. Visible gradient in the composition over the fibre-matrix interface was observed only for silicon. The content of the silicon deep in the Nextel fibre is rather constant, but

in the proximity of the fibre surface, the content of silicon increases. At the fibre surface, the slope of the curve increases much faster until it continues in the matrix, where the content of silicon becomes constant again. It can be assumed that the silicon diffuses from the T3D1 matrix to the Nextel fibre. The peaks on the silicon (blue) curve, observed also on the aluminium (yellow) curve in the fibre, indices crystallisation of aluminium-rich α-alumina needle-shaped grains.

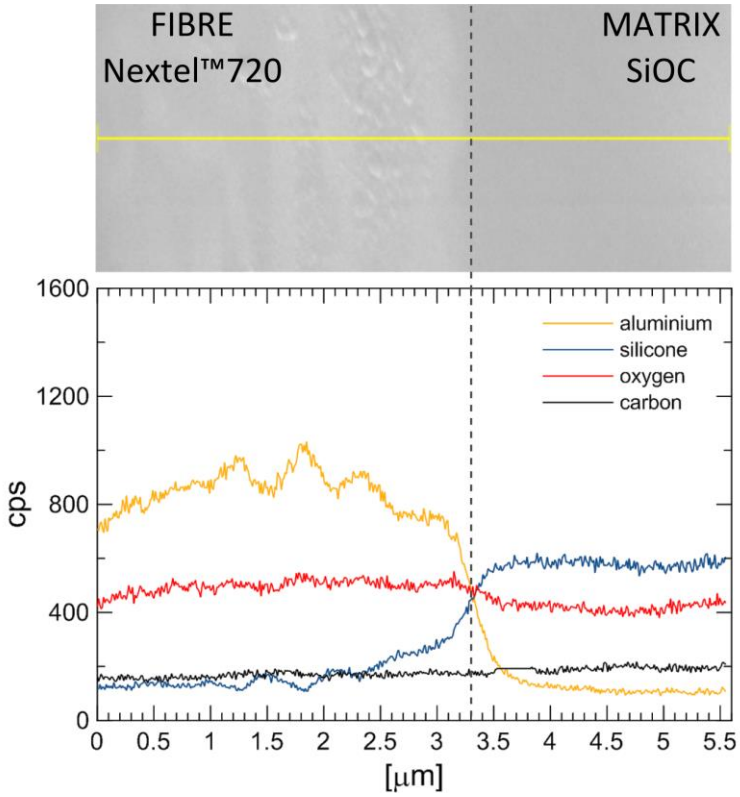

Figure 4.73 *Elemental composition over the fibre-matrix interface of the composite made of T3D1 material reinforced with with Nextel™ 720.*

5 DISCUSSION

In this work were studied composites with fully (SiOC glass) and partially pyrolyzed matrix and basalt or Nextel™ 720 fibres as reinforcements. Two types of composites were obtained: low-cost composite material on the one hand and composite for high temperature application on the other hand. The low cost composite was designed of commercial resin (MS or MPS) and basalt fibres (fibrous or woven fabric preforms). For high temperature composite was composed of synthesized resin (T3D1) and Nextel™ 720 fibres (aligned).

5.1 MS AND MPS MATERIALS

5.1.1 Microstructure

Prior to mechanical and microstructural characterization of the composites, the materials used for matrices were characterised by means of microstructural observation and mechanical testing in their particular processing states, too. During the transformation of polysiloxane resins into SiOC glass via pyrolysis, they change from transparent to opaque black (**Figure 4.1**). This process is influenced by evolution of turbostratic carbon [86]. Process for preparation of fully transparent SiOC glass was described in [187], but it is not necessary for currently intended application (thermal barriers, automotive).

According to the observed colour change of MS and MPS materials in various pyrolysis states (cured at 250°C, pyrolyzed at 400-1000°C), the evolution of turbostratic carbon starts above 600°C for MS and above 500°C for MPS, indicating becoming structural changes. Initially in the cured state, MS was colourless and MPS was beige. Similar observation was performed on polymethylsilsesquioxane, which turned black at around 800°C [123].

Pyrolysis at 650°C with the dwells from 0 to 5 hours showed that MS material becomes black after 5 hours treatment, whereas MPS becomes black immediately after it reaches 650°C, without dwell (see **Figure 4.2**). On the contrary, even pyrolysis for 10 hours at 520°C does not lead to black colour of MPS, which remains brown but transparent. It indices that the pyrolysis temperature of 520°C is too low for polymer-to-ceramics transformation and thus higher temperature (600 – 650°C) is required.

5.1.2 Density

Density of MS and MPS materials depends on the pyrolysis temperature (see **Figure 4.7**). Below 600°C, the MS material has low density in cured (250°C) and pyrolyzed (400 and 500°C) states. Both the MS and MPS materials reach comparable density values at pyrolysis state of 700°C. At the pyrolysis temperatures of 800-1000°C the MS material reaches higher density comparing to MPS material. The density evolution is associated with different initial polymer network structure of both MS and MPS materials and its rearrangement into amorphous glass.

Density of MS and MPS materials pyrolyzed at 650°C at various dwell time (0, 1, 2, 5 hours) increased linearly with increasing dwell time for MS material. Density of MPS material decreased from 0 to 2 hours dwell time, where the lowest density value was obtained. This can be caused by the swelling of the polymer structure, probably caused by the present phenyl group. Although the

density of both MS and MPS materials evolves in a different manner, both the materials reached comparable density when pyrolyzed at 650°C for 5 hours (**Figure 4.8**, **Table A.2**). A reason can be found in the polymer network decomposition and structural rearrangement during the polymer-to-ceramic transformation of the materials. The blackening of MPS material caused by increasing content of turbostratic carbon was associated with the polymer-to-ceramic transformation. As it was observed that the MPS material starts to change at pyrolysis temperature lower than for MS material, pyrolysis at 520°C with various dwells (0, 1, 2, 5 hours) was conducted. However, the pyrolysis temperature of 520°C is too low for polymer-to-ceramic transformation, as can be stated from the density evolution in **Figure 4.9** (**Table A.2**), as well as the colour change. The density of MPS material pyrolyzed at 520°C has similar trend as in case of the pyrolysis at 650°C, but it is lower by 11 %. The MPS material did not fully blackened even after 10 hours dwell time at 520°C.

Pyrolysis heat rate does not have an influence on density of the MS and MPS materials, as no dependence of the density on the heat rate was observed in **Figure 4.10**. The difference in the density values is observed at the level of hundredth and both MS and MPS materials evolved with the identical trend, only the density of the MPS material was lower by 5 % and the scatter in data was lower, comparing to MS material (see **Table A.4**.

5.1.3 Instrumented indentation hardness and elastic modulus

Hardness and elastic modulus of MS and MPS materials evolve with pyrolysis temperature in the same trend as in the case of density, i.e., the Martens hardness and elastic modulus values of MPS material are in this case only negligibly higher comparing to MS material. Both the materials exhibit comparable Martens hardness (see **Table A.5**), as well as the indentation elastic modulus (see **Table A.6)**) at pyrolysis state of 800°C, and above this temperature the MS material reaches higher values of both Martens hardness and elastic modulus. Vickers hardness was initially employed, too. It was found out that it is not reliable method for evaluation of SiOC materials pyrolyzed under 1000°C, because the materials exhibit relaxation behaviour (see **Figure 4.19**).

The measurement of density of MS and MPS materials was conducted with 2 years delay, to investigate the material stability. It was revealed that the density remains stable in the whole range of investigated pyrolysis temperatures, even for the low pyrolysis states bellow the pyrolysis temperature of 700°C, as well as in the cured state (250°C). This finding possesses a good information for long-term use of partially transformed SiOC materials – for example for storage of MS or MPS prepregs, made of a reinforcement infiltrated by MS or MPS resins and stored in a cured form.

Generally, below 600°C the properties of MS and MPS materials are low compared to fully transformed materials at 1000°C. The significant change in material properties starts between 600 and 700°C. Evolution of the MS materials starts later than for MPS. At the pyrolysis temperature of 800°C (700°C for density) the trend of hardness and indentation elastic modulus becomes identical and above that pyrolysis temperature the MS properties are higher than for MPS (the trends cross).

In the pyrolysis temperature interval of 500-600°C the MS and MPS materials exhibited high ability to recover from the indentation. For MS material was observed a non-linearity in measured maximum and minimum indentation depth (h_{max}, h_{min}, respectively) in the case of material partially

pyrolyzed at 600°C. Regarding the fact that with increasing pyrolysis temperature the density, modulus or hardness of MS material increased linearly, this finding was not clear and it rather indicated substituted specimens. Nevertheless, repeating of the experiment declined this variant. High elasticity of the MS material pyrolyzed at 600°C may be associated with thermal degradation of methyl groups and hydrogen loss, described in [166].

5.2 LABORATORY SYNTHESIZED MATERIALS

Modification of the structure and properties of the SiOC glass by optimizing the ratio of linear and branching units were studied in [93, 96, 119] and the investigation of laboratory prepared matrices SiONC, T4D1-B, T4D1-Fe and T19D1 contributes to this study. The preliminary results characterizing SiONC material was published in [167]. Modification of T4D1 by addition of iron was conducted because of promising properties of this combination, i.e., only ~10 % weight loss of T4D1 material and expected good mechanical response in a composite, due to formation of required weak fibre-matrix interface modified by iron ions [149]. Addition of boron to T4D1 was conducted to positively affect the reorganisation of pyrolysing polymer and to decrease thermal expansion (i.e., internal stresses in material) in final product. Using of boron in polysiloxane material was reported in [102]. Weight loss data confirmed that the boron was successfully incorporated into the structure of SiOC glass. Mechanical response of particular states of T4D1-B can be compared with data of T4D1 (reported in [93]). The mechanical properties of T4D1-B worsened in all the pyrolysis states. Pyrolyzed (1000°C) T4D1-B performed lower values in HV 0.2, HM and E_{IT} by 5 %. Comparing to properties of T4D1, for T4D1-B material pyrolyzed at 1000°C and annealed at 1300°C, the data was 20-25 % lower and at 1500°C the properties were lower by 15-25 %. The deterioration of the properties can be ascribed to the material structure, containing high amount of pores and also a lot of cracks. Comparison of HV 0.2, HM and E_{IT} of the T4D1 with T4D1-Fe (both pyrolyzed at 1000°C) showed that the modified T4D1-Fe reached identical properties as T4D1. Annealing of T4D1-Fe at 1300°C and 1500°C led to drop of analysed properties by ~25 %, comparing to T4D1.

Optimisation of SiOC and its properties by combining T and D siloxane units has been reported in many works [92, 93, 96, 119]. Preparation of T19D1 might have been induced by the intention to prepare material with low weight loss and thus, low shrinkage. The mass and volume change is the main limiting factor in the use of SiOC materials. In work of Havelcová [188] are compared weight losses in Q1D3, T2D1, T3D1 and T4D1. The weight loss decreases with increasing T unit in the structure and T4D1 had the lowest weight loss from all the tested materials, at the level of 10 %. Weight loss of T19D1 was not measured in this work, thus, the materials can be compared only by their hardness (Vickers, Martens) and indentation elastic modulus. Mechanical properties of matrices with varying T/D ratio are published in [93, 189]. In comparison with T4D1, T19D1 exhibited lower values of Martens hardness and indentation modulus by 25–35 %. Vickers hardness of T19D1 was lower only by 5–10 % than the hardness of T4D1 in both annealed states (1300, 1500°C). For T19D1 pyrolyzed at 1000°C was higher by 10 % compared to T4D1.

Evolution of the microstructure with varying T/D content is discussed in [113]. In work of Parmentier [190] are shown fracture surfaces of two T/D systems when discussed the effect of

hydrolysis ratio on the SiOC structure. Morphology of fracture surfaces of T/D is displayed also in [96, 128]. Many works are interested in phase distribution, providing TEM or High-Resolution TEM (HRTEM) images [86, 191].

T19D1 can be compared with other T/D systems by means of T/D ratio and its effect on the microstructure appearance. Materials T2D1, T3D1 and T4D1 pyrolyzed at 1000°C and annealed in range of 1200 – 1500°C were mechanically characterized in [93, 119]. Microstructure of these materials in pyrolyzed state (at 1000°C) and annealed states (1300 and 1500°C) is displayed in **Figure 5.1**, together with T19D1 at the respective states. Influence of annealing temperature on material structure is clearly visible for particular materials. T19D1 is extensively damaged by cracks and pores already in its pyrolyzed state (1000°C). At annealing temperatures (1300 and 1500°C), the pores seem to grow and group with others to form even larger pores.

Formation of pores is usually associated with evolution of gaseous CO_x products [113], preferably in SiOC with excess of free carbon. Presence of free carbon is associated with linear unit diethoxydimethylsilane (D) [189] and it is present for example in stoichiometric SiOC, i.e., T2D1 ratio [92]. On the other hand, the pores can also be a result of evolution of gaseous SiO, as reported in literature [92] for T^H/D^H 9 system (i.e., T9D1). In material T19D1 will probably take place the second mechanism, i.e., evolution of gaseous SiO, formed by the reaction of elemental Si with domains of silica at temperatures above 1200°C [92, 191, 192]. After anneling at 1500°C, significant oxidation is observed at the cracks in all the materials except T2D1. The cracks became wider and covered with layer of oxidation products. In the case of T3D1 and T4D1 the cracks became wide and the oxidation layer was cracked. In T19D1 structure the oxidation products filled the tiny cracks of SiOC material and no cracks in the oxidation product were observed. Overall, tendency of extensive cracking of T19D1 might have been caused by high internal stresses, caused by excess of T (triethoxymethylsilane, trifunctional branching unit [96]).

To sum up, new laboratory synthesized materials (SiONC, T4D1-B, T4D1-Fe and T19D1) did not exhibit any significant enhancement of mechanical properties comparing to common used basic materials, the properties rather deteriorated. Therefore, the materials T4D1-Fe, T4D1-B and T19D1 were not applied in composites. In case of commercial materials (MS and MPS) was found that their excellent mechanical properties described in [111] may be associated with their polymer-to-ceramics transformation in particular temperature interval around 650°C for MS-based matrix. MPS-based matrix transforms slightly earlier, around 600°C, due to the presence of phenyl substituent.

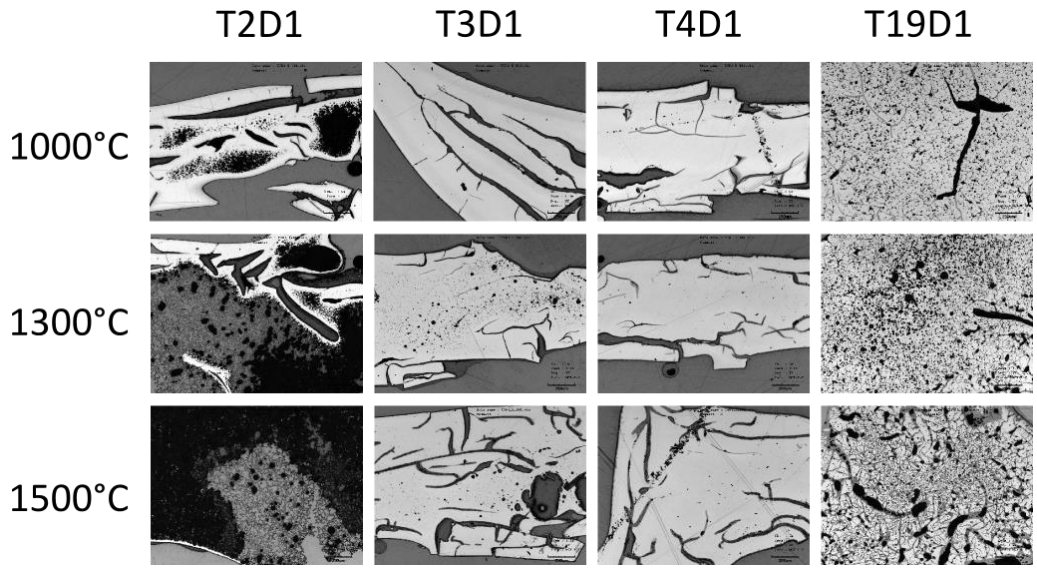

Figure 5.1 *Microstructure of pyrolyzed and annealed SiOC derived from various T/D ratios.*

5.3 COMPOSITES WITH MS AND MPS MATERIALS

In this work were mainly investigated partially pyrolyzed basalt reinforced composites. Basalt is a promising material, broadly available, which can be easily blown into a fibre, by simple melting of ingenious rock. The blowing process was first described by Dzhigiris [193]. Basalt fibre is often compared to E-glass, which is probably due to their similar chemical composition [149]. In contrast, the basalt fibre exhibits better mechanical properties and thermal stability than E-glass [149], also under the dynamic loading, as reported for the composite with epoxy resin-based matrix [194]. Properties of composites with basalt reinforcement depend also on reinforcement surface adjustment [195].

The investigation of basalt fibre composites in this work follows on the work of Černý et al. [111], in which mechanical properties of basalt reinforced composites with partially pyrolyzed MS and MPS matrices under the static loading were studied. The composites with MS matrix partially pyrolyzed at 650°C exhibited flexural strength on the level of 900 MPa and fracture toughness of 20 MPa·m$^{1/2}$. In comparison, under the dynamic loading they reached flexural strength of 431 MPa in flatwise and 328 MPa in edgewise orientation. The result was influenced by the inhomogeneity of the reinforcement, as the composite was manufactured by layering of the fibre roving. Specimens tested under dynamic loading in the edgewise orientation exhibited extensive delamination along the roving layers. Measuring the fracture toughness in the transversal direction confirmed that fibre-matrix bonding in these materials is on very low level (~0.3 MPa·m$^{1/2}$, maximum 0.6 MPa·m$^{1/2}$ in horizontal direction of the fracture toughness test).

Due to the potential of basalt fibres, mechanical behaviour of the woven fabrics was investigated in this work. Initially, apparent density evaluated from weight and dimensions of specimen was compared with the density of the composite calculated using the rule of mixture. The comparison was provided for pyrolysis states prepared at 600, 700 and 800°C, due to known density values of the materials used for matrices at these pyrolysis states. Apparent density of the composite with MS matrix pyrolyzed at 700 and 800°C was slightly higher than the value

calculated from the rule of mixture. Density of MPS-based composite was practically identical at the same pyrolysis states. At the pyrolysis temperature of 600°C, the measured density was lower in both composites. The differences may be caused by presence of pores in composites, which are not included in the rule of mixture. Nevertheless, porosity of the composites was calculated in [168] and according to that, the porosity is the lowest, i.e., the composites are most compact, when pyrolyzed at 700°C.

Note that the density of MS and MPS materials in the interval of pyrolysis temperatures 600–800°C is basically identical (see **Table A.1**), only at pyrolysis state of 800°C the MS material reaches density higher by ~0.1 $g \cdot cm^{-3}$ than the MPS material. In the composites with basalt fabric reinforcement the difference in the density of individual matrix types is hindered, because the density of the composite is affected by pores introduced with the fabric reinforcement. The apparent density (evaluated from mass and dimensions of the specimens) of the MS composite increases linearly with pyrolysis temperature up to 750°C and at 800°C it slightly decreases, which is associated with present pores. Comparison of the density of both the composite types, the density is less scattered with MPS matrix and between 700-800°C is negligibly lower (by 3 % in average) than the density of the composite with MS matrix. The biggest difference in the density of MSC and MPSC was observed at 700°C, where the density of MPSC was lower by ~5 %. The decrease of the MPSC density at 700°C is associated with higher porosity of the composite. The porosity of MS and MPS composites pyrolyzed in the temperature range of 600–800°C was reported in [168]. The porosity of the MPS composite influenced the elastic modulus, flexural strength and the impact strength (in both directions), as can be seen by comparison of the curves (**Figure 4.38**, **Figure 4.39** and **Figure 4.43 b)**). The increase of the elastic modulus of the fabric reinforced composite (**Figure 4.38**) is attributed to the matrix material, which elastic modulus increases from ~1 GPa to ~32 GPa for MS material and from ~7 GPa to ~32 GPa for MPS material in the interval of pyrolysis states from 600°C to 800°C (**Figure 4.15**). To remind, the elastic modulus of composites was estimated by flexural test, the elastic modulus of matrix materials was evaluated by instrumented indentation test.

Comparison of mechanical properties with respect to the reinforcement type can be accomplished on composites with MS matrix pyrolyzed at 650 and 750°C. The composite with the unidirectional reinforcement (1D) exhibited the elastic modulus of 65 and 75 GPa at pyrolysis state of 650 and 750°C, respectively. Composite with basalt woven fabric had the elastic modulus of only 29 GPa (~45 %) and 38 GPa (~51 %), after pyrolysis at 650 and 750°C, respectively. With respect to the reinforcement distribution and especially volume fraction, obtained result for fabric reinforced composite is still in a good agreement with unidirectionally reinforced composite. The elastic modulus of fabric reinforced composite was mainly affected by lower volume fraction of the reinforcement and higher porosity, comparing to the unidirectionaly reinforced MS composite. To remind, the unidirectionally reinforced MS composite with basalt fibres pyrolyzed at 650°C contained ~65 vol. % of fibres. The fabric reinforced MS composite pyrolyzed at 650°C contained only 43 vol. % of fabric reinforcement. Porosity of the MS composite pyrolyzed at 650°C in both fibre [111] and fabric [168] reinforced composites reached ~7 %. Reaching the same porosity with lower volume fraction of the reinforcement may be given by lower impregnation capability of the fabric reinforcement. At pyrolysis temperature of 750°C the porosity of fabric reinforced MS

composite decreased to ~5 % [168] whereas in the fibre reinforced composite pyrolyzed at 750°C even increased to ~9 % [111].

Drop of the flexural strength is even larger for fabric reinforced MS composite comparing to the fibre reinforced MS composite. From 900 MPa measured for unidirectionally reinforced composite (with MS matrix) pyrolyzed at 650°C the strength with using the woven fabrics dropped to 119 MPa (~13 %) and from 300 MPa (when pyrolyzed at 750°C) it dropped to 88 MPa (~29 %). The volume fraction of 43 vol. % in the fabric reinforced MS composite pyrolyzed at 650°C was lower by 33 %, comparing to the MS composite pyrolyzed at 650°C with 65 vol. % of unidirectional fibre reinforcement. The fabric was weaved as a plain structure, i.e., 50 % of fibres were in longitudinal direction and 50 % in transversal direction to the direction of composite loading. That makes only ~21.5 % (i.e., a half of the fibre volume fraction of 43 vol. %) of all fibres aligned in the longitudinal direction, which together with the porosity explains the low obtained values of the flexural strength for fabric reinforced composites.

Fracture toughness of the composite with MS matrix and the woven fabrics pyrolyzed at 650°C dropped from 20 $MPa \cdot m^{1/2}$ (for unidirectionally reinforced MS composite) to 9.5 $MPa \cdot m^{1/2}$ (47.5 %) for woven fabrics and at 750°C from 13 $MPa \cdot m^{1/2}$ (for unidirectionally reinforced MS composite) to 2 $MPa \cdot m^{1/2}$ (15.4 %) when using the woven fabrics. For the composites pyrolyzed at 650°C the values of the fracture toughness can be explained by the lower volume fraction and orientation of the reinforcement in the composite with fabric. The same explanation can be provided for the extensive decrease of the fracture toughness at 750°C, but the key role in the decrease of the fracture toughness can be played by upcoming degradation of fibres, which in the fabric reinforcement may resulted in formation of joints between the crossing fibres or even between the neighbouring layers.

The overall decrease in mechanical properties of composite with woven fabrics is understandable. In plain woven fabrics the fibres are more or less equally distributed in both directions (0° for longitudinal and 90° for transversal direction to the loading direction) [4]. Thus, the content of the fibres in fabric (plain-woven) reinforced composite in the longitudinal direction is lower by ~50 % (in comparison to unidirectionally reinforced composite of the same volume fraction). Moreover, the fabric has slightly worse impregnation capability and thus, higher porosity in the final composite. Additionaly, the decrease of the properties in fabric composites was higher comparing to unidirectional composites due to the fact that the volume fraction of the fabric reinforcement was only ~43 %, which is 21.5 % of the fibres in the longitudinal direction. On the contrary, contribution to the improvement of mechanical properties of fabric reinforcement can be performed by the interactions between crossing yarns [196].

Composites with basalt fabrics showed similar trends in static (flexural) and dynamic (impact) strength. The flexural strength was measured in the flatwise (in-plane) orientation [168], therefore the results for dynamic loading in the same orientation can be compared. MS matrix under dynamic loading reaches two times higher values of strength in comparison with static loading. At pyrolysis state of 800°C the impact strength is only ~20 % higher than under static loading. On the contrary, composite with MPS matrix reached in the dynamic test comparable (or only a little higher) values than in the static flexural test.

The failure of the fabric reinforced composites under static loading depends on the type of used matrix material. For the composite with MS matrix, both flexural strength and fracture toughness reached its maximum at pyrolysis state of 650°C (see **Figure 4.39** and **Figure 4.40**) and with increasing pyrolysis temperature (above 650°C) the properties decreased. Deterioration of the mechanical properties (flexural strength and fracture toughness) of the MS composite is associated with upcoming fibre degradation at temperature 700°C [111, 162, 197]. The MPS composite reached higher flexural strength than MSC in the whole temperature range. Except the pyrolysis temperature of 650°C, the fracture toughness was better as well. The most important finding is that the MPS composite showed more reliable mechanical response, i.e., the property values varied less with the pyrolysis temperature, even at the temperatures above 700°C, associated with earlier mentioned basalt fibre degradation. The basalt fibre degradation is clearly reflected in the flexural strength and fracture toughness of MPS composite pyrolyzed at 800°C.

The failure of the fabric reinforced composites under dynamic loading was dependent on the matrix material. The out-of-plane orientation possesses generally higher impact strength due to possible buckling mechanism of individual fabric layers in the composite [28]. The trends of fracture energy (see **Table A.16**) in both loading orientations were similar to the trends of fracture toughness under the static loading. Regardless the matrix material and specimen orientation (in-plane and out-of-plane) both MSC and MPSC reached the maximum fracture energy at the pyrolysis state of 650°C. The fracture energy was composed of elastic and damage part, where the damage part represented the toughening ability of the composite (see **Figure 4.45**). The toughening took place in composites pyrolyzed at the range of 600–700°C and at 750–800°C the toughening ability of the composites was supressed due to fibre deterioration, i.e., the composites failed in brittle manner.

Besides the contribution of the fibre degradation to the overall composites properties, the mechanical response of MS and MPS composites may be influenced by the matrix material as well. The composite properties correlates with MS and MPS weight loss and the chemical composition, i.e., molar rate of O/Si, both reported in [166]. The increase in the O/Si ratio occurs at the same pyrolysis temperature at which the decrease in both static and dynamic strength was observed. In the investigated temperature interval, the content of Si can be considered as constant (57 wt. % in MS, 47 wt. % in MPS) and the content of oxygen increases (see Table 1 in [168]). Also, due to the presence of phenyl units increases the amount of carbon in the structure and thus the MPS material contains double amount of carbon in form of free-carbon phases in comparison to MS material. The presence of free carbon phases may decrease the mechanical response of the material, as reported for polysiloxane-derived SiOC material pyrolyzed at 600°C and 800°C with excess of free carbon in [92].

5.4 COMPOSITE INTERFACE

The MS and MPS matrix materials shows specific interaction with basalt fibres, as can be seen in the work of Glogar et al. [197], where was reported the microstructure of basalt fibre reinforced composites with the same MS and MPS matrix as used in this work. The composites studied in [197] were pyrolyzed at 800°C (processing conditions were not closer defined in the article). On the one hand, the fibres in both the composites exhibited certain level of degradation –

visible structure roughening on the fibre cross-sections, indicating upcoming fibre crystallisation. This behaviour was observed already for composite prepared at pyrolysis state of 700°C [168].

The elemental composition of the fibre-matrix interface of MS matrix composites with basalt fibres pyrolyzed at 650 and 750°C was evaluated using point and line EDS analysis. The data of the chemical analysis was evaluated in atomic percent, to reflect the true atom-to-atom ratio. According to the point EDS analysis, the O/Si ratio in basalt fibre decreased from O/Si = 0.96 (calculated from producer´s data) to O/Si = 0.78 for basalt fibre pyrolyzed at 650°C and to O/Si = 0.62 when annealed at 550°C for 10 minutes (according to the scheme in **Figure 3.7**). Molar ratio O/Si of the MS material used for matrix prepared in the pyrolysis range of 600–800°C is 0.44. The data of the point EDS analysis for the MS material in the pyrolysis state of 650°C is not available but after annealing at 550°C the molar ratio was 0.56. In the interface of the composite pyrolyzed at 750°C was silicon- and oxygen-rich region (spectrum No. 32 in **Figure 4.63 b)**) in the distance up to 0.7 μm from the fibre surface towards the fibre centre. The line analysis toghether with the point EDS analysis indices transport of silicon from the matrix to the basalt fibres. In the composite pyrolyzed at 750°C and annealed at 550°C was observed slight gradient in element composition, which may support the hypothesis of the diffusion of elements over the fibre-matrix interface, which is a remark of strong chemical bonding between both composite components observed for this temperature.

The interface between partially pyrolyzed polysiloxane matrix with basalt reinforcement in the composites pyrolyzed in the temperature range of 600-700°C was rather weak. At higher temperatures (700–800°C) increased the composite strength and decreased fracture toughness, which can be associated with mechanical and chemical bonding at the composite interface. The mechanical bonding is induced by the matrix shrinkage and the chemical bonding between the reinforcement and matrix occurs due to element diffusion.

On the one hand, in literature [149, 159] the presence of silicon in both fibres (E-glass and Nextel™720) and the siloxane-based matrix was announced as a reason of strong interfacial bond in the composites. On the other hand, in the basalt reinforced MS matrix composite the basalt has very similar content of silicon and oxygen on its surface as in the MS matrix and yet the composite interface remained weakly bonded in the pyrolysis state of 600–700°C. In the literature [149] the presence of the iron in the fibre structure was understood as possible reason of the absence of strong interfacial bond at the fibre-matrix interface. Another reason may be the partial polymer character of the matrix, which was observed during fractographic analysis of fracture surfaces.

The composites with Nextel fibres and fully pyrolyzed SiOC matrix intended for high temperature applications showed deterioration of mechanical properties when annealed above 1200°C. By the analysis of the composite interface was found significant grain growth of the fibres and formation of silicon-rich layer, strongly bonding both fibre and matrix together, which inhibited the toughening mechanisms of the composite, i.e., delamination at the fibre-matrix interface, crack bridging and fibre pull-out. However the formation of mullite surface layer protects the fibre and keep the surface region from coarsening of the microstructure. Together with formation of microcrack in the vicinity of the fibre-matrix interface the mechanical properties were

not significantly affected up to the temperature of 1500°C. In this particular case high temperature damage led to toughening even when the interfacial bond strengthened.

6 CONCLUSIONS

The presented work describes the evolution of properties of the polysiloxane-derived materials predetermined as a matrix in composites on the chemical and processing parameters. The reinforcement in the form of long fibres or fabrics was infiltrated with selected polysiloxane resin to form composites, in which the fibre-matrix interfaces were evaluated. The properties of the created interface changed accordingly to the pyrolysis temperature, used fibres and polymeric precursors. It was found that the character of the matrix influences the interaction with the reinforcement, in a result, the mechanical behaviour of the composite can be optimised. The main findings from the investigation can be summarised as follows.

The materials based on commercial as well as laboratory prepared precursors were investigated under various processing conditions, namely pyrolysis temperature, dwell time and heating rate, and the dependences of density, elastic modulus and hardness were determined. The main finding in this group of materials is the observed viscoelastic behaviour of materials made of commercial precursors MS and MPS pyrolyzed at temperatures 520°C and 650°C, respectively. The laboratory synthesized polymeric precursors modified by nitrogen, boride or iron were found not suitable for application in the composites. The reason was their problematic storage, significant porosity and tendency to form microcracking network, due to extensive shrinkage. Based on the results, only MS and MPS precursors were further used in the composites.

The fibre-matrix interface as governing parameter predetermining behaviour of the composite was investigated. The modification of the interface behaviour through the selection of matrix material and its processing parameters was the main goal of the work. The proven ability to tune the properties of the composite through the modification of matrix materials only can be identified as the main result of the work. Except this ability many others achievements were reached.

In the case of composites with a partially pyrolyzed polysiloxane matrix reinforced by basalt fibres was the interface rather weak when the pyrolysis temperature range from 400°C to 600°C due to the formation of mainly adhesive bonding. The pyrolysis temperature of the composite below 600°C led to the easy delamination along the fibre-matrix interface resulting in its low strength. At higher temperatures above 700°C the matrix material shrinkage led to the additional strong mechanical bonding accompanied by chemical bonding at the fibre-matrix interface. The chemical bonding increased with the increasing pyrolysis temperature as well as with application of additional heat treatment. This was caused by diffusion processes leading to suppression of the toughening mechanisms. The optimal interface behaviour was confirmed for the processing temperature of partially pyrolyzed polysiloxane matrix composites reinforced by basalt fibres between 650–700°C. The processing window is relatively small because the onset of mechanical and chemical bonding is rapid. Additionally, above the temperature of 700°C the basalt fibres start to crystallize, which deteriorates their mechanical properties, thus, the toughening mechanisms in the composite are limited. Also, as was shown, the brittleness of partially pyrolyzed matrix above 700°C increases rapidly. At pyrolysis temperature of 650°C and 700°C (depending on the starting material) the composite showed the best mechanical properties, regardless the reinforcement shape (unidirectional fibres or fabrics) or the speed of loading (static

vs dynamic). The advantage of combination of basalt fibres with polysiloxane-based matrix is that the composite is processed at relatively low temperature (~650°C) providing superior mechanical properties. The detailed investigation of the fibre-matrix interface of the composites prepared at the pyrolysis temperature of 650°C, and 750°C by TEM revealed the activity of diffusional processes and at higher pyrolysis temperature formation of crystalline phase within the fibre was observed. The iron crystals were identified as the new phase and they were always found in the given distance of approximately 0.001 mm from the interface. This finding changes the published identification of the crystalline phase from forsterite to pure ferrite.

The second type of composite with fully pyrolyzed polysiloxane-based matrix and polycrystalline Nextel™720 fibres were processed at pyrolysis temperature of 1100°C. The polymer-derived matrix was fully transformed into amorphous SiOC glass and thermal stability was analysed. Despite of an excellent high temperature resistance of SiOC glass, the long term application temperature of such composites should not exceed 1200°C, because of observed microstructural changes like grain coarsening in the fibre, which in combination with present matrix shrinkage could lead to inhibition of the toughening mechanisms. On the other hand, the resulting properties of the composite remain comparable up to the short term exposition at 1500°C for 3 h, where severe microstructural changes were found. Main effect was the grain coarsening reaching the ratio of 10 compared with the as pyrolyzed state. There was also observed a diffusional exchange of atoms between matrix and fibres enhancing the interfacial chemical bonding and also influencing the formation of mullite layer in the alumina fibre surface region. Although the interface was stronger the toughening mechanism were acting similarly to unaffected composite. The reason of this fact can be ascribed to the formation of microcracks network in the matrix in the vicinity of the fibre-matrix interface. This microcrack network is formed as a thermally activated damage due to increased residual stresses in the matrix and fibre, given by a mismatch of coefficient of thermal expansion (CTE) between them, accompanied with volume changes due to the microstructural changes in the surface layer of fibre. In fact, the formation of the microcrack network compensates the strengthening effect of interface bond by above described mechanisms finally resulting in the similar properties, mainly fracture toughness and strength.

Finally can be concluded that all objectives of the work were successfully achieved and the feasibility of the way to control the fibre-matrix interface behaviour through the modification of matrix materials was demonstrated.

LIST OF FIGURES

LIST OF TABLES

LIST OF TERMS AND ACRONYMS GLOSSARY

ABS ..... acrylonitrile butadiene styrene (thermoset polymer)

a.s. ..... czech abbreviation for 'public limited company'

BFRC ..... Basalt Fibre Reinforced Composite

Blade rate ..... rotation of the cutting wheel (unit: revolutions per minute, abbreviated as rpm)

CMC ..... Ceramic Matrix Composite

Cross-head speed ..... loading rate (unit: millimetres/micrometres per minute, $mm \cdot min^{-1}$)

Feed rate ..... relative velocity at which the cutter is advanced along the specimen

EDS ..... Electron Dispersive Spectroscopy

FAST ..... Field-Activated Sintering Technique

FRC ..... Fibre-reinforced Composite

FRPC ..... Fibre-reinforced Polymer Composite

HP ..... Hot Pressing

HPPE ..... High-Performance Polyethylene, also abbreviated as UHMW or UHMWPE

MMC ..... Metal Matrix Composite

MS ..... methylsiloxane

MSC ..... composite based on methylsiloxane-derived matrix

MPS ..... methylphenylsiloxane

MPSC ..... composite based on methylsiloxane-derived matrix

NDT ..... non-destructive testing

Oligomer ..... molecule composed of 2 to 10 monomeric units, which can change its physical and chemical properties dependently on the number of constitutional units

PIP ..... Polymer infiltration (impregnation) and pyrolysis

PMC ..... Polymer Matrix Composite

PMMA ..... polymethylmethacrylate

PC ..... polycarbonate

PP ..... polypropylene

PS ..... polystyrene

Roving .....A loose assemblage of filaments in single strand, with very little twist. Also known as strand or tow [172]

SPS.....Spark Plasma Sintering

T_g.....glass transition temperature

T_m.....melting temperature

REFERENCES

1. Chawla, K.K., *Composite Materials: Science and Engineering*. Third edition ed. 2012: Springer Science +Business Media New York 2012.
2. Mallick, P.K., *Fiber-reinforced composites: materials, manufacturing, and design*. 2007: CRC press.
3. Harris, B., *Engineering composite materials*. 1986: Institute of metals London.
4. Mazumdar, S., *Composites Manufacturing: Materials, Product, and Process Engineering*. 2001: CrC press. 416.
5. Heymann, H., E.J. Swift, and A. Ritter, *Sturdevant's Art and Science of Operative Dentistry*. 6th ed. 2012: Mosby. 568.
6. Greil, P., *Active-Filler-Controlled Pyrolysis of Preceramic Polymers.* Journal of the American Ceramic Society, 1995. **78**(4): p. 835-848.
7. Rothon, R., *Particulate-filled polymer composites*. 2003: iSmithers Rapra Publishing.
8. Hull, T.R., A. Witkowski, and L. Hollingbery, *Fire retardant action of mineral fillers.* Polymer Degradation and Stability, 2011. **96**(8): p. 1462-1469.
9. Park, S.-J. and M.-K. Seo, *Interface Science and Composites*, ed. A. Hubbard. Vol. 18. 2011: Academic Press. 852.
10. Bansal, N.P., ed. *Handbook of Ceramic Composites*. 2005, Kluwer Academic Publishers.
11. Voss, H. and K. Friedrich, *Influence of short-fibre reinforcement on the fracture behaviour of a bulk liquid crystal polymer.* Journal of materials science, 1986. **21**(8): p. 2889-2900.
12. Nakao, W. and L. Nicolais, *Ceramic Matrix Composites: SiC Whisker–Reinforced*, in *Wiley Encyclopedia of Composites*. 2011, John Wiley & Sons, Inc.
13. Yasmin, A. and I.M. Daniel, *Mechanical and thermal properties of graphite platelet/epoxy composites.* Polymer, 2004. **45**(24): p. 8211-8219.
14. Boccaccini, A. and P. Trusty, *Toughening and strengthening of glass by Al2O3 platelets.* Journal of materials science letters, 1996. **15**(1): p. 60-63.
15. Kotoul, M., et al., *Toughening effects quantification in glass matrix composite reinforced by alumina platelets.* Acta Materialia, 2008. **56**(12): p. 2908-2918.
16. Tu, W.C., F.F. Lange, and A.G. Evans, *Concept for a Damage-Tolerant Ceramic Composite with "Strong" Interfaces.* Journal of the American Ceramic Society, 1996. **79**(2): p. 417-424.
17. Bagherpour, S., *Fibre reinforced polyester composites.* Edited by Hosam El-Din M. Saleh, 2012: p. 167.
18. Meissner, B. and V. Zilvar, *Fyzika polymerů. Struktura a vlastnosti polymerních materiálů*. 1987: Státní nakladatelství technické literatury.
19. Campbell, F.C., *Structural composite materials*. 2010: ASM international.
20. *3M™ Nextel™ Structural Roving 720*. [cited 2017 23.5.]; Available from: http://www.3m.com/3M/en_US/company-us/all-3m-products/~/3M-Nextel-Structural-Roving-720?N=5002385+8710650+3292678614&rt=rud.
21. Zoltek™. *Prepreg*. Available from: http://zoltek.com/products/panex-35/prepreg/.
22. *The Headset press. Craddock cycles handmade custom carbon.* [cited 2017 23.5.]; Available from: http://www.headsetpress.co.uk/craddock-cycles-handmade-custom-carbon/.
23. *Castro composites. Fibras de refuerzo*. [cited 2017 23.5.]; Available from: https://www.castrocompositesshop.com/es/6-fibras-de-refuerzo.
24. Feih, S., et al., *Tensile Strength Modeling of Glass Fiber—Polymer Composites in Fire.* Journal of Composite Materials, 2007. **41**(19): p. 2387-2410.
25. Olabisi, O. and K. Adewale, *Handbook of thermoplastics*. Vol. 41. 2016: CRC press.

26. Dodiuk, H. and S.H. Goodman, *Handbook of thermoset plastics*. 2013: William Andrew. 800.
27. Kinloch, A.J. and R.J. Young, *Fracture Behaviour of Polymers*. 1995: Springer Netherlands.
28. Anderson, T.L. and T.L. Anderson, *Fracture mechanics: fundamentals and applications*. 2005: CRC press.
29. Lewandowski, J. and A. Greer, *Temperature rise at shear bands in metallic glasses.* Nature materials, 2006. **5**(1): p. 15-18.
30. Greil, P., *Polymer Derived Engineering Ceramics.* Advanced Engineering Materials, 2000. **2**(6): p. 339-348.
31. Davidge, R.W., *Mechanical behaviour of ceramics*. 1979: Cambridge University Press.
32. Colombo, P.R., Ralf, G.D. Soraru, and H.-J. Kleebe, eds. *Polymer Derived Ceramics From Nano-Structure to Applications* 2009, DEStech Publications, Inc.
33. Mehrotra, P.K. and R.D. Nixon, *Silicon nitride ceramic and cutting tool made thereof*. 1996, Google Patents.
34. Buljan, S.T. and S.F. Wayne, *Wear and design of ceramic cutting tool materials.* Wear, 1989. **133**(2): p. 309-321.
35. Danon, A. and A. Amirav, *Ceramic nozzle for molecular acceleration and its temperature measurement.* Review of scientific instruments, 1987. **58**(9): p. 1724-1726.
36. Carter, B.C. and G.M. Norton, *Ceramic Materials: Science and Engineering*. 2007, New York: Springer Science+Business media.
37. Johnston, R.D., R.D. Chipman, and W.J. Knapp, *Prestressed Ceramics as a Structural Material*. Journal of the American Ceramic Society, 1953. **36**(4): p. 121-126.
38. Hull, D., *Fractography: observing, measuring and interpreting fracture surface topography*. 1999: Cambridge University Press.
39. Flores, O., et al., *Ceramic Fibers Based on SiC and SiCN Systems: Current Research, Development, and Commercial Status.* Advanced Engineering Materials, 2014. **16**(6): p. 621-636.
40. Mecholsky, J.J., R.W. Rice, and S.W. Freiman, *Prediction of Fracture Energy and Flaw Size in Glasses from Measurements of Mirror Size.* Journal of the American Ceramic Society, 1974. **57**(10): p. 440-443.
41. Motz, G., S. Schmidt, and S. Beyer, *The PIP-Process: Precursor Properties and Applications*, in *Ceramic Matrix Composites*. 2008, Wiley-VCH Verlag GmbH & Co. KGaA. p. 165-186.
42. Bansal, N.P. and A.R. Boccaccini, *Ceramics and composites processing methods*. 2012: John Wiley & Sons.
43. Sumio, S., ed. *Handbook of Sol-Gel Science and Technology*. Vol. Volume I: Sol-gel processing. 2004, Kluwer Academic Publishers.
44. Brus, J. and P. Kotlík, *Sol-gel polykondenzace alkoxysilanů, struktura a vlastnosti siloxanových materiálů.* Chemické listy, 1998. **92**: p. 302-311.
45. Wali, N. and J.M. Yang, *Reactive Melt-Infiltration Processing of Fiber-Reinforced Ceramic Matrix Composites*, in *Ceramics and Composites Processing Methods*. 2012, John Wiley & Sons, Inc. p. 351-390.
46. Einset, E.O., *Analysis of reactive melt infiltration in the processing of ceramics and ceramic composites.* Chemical Engineering Science, 1998. **53**(5): p. 1027-1039.
47. Kopeliovich, D., *5 - Advances in the manufacture of ceramic matrix composites using infiltration techniques A2 - Low, I.M*, in *Advances in Ceramic Matrix Composites*. 2014, Woodhead Publishing. p. 79-108.

48. Gern, F.H. and R. Kochendörfer, *Liquid silicon infiltration: description of infiltration dynamics and silicon carbide formation.* Composites Part A: Applied Science and Manufacturing, 1997. **28**(4): p. 355-364.
49. Naslain, R.R., *The design of the fibre-matrix interfacial zone in ceramic matrix composites.* Composites Part A: Applied Science and Manufacturing, 1998. **29**(9–10): p. 1145-1155.
50. Lackey, W.J., *Review, Status, and Future of the Chemical Vapor Infiltration Process for Fabrication of Fiber-Reinforced Ceramic Composites*, in *A Collection of Papers Presented at the 13th Annual Conference on Composites and Advanced Ceramic Materials: Ceramic Engineering and Science Proceedings*. 1989, John Wiley & Sons, Inc. p. 577-584.
51. Caputo, A. and W. Lackey, *Fabrication of fiber reinforced ceramic composites by chemical vapor infiltration.* 1984.
52. Boccaccini, A.R., et al., *Electrophoretic deposition of carbon nanotubes.* Carbon, 2006. **44**(15): p. 3149-3160.
53. Low, I.M., ed. *Ceramic Matrix Composites: Microstructure, properties and applications*. 2006, Woodhead Publishing Limited: Cambridge England. 633.
54. De Riccardis, M.F., *Ceramic coatings obtained by electrophoretic deposition: fundamentals, models, post-deposition processes and applications*. 2012: INTECH Open Access Publisher.
55. Vogt, U.F., et al., *Improving the properties of ceramic foams by a vacuum infiltration process.* Journal of the European Ceramic Society, 2010. **30**(15): p. 3005-3011.
56. Decottignies, M., J. Phalippou, and J. Zarzycki, *Synthesis of glasses by hot-pressing of gels.* Journal of Materials Science, 1978. **13**(12): p. 2605-2618.
57. Lange, F., *Hot-pressing behaviour of silicon carbide powders with additions of aluminium oxide.* Journal of Materials Science, 1975. **10**(2): p. 314-320.
58. Wei, B., H. Cao, and S. Song, *Degradation of basalt fibre and glass fibre/epoxy resin composites in seawater.* Corrosion Science, 2011. **53**(1): p. 426-431.
59. Grasso, S., et al., *Joining of β-SiC by spark plasma sintering.* Journal of the European Ceramic Society, 2014. **34**(7): p. 1681-1686.
60. Ritchie, R.O., *The conflicts between strength and toughness.* Nat Mater, 2011. **10**(11): p. 817-822.
61. DiCarlo, J.A. and S. Dutta, *Continuous ceramic fibers for ceramic matrix composites.* 1995.
62. Johnson, D., et al., *Ceramic fibers and coatings: advanced materials for the twenty-first century.* Publication NMAB-494, 1998: p. 20-36.
63. Saruhan, B., *Oxide-based Fiber-reinforced Ceramic-matrix Composites: Principles and Materials*. 2003: Springer Science & Business Media.
64. Evans, A.G., *Perspective on the Development of High-Toughness Ceramics.* Journal of the American Ceramic Society, 1990. **73**(2): p. 187-206.
65. Mukerji, J., *Ceramic Matrix Composites.* Defence Science Journal, 1993. **43**(4): p. 385.
66. Evans, A. and F. Zok, *The physics and mechanics of fibre-reinforced brittle matrix composites.* Journal of Materials Science, 1994. **29**(15): p. 3857-3896.
67. Cazzato, A., et al., *Monazite Interface Coatings in Polymer and Sol-Gel Derived Ceramic Matrix Composites*, in *Proceedings of the 21st Annual Conference on Composites, Advanced Ceramics, Materials, and Structures—A: Ceramic Engineering and Science Proceedings*. 1997, John Wiley & Sons, Inc. p. 267-277.
68. Rice, R.W., *BN coating of ceramic fibers for ceramic fiber composites*. 1987, Google Patents.
69. Hutchinson, J.W., *Mechanisms of toughening in ceramics.* Theoretical and applied mechanics, 1989: p. 139-144.

70. Kim, J.-K. and Y.-W. Mai, *Engineered interfaces in fiber reinforced composites*. 1998: Elsevier.
71. Lewis, M.H., et al., *Oxide CMCs: interphase synthesis and novel fibre development.* Journal of the European Ceramic Society, 2000. **20**(5): p. 639-644.
72. Naslain, R., *Fibre-matrix interphases and interfaces in ceramic matrix composites processed by CVI.* Composite Interfaces, 1993. **1**(3): p. 253-286.
73. Tressler, R.E., *Recent developments in fibers and interphases for high temperature ceramic matrix composites.* Composites Part A: Applied Science and Manufacturing, 1999. **30**(4): p. 429-437.
74. Callister, W.D. and D.G. Rethwisch, *Materials science and engineering: an introduction*. Vol. 7. 2007: Wiley New York.
75. Basu, B. and K. Balani, *Advanced structural ceramics*. 2011: John Wiley & Sons.
76. Saheb, D.N. and J. Jog, *Natural fiber polymer composites: a review.* Advances in polymer technology, 1999. **18**(4): p. 351-363.
77. Kott, A. and T. Vogel, *Structural behaviour of broken laminated safety glass.* Proc., Glass in Buildings, 2005. **2**.
78. Weaver, J.H., J. Yang, and F.W. Zok, *Control of Interface Properties in Oxide Composites Via Fugitive Coatings.* Journal of the American Ceramic Society, 2008. **91**(12): p. 4003-4008.
79. Volkmann, E., et al., *Oxidation-induced microstructural changes of a polymer-derived Nextel™ 610 ceramic composite and impact on the mechanical performance.* Journal of Materials Science, 2014. **49**(2): p. 710-719.
80. Hunston, D.L. and R. Dehl, *The role of polymer toughness in matrix dominated composite fracture*. 1987: Society of Manufacturing Engineers.
81. Hutchinson, J.W., *Crack tip shielding by micro-cracking in brittle solids.* Acta Metallurgica, 1987. **35**(7): p. 1605-1619.
82. Ming-Yuan, H. and J.W. Hutchinson, *Crack deflection at an interface between dissimilar elastic materials.* International Journal of Solids and Structures, 1989. **25**(9): p. 1053-1067.
83. Ionescu, E., et al., *High-Temperature Creep Behavior of SiOC Glass-Ceramics: Influence of Network Carbon Versus Segregated Carbon.* Journal of the American Ceramic Society, 2014. **97**(12): p. 3935-3942.
84. Colombo, P., et al., *Polymer-Derived Ceramics: 40 Years of Research and Innovation in Advanced Ceramics.* Journal of the American Ceramic Society, 2010. **93**(7): p. 1805-1837.
85. Sorarù, G.D., et al., *Structural Characterization and High-Temperature Behavior of Silicon Oxycarbide Glasses Prepared from Sol-Gel Precursors Containing Si-H Bonds.* Journal of the American Ceramic Society, 1995. **78**(2): p. 379-387.
86. Kleebe, H. and Y. Blum, *SiOC ceramic with high excess free carbon.* Journal of the European Ceramic Society, 2008. **28**(5): p. 1037-1042.
87. Mera, G., et al., *Polymer-derived SiCN and SiOC ceramics–structure and energetics at the nanoscale.* Journal of Materials Chemistry A, 2013. **1**(12): p. 3826-3836.
88. Renlund, G.M., S. Prochazka, and R.H. Doremus, *Silicon Oxycarbide Glasses .2. Structure and Properties.* Journal of Materials Research, 1991. **6**(12): p. 2723-2734.
89. Renlund, G.M., S. Prochazka, and R.H. Doremus, *Silicon Oxycarbide Glasses .1. Preparation and Chemistry.* Journal of Materials Research, 1991. **6**(12): p. 2716-2722.
90. Hasegawa, Y., M. Iimura, and S. Yajima, *Synthesis of continuous silicon carbide fibre.* Journal of Materials Science, 1980. **15**(3): p. 720-728.
91. Sorarù, G.D., E. Dallapiccola, and G. D'Andrea, *Mechanical Characterization of Sol–Gel-Derived Silicon Oxycarbide Glasses.* Journal of the American Ceramic Society, 1996. **79**(8): p. 2074-2080.

92. Walter, S., et al., *Microstructural and mechanical characterization of sol gel-derived Si–O–C glasses.* Journal of the European Ceramic Society, 2002. **22**(13): p. 2389-2400.
93. Halasova, M., et al., *Mechanical response of novel SiOC glasses to high temperature exposition.* Journal of the European Ceramic Society, 2012. **32**(16): p. 4489-4495.
94. Sorarù, G. and D. Suttor, *High Temperature Stability of Sol-Gel-Derived SiOC Glasses.* Journal of Sol-Gel Science and Technology, 1999. **14**(1): p. 69-74.
95. Brequel, H., et al., *Study of the phase separation in amorphous silicon oxycarbide glasses under heat treatment.* Nanostructured Materials, 1999. **11**(6): p. 721-731.
96. Strachota, A., et al., *Optimization of sol–gel/pyrolysis routes to silicon oxycarbide glasses.* Journal of Non-Crystalline Solids, 2012. **358**(20): p. 2771-2782.
97. Jones, R.G., W. Ando, and J. Chojnowski, *Silicon-containing polymers: the science and technology of their synthesis and applications*. 2001: Springer Science & Business Media. 768.
98. Corriu, R., et al., *Preparation and structure of silicon oxycarbide glasses derived from polysiloxane precursors.* Journal of Sol-Gel Science and Technology, 1997. **8**(1-3): p. 327-330.
99. Harshe, R., C. Balan, and R. Riedel, *Amorphous Si(Al)OC ceramic from polysiloxanes: bulk ceramic processing, crystallization behavior and applications.* Journal of the European Ceramic Society, 2004. **24**(12): p. 3471-3482.
100. Ionescu, E., et al., *Thermodynamic Control of Phase Composition and Crystallization of Metal-Modified Silicon Oxycarbides.* Journal of the American Ceramic Society, 2013. **96**(6): p. 1899-1903.
101. Pena-Alonso, R., et al., *New insights on the high-temperature nanostructure evolution of SiOC and B-doped SiBOC polymer-derived glasses.* Chemistry of Materials, 2007. **19**(23): p. 5694-5702.
102. Suttor, D., et al., *Fiber-Reinforced Ceramic-Matrix Composites with a Polysiloxane/Boron-Derived Matrix.* Journal of the American Ceramic Society, 1997. **80**(7): p. 1831-1840.
103. Majidian, H., et al., *Phase Evolution, Microstructure, and Mechanical Properties of Alumina–Mullite–Zirconia Composites Prepared by Iranian Andalusite.* International Journal of Applied Ceramic Technology, 2016. **13**(6): p. 1024-1032.
104. Rouxel, T., et al., *Surface Damage Resistance of Gel-Derived Oxycarbide Glasses: Hardness, Toughness, and Scratchability.* Journal of the American Ceramic Society, 2001. **84**(10): p. 2220-2224.
105. Gonczy, S.T. and J.G. Sikonia, *Nextel™ 312/Silicon Oxycarbide Ceramic Composites*, in *Handbook of Ceramic Composites*, N.P. Bansal, Editor. 2005, Springer US: Boston, MA. p. 347-373.
106. Marshall, D.B. and J.B. Davis, *Ceramics for future power generation technology: fiber reinforced oxide composites.* Current Opinion in Solid State and Materials Science, 2001. **5**(4): p. 289.
107. Volkmann, E., et al., *Influence of heat treatment and fiber orientation on the damage threshold and the fracture behavior of Nextel fiber-reinforced Mullite-SiOC matrix composites analysed by acoustic emission monitoring.* Journal of Materials Science, 2014. **49**(22): p. 7890-7899.
108. Esfehanian, M., et al., *Development of Dense Filler-Free Polymer-Derived SiOC Ceramics by Field-Assisted Sintering.* Journal of the American Ceramic Society, 2008. **91**(11): p. 3803-3805.
109. Ionescu, E. and R. Riedel, *Polymer Processing of Ceramics*, in *Ceramics and Composites Processing Methods*. 2012, John Wiley & Sons, Inc. p. 235-270.

110. Liu, X., Y.-L. Li, and F. Hou, *Fabrication of SiOC Ceramic Microparts and Patterned Structures from Polysiloxanes via Liquid Cast and Pyrolysis.* Journal of the American Ceramic Society, 2009. **92**(1): p. 49-53.
111. Černý, M., et al., *Partially pyrolyzed composites with basalt fibres - Mechanical properties at laboratory and elevated temperatures.* Composites Part A - Applied Science and Manufacturing, 2009. **40**(10): p. 1650-1659.
112. Brus, J., et al., *Structure of silicon oxycarbide glasses derived from poly (methylsiloxane) and poly [methyl (phenyl) siloxane] precursors.* Journal of non-crystalline solids, 2001. **289**(1): p. 62-74.
113. Brewer, C., et al., *Insights into the oxidation chemistry of SiOC ceramics derived from silsesquioxanes.* Journal of Sol-Gel Science and Technology, 1999. **14**(1): p. 49-68.
114. Hurwitz, F.I., et al., *Characterization of the pyrolytic conversion of polysilsesquioxanes to silicon oxycarbides.* Journal of Materials Science, 1993. **28**(24): p. 6622-6630.
115. Sorarù, G.D., et al., *On the shrinkage during pyrolysis of thin films and bulk components: The case of a hybrid silica gel precursor for SiOC glasses.* Journal of the European Ceramic Society, 2012. **32**(3): p. 627-632.
116. Wu, J., et al., *Simple fabrication of micro/nano-porous SiOC foam from polysiloxane.* Journal of Materials Chemistry, 2012. **22**(14): p. 6542-6545.
117. Rouxel, T., G. Massouras, and G.-D. Sorarù, *High Temperature Behavior of a Gel-Derived SiOC Glass: Elasticity and Viscosity.* Journal of Sol-Gel Science and Technology, 1999. **14**(1): p. 87-94.
118. Kamiya, K., *Oxycarbide Glasses and Carbides*, in *Handbook of Sol-Gel Science and Technology*, S. Sakka, Editor. 2005, Kluwer Academic Publisher: New York. p. 185-201.
119. Chlup, Z., et al., *Properties of modified polysiloxane based ceramic matrix for long fibre reinforced composite materials.* Plastics, Rubber and Composites, 2011. **40**(6-7): p. 380-385(6).
120. Moysan, C., et al., *Mechanical characterization of a polysiloxane-derived SiOC glass.* Journal of the European Ceramic Society, 2007. **27**(1): p. 397-403.
121. Eom, J.-H. and Y.-W. Kim, *Flexural Strength of Polysiloxane-Derived Strontium-Doped SiOC Ceramics.* Journal of the Korean Ceramic Society, 2015. **52**(1): p. 61-65.
122. Narisawa, M., *Silicone resin applications for ceramic precursors and composites.* Materials, 2010. **3**(6): p. 3518-3536.
123. Haußmann, M., et al., *Thermal degradation of polymethylsilsesquioxane and microstructure of the derived glasses.* Journal of Analytical and Applied Pyrolysis, 2011. **91**(1): p. 224-231.
124. Bargain, M. and M. Lefort, *Polysiloxane thermoplastic elastomers*. 1979, Google Patents.
125. Takegami, R., *Polymer sheet, back protective sheet for solar cell, and solar cell module*. 2014, Google Patents.
126. Mark, J.E., *Some interesting things about polysiloxanes.* Accounts of chemical research, 2004. **37**(12): p. 946-953.
127. Furukawa, N., et al., *Synthesis and properties of novel thermosetting polysiloxane-block-polyimides with vinyl functionality.* Polymer, 1998. **39**(13): p. 2941-2949.
128. Martínez-Crespiera, S., et al., *Pressureless synthesis of fully dense and crack-free SiOC bulk ceramics via photo-crosslinking and pyrolysis of a polysiloxane.* Journal of the European Ceramic Society, 2011. **31**(5): p. 913-919.
129. Chlup, Z., et al., *Influence of pyrolysis temperature on fracture response in SiOC based composites reinforced by basalt woven fabric.* Journal of the European Ceramic Society, 2014. **34**(14): p. 3389-3398.
130. Porte, L. and A. Sartre, *Evidence for a silicon oxycarbide phase in the Nicalon silicon carbide fibre.* Journal of Materials Science, 1989. **24**(1): p. 271-275.

131. Le Coustumer, P., M. Monthioux, and A. Oberlin, *Understanding Nicalon® Fibre.* Journal of the European Ceramic Society, 1993. **11**(2): p. 95-103.
132. *Tyranno fiber*. [cited 2017 23.5.]; Available from: http://www.ube-ind.co.jp/english/products/chemical/chemical_19.htm.
133. Berger, M. and A. Bunsell, *Fine Ceramic Fibers*. 1999: CRC Press.
134. Murthy, V.S.R., et al., *Structure and degradation of tyranno fibres.* Materials Letters, 1989. **8**(8): p. 263-268.
135. Bunsell, A.R. and M.H. Berger, *Fine diameter ceramic fibres.* Journal of the European Ceramic Society, 2000. **20**(13): p. 2249-2260.
136. Rice, J.A., C.S. Hazelton, and P.E. Fabian, *Ceramic electrical insulation of electrical coils, transformers, and magnets*. 2002.
137. Honeywell. *Our history*. [cited 2017 23.5.]; Available from: http://www.honeywell.com/who-we-are/our-history.
138. Trademarkia. *Northrop Grumman Systems Corporation Trademarks*. [cited 2017 23.5.]; Available from: http://trademarkia-notices.com/company-northrop-grumman-systems-corporation-882150-page-5-2.
139. *Composites world. Lancer Systems acquires CeraComp technology from Greene, Tweed*. [cited 2017 23.5.]; Available from: http://www.compositesworld.com/news/lancer-systems-acquires-ceracomp-technology-from-greene-tweed.
140. Gerendás, M., et al. *Improvement of oxide/oxide CMC and development of combustor and turbine components in the HIPOC program*. in *ASME 2011 Turbo Expo: Turbine Technical Conference and Exposition*. 2011. American Society of Mechanical Engineers.
141. Singh, D., J. Salem, and S. Widjaja, *Mechanical Properties and Performance of Engineering Ceramics and Composites VI: Ceramic Engineering and Science Proceedings, Volume 32*. 2011: John Wiley & Sons.
142. Ishikawa, T., *Special Issue Advances in Inorganic Fibre TechnologyRecent developments of the SiC fiber Nicalon and its composites, including properties of the SiC fiber Hi-Nicalon for ultra-high temperature.* Composites Science and Technology, 1994. **51**(2): p. 135-144.
143. Xia, K.-d., C.-x. Lu, and Y. Yang, *Improving the oxidation resistance of carbon fibers using silicon oxycarbide coatings.* Carbon, 2015. **93**: p. 1086.
144. Manocha, L., et al., *Morphological Studies on CNT Reinforced SiC/SiOC Composites.* Eurasian Chemico-Technological Journal, 2010. **13**(1-2): p. 41-47.
145. Lee, D.B. and D.J. Kim, *Oxidation of SiOC/MoSi2/SiC composites prepared by polymer pyrolysis.* Oxidation of metals, 2004. **61**(5-6): p. 423-437.
146. Gumula, T. and S. Blazewicz, *Thermal conversion of carbon fibres/polysiloxane composites to carbon fibres/ceramic composites.* Ceramics International, 2013. **39**(4): p. 3795-3802.
147. Colombo, P., *Polymer derived ceramics: from nano-structure to applications*. 2010: DEStech Publications, Inc.
148. *Business wire. Starfire's Composite Motorcycle Brakes Excel on Test Track*. 2005 [cited 2017 23.5.]; Available from: http://www.businesswire.com/news/home/20050110005093/en/Starfires-Composite-Motorcycle-Brakes-Excel-Test-Track.
149. Černý, M., et al., *Influence of the Organic/Inorganic Pyrolysis Conversion Level on Mechanical Properties of Composites with E-Glass or Basalt Fibre Reinforcement.* Ceramics-Silikaty, 2010. **54**(4): p. 345-351.
150. Černý, M., et al., *SiOC ceramic foams derived from polymethylphenylsiloxane precursor with starch as foaming agent.* Journal of the European Ceramic Society, 2015. **35**(13): p. 3427-3436.

151. Duan, W., et al., *Synthesis and microwave absorption properties of SiC nanowires reinforced SiOC ceramic.* Journal of the European Ceramic Society, 2014. **34**(2): p. 257-266.
152. Strachota, A., et al., *Preparation of finely macroporous SiOC foams with High mechanical properties and with hierarchical porosity via pyrolysis of a siloxane/epoxide composite.* Ceramics International, 2015(0).
153. Colombo, P. and E. Bernardo, *Macro- and micro-cellular porous ceramics from preceramic polymers.* Composites Science and Technology, 2003. **63**(16): p. 2353-2359.
154. Tian, H. and Q.-s. Ma, *Effects of heating rate on the structure and properties of SiOC ceramic foams derived from silicone resin.* Ceramics International, 2012. **38**(3): p. 2101-2104.
155. Colombo, P. and J.R. Hellmann, *Ceramic foams from preceramic polymers.* Materials Research Innovations, 2002. **6**(5-6): p. 260-272.
156. Zocca, A., et al., *SiOC ceramics with ordered porosity by 3D-printing of a preceramic polymer.* Journal of Materials Research, 2013. **28**(17): p. 2243-2252.
157. Eckel, Z.C., et al., *Additive manufacturing of polymer-derived ceramics.* Science, 2016. **351**(6268): p. 58-62.
158. Militký, J., M. Černý, and P. Jakeš, *Composite Materials with Basalt Fibre Reinforcement and Pyrolysed Polysiloxane Matrix.* 2008, Institute of Rock Structure and Mechanics: Prague. p. 31-36.
159. Černý, M., et al., *Strength, elasticity and failure of composites with pyrolyzed matrices based on polymethylsiloxane resins with optimized ratio of D and T components*. Journal of Composite Materials, 2012. **47**(8): p. 1055-1066.
160. Casas, L. and J.M. Martínez-Esnaola, *Microstructural characterisation of an alumina/mullite composite tested in creep.* Materials Science and Engineering: A, 2004. **368**(1–2): p. 139-144.
161. Colombo, P., et al., *Joining of reaction-bonded silicon carbide using a preceramic polymer.* Journal of Materials Science, 1998. **33**(9): p. 2405-2412.
162. Černý, M., et al., *Comparison of Mechanical Properties and Structural Changes of Continous Basalt and Glass Fibres at Elevated Temperatures.* Ceramics - Silikáty, 2007. **51**(2): p. 82-88.
163. Černý, M., Z. Sucharda, and P. Glogar, *Mechanical Behavior of Polysiloxane Matrix-based Composite Reinforced with Basalt Fibres at Elevated Temperatures.* Acta Geodynamica et Geomaterialia, 2008. **5**(4): p. 399-406.
164. Sigma-Aldrich. *Poly(dimethylsiloxane)*. [cited 2017 23.5.]; Available from: http://www.sigmaaldrich.com/catalog/product/aldrich/469319?lang=en&region=CZ.
165. Sigma-Aldrich. *Poly(methylphenylsiloxane)*. [cited 2017 23.5.]; Available from: http://www.sigmaaldrich.com/catalog/product/aldrich/378496?lang=en&region=CZ.
166. Černý, M., et al., *Changes in structure and in mechanical properties during the pyrolysis conversion of crosslinked polymethylsiloxane and polymethylphenylsiloxane resins to silicon oxycarbide glass.* Ceramics International, 2015. **41**(5, Part A): p. 6237-6247.
167. Strachota, A., et al., *Preparation of silicon oxynitrocarbide (SiONC) and of its ceramic-fibre-composites via hydrosilylation/radical polymerization/pyrolysis.* Journal of Non-Crystalline Solids, 2015. **423–424**: p. 9-17.
168. Černý, M., et al., *Mechanical properties of partially pyrolysed composites with plain weave basalt fibre reinforcement.* Ceramics International, 2014. **40**(5): p. 7507-7521.
169. Deák, T. and T. Czigány, *Chemical composition and mechanical properties of basalt and glass fibers: a comparison.* Textile Research Journal, 2009. **79**(7): p. 645-651.

170. Basfiber. *Basfiber - Mechanical properties*. [cited 2017 23.5.]; Available from: http://www.basfiber.com/1.
171. Braue, W., et al., *Failure Analysis of Nextel™ 720 Fibers Subjected to High-Temperature Testing: The Role of Intrinsic Fiber Impurities.* High Temperature Ceramic Matrix Composites, 2001: p. 90-95.
172. 3M. *3M™Nextel™ Woven Ceramic Fabrics3M™ Nextel™ Ceramic Fibers and Textiles*. [cited 2017 23.5.]; Available from: http://multimedia.3m.com/mws/media/1327055O/3m-nextel-technical-reference-guide.pdf.
173. Wilson, D.M., *New high temperature oxide fibers.* High Temperature Ceramic Matrix Composites, HT-CMC4, W. Krenkel, R. Naslain, H. Schneider, eds., Wiley VH, Munich Germany, 2002.
174. Wilson, D.M., S.L. Lieder, and D.C. Lueneburg. *Microstructure and high temperature properties of Nextel 720 fibers*. John Wiley & Sons.
175. Černý, M., P. Glogar, and Z. Sucharda, *Mechanical Properties of Basalt Fiber Reinforced Composites Prepared by Partial Pyrolysis of a Polymer Precursor.* Journal of Composite Materials, 2009. **43**(9): p. 1109-1120.
176. *Kern&Sohn GmbH, Operating instructions Set for Density determination for Analytical Balances KERN ACJ / ACS*. [cited 2017 23.5.]; Available from: http://dok.kern-sohn.com/manuals/files/English/ACS-A03-BA-e-1210.pdf.
177. Smith, L.R., et al., *Springer handbook of materials measurement methods*. 2006: Springer Science & Business Media.
178. *EN 843-4. Advanced technical ceramics - Monolithic ceramics - Mechanical properties at room temperature - Part 4: Vickers, Knoop and Rockwell Superficial hardness tests*. January 1995, CEN: Brussels.
179. *EN 843-2. Advanced technical ceramics - Monolithic ceramics - Mechanical properties at room temperature - Part 2: Determination of elastic moduli (ENV)*. December 1995, CEN: Brussels.
180. *ASTM E 1304-97 Standard Test Method for Plane-Strain (Chevron-Notch) Fracture Toughness of Metallic Materials*. April 1997, ASTM International: United States.
181. Norman, D.A. and R.E. Robertson, *The effect of fiber orientation on the toughening of short fiber-reinforced polymers.* Journal of Applied Polymer Science, 2003. **90**(10): p. 2740-2751.
182. Bluhm, J.I., *Slice synthesis of a three dimensional "work of fracture" specimen.* Engineering Fracture Mechanics, 1975. **7**(3): p. 593-604.
183. *EN 843-1. Advanced technical ceramics - Monolithic ceramics - Mechanical properties at room temperature - Part 1: Determination of flexural strength*. January 1995, CEN: Brussels.
184. Valentino, P., et al. *Mechanical characterization of basalt fibre reinforced plastic with different fabric reinforcements–Tensile tests and FE-calculations with representative volume elements (RVEs)*. in *CONVEGNO IGF XXII ROMA 2013*. 2013.
185. Chlup, Z., et al., *Fibre-matrix interface development during high temperature exposition of long fibre reinforced SiOC matrix.* Key Engineering Materials, 2014. **592**: p. 401-404.
186. Schmücker, M., F. Flucht, and H. Schneider, *Temperature Stability of 3M Nextel™ 610, 650, and 720 Fibers-A Microstructural Study*. High Temperature Ceramic Matrix Composites, 2001: p. 73-78.
187. Liang, T., et al., *Silicon oxycarbide ceramics with reduced carbon by pyrolysis of polysiloxanes in water vapor.* Journal of the European Ceramic Society, 2010. **30**(12): p. 2677-2682.

188. Havelcová, M., et al., *Effect of the dimethylsilyloxy co-monomer "D" on the chemistry of polysiloxane pyrolysis to SiOC.* Journal of Analytical and Applied Pyrolysis, 2016. **117**: p. 30-45.
189. Strachota, A., et al., *Preparation of Silicon Oxycarbide Composites Toughened by Inorganic Fibers via Pyrolysis of Precursor Siloxane Composites.* Acta Physica Polonica a, 2011. **120**(2): p. 326-330.
190. Parmentier, J., G.D. Soraru, and F. Babonneau, *Influence of the microstructure on the high temperature behaviour of gel-derived SiOC glasses.* Journal of the European Ceramic Society, 2001. **21**(6): p. 817-824.
191. Turquat, C., et al., *Transmission Electron Microscopy and Electron Energy-Loss Spectroscopy Study of Nonstoichiometric Silicon-Carbon-Oxygen Glasses.* Journal of the American Ceramic Society, 2001. **84**(10): p. 2189-2196.
192. Gulbransen, E.A. and S.A. Jansson, *The high-temperature oxidation, reduction, and volatilization reactions of silicon and silicon carbide.* Oxidation of Metals, 1972. **4**(3): p. 181-201.
193. Dzhigiris, D.D., et al., *Continuous basalt fiber.* Glass and Ceramics, 1983. **40**(9): p. 467-470.
194. Farsani, R.E., S. Khalili, and V. Daghigh, *Charpy impact response of basalt fiber reinforced epoxy and basalt fiber metal laminate composites: Experimental study.* International Journal of Damage Mechanics, 2014. **23**(6): p. 729-744.
195. Černý, M., et al., *Fracture properties of basalt fibre composites with cured or pyrolysed matrix.* Fractography of Advanced Ceramics Iii, 2009. **409**: p. 326-329.
196. Pan, N., *Analysis of woven fabric strengths: Prediction of fabric strength under uniaxial and biaxial extensions.* Composites Science and Technology, 1996. **56**(3): p. 311-327.
197. Glogar, P., et al., *Microstructure and mechanical properties of heat resistant composites reinforced with basalt fibres.* Ceramics-Silikaty, 2007. **51**(4): p. 190-197.

LIST OF PUBLICATIONS RELATED TO THE WORK

JOURNALS

Martina Halasova, Zdenek Chlup, Adam Strachota, Martin Cerny, Ivo Dlouhy: *Mechanical response of novel SiOC glasses to high temperature exposition*, Journal of the European Ceramic Society 32 (2012) 4489–4495.

Zdeněk Chlup, Martin Černý, Adam Strachota, Martina Halasova and Ivo Dlouhy: *Fibre-matrix interface development during high temperature exposition of long fibre reinforced SiOC matrix*; Key Engineering Materials Vols. 592-593 (2014) pp 401-404.

Zdeněk Chlup, Martin Černý, Adam Strachota, Zbyněk Sucharda, Martina Halasová, Ivo Dlouhý: *Influence of pyrolysis temperature on fracture response in SiOC based composites reinforced by basalt woven fabric*, Journal of the European Ceramic Society 34 (2014), pp. 3389-3398.

Martin Černý, Martina Halasová, Jana Schwaigstillová, Zdeněk Chlup, Zbyněk Sucharda, Petr Glogar, Jaroslava Svítilová, Adam Strachota, Šárka Rýglová: *Mechanical properties of partially pyrolysed composites with plain weave basalt fibre reinforcement*, Ceramics International 40 (2014) 7507-7521.

Martin Černý, Zdeněk Chlup, Adam Strachota, Martina Halasová, Šárka Rýglová, Jana Schweigstillová, Jaroslava Svítilová, Martina Havelcová: *Changes in structure and in mechanical properties during the pyrolysis conversion of crosslinked polymethylsiloxane and polymethylphenilsiloxane resins to silicon oxycarbide glass*, Ceramics International 41 (2015) 6237-6247.

Adam Strachota, Martin Černý, Zdeněk Chlup, Miroslav Šlouf, Jiří Brus, Josef Pleštil, Zbyněk Sucharda, Martina Havelcová, Martina Halasová: *Preparation of silicon oxynitrocarbide (SiONC) and of its ceramic-fibre-composites via hydrosilylation/radical polymerization/pyrolysis*, Journal of Non-Crystalline Solids 423-424 (2015) 9–17.

Martina Halasová, Martin Černý, Adam Strachota, Zdeněk Chlup, Ivo Dlouhý: *Fracture response of SiOC based composites on dynamic loading*, Journal of Composite Materials 50[11] (2016) 1547–1554.

INTERNATIONAL CONFERENCES

Martina Halasova, Martin Cerny, Adam Strachota, Zdenek Chlup: *Mechanical properties of SiOC materials exposed to the high temperatures*, Junior Euromat 2012, Laussane, Switzerland, 23-27 July 2012.

Martina Halasová, Zdeněk Chlup, Martin Černý, Adam Strachota, Zbyněk Sucharda, Ivo Dlouhý: *Effect of Loading Rate on the Behaviour of Partially Pyrolyzed Basalt Fibre Reinforced Composite*, CIMTEC 2014 - 13th International Conference on Modern Materials and Technologies, Montecatini Terme, Italy, June 8-13, 2014.

NATIONAL CONFERENCES

Martina Halasová, Zdeněk Chlup, Adam Strachota, Martin Černý: *Hodnocení vlastností pyrolyzovaných pryskyřic*, Víceúrovňový design pokrokových materiálů, 2011.

Halasova, M., Chlup, Z., Černý, M., Dlouhý, I.: *Stress relaxation in partially pyrolysed SiOC materials*; Multi-level Design of Advanced Materials, doctoral conference, Velké Bílovice, CR (2015), s. 100-105.

APPENDIX

Table A.1 Density of MS and MPS materials cured at 250°C and pyrolyzed at temperatures from 400 to 1000°C.

Curing and pyrolysis temperature [°C]	Density [g·cm^{-3}]	
	MS	MPS
250 (curing)	1.23 ± 0.00	1.27 ± 0.01
400	1.20 ± 0.01	1.25 ± 0.00
500	1.18 ± 0.00	1.22 ± 0.01
600	1.21 ± 0.02	1.22 ± 0.01
700	1.38 ± 0.01	1.38 ± 0.00
800	1.69 ± 0.02	1.63 ± 0.01
900	1.88 ± 0.02	1.73 ± 0.01
1000	2.04 ± 0.02	1.82 ± 0.01

Table A.2 Density of MS and MPS materials pyrolyzed at 650°C and MPS material pyrolyzed at 520°C, at various heating rates.

Dwell time	Density [g·cm^{-3}]		
	MS	MPS (650°C)	MPS (520°C)
0 hours (5 min)	1.16 ± 0.01	1.39 ± 0.01	1.23 ± 0.01
1 hour	1.23 ± 0.01	1.34 ± 0.01	1.20 ± 0.01
2 hours	1.29 ± 0.01	1.32 ± 0.01	1.18 ± 0.01
5 hours	1.35 ± 0.01	1.35 ± 0.01	1.19 ± 0.00
10 hours	NA*	NA*	1.21 ± 0.01

*NA… not analysed

Table A.3 Density of MS and MPS materials pyrolyzed at 1000°C with various heating rates.

Heating rate [°C·min^{-1}]	Density [g·cm^{-3}]	
	MS	MPS
0.5	2.00 ± 0.02	1.80 ± 0.02
1	2.04 ± 0.03	1.84 ± 0.01
2	2.01 ± 0.02	1.80 ± 0.01
4	2.04 ± 0.02*	1.83 ± 0.00
6.4	2.06 ± 0.02	1.84 ± 0.01
10	2.03 ± 0.03	1.85 ± 0.01

* The value was estimated from previous experiment for MS material prepared at identical conditions (MS material pyrolyzed at 1000°C with heating rate of 4°C·min^{-1} – see **Table A1**).

Table A.4 Density of MS and MPS materials cured at 250°C and pyrolyzed at 400–1000°C after two years from the first measurement – a comparison. Labels MS/MPS+2Y denote the measurement conducted two years later from the initial measurement.

Curing and pyrolysis temperature [°C]	Density [g·cm^{-3}]			
	MS	MS+2Y	MPS	MPS+2Y
250 (curing)	1.23 ± 0.00	1.23 ± 0.00	1.27 ± 0.01	1.27 ± 0.01
400	1.20 ± 0.01	1.19 ± 0.01	1.25 ± 0.00	1.25 ± 0.00
500	1.18 ± 0.00	1.18 ± 0.00	1.22 ± 0.01	1.21 ± 0.01
600	1.21 ± 0.02	1.19 ± 0.02	1.22 ± 0.01	1.23 ± 0.00
700	1.38 ± 0.01	1.38 ± 0.00	1.38 ± 0.00	1.38 ± 0.00
800	1.69 ± 0.02	1.68 ± 0.01	1.63 ± 0.01	1.62 ± 0.00
900	1.88 ± 0.02	1.87 ± 0.01	1.73 ± 0.01	1.72 ± 0.00
1000	2.04 ± 0.02	2.05 ± 0.01	1.82 ± 0.01	1.81 ± 0.01

Table A.5 Vickers and Martens hardness of MS and MPS materials in cured (250°C) and pyrolyzed (400–1000°C) states.

Curing and pyrolysis temperature [°C]	HV 0.2		HM [MPa]	
	MS	MPS	MS	MPS
250 (curing)	10.11 ± 1.78	11.56 ± 0.43	57.69 ± 6.45	82.73 ± 2.60
400	7.35 ± 0.64	10.95 ± 0.22	53.18 ± 9.10	81.83 ± 1.57
500	NA*	164.6	79.22 ± 7.91	96.80 ± 3.54
600	NA*	147.1 ± 17.0	72.00 ± 6.60	456.7 ± 42.0
700	227.8 ± 35.1	259.5 ± 59.8	861.4 ± 21.7	1196 ± 47
800	467.9 ± 41.4	487.8 ± 39.0	1978.6 ± 55.4	1955 ± 41
900	830.8 ± 96.1	958.3 ± 81.7	3249± 125	2979 ± 63
1000	1065 ± 117	1080 ± 162	4137 ± 216	3313 ± 107

*NA... not analysed due to full recovery of the indents.

Table A.6 Indentation elastic modulus of MS and MPS materials cured at 250°C and pyrolyzed at 400–1000°C.

Curing and pyrolysis temperature [°C]	Indentation elastic modulus [GPa]	
	MS	MPS
250 (curing)	1.32 ± 0.06	2.53 ± 0.17
400	0.95 ± 0.08	2.58 ± 0.02
500	1.17 ± 0.11	1.57 ± 0.04
600	1.15 ± 0.07	6.59 ± 0.59
700	12.53 ± 0.37	18.19 ± 0.73
800	31.81 ± 0.88	32.25 ± 0.73
900	52.78 ± 1.74	47.97 ± 0.89
1000	67.29 ± 3.89	53.66 ± 2.00

Table A.7 Martens hardness (a) and indentation modulus (b) for MS and MPS materials pyrolyzed at 650 °C for 0–5 hours.

Dwell time	HM [MPa]		E_{IT} [GPa]	
	MS	MPS	MS	MPS
0 hour (5 min)	97.57 ± 20.41	335.29 ± 28.19	1.21 ± 0.16	4.42 ± 0.30
1 hour	306.00 ± 18.80	666.67 ± 18.75	3.92 ± 0.18	9.06 ± 0.23
2 hours	543.14 ± 16.20	804.29 ± 19.61	7.05 ± 0.16	10.84 ± 0.31
5 hours	924.43 ± 95.88	1144.57 ± 44.95	11.89 ± 1.17	14.90 ± 0.36

Table A.8 Martens hardness and indentation modulus for MS and MPS materials pyrolyzed at 520°C for 0–10 hours.

Dwell time	HM [MPa]	E_{IT} [GPa]
0 hour (5 min)	72.70 ± 2.11	1.54 ± 0.11
1 hour	63.89 ± 8.49	0.98 ± 0.16
2 hours	113.75 ± 4.03	1.51 ± 0.05
5 hours	245.00 ± 20.72	3.14 ± 0.28
10 hours	288.00 ± 31.74	3.69 ± 0.46

Table A.9 Maximum and minimum indentation depth in MS and MPS collected during the indentation and the depth measured after 24 hours from the indentation test. The relaxation expresses the difference between h_{min} captured in the indentation test and after 3D reconstruction (h_{conf}).

Material	Curing and pyrolysis temperature [°C]	Machine data		3D reconstruction	Relaxation [%]
		h_{max} [μm]	h_{min} [μm]	h_{conf} [μm]	
MS	250 (curing)	34.04 ± 1.14	11.65 ± 1.37	1.56 ± 0.02	86.7
	400	34.49 ± 1.42	8.54 ± 0.68	0.50 ± 0.03	94.1
	500	28.75 ± 0.66	6.49 ± 0.11	0.22 ± 0.06	96.6
	600	30.19 ± 1.19	7.10 ± 0.40	0.29 ± 0.04	95.9
	700	9.20 ± 0.14	3.32 ± 0.10	1.84 ± 0.05	44.8
	800	6.02 ± 0.08	2.93 ± 0.06	2.12 ± 0.03	27.6
	900	4.68 ± 0.09	2.38 ± 0.06	2.09 ± 0.06	12.3
	1000	4.13 ± 0.11	2.07 ± 0.07	1.86 ± 0.02	10.0
MPS	250 (curing)	29.11 ± 0.26	17.43 ± 0.23	5.23 ± 0.01	70.0
	400	29.17 ± 0.34	16.97 ± 0.45	3.24 ± 0.05	80.9
	500	27.07 ± 0.32	7.42 ± 0.43	0.04 ± 0.02	99.5
	600	12.80 ± 0.60	3.38 ± 0.09	0.65 ± 0.06	80.9
	700	7.77 ± 0.19	2.81 ± 0.06	1.19 ± 0.05	57.8
	800	6.08 ± 0.07	2.83 ± 0.07	1.56 ± 0.02	45.1
	900	4.89 ± 0.05	2.30 ± 0.02	1.69 ± 0.04	26.7
	1000	4.63 ± 0.06	2.20 ± 0.04	1.76 ± 0.02	19.9

Table A.10 Vickers hardness of laboratory synthesized materials.

HV0.2	Pyrolysis [°C]	Annealing [°C]	
	1000	1300	1500
SiONC	1439 ± 87	1137 ± 90	1212 ± 149
T4D1-B	1074 ± 45	1064 ± 48	998 ± 35
T4D1-Fe	1092 ± 47	969 ± 24	938 ± 96
T19D1	1214 ± 1267	1291 ± 124	1089 ± 96

Table A.11 Martens hardness of laboratory synthesized materials.

HM [MPa]	Pyrolysis [°C]	Annealing [°C]	
	1000	1300	1500
SiONC	5695 ± 229	4769 ± 269	4820 ± 362
T4D1-B	4216 ± 392	3611 ± 580	3710 ± 474
T4D1-Fe	4311 ± 118	3520 ± 487	3565 ± 165
T19D1	3299 ± 687	3393 ± 598	3214 ± 727

Table A.12 Indentation elastic modulus of laboratory synthesized materials SiONC, T4D1-B, T4D1-Fe and T19D1.

E_{IT} [GPa]	Pyrolysis [°C]	Annealing [°C]	
	1000	1300	1500
SiONC	99.09 ± 3.18	86.19 ± 2.71	73.05 ± 14.22
T4D1-B	70.93 ± 5.97	62.58 ± 7.68	64.02 ± 7.50
T4D1-Fe	71.68 ± 3.25	59.29 ± 6.19	59.01 ± 2.59
T19D1	56.83 ± 8.63	54.46 ± 8.32	52.31 ± 10.82

Table A.13 Apparent density of MS and MPS composites (MSC and MPSC, respectively).

Pyrolysis temperature [°C]	Apparent density [$g \cdot cm^{-3}$]	
	MSC	MPSC
600	1.75 ± 0.04	1.82 ± 0.02
650	1.91 ± 0.03	1.92 ± 0.02
700	2.05 ± 0.07	1.95 ± 0.02
750	2.18 ± 0.02	2.13 ± 0.03
800	2.16 ± 0.02	2.13 ± 0.02

Table A.14 Elastic modulus of MSC and MPSC with basalt fabric.

Pyrolysis temperature [°C]	Elastic modulus [GPa]	
	MSC	MPSC
600	16.4 ± 1.4	25.5 ± 0.4
650	29.0 ± 2.3	32.6 ± 1.4
700	32.7 ± 2.6	33.6 ± 0.9
750	37.7 ± 2.3	40.3 ± 2.0
800	44.2 ± 4.0	49.6 ± 1.1

Table A.15 Flexural strength of MSC and MPSC with basalt fabrics.

Pyrolysis temperature [°C]	Flexural strength [MPa]	
	MSC	MPSC
600	42.2 ± 9.0	111.2 ± 5.0
650	118.8 ± 22.5	132.6 ± 4.5
700	99.6 ± 6.8	121.3 ± 8.5
750	87.5 ± 6.0	127.7 ± 5.0
800	77.3 ± 5.0	116.3 ± 8.0

Table A.16 Total fracture energy of MS and MPS composites.

Pyrolysis temperature [°C]	Fracture energy [kJ·m^{-2}]			
	MSC		MPSC	
	out-of-plane	in-plane	out-of-plane	in-plane
600	0.51 ± 0.15	1.39 ± 0.67	1.26 ± 0.64	2.52 ± 0.24
650	3.60 ± 1.71	6.32 ± 1.12	2.15 ± 0.82	3.00 ± 0.21
700	2.92 ± 0.94	2.64 ± 0.34	2.12 ± 0.22	2.55 ± 0.13
750	1.03 ± 0.16	0.97 ± 0.21	1.53 ± 0.60	2.20 ± 0.26
800	0.90 ± 0.48	0.72 ± 0.04	0.84 ± 0.44	0.89 ± 0.25

Table A.17 Point analysis of composite pyrolyzed at 650°C and annealed at 550°C.

Specimen	Component	Element [at. %]								
		O	Mg	Al	Si	K	Ca	Ti	Fe	Σ
650RT	Fibre	52.43	-	2.59	41.01	0.14	0.72	0.14	2.96	99.99
650RT	Fibre	51.81	0.50	2.16	43.89	0.16	0.71	0.07	0.70	100.00
650/550	Fibre	60.87	-	0.70	37.98	-	0.18	0.05	0.22	100.00
650/550	Matrix	64.29	-	-	35.71	-	-	-	-	100.00

Table A.18 Elemental analysis on composite pyrolyzed at 750°C and annealed at 550°C.

Specimen	Spectrum	F/M	P	Element [at. %]									
				O	Na	Mg	Al	Si	K	Ca	Ti	Fe	Σ
750RT	9	F	G	25.59			0.62	14.32				59.47	100
750RT	10	M	A	50.65	2.56	2.39	10.65	28.15	1.18	3.24	0.38	0.79	99.99
750RT	11	M	A	64.11	-	-	-	35.89	-	-	-	-	100
750RT	12	F	G	10.74			1.47	6.42		0.57		80.80	100
750RT	13	F	A	52.12	2.6	0.72	10.80	29.41	1.59	2.11	0.38	0.26	99.99
750RT	14	F	A	48.94	1.44	3.52	10.43	27.11	0.77	5.48	0.37	1.93	99.99
750RT	15	F	A	49.16	1.42	3.96	9.95	27.23	0.71	5.07	0.45	2.04	99.99
750RT	16	F	A	51.33	2.56	0.84	11.23	29.54	1.64	2.19	0.38	0.29	100
750RT	23	F	G	6.24	-	-	0.35	2.59	-	0.12	-	90.70	100
750RT	24	F	G	9.30	-	-	1.22	6.57	-	0.38	0.10	82.43	100
750RT	25	F	G	14.52	-	-	0.31	5.85	-	0.09	-	79.23	100
750RT	26	F	G	26.87	-	-	0.49	13.80	-	0.16	-	58.68	100
750RT	27	F	G	15.93	-	-	0.38	7.22	-	0.11	-	76.36	100
750RT	28	F	G	23.36	-	0.86	2.76	18.77	-	0.94	0.13	53.19	100.01
750RT	29	F	G	15.92	-	-	2.43	12.50	-	0.96	0.16	68.03	100
750RT	30	F	G	11.16	-	-	0.33	4.13	-	0.12	-	84.26	100
750RT	31	F	G	26.17	-	-	0.40	14.44	-	0.08	-	58.90	99.99
750RT	32	F	A	52.61	-	-	1.96	45.02	-	0.24	0.08	0.09	100
750RT	33	F	G	20.73	-	-	0.91	11.49	0.06	0.37	0.11	66.33	100
750RT	34*	F	G	18.24	-	-	1.24	10.43	0.05	0.50	0.13	64.69	100
750/550	1**	F	G	56.29	-	0.44	1.87	40.06	0.10	0.58	0.08	0.57	99.99
750/550	2	F	A	55.79	-	0.35	1.58	41.16	0.09	0.52	0.07	0.47	100.03
750/550	3	F	G	56.25	-	2.32	2.12	36.72	-	0.81	0.23	1.55	100
750/550	4***	F	G	23.37	-	-	0.53	11.74	-	0.14	0.06	64.16	100
750/550	17	F	A	49.85	1.86	2.83	9.53	26.80	0.70	4.07	0.49	3.88	100.01
750/550	18	F	A	53.45	1.88	2.02	9.71	24.79	0.89	3.56	-	3.70	100
750/550	19	F	A	51.14	1.54	2.38	9.51	26.20	0.82	4.43	0.44	3.54	100
750/550	20	F	A	55.81	1.67	1.58	9.57	23.11	0.86	3.90	0.28	3.23	100.01
750/550	21	F	G	54.31	-	7.96	4.95	25.94	-	1.76	0.54	4.54	100
750/550	22	F	G	56.22	-	6.02	4.89	25.17	-	2.82	0.87	4.00	99.99

F/M... fibre or matrix

P... phase: A – amorphous, G – grain (crystalline or spherulitic)

** The only spectrum where was analysed also Cu in amount of 4.72 at. %*

*** needle-like particle*

**** iron particle*